



K A U N O
TECHNOLOGIJOS
UNIVERSITETAS

ISSN 1822-5721

2009

MEDICAL PHYSICS in the BALTIC STATES

PROCEEDINGS OF THE 7th INTERNATIONAL
CONFERENCE ON *MEDICAL PHYSICS*

Kaunas, Lithuania
8-10 October , 2009

ISSN 1822-5721

KAUNAS UNIVERSITY OF TECHNOLOGY

MEDICAL PHYSICS IN THE BALTIC STATES

Proceedings of the 7th International Conference on Medical Physics

**Kaunas, Lithuania
8 – 10 October, 2009**

Executive editor: **D.Adlienė**

CONFERENCE IS ORGANIZED BY:

Kaunas University of Technology
Malmö University Hospital, Lund University
Lithuanian Radiation Protection Centre
Kaunas Medical University Hospital

PROGRAM COMMITTEE

Diana ADLIENĖ - Kaunas University of Technology, *chairwoman*
Sören MATTSSON - Lund University, Malmö University Hospital, *chairman*
Ričardas ROTOMSKIS – Vilnius University
Albinas MASTAUSKAS – Lithuanian Radiation Protection Centre
Elona JUOZAITYTĖ – Medical University of Kaunas

ORGANIZING COMMITTEE

Lena ANCEVIČIENĖ – Kaunas University of Technology
Jurgita LAURIKAITIENĖ – Kaunas University of Technology

CONFERENCE IS SUPPORTED BY:

Lithuanian State Science and Studies Foundation
Kaunas University of Technology
Malmö University Hospital
Lithuanian Radiation Protection Centre
Lithuanian Society of Medical Physicists
Lithuanian Radiation Protection Society
UAB „Lokmis“
UAB „Medicinos fizikai“

Papers included in the Proceedings were referred by independent peer referees

© Kaunas University of Technology

CONFERENCE & WORKSHOP PROGRAM

Thursday, 8 October 2009

RADIOLOGY SEMINAR

Klaipėda University Hospital, (Central building, 2nd floor conference hall), Liepojos street 41, Klaipėda

- 10.00-10.15** Reception of guests by director of the Klaipėda University hospital, *prof. habil. dr. Vinsas Janušonis*
- 10.30–11.30** *Igoris Kniažėvas* (head of radiology department), *Marius Laurikaitis* (major medical physicist), *Aista Plieskienė* (head of high energy department), Presentations about the structure, work and equipment at Klaipėda University Hospital, Radiology Clinic and Nuclear Medicine Centre.

Coffee for participants

- 11.30-11.40** *Diana Adlienė, Sören Mattsson*. Introduction to seminar
- 11.40-12.10** *Dr. Aista Plieskienė*. Presentation of Radiotherapy Center, University Hospital of Klaipėda
- 12.10-12.50** *Torsten Landberg* and *Per Nilsson* (*MalmöUniversity Hospital, Umea University Hospital, Sweden*). Prescribing, recording and reporting external beam radiotherapy. Questions and answers.
- 12.50-13.15** *Ulrika Svanholm* (*MalmöUniversity Hospital, Sweden*). Quality assurance programs for gammacameras and SPECT
- 13.15-13.40** *Carl-Magnus Nilsson* (*MalmöUniversity Hospital, Sweden*): Quality assurance programs for a linear accelerator
- 13.40-14.00** *Darius Mikšys*. Positron emitting radionuclides in medicine
- 14.00** Discussions

Coffee for participants

Friday, 9 October 2009

- 9.00-10.00** Registration of participants at **Kaunas University of Technology, Studentų g.50–325Fa., Kaunas**
- 9.45-10.00** Conference opening: *Vytautas Janilionis*, *Dean of the Faculty of Fundamental Sciences*; *Sören Mattsson*, *Lund University*, *MalmöUniversity Hospital*, *Diana Adlienė*, *Kaunas University of Technology*

Session 1, Chair: prof. Diana Adlienė

- 10.00-10.30** *Sören Mattsson*. Recent advances and trends in X-ray and molecular imaging.
- 10.30-10.45** *Lada Bumbure, Yuri Dekhtyar, Tatyana Kirsanova, Zanna Yakovleva*. Practical Application of Statistical Approach on Digital X-ray Imaging Quality verification.
- 10.45-11.00** *Marcus Söderberg, Mikael Gunnarsson*. Dose reduction and image quality evaluations of automatic exposure control systems from four different CT manufacturers
- 11.00-11.15** *Ulrika Svanholm*. Quality assurance programs for gammacameras and SPECT

- 11.15-11.30 *Daiva Leščiute, Valdas Šablinskas, Valdemaras Aleksa, Arunas Maršalka, Feliksas Jankevičius*. Diagnostics of cancerous prostate tissue by means of infrared spectroscopical imaging

Coffee break 11:30-11:45

Session 2, Chair: Lada Bumbure

- 11.45-12.00. *Dalia Kaškelytė, Arūnas Čiburys, Saulius Bagdonas, Giedrė Streckytė, Ričardas Rotomskis, Roaldas Gadonas*. Fiber –optics based laser system for 2-D fluorescence detection and optical biopsy.
- 12.00-12.15 *Vilius Poderys, Deividas Motekaitis, Ričardas Rotomskis*. CdTe quantum dots stabilization by protein in aqueous solution.
- 12.15-12.30 *Augustinas Kulbickas*. Nanodiamonds as cell biomarkers.
- 12.30-12.45 *Marius Franckevičius*. Dendrimers as drug nanocontainers.
- 12.45-13.00 *Judita Puišo, Igoris Prosyčėvas, Asta Guobienė*. Investigations of silver nanoparticles for UV personal dosimeters.

Time for lunch 13:00 – 14:00

Session 3. Chair: Dalia Kaškelytė

- 14.00-14.30 *Torsten Landberg* and *Per Nilsson* Prescribing, recording and reporting external beam radiotherapy.
- 14.30-14.45 *Sandija Plaude, Sergey Popov, Arturs Meijers, Albert Miller, Yuri Dekhtyar*. Modelling of the response of the ionization chambers in radiotherapy fields with dynamic intensity modulation.
- 14.45-15.00 *Arturs Meijers, Sergey Popov*. Modeling of field parameters for dose verification in external beam radiotherapy
- 15.00-15.15 *Carl-Magnus Nilsson*. Quality assurance programs for a linear accelerator
- 15.15-15.30 *Alexander Kouznetsov*. AtomMed Center: strategic goals and overview of ongoing activities

Coffee break 15:30-16:00

Session 4. Chair: dr. Judita Puišo

- 16.00-16.30 *Christian Bernhardsson, Maria Christiansson, Christopher Rääf, Sören Mattsson*. OSL in household salt (NaCl) for environmental, occupational and medical dosimetry
- 16.30-16.45 *Yuri Dekhtyar, Linda Lancere, Nataliya Polayka, Alexander Rapoport, Anna Rusakova, Alexander Sudnikov, Valdis Valters*. Ultraviolet radiation influenced wettability and biological properties of PMMA surface. Riga Technical University
- 16.45-17.00 *Skirmantė Mockevičienė, Igoris Prosyčėvas, Vaida Kačiulytė, Rita Pikaitė, Diana Adlienė*. Investigation of porous silicon irradiated with X-ray photons.
- 17.00-17.15 *Inga Cibulskaitė, Diana Adlienė*. Total and scatter dose modeling in photon irradiated Si samples covered by protective coatings.
- 17.15-17.30 *Jurgita Laurikaitienė, Judita Puišo, Šarūnas Meškinis, Valdas Šablinskas, Diana Adlienė*. Photon induced modification of protective a-C:H coatings.
- 17.30-17.45 *Nikolay Kazuchits, M. Rusetskyi, A. Shulenkov, V. Kukushkin, S. Martynov, V.Khrunov, J. Tuzov, G. Gatskevich, D. Kandybovich*. Application of a synthetic diamond detector for the measurement of relative dose distributions in radiotherapy.

19:00-22:00 Get-together party
“Perkūnas House“, Aleksoto g. 6, Kaunas

Saturday, 10 October 2009

9.00-10.0 Registration of participants at Kaunas University of Technology, Studentų g.50-325F, Kaunas.

Session 5. Chair: Inga Cibulskaitė

- 10.00-10.15** *Virgilijus Minialga, Birutė Statkevičienė.* Changes of swimmers body temperature obtained by thermovision method.
- 10.15-10.30** *Oleg Klepalov, Kęstutis Gediminskas, Romas Vilkas, Mindaugas Zikas.* Ignalina nuclear power plant dose monitoring system.
- 10.30-10.45** *Gediminas Adlys.* Application of neutrons in radiotherapy.
- 10.45 -11.00** *Darius Mikšys.* Positron emitting radionuclides in medicine
- 11.00-11.15** *Dovilė Šerenaitė.* Radiation protection of medical staff in Lithuania.
- 11.15-11.30** *Leonidas Krynkė, Julius Žiliukas.* Preliminary patient dose estimation for CT examinations in Lithuania.

Coffee break 11:30-12:00 & Poster session

11.30-12.00 Poster session

1. *Milda Pučetaite, Valdas Šablinskas, Vaiva Hedrixson, Zita Kučinskienė Arūnas Želvys, Feliksas Jankevičius.* Infrared spectroscopy studies of distribution of chemical components in urinary stones
2. *Irma Gajauskaite, Tatjana Zyk, Gediminas Adlys, Edvardas Kielius.* Health physics aspects of Tritium in nuclear sector
3. *Dainius Bernatavičius, Vladas Zaleskas. Darius Kybartas.* Investigation of the time and location dependent electromagnetic field radiation of mobile phones.
4. *Pranas Kanapeckas, Stasys Maciulevičius, Alfredas Otas, Algis Valys, Vytautas Petrauskas, Neringa Vaiciunaite.* Electromagnetic radiation at computerized workplaces and the impact of the magnetic field on human health.

Session 6. Chair: Christian Bernhardsson

- 12.00-12.15** *Diana Adlienė, Violeta Karenauskaitė, Ričardas Rotomskis.* Education of Medical Physicists in Lithuania
- 12.15-12.30** *Slavik Tabakov, Peter Smith, Franco Milano, Sven-Erik Strand, Inger-Lena Lamm, Cornelius Lewis, Magdalena Stoeva, Diana Adlienė.* e-Encyclopedia of medical physics with multilingual dictionary of terms - EMITEL
- 12.30** *Sören Mattsson.* Poster overview & final remarks

**RECENT ADVANCES AND TRENDS IN
MEDICAL X-RAY AND MOLECULAR IMAGING**

Sören MATTSSON

Medical Radiation Physics Malmö, Lund University, Malmö University Hospital, SE-205 02 Malmö, Sweden

Abstract: This paper is intended to give an overview of clinically used imaging methods with special reference to digital techniques and 3D techniques for X-ray and nuclear medicine/molecular imaging such as CT, SPECT and PET. The paper will focus on recent advances and trends.

Keywords: Medical imaging, tomography, X-ray, CT, PET, MRI, tomosynthesis, hybrid imaging

1. Introduction

Medical imaging is an invaluable part of modern health care. It is used for disease detection, classification, prognostic staging and to validate therapeutic response. In fact, recent advances in imaging technology have redefined how physicians diagnose and treat some of the most life threatening diseases like cancer and heart disease, and have nearly eliminated the need for exploratory surgery. Good images are the base for planning of therapies such as surgery and radiotherapy.

Imaging is also an important instrument for clinical research, where the requirements for quantitative and reproducible image data are especially high.

Clinical diagnostic imaging is currently using five major modalities: 1) Planar X-ray imaging, 2) computed tomography (CT), 3) magnetic resonance imaging (MRI), 4) nuclear medicine imaging (using planar gamma cameras, single-photon-emission-computed tomography (SPECT) and positron-emission tomography (PET)) and 5) ultrasound.

This paper will concentrate on X-ray and nuclear medicine imaging – methods that use ionising radiation. These techniques are currently undergoing major improvements and a change towards technologies that facilitate quantitative tomographic imaging.

2. X-ray imaging

2.1 Planar X-rays

X-ray imaging is still based on the X-ray tube as radiation source. Tungsten is the most common anode

material, except for mammography, which use Mo- and Rh- anodes. Filters of Al, Cu, Mo, and Rh are used to cut off different parts of the photon energy distribution. Currently used X-ray tubes are very efficient radiation sources. They have, however, shortcomings as high operating temperature. With a new cooling principle utilizing convective cooling, the need for waiting times due to cooling has been reduced. Moreover, an electronic beam deflection system for focal spot position and size control has opened for advanced applications. The ongoing nanotechnology based field emission X-ray source technology (Xintek, www.xintex.com), enables the generation of radiation with fine control of the spatial distribution of the X-rays and temporal modulation of the radiation [1]. The technology also enables the design of gantry-free stationary tomography imaging systems with faster scanning speed and potentially better imaging quality compared to today's commercial tomographic systems.

For the detection and imaging of the X-rays transmitted through the patient, flat-panel detectors have been developed for use in radiography and fluoroscopy to replace standard X-ray film, film-screen combinations and image intensifiers. Current technology use flat-panel detectors, made from evaporated CsI or Gd₂O₂S on a matrix of a-Si photodiodes for higher energies or a layer a-Se, directly converting the absorbed energy to a current for low energies (mammography).

The development of detectors for planar X-ray imaging has resulted in increased detection efficiency without significant loss of spatial resolution.

The availability of flat panel detector technology has also stimulated a number of new developments for tomographic imaging (See section 2.2).

2.1.1. Photon counting detection and energy resolved methods

Until now, conventional X-ray systems have used charge (energy) integrating film or detectors recording the total energy of all the X-rays transmitted through the patient's body. Photon counting is an alternative method to get an image from the detection of incoming photons. Photon counting detectors not only provide photon interaction counts and positions, but also photon energy information. This information can be used to produce "count images" or "energy weighting images" [2], which can achieve contrast enhancement when compared with "integrating images". The photon counting enables discrimination of electronic noise and more optimal use of the information in each X-ray photon. The absence of electronic noise is particularly important in low dose applications, for example in tomosynthesis (see below under 2.2.2.), where a number of exposures from different angles are required and since the dose in each projection is low, the sensitivity to electronic noise is high using today's "integrating images".

The photon-counting X-ray detectors can discriminate between photons with different energies and count them in a small number (2-5) of energy windows. The data in these energy windows may be thought of as arising from multiple simultaneous X-ray beams with individual energy distributions, and could thus potentially be used to perform tissue composition analysis.

In mammography, this could for example be used to enhance microcalcifications relative to soft tissue. In contrast X-ray investigations, a photon counting detector gives a unique opportunity to image the iodine through spectral imaging by adjusting one of the thresholds to its K-edge. Photon counting is also of advantage in CT systems and facilitates measurements of photons in several energy windows.

A major challenge for photon counting detectors is to enable the high count rate that is required for medical imaging.

2.1.2. Phase contrast imaging

The conventional X-ray imaging relies solely on X-ray absorption as a source of contrast in the image. Using also the phase information, details, which remain barely visible with conventional methods, can be seen. The method has been demonstrated using coherent synchrotron radiation. The main limitation to a widespread application of phase contrast imaging is the necessity to have a coherent X-ray source and a detector with high spatial resolution. Micro-focus X-ray tubes seems to be the only possible source for clinical work for the moment. It has been shown that such tubes deliver sufficiently coherent radiation for phase contrast and dark field imaging [3, 4]. This is important, as synchrotrons are rarely available in clinical practice. The X-ray tubes give, however, a low photon fluence rate compared to synchrotron radiation,

which means that only very compact geometries can be used with X-ray tubes.

2.2 Tomographic imaging

There are two trends in tomographic X-ray imaging: 1) increased use of CT, which is a high-dose technique; and 2) development of limited-angle tomography, also called tomosynthesis.

2.2.1 CT

The detector material in the CT-units has varied throughout the years. In the early 1970's NaI(Tl) coupled to PM-tubes were used, then CsI(Tl) in combination with photodiodes. In the 1980's Xe ion chambers were popular. Then again scintillators. Today different vendors use different scintillator material, e.g. Gd₂O₂S:Ce (Siemens, Philips), Gd₂O₂S:Pr (Toshiba), (Y,Gd)₂O₃:Eu (GE) in combination with photodiodes. The scintillator material must have a fast light decay to facilitate high count-rate. The sensitivity of the photodiode is temperature dependent. Therefore, the whole detector is kept at a temperature of 35-40° C. Presently a number of pure semiconductors are under development (no step with light). Examples of such semiconductors are: PbI₂, PbO, HgI₂, and CdZnTe.

Modern spiral CT can scan a whole body in 25 s using a gantry rotation time of 0.33 s. This gives the possibility to image even a beating heart. Multi-slice detectors recording up to 128 and now even 320 slices per revolution are available.

Dual energy X-ray techniques

The use of dual-energy X-ray techniques has traditionally been limited to conventional projection techniques. Dual-energy X-ray absorptiometry bone densitometry is used widely to quantify bone mineralisation for osteoporosis screening and therapy monitoring. Dual-energy chest radiography improves the detection of pulmonary masses by specifically highlighting bone and calcified structures or soft tissue. Some earlier CT scanners used rapid switching of the tube voltage during rotation. They could not, however, adapt the tube current fast enough, resulting in artefacts and loss of resolution. Another approach to dual-energy CT is to use just one X-ray source and a multilayered detector, each layer registering a specific band of energy for the attenuated x-rays. The latest generations of dual-energy CT systems that work according to this principle are being built with energy-sensitive photon counting detectors that can be used with a single kVp X-ray source.

Dual-energy CT is now available for clinical use on scanners that have two complete detector-tube assemblies in one rotating gantry. This dual source setup has been designed primarily to increase temporal resolution for cardiac imaging. It also allows simultaneous acquisition of data at two tube kV without the limitations imposed by the energy spectrum

of a single-tube x-ray or by the necessity of rapid tube current adaptation [5].

Imaging of a given material mixture using dual-source CT is performed with two X-ray beams of different effective photon energies. The combined absorption spectrum of the mixture is sampled at two points of the energy spectrum. These two data points, together with *a priori* knowledge of the mixture's components and their relative densities, can be used to determine the concentration of three materials in each voxel examined.

CT with flat panel detectors

Large-area flat panel detectors are now more and more used as an alternative to the conventional CT [6]. Examples of use are 1) routine interventional and intraoperative imaging using C-arm-based interventional flat panel detector CT e.g in connection with brachytherapy, 2) CT image-guided external tumor therapy, which is one of the fastest growing applications. Attaching a standard X-ray tube and a flat panel detector to a rotating linear accelerator allows for CT imaging of the patient on the therapy couch. The system is capable of producing images of soft tissue with good spatial resolution at acceptable imaging doses [7]. 3) CT for dedicated maxillo-facial scanning [8] and 4) CT for dedicated imaging of the breast. Last, but not least, 5) flat panel detector technology has also been used in standard CTs [9, 10].

The development of the flat panel detector technology has stimulated much of the developments and research in 3D imaging. Micro-CT also receives increasing attention due to the interest in molecular and small-animal imaging.

In external beam radiotherapy, the use of the treatment beam for imaging is of high interest because this application requires no additional hardware and the image obtained gives an exact image of the treatment. Such imaging has been possible thanks to the development of electronic portal imaging devices (EPID). Megavoltage cone beam computed tomography can be used for treatment planning in 3D conformal radiotherapy and IMRT, adaptive radiation therapy, single fraction palliative treatment and for the treatment of patients with metal prostheses.

2.2.2. Tomosynthesis

Tomosynthesis is a form of limited angle tomography that produces "slice" images from a series of projection images acquired as the X-ray tube moves over a prescribed angular range, typically from -25 degrees to $+25$ degrees in relation to the angle for the ordinary projection image. Because the projection images are not acquired over a full 360° rotation around the patient, the resolution in the z direction i.e., in the depth direction perpendicular to the x - y plane of the projection images is limited. However, the spatial

resolution in the x - y plane of the reconstructed slices is often superior to CT, and the ease of use in conjunction with conventional radiography makes tomosynthesis a potentially quite useful imaging modality [11].

3. Molecular imaging

Nuclear medicine or molecular imaging is based on an i.v. injection, oral administration or inhalation of a radioactive tracer. Upon administration one awaits distribution and accumulation of the tracer in the region of interest, e.g. an organ or a tumour. The emitted radiation is mapped by a collimator (planar nuclear medicine and SPECT) or coincidence using two detectors (PET), 2D or 3D, iterative reconstruction or filtered back projection, and attenuation correction. Focus in imaging has changed from structures to a combination of structures and functions, creating a renewed interest for nuclear medicine methods, which can visualise physiologic functions and metabolism in the human body and also have a potential for molecular imaging. This will be of high importance for the advancement of molecular medicine [12], drug development and delivery techniques [13].

3.1. Planar nuclear medicine

The basic measurement instrument in nuclear medicine is still the gamma cameras using a NaI(Tl) scintillator block coupled to an array of photomultiplier tubes. In recent years there has been a growing interest in developing compact gamma cameras to improve nuclear medicine imaging. These are of three types:

1. One or more scintillation crystals coupled to a single position-sensitive photomultiplier tube
2. A position-sensitive solid-state detector
3. An array of scintillation crystals coupled to an array of solid-state photo detectors.

Type 1 cameras are expensive, have significant dead area, and have geometric distortion and non-uniform gain that can vary with both time and count rate. Type 2 cameras have been under development for over 20 years. The best candidate for room temperature operation is CdZnTe, a high-atomic-number, solid-state crystal. However CdZnTe tends to be expensive and is difficult to manufacture in volumes large enough to form arrays of useful imaging size. Type 3 cameras typically use silicon photodiode arrays.

3.2. SPECT

Conventional nuclear medicine images compress the 3-dimensional (3D) distributions of radiotracers into a 2-dimensional image. Tomographic images remove these difficulties but at the price of longer acquisition times, poorer spatial resolution, and the susceptibility to artefacts. Recent advances in SPECT instrumentation

and processing have however made marked improvements in each of these areas [14].

3.3. PET

In PET, the camera encircles the patient with multiple rings of radiation detectors. Each pair of detectors measures the number of positron decays that lie along the line joining them. Soon after a positron is emitted by the radionuclide, it hits an electron, and the pair annihilates emitting two gamma rays. These gamma rays travel in nearly opposite directions until they strike the detectors. Detectors use scintillators such as bismuth germanite oxide ($\text{Bi}_4\text{Ge}_3\text{O}_{12}$) also called BGO, gadolinium oxyorthosilicate ($\text{Gd}_2\text{SiO}_5:\text{Ce}$) also called GSO, lutetium oxyorthosilicate ($\text{Lu}_2\text{SiO}_5:\text{Ce}$) also called LSO and lutetium yttrium oxyorthosilicate ($\text{LuYSiO}_5:\text{Ce}$) also called LYSO. An alternative in the future may be semiconductor detectors such as the earlier mentioned CdZnTe (also called CZT) [15].

Time-of-flight technique

In a conventional PET-camera, positron annihilation would be registered, along the line joining the two detectors, but its position along the path would be unknown. Time of flight technique is well known in nuclear physics and was also early used to improve image reconstruction in positron emission tomography (PET). The discovery of lutetium oxyorthosilicate (LSO) now provides a scintillator with both the stopping power and time resolution to make time of flight PET clinically possible. In time of flight PET, the detectors are able to measure the difference in the arrival time of the two gamma rays, thus estimating the position of the positron annihilation along the path. The current time resolution is about 600 ps, which is equivalent to resolved distance of 10 cm. This added position information enables the reconstruction algorithm to produce an image with less iterations and less image noise.

4. Hybrid imaging

Hybrid imaging with PET/CT, SPECT/CT and PET/MR, in combination with more and more advanced reconstruction software, respiratory or cardiac gating and new tracer substances has increased the accuracy of imaging and enable diagnosis in earlier stages of the disease. In PET/CT and SPECT/CT systems, attenuation mapping is performed based on available CT transmission data. In PET/MR, MR does not give the same direct possibility. A combined PET/MRI cannot provide accurate, reliable images unless it includes a method to account for PET attenuation. However, work is going on to create databases with MR- and corresponding CT-images.

5. Dosimetry

The development of the imaging methods has also changed the radiation exposure situation for patients and staff. The increasing use of CT has increased the patient doses considerably. The effective dose from a CT-investigation is from about 2 mSv (brain) to 10 mSv (abdomen). A total body investigation (brain, chest, abdomen and pelvis) gives around 30 mSv. This is roughly a factor of ten higher than conventional planar X-ray investigations. The local doses from a CT-investigation can come up to hundred mSv [16]. For PET investigations the effective doses are also considerable. An investigation with 350 MBq of ^{18}F -FDG gives for example an effective dose of 6.7 mSv [17]. The highest organ doses are 20-50 mGy. If this PET-study is combined with a CT-investigation of for example chest, abdomen, and pelvis, which gives an additional dose of 10 mSv, this together comes up to an effective dose of 20 mSv. If the PET-study instead is combined with a "low-dose" CT just for attenuation correction and anatomical orientation the CT contribution can be reduced to 2 mSv and the total to 10 mSv.

The introduction of the PET-technique and the increasing use of positron emitters have already increased the doses to the staff at the hospital as well as at the cyclotrons and the hot labs for production of the radiopharmaceuticals.

6. Trends in medical imaging

To summarise, there are a number of clear trends in medical imaging. All images will soon become digital. 3D-methods are gaining preference over 2D-methods. There is an advantage to combine investigations with different modalities, like SPECT/CT, PET/CT, and now also PET/MR. The increasing importance of functional, time-dependent, dynamic measurements is clearly seen. The new nuclear medicine methods open for a "molecular" imaging. The value of quantitative methods is more and more recognized. Imaging is increasingly used for planning of therapy, using also virtual reality technology, both in surgery and radiation therapy. In both areas, there is an increasing interest for image-guided interventions, operations and treatments. Hospital care goes towards individual treatments. As the images are digital, they can – together with the electronic patient record - be made available throughout the whole health care system, locally, regionally and between countries. In spite digital imaging systems are all produced in conformance to DICOM standards, there are still problems to connect equipment from different manufacturers. To improve that situation is critical for the clinical use.

The digital images are also a base for computer-assisted diagnosis (CAD).

Imaging is also an important instrument for clinical research, where there is a high need for quantitative and reproducible image data, especially for the

advancement of molecular medicine and drug development and delivery techniques. Should gene therapy deliver even a fraction of its promise, imaging will be heavily involved in both evaluating rates/sites of delivery and in assessing outcomes.

7. References

1. Liu Z, Yang G, Lee Y Z., Bordelon D, Lu J, Zhou O.. Carbon nanotube based microfocuss field emission x-ray source for microcomputed tomography. *Appl Phys Letters* 89, 103111, 2006. p. 1-3.
2. Shikhaliev P M. Projection x-ray imaging with photon energy weighting: experimental evaluation with a prototype detector. *Phys Med Biol* 54, 2009. p. 4971-4992.
3. Pfeiffer F, Weitkamp T, Bunk O, David C. Phase retrieval and differential phase-contrast imaging with low-brilliance x-ray sources. *Nature Physics* 2, 2006. p. 258-61.
4. Pfeiffer F, Bunk O, David C, Bech M, Le Duc G, Bravin A, Cloetens P. High-resolution brain tumor visualization using three-dimensional x-ray phase contrast tomography. *Phys Med Biol* 52, 2007. p. 6923-6930.
5. Panknin C, Ruehm S G, Lell M M. CT moves ahead with multiple energy sources. *Diagnostic Imaging Europe*, Febr 1, 2009.
6. Kalender W A, Kyriakou Y. Flat-detector computed tomography (FD-CT). *Eur Radiol* 17, 2007. p. 2767-2779.
7. Jaffray D A, Siewerdsen J H, Wong J W, Martinez A A. Flat-panel cone beam computed tomography for image guided radiation therapy. *Int J Radiation Oncology Biol Phys*, 53(5), 2002. p. 1337-1349.
8. Mozzo P, Procacci C, Tacconi A, Tinazzi Martini P, Bergamo Andreis I A. A new volumetric CT machine for dental imaging based on the cone-beam technique: preliminary results *Eur Radiol* 8, 1998. p. 1558-1564.
9. Shikhaliev P M. Computed tomography with energy-resolved detection: a feasibility study. *Phys Med Biol* 53, 2008a. p. 1475-1495.
10. Shikhaliev P M. Energy-resolved computed tomography: first experimental results. *Phys Med Biol* 53, 2008b. p. 5595-5613.
11. Timberg P, Ruschin M, Svahn T, Andersson I, Hemdal B, Mattsson S, Båth M, Tingberg A. Breast tomosynthesis – a novel three-dimensional x-ray imaging technique. In: *Proceedings of the 5th International Conference on Medical Physics in the Baltic States, Kaunas, Lithuania, 5-6 October, 2007.* ISSN 1822-5721.
12. Lucignani G. Nanoparticles for concurrent multimodality imaging and therapy: The dawn of new theragnostic synergies. *Eur J Nucl Med Mol Imaging* 36, 2009. p. 869-874.
13. Seo Y. Quantification of SPECT and PET for drug development. *Current Radiopharmaceuticals* 1, 2008. p. 17-21.
14. Madsen M T. Recent advances in SPECT imaging. *J Nucl Med* 48(4), 2007. p. 661-673.
15. Mawlawi O, Townsend D W. Multimodality imaging: an update on PET/CT technology. *Eur J Nucl Med Mol Imaging* 36 (Suppl 1):S15-S29 2009.
16. ICRP, International Commission on Radiological Protection. Managing patient dose in computed tomography. ICRP Publication 87, *Ann ICRP*, 30(4). 2000.
17. ICRP, International Commission on Radiological Protection. Radiation dose to patients from radiopharmaceuticals. ICRP Publication 106, *Ann ICRP*, 38(1-2). 2008.

PRACTICAL APPLICATION OF STATISTICAL APPROACH ON DIGITAL X-RAY IMAGING QUALITY VERIFICATION

Lada BUMBURE, Yuri DEKHTYAR, Tatyana KIRSANOVA, Zhanna YAKOVLEVA
Biomedical Engineering and Nanotechnology Institute of Riga Technical University, Riga, Latvia

Abstract: An x-ray digital imaging technology makes possible to achieve an evaluation of x-ray image quality by using digital data array. Brightness histograms were constructed and then examined in order to establish a variance and an average for each histogram. A variance and an average of the brightness statistics correlated to a voltage applied independence on the tested x-ray machine and CR system used. The achieved results demonstrate that image brightness digitalization could be in use for quality assessment of digital x-ray imaging.

Keywords: Digital x-ray image, image contrast, quality, brightness histogram.

1. Introduction

An x-ray digital imaging technology makes possible to achieve an evaluation of x-ray image quality by using digital data array [1]. A digital image data array is in use to produce a pixel distribution over brightness related to the quality parameters of the image. A variance and an average of these brightness histograms correlate to x-ray image contrast which in turn depends on high voltage [2]. Image brightness digitalization could be used by medical physicists in any x-ray diagnostics department for quality assessment of digital x-ray imaging. To verify that the above could be applied as the general approach on x-ray beam quality test the present article is targeted to analyse digital images acquired from different x-ray machines.

2. Materials and methods

The x-ray machines „MOVIPLAN 800TA”, „Bucky Diagnost TH” and „GENESIS 50” were employed to supply a flow of radiation to acquire the digital x-ray images. The images were displayed using the computed radiography systems „AGFA CR 35X”, „Philips PCR Eleva” and “Kodak Orex PcCR” respectively.

The images were acquired using an automatic exposure control (AEC) mode. The x-ray tubes were provided with the voltage (kV) in a range from 50 to 100 kV.

The test plate “ETR-1” from the set “QC Kit Roland 8” was applied as the test object.

A Plexiglas phantom (40 mm PMMA) was in use as the phantom.

The Source Image Distance (SID) was 1m. The irradiated field was sized to 19x25 cm for each exposure.

All acquired digital x-ray images were burned onto a CD in the DICOM (Digital Imaging and Communications in Medicine) format.

Black, grey and white areas from the images (Fig.1) were analysed.

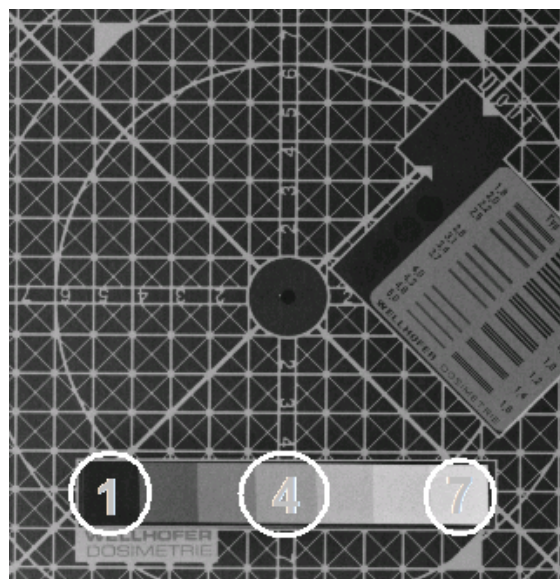


Fig. 1. The analyzed areas of the test object digital image

For this the DICOM image was transferred to TIFF (Tagged Image File Format) format, and the pixel brightness was digitalized using special software.

Histograms of digitalized pixel distribution over brightness were constructed using “Microsoft Excel” program (Fig.2).

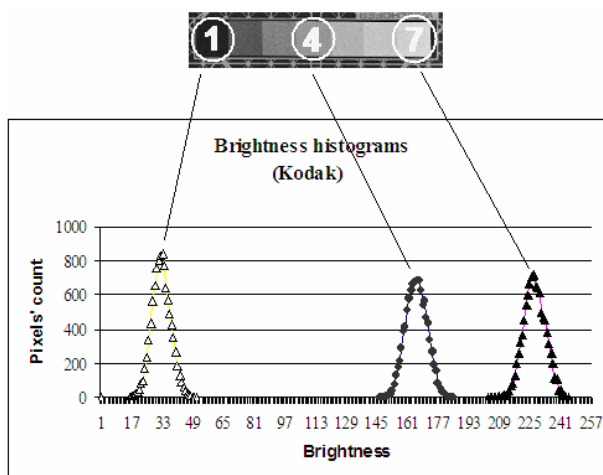


Fig. 2. Brightness histograms

An average of brightness \bar{x} for each histogram was calculated using formula [3]:

$$\bar{x} = \frac{1}{n} \sum_{i=1}^k x_i n_i \quad (1)$$

where:

\bar{x} – average brightness,
 x - brightness gradation,
 n - number of gradations.

Brightness range for each image was defined as a brightness range between calculated average brightness of 1st and 7th area of each digital x-ray image (Fig. 3-5). The brightness range for each image was calculated using formula:

$$BR = \bar{X}_7 - \bar{X}_1 \quad (2)$$

where:

BR – brightness range

\bar{X}_7 – average brightness of 7th area

\bar{X}_1 – average brightness of 1st area

Then brightness ranges of digital X-ray images acquired with different kilovolts were compared.

A variance of each histogram was calculated using formulae [3]:

$$S^2 = \left(\sum_{i=1}^k (x_i - \bar{x})^2 \right) / (n - 1) \quad (3)$$

where:

\bar{x} – average brightness

x - brightness gradation,

n - number of gradations,

S^2 – variance.

Then calculated variances were compared.

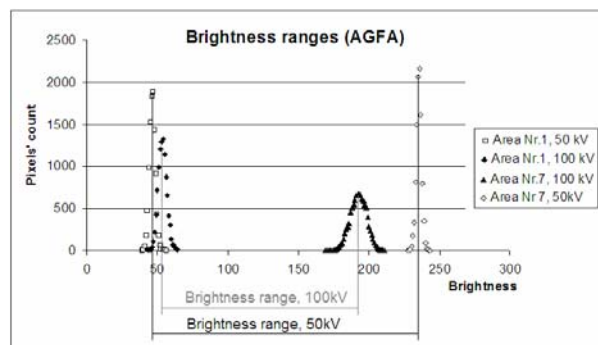


Fig. 3. Brightness ranges, AGFA

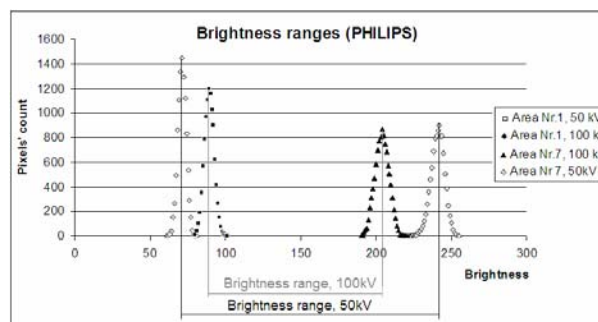


Fig. 4. Brightness ranges, PHILIPS

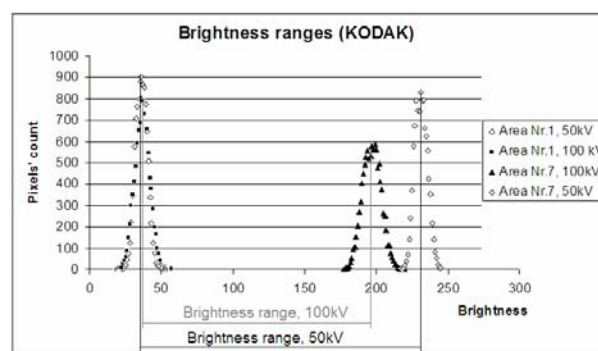


Fig. 5. Brightness ranges, KODAK

3. Results

The results of the calculations are shown in the Table 1, 2, 3 and Figures 6-12.

All results independently on used x-ray machines and computed radiography (CR) systems showed the same:

1. The higher kV for x-ray tubes were provided, the smaller were brightness average of 7th and 4th image areas, but bigger of 1st area (Fig. 6-8).

- The higher kV for x-ray tubes were provided, the smaller was the range of digital x-ray image brightness (Fig.9).
- The higher kV for x-ray tubes were provided, the larger was variance of each histogram (Fig. 10-12)

Table 1. Average brightness in dependence on kV

Nr. of Area	Computed radiography system		
	Agfa	Philips	Kodak
50kV			
1	46	71	36
4	201	201	174
7	235	241	231
60kV			
1	49	77	31
4	181	189	165
7	227	226	226
70kV			
1	55	83	39
4	174	181	160
7	221	218	222
80kV			
1	53	86	37
4	166	176	147
7	215	212	210
90kV			
1	53	88	33
4	146	171	142
7	199	208	207
100kV			
1	54	89	37
4	140	168	136
7	193	204	197

Table 2. Brightness range in dependence on kV

kV	Amount of brightness gradations (brightness range) in dependence of kV		
	CR system		
	Agfa	Philips	Kodak
50	188	168	193
60	175	150	191
70	166	134	184
80	160	127	176
90	144	119	175
100	136	116	161

Table 3. Variance in dependence on kV

kV	CR system		
	Agfa	Philips	Kodak
Variance of 1st area of brightness histogram			
50	4.39	7.82	16.86
60	6.48	8.7	18.42
70	7.1	9.3	20.57
80	7.87	9.9	24.28
90	8.02	10.14	26.83
100	8.4	12.48	27.43
Variance of 4th area of brightness histogram			
50	16.1	9.3	21.47
60	25.76	18.34	29.6
70	32.86	20.9	29.24
80	43.77	25.42	31.07
90	43.81	26.03	31.89
100	47.72	26.82	32.82
Variance of 7th area of brightness histogram			
50	2.476	18.602	18.782
60	7.928	22.128	37.247
70	9.519	22.276	39.37
80	19.138	22.353	40.05
90	27.845	22.584	42.25
100	36.433	26.95	42.6

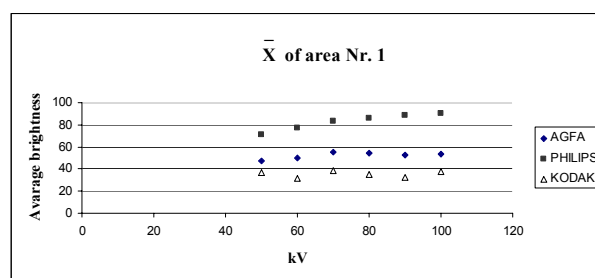


Fig. 6. Average Brightness of black area (the area Nr.1)

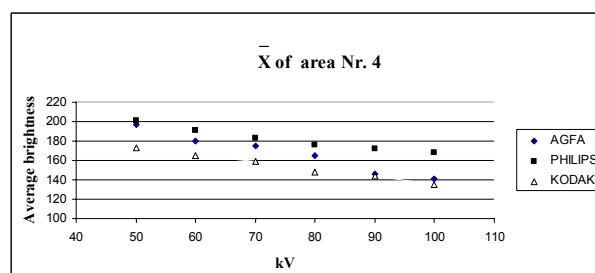


Fig. 7. Average Brightness of grey area (the area Nr.4)

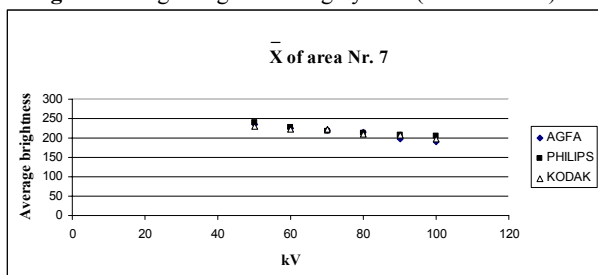


Fig. 8. Average Brightness of white area (the area Nb.7)

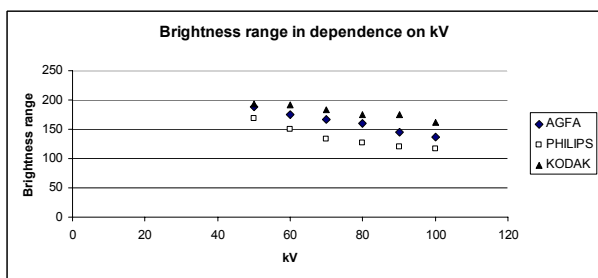


Fig. 9. Brightness range in dependence on kV

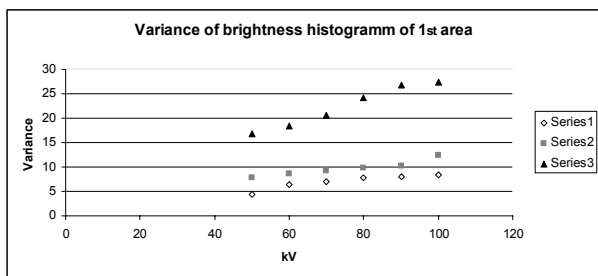


Fig. 10. Variance of black area (the area Nb.1)

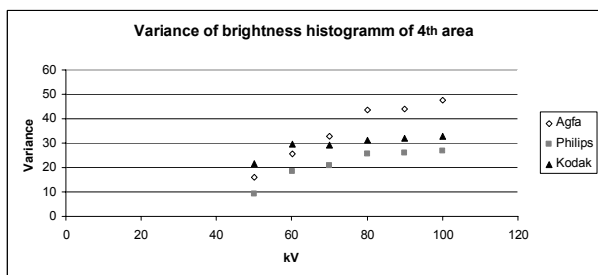


Fig. 11. Variance of grey area (the area Nb.4)

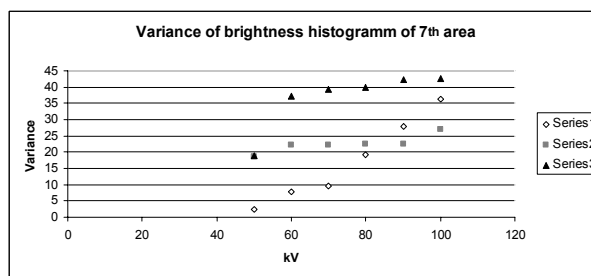


Fig. 12. Variance of white area (the area Nb.7)

4. Conclusions

The achieved results demonstrate that digital image brightness statistical parameters – Brightness Average, Variance and Brightness range could be in use for quality assessment of the x-ray beam independently on x-ray machines and CR systems.

5. References

1. Bumbure L., Dekhtyar Y., Glazs A., Katashev A., Krechetova K., Mortuzane A. Evaluation of quality of digital X-ray image, Biomedical Engineering, Kaunas University of Technology, Technologija, 2008. p. 205-208.
2. Bumbure, J. Dehtjars, T. Kirsanova. Statistics of digital X-ray image brightness histograms, IFMBE Proceedings, 2009. Springer, p. 3.
3. Arhipova I., Bāliņa S. Statistika ar EXEL ikvienam, Datorzināibu centrs – 1999.

**DOSE REDUCTION AND IMAGE QUALITY EVALUATIONS OF
AUTOMATIC EXPOSURE CONTROL SYSTEMS FROM FOUR
DIFFERENT CT MANUFACTURERS**

Marcus SÖDERBERG, Mikael GUNNARSSON

Department of Medical Radiation Physics, Malmö, Lund University, Malmö University Hospital, SE-205 02 Malmö,
Sweden

Purpose: To evaluate automatic exposure control (AEC) systems from four different CT scanner manufacturers: General Electric (GE), Philips, Siemens, and Toshiba, considering their potential for reducing radiation exposure to the patient while maintaining adequate image quality.

Material and Methods: An anthropomorphic chest phantom was used to simulate an adult patient. Measurements were performed using 16-slice and 64-slice CT-scanners from each manufacturer with the AEC system activated and inactivated. The adaptation of the tube current along the longitudinal axis of the phantom and the potential for reducing radiation dose were evaluated using parameters in the DICOM image information. The image quality was evaluated based on image noise (standard deviation of CT numbers), calculated in 0.5-cm² circular regions of interest, situated throughout the spine region of the chest phantom.

Results: The tube current modulation dynamics were similar among the different AEC systems, especially between GE and Toshiba systems and between Philips and Siemens systems. The AEC systems resulted in a considerable reduction in radiation dose, ranging from approximately 30% to 60%. The image noise increased when the AEC systems were used, especially in regions where the tube current was greatly decreased, such as the lung region. However, the image noise in different anatomical regions of the chest phantom became more uniform when using the AEC systems compared to fixed mAs scans.

Conclusion: The use of AEC systems available in modern CT scanners can significantly reduce the radiation exposure to the patient and the variation in image noise among images can be lower.

DIAGNOSTICS OF CANCEROUS PROSTATE TISSUE BY MEANS OF INFRARED SPECTROSCOPICAL IMAGING

Daiva LEŠČIŪTĖ*, Valdas ŠABLINSKAS*, Valdemaras ALEKSA*, Arūnas MARŠALKA*, Feliksas JANKEVIČIUS**

*Dept. of General Physics and Spectroscopy, Faculty of Physics, Vilnius University; ** Dept. of Physiology, Biochemistry and Laboratory Medicine, Faculty of Medicine, Vilnius University; ***Centre of Urology, Vilniaus University Hospital Santariskių klinikos, Faculty of Medicine, Vilnius University

Abstract: Method of Fourier transform infrared microscopy (FTIR-MC) for the first time is applied for studies of prostate cancerous tissue. The chemical images are obtained by combining mapping technique with imaging with focal plane array (FPA) MCT detector. It is shown that ratio of intensity of amide I and amide II spectral absorption bands can be used for distinguishing cancerous tissue from healthy one. By combining infrared spectral images with optical ones it is shown that infrared imaging is preferable method for defining edges of cancerous tissue of prostate samples compared to the method of conventional histological imaging. It is shown that infrared images allow to define such edges with 10 microns lateral resolution.

Keywords: FTIR-MC, FPA detector, prostate, cancer

1. Introduction

Modern infrared spectroscopy combined with infrared microscopy allows investigate features of samples in micrometric scale. Just recently this method was started to be applied for studies of biological tissues. Determination of spatial distribution of different chemical components in biological tissues is even possible by using this method. Sensitivity of the method enables to identify tumors even in very early stage of this disease.

Early diagnosis of the tumor is very important for its prevention or successful curing of the patient. Tumor formation can be caused by very different reasons such as some genetic miss functioning or some cancerous substances which can present in our surrounding or can be taken in to the body by breathing or with food. Biochemical changes in various tumors usually are very different [1]. FTIR method supplies very useful information about molecular structure of biological tissue. Chemical information obtained by means of infrared spectroscopical microscopy is molecular level information taken from volume of the sample sized to micrometric scale [2].

2.1 Focal plane array detector

For any optical imaging some multichannel detector is needed. Focal plane Mercury Cadmium Tellurate (FPA

MCT) detector is detector of choice in case of infrared imaging. A FPA MCT detector consists from many small single detectors sized to 6 - 10 μm^2 . Every single detector in the array collects the spectral information from different parts of the sample. Set of spectra obtained by different single detectors of the array can be used for constructing of infrared image of the sample in desired spectral window located in infrared spectral region from 500 to 4000 cm^{-1} . Such image is considered to be chemical image of the sample when the spectral windows coincide with spectral band specific to one of chemical components of the sample [3]. At present stage of technology the FPA MCT detectors consist from 4096 single detectors, which form 64 \times 64 matrix. In such a way 4096 spectra are captured at a time. Infrared imaging becomes rather fast by using such a detector. Sensitivity is another feature of this technology. Lateral resolution obtained with use of such detectors can be achieved as high as size of biological cells. Due to this fact this technology is preferable compare to other imaging technologies which are in use in medical laboratories or operational rooms. It is notable, that in order to extract chemical information from infrared microscopical images some statistical analysis of the images should be applied, including principal component analysis (PCA) and some other unsupervised or supervised statistical methods. Basically, processing of spectral information from the FPA detector is rather complicated. A set of interferograms is primary spectral information, obtained

from the FPA detector. Firstly, the interferograms has to be recalculated to the infrared spectra by using fast Fourier transformation (FFT) and secondly, all spectra has to be baseline corrected. The main feature of spectral data obtained from an array detector is large amount of data. Mathematical treatment of the data with aim to reduce its amount has to be performed. Common procedure is integration of spectra over certain spectral regions. The chemical images representing distribution of different chemical components in the sample can be rationed to each other. This procedure is very efficient in determination of cancerous areas of a biological sample. Usually cancer cells are assumed to have only very small differences from healthy cells in respect to relative concentration of different chemical component presenting in the cells. Such differences can be visualized only in so called rationed images and finally used for recognition of cancerous cells [4].

2. Infrared spectral features of biological molecules

The biological cells are classified according to their primary physiological functions. In such a way the cells can be assigned to the different groups. Epithelia, nerve, sex and blood cells are examples of such grouping. From molecular point of view all biological cells consist from molecules of four types: proteins, lipids, nucleonic acids and hydrocarbons [5]. Spectral bands arising from all these molecules are found in infrared absorption spectra of a biological tissue. Relative intensity of the bands is changing in process of development of cancer.

All the amino acids are constituted from four major parts according to general structure where central or α - atom of carbon is attached to the carbonyl group, amino group and hydrogen atom (Fig. 1). Every amino acid has distinctive structure in the secondary chain, which is denoted by letter R in figure 1.

Primary structure of the protein or polypeptide is formed by combining separate segments (blocks) of amino acid to the linear chain via condensation reaction between amino and carboxyl groups adjacent in the linear acids chain. The bond between the blocks of amino acid is called peptide bond. The structural unit of the main polypeptide chain is constituted from several functional groups: C-N group, C-H group, NH₂ group and C=O group. All the groups determine IR absorption spectrum of protein. [6]

The main absorption bands are as follows: amide I band at 1650 cm⁻¹ caused by C=O bond vibration (80%) and C-N bond vibration (20%); amide II band at 1545 cm⁻¹ caused by N-H vibration (60%) and C-N vibration (40%); amide III band at 1236 cm⁻¹ caused by C-N vibration; amide A - at 3290 cm⁻¹ caused by N-H vibration.

Most of the proteins have non linear structures forming complex secondary structures which locate in more than one plane. Regular secondary structures of proteins are α -helix and β -pleated sheet. Both of these periodic secondary structures have hydrogen bond

between oxygen atoms in main carboxyl group and hydrogen atoms in main NH- group. These structural changes are followed by shifting of corresponding spectral bands. The shift depends on the vibrations of the main chain. Analysis of these shifts gives empirical rules: IR absorption band at 1660 - 1650 cm⁻¹ is ascribed to α -helix, 1640 - 1620 cm⁻¹ - to β -pleated sheet conformation, 1695 - 1660 cm⁻¹ - to β -pleated sheet and β -strand conformations with absorption band at 1650 - 1640 cm⁻¹ is ascribed to unorganized structure [7]. These empirical rules are useful for studies of biological tissues analyzing the data from the vibrational spectra.

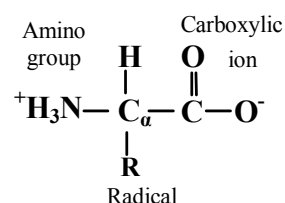


Fig. 1. The main structural components of amino acids

Proteins are the second most abundant compounds in human body after water (70%). Human DNA (deoxyribonucleic acid), which contains all the genetic information, is constituted from proteins. Also, molecules of proteins are present in many fundamental parts of the cells. Therefore, proteins are very significant in biological organisms. They have functions like ferment catalysis, transportation and accumulation of nutrients, immune protection, exciting and transmitting nerve impulses, governing the processes of reproduction and development of cells.

Primary structure of all the proteins is made of linear amino acids chain, which can form various secondary and tertiary structures. Eukaryotic proteins are mostly consisted from 20 different α -amino acids complex. The acids in that complex have unique side chains.

Lipids are other important compounds of the cell. They are constructional material in the cells, responsible for supply of energy and water, also they have protective function. Mostly, long chains of fatty acids make lipids hydrophobic. Lipids have a lot of absorption bands in the so called 'fingerprint' spectral region caused by vibrations of C-H group. Four absorption bands at 3000 - 2800 cm⁻¹ are common to most of the lipids: absorption bands at 2962 cm⁻¹ are caused by antisymmetric vibration of methyl group ($\nu_{as}\text{CH}_3$), the bands at 2872 cm⁻¹ - by symmetric vibration of methyl group ($\nu_s\text{CH}_3$), absorption bands between 2936 - 2916 cm⁻¹ are caused by antisymmetric vibration of CH₂ group ($\nu_{as}\text{CH}_2$) and the bands between 2863 - 2843 cm⁻¹ - by symmetric vibration of CH₂ group ($\nu_s\text{CH}_2$) [8]. In most standard tissue preparation methods non polar solvents like ethanol are used to eliminate lipids from the tissue. FTIR spectroscopy does not require such separation methods.

Nucleic acids are responsible for transferring genetic information and proteins biosynthesis in living organism. IR absorption of nucleic acids is caused by vibrations of several functional groups. Functional groups are located on the main periodic structure of nucleic acid. Spectral

band at 1080 cm^{-1} is caused by symmetric vibration of PO_2 and at 1240 cm^{-1} – by antisymmetric vibration of PO_2 [7].

3. Experimental

Prostate samples were obtained from Vilnius University hospital Santariskiu Klinikos by means of cancerous tissue surgery. The prostate slices were taken from inner tissue and outer tissue. Such 10 microns thick slices were prepared by microtome from frozen samples. Similar slices from neighbouring layers of the tissue were prepared for histological observation.

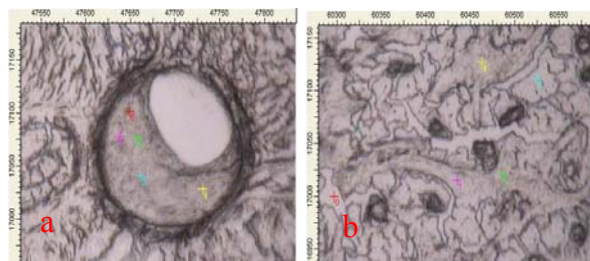


Fig. 2. Optical images of two prostate tissue slices: a) taken from inner tissue; b) taken from outer tissue.

Spectra were obtained using FTIR spectrometer Vertex 70 combined with microscope “Hyperion 3000” from “Bruker” and with FPA MCT 64×64 detector. The resolution of the spectrometer was set to 8 cm^{-1} . False-colour images representing the distribution of cancerous cells in the tissue were obtained by integrating the area under the spectral band of specific amide I and amide II spectral bands. The OPUS software was used for this purpose.

4. The results and discussions

The samples - 20 microns slices of cancerous prostate tissue - were investigated in this work by using two methods: infrared absorption spectroscopy at selected points of the sample and infrared spectroscopical imaging of whole area of the sample. Firstly, the samples were analyzed visually and only areas of very different density (e.g. transparent or completely dark) have been chosen for the single point infrared measurements. Optical images of selected areas are presented in fig. 2. The optical images were captured with optical microscope set to $\times 15$ magnification.

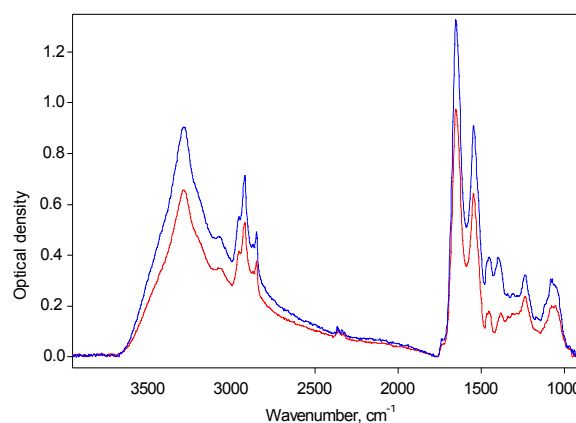


Fig. 3. FTIR absorption spectra of slice taken from outer prostate tissue: red – dark spots; blue – light spots.

The IR spectra were recorded in $4000 - 900\text{ cm}^{-1}$ spectral region e.g. in the region where CaF_2 support plate for the tissue slices is transparent. The spectra typical for transparent and dark areas of the slices taken from outer prostate tissue are presented in fig. 3.

Close look to the spectra reveals that they correspond to the same type of the cells, just thickness of the slice corresponding to blue spectrum is larger than that corresponding to the red spectrum.

Identification of the spectral bands is presented in table 1. The assignment was made using data obtained for other biological tissues [3].

Table 1. Assignment of the spectral bands to normal vibrations

Wave number (cm^{-1})	Assignment
3295	Amide A (N-H bond)
3050	Amide B
2960	$\nu_{\text{as}} \text{CH}_3$
2930	$\nu_{\text{as}} \text{CH}_2$
2874	$\nu_{\text{s}} \text{CH}_3$
2852	$\nu_{\text{s}} \text{CH}_2$
1655	Amide I ($\nu \text{C}=\text{O}$, $\delta \text{C}-\text{N}$, $\delta \text{N}-\text{H}$)
1545	Amide II ($\delta \text{N}-\text{H}$, $\nu \text{C}-\text{N}$)
1476	δCH_2
1380	δCH_3
1240	$\nu_{\text{as}} \text{PO}_2^-$
1170	$\nu_{\text{as}} \text{CO}-\text{O}-\text{C}$
1078	$\nu_{\text{s}} \text{PO}_2^-$
1050	$\nu_{\text{s}} \text{CO}-\text{O}-\text{C}$
1030	$\nu_{\text{s}} \text{C}-\text{O}$

It is known that some changes in structure of amide groups are taking place when cancerous tissue is forming [7]. Therefore amide I (1655 cm^{-1}) and amide II (1545 cm^{-1}) spectral bands were taken for further analysis. Intensity of the bands was evaluated fitting them with Gaussian and Lorentzian functions. The results are presented in table 2.

The results reveal that the cancerous cells are present in both slices. The cancerous tissue is very unhomogenous and single point measurements are very inefficient since they do not give correct picture about distribution of cancerous cells. Therefore, the further measurements were performed using infrared imaging technique. Some examples of chemical maps, obtained using this technique, are presented in fig. 4.

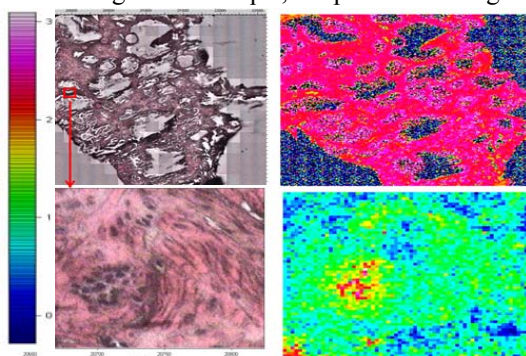


Fig. 4. Optical images and chemical maps of cancerous prostate tissue

The type of the colours in chemical maps corresponds to ratio of integral intensities of amide I and amide II. Deep red colour corresponds to high concentration of cancerous cells while blue colour corresponds to very low concentration of cancerous cells.

From these maps it is possible to see the distribution of intensities ratio of amide groups. If the ratio of the intensities is higher than 1.3 then there are cancerous cells in this area [9]. Having these chemical maps it can be seen the distribution of healthy and cancerous cells. Therefore, the exact boundaries of cancerous tissue can be defined. Our results coincide with the ones obtained using staining method which is very well approved in pathology. Comparing the information obtained from single element measurements with imaging the whole sample, it can be concluded that the later method gives much more information about the sample and the analysis can be more detailed, but also it is more complex and requires more computational recourses for the data processing. For more detailed analysis it is important to apply statistical data analysis of FTIR images. For such analysis it is necessary to obtain more spectral data of healthy and various stage cancerous tissue samples.

5. Conclusions

Studies of healthy and cancerous tissues using common infrared spectroscopy and microscopy with single element detector showed that the ratio of intensities of amide I and amide II absorption bands is

Table 2. Ratios of integral intensities of spectral bands at $\nu=1655\text{ cm}^{-1}$ and $\nu=1545\text{ cm}^{-1}$

Spot number	Slice from prostate inner tissue				Slice from prostate outer tissue			
	Light spot		Dark spot		Light spot		Dark spot	
	Lorentz	Gauss	Lorentz	Gauss	Lorentz	Gauss	Lorentz	Gauss
0	1.36	1.35	1.30	1.3	1.28	1.3	1.14	1.2
1	1.34	1.35	1.30	1.3	1.28	1.3	1.14	1.2
2	1.35	1.35	1.30	1.3	1.30	1.3	1.15	1.2
3	1.35	1.35	1.29	1.3	1.25	1.3	1.16	1.2
4	1.30	1.31	1.34	1.3	1.27	1.3	1.18	1.2

the most sensitive parameter to determine cancerous cells in the tissue. It was found that for the infrared imaging of biological tissue both technique- imaging with FPA MCT array detector and mapping with single point MCT detector can be performed. Notable, that the imaging by the array detector is much faster than imaging by single point detector. In case of the 64×64 FPA MCT detector the image can be captured up to 400 faster than in case of single point MCT detector. Chemical maps of biological tissue obtained using infrared microscopical technique allow determine the boundary between healthy and cancerous tissue with accuracy of appr. 10 microns.

6. References

1. Mordechaj, R. K. Sahu, Z. Hammody, Possible common biomarkers from FTIR microspectroscopy of cervical cancer and melanoma, *Journal of Microscopy*, Vol. 215, 2004. p. 86–91.
2. C. Conti, P. Ferraris, E. Giorgini, Microimaging FT-IR of oral cavity tumours. Part III: Cells, inoculated tissues and human tissues, *Journal of Molecular Structure*, 2007. p. 86–94.
3. Ira W. Levin and Rohit Bhargava, Fourier transform infrared vibrational Spectroscopic imaging: Integrating Microscopy and Molecular Recognition *Annu. Rev. Phys. Chem.*, 2005. p. 429-474.
4. Allan Hynes, David A Scott, Angela Man, Molecular mapping of periodontal tissues using infrared microspectroscopy, *BMC Medical Imaging*, 2005. p. 1-10.
5. Reginald H. Garrett, Charles M. Grisham, *Biochemistry*, 2005. p. 209-233.
6. Rosette M. Roat-Malone, *Bioinorganic Chemistry*, 2002. p. 25.
7. Jackson, M. and H.H. Mantsch, *Biomedical Infrared Spectroscopy*, in *Infrared spectroscopy of biomolecules*, 1996. p. 311-340.
8. Lewis, R.N.A.H. and R.N. McElhaney, *Fourier Transform Infrared Spectroscopy in the Study of Hydrated Lipids and Lipid Bilayer Membranes*, in *Infrared spectroscopy of biomolecules*, 1996. p. 159.
9. C. Paluszkiwicz, W. M. Kwiatek, Analysis of human Canter prostate tissues using FTIR microspectroscopy and SRIXE techniques, *Molecular structure*, 2001. p. 565-566.

**FIBER-OPTICS BASED LASER SYSTEM FOR 2-D FLUORESCENCE
DETECTION AND OPTICAL BIOPSY**

Dalia KAŠKELYTĖ*, Arūnas ČIBURYS*, Saulius BAGDONAS*, Giedrė STRECKYTĖ*,
Ričardas ROTOMSKIS***, Roaldas GADONAS*

* Department of Quantum Electronics & Laser Research Center, Vilnius University. Saulėtekio ave. 9, bldg. 3, LT-10222 Vilnius, Lithuania;

** Laboratory of Biomedical Physics, Institute of Oncology of Vilnius University. P. Baublio 3, LT-08406 Vilnius, Lithuania

Abstract: The constructed fluorescence excitation / collection unit was specifically designed to utilize a single fiber probe for excitation of a green fluorescing marker and its emission collection within the sample depth. Model layered specimens consisting of a slice of rhodamine 6G stained gelatine or suspension of PKH 67 marked cells incorporated between gelatine-milk slices were used to characterize the performance of the constructed system. Localization of the green fluorescing markers was evaluated with the needle based fiber probe tip registering fluorescence spectra at various probing depths. Experimental results demonstrate the sensitivity of the fiber-optics based laser system in measuring thin fluorescing objects within the model layered specimen. The obtained spatial resolution was better than 1 mm which is basically due to the active fiber probe dimensions.

Keywords: fluorescence, optical biopsy

1. Introduction

There are many fields in biomedicine where fiber based optical probes are used for fluorescence diagnostics and imaging purposes [1,2]. Fluorescence probes that can collect and distinguish depth-related spectroscopic data representing tissue optical signatures from those of native chromophores or supplied molecular markers have important diagnostic significance. Information concerning the localization and distribution of fluorescing substance within the biological tissue as well as its specific optical signatures may improve the facilities of fiber-optic spectroscopy methods to evaluate biochemical alterations or tissue viability during the real-time measurements.

The goal of this work was to construct the portable unit for fluorescence measurements based on fiber-optics and the laser system, which would be sensitive to the labelled object localized within tissue (cells) volume of

about a few cubic millimetres. The premises of the present work deal with the problem of the in vivo detection of cells labelled by a fluorescent marker within the tissue.

2. Materials and methods

We used a diode-pumped solid state laser (DPSSL) operating in cw regime at the wavelength 473 nm with tunable output power up to 15 mW to excite fluorescence of molecular markers inoculated into biological tissue. A spectrometer (Avaspec-2048, Avantes, Inc.) was used to register the fluorescence spectra detected at the given probing depth within the sample. The laser light and a tip for fluorescence registration were all coupled to fiber optics for guiding light into the sample and out of it. The structural arrangement of a fluorescence excitation / collection unit is presented in Fig. 1.

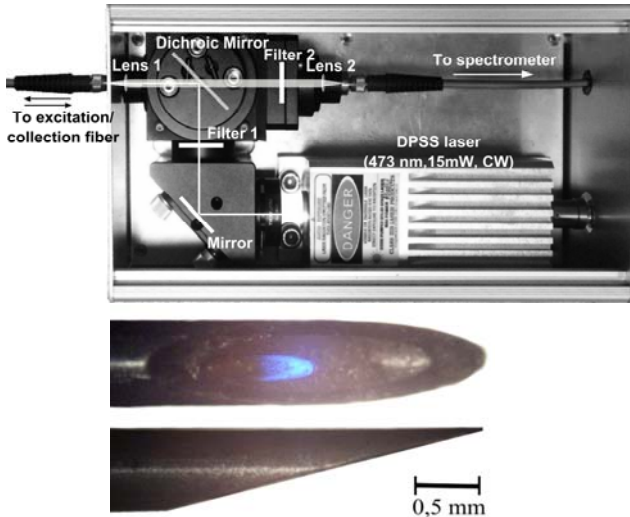


Fig. 1. Set-up of the constructed unit for fluorescence measurements (upper view). The tip of the fiber (bottom view) inserted into the needle for the fluorescence measurements in the deeper layer of the sample. The fiber probe tip is polished to form elliptical geometry with the active zone of about 1 mm along the x - axis.

The set-up of fluorescence excitation / collection unit was specifically designed applying a single fiber probe for fluorescence measurements in tissue based on detection of the green marker emission [3].

The performance of the constructed unit for fluorescence measurements is realized through the following steps (Fig.1): laser light is directed to the fluorescence excitation / collection guiding optical unit with the mirror. The excitation light passes the excitation filter 1 and being reflected from the dichroic beam splitter is focused by the coupling lens 1 to the fluorescence excitation / collection optical fiber probe with the coupling effectiveness of about 92 %. The excitation and the collection of the fluorescence signal are realized through the same optical fiber (200 μm in diameter), the tip of which is specifically modified by inserting it into the 22 gauge needle thus enabling to prick the tissue sample for the detection of the fluorescence signal at different probing depths.

Fluorescence signals collected inside the biological tissue are guided back with the same fiber to the fluorescence excitation / collection optical unit, where spectral discrimination between the fluorescence signal and the fluorescence excitation light is realized by the dichroic beam splitter and the fluorescence cut-off filter 2. The collection lens 2 focuses the fluorescence light into the optical fiber (200 μm in diameter) and guides the signal to the spectrometer. We used Brightline laser fluorescence LF488-A filter set (Semrock, Inc.) to ensure collection of fluorescence signals from rhodamine 6G and PKH 67 marker in the spectral range from 500 nm to 545 nm (Fig.2).

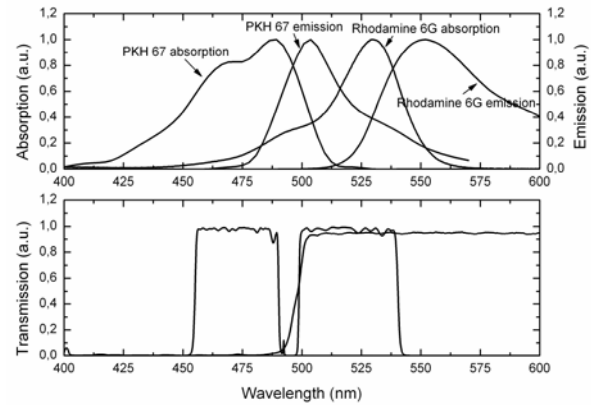


Fig. 2. Rhodamine 6G and PKH 67 absorption and emission spectra (upper plot). Transmission characteristics of the Brightline laser fluorescence LF488-A filter set (bottom plot)

In this work the fluorescence intensity values were measured by changing the inner position of the optical fiber probe in model layered specimens. The experimental set-up for fluorescence measurements is presented in Fig.3. The needle probe pricking control along the layered sample was realized by fixing the needle at the motorized translation stage (Standar, Ltd., model 8MT175-50) at vertical position. The achievable maximal stage travel range was 50 mm with the minimal step - up to 2.5 μm.

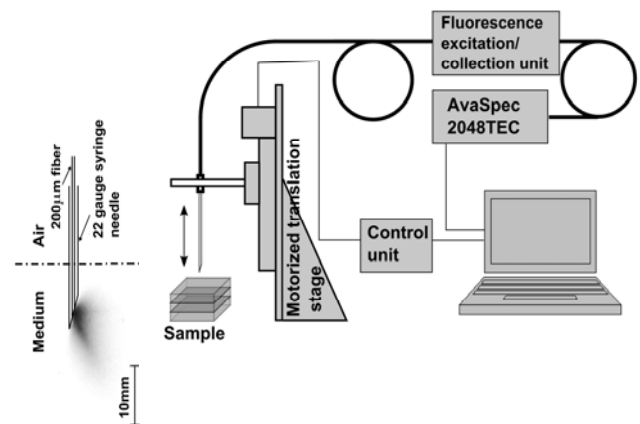


Fig. 3. Experimental set-up prepared for fluorescence measurements at different depths (right side): the sample pricking control realized by motorized translation stage; a cross-sectional view of the tip of the fiber inserted into the needle. Spatial distribution of excitation light coming out of the end of the fiber probe within the sample (myogenic cells in suspension) (left side).

The constructed unit for fluorescence measurements was tested for the detection of two green fluorescing markers incorporated within the gelatine layered specimen. We used chicken breast tissue and slices of gelatine (thickness was about 3 mm) containing rhodamine 6G with couple drops of milk as experimental layered specimen to detect the fluorescence of the marked object within it. In addition,

we measured the fluorescence of the myogenic cells stained with PKH 67 marker in suspension being squeezed between gelatine-milk slices. The data obtained by changing fiber probe's depth in the samples were used to construct 2D fluorescence intensity plots to determine the sensitivity of the fluorescence excitation / collection unit and to evaluate the resolvable spatial range in the fluorescing specimen.

3. Results

The fluorescence intensity values of rhodamine 6G in gelatine layer were collected automatically by changing the depth of fiber probe within the sample in every 0.07 mm while for PKH 67 – in every 0.05 mm. The sensitivity of the designed system during the measurements was sufficiently high to register the changes in the fluorescence signal of the markers while fiber probe was gradually moved from one layer to the next deeper laying layer. Fig.4 shows the fluorescence intensity of rhodamine 6G marker being collected by passing the needle fiber tip through the model layered sample, which is plotted as a depth and wavelength function. The measurements indicate that the fiber-optic probe collects information about the localization of the marked layer.

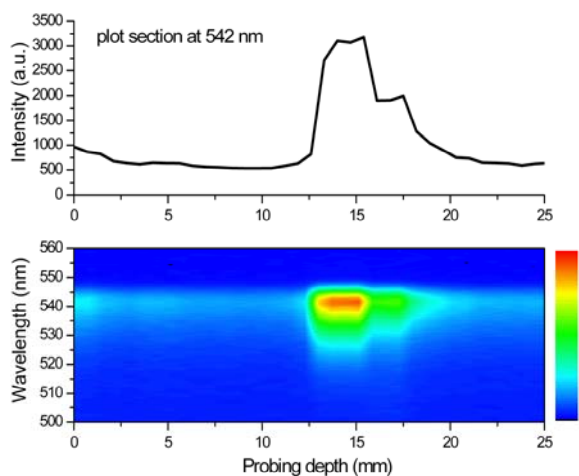


Fig. 4. Set of fluorescence intensity of rhodamine 6G marker layer, which has been collected at different fiber tip probing depths (bottom plots). Fluorescing rhodamine 6G – gelatine–milk layer (3 mm in thickness) has been covered with the thick slice (13 mm) of breast tissue. Upper plot represents distribution of the fluorescence intensity of the marker at 542 nm emission wavelength along the layered specimen.

Slight increase in the background fluorescence signal measured under the fluorescing layer was observed for rhodamine 6G / gelatine layer system. It can be explained as a result of slight staining of the needle fiber tip caused by the rhodamine 6G, attached to it from the marked layer. The increased background fluorescence signal vanished moving the needle deeper into the sample for about 2 mm.

The problem of the stained probe disappeared for the specimens containing the layer of PKH 67 stained cells as in this case the marker has been localized within the cells. To determine the sensitivity of the constructed unit to detect the fluorescence of the PKH67 stained myogenic cells in gelatine layered sample we measured the fluorescence signal intensity dependence on the concentration of myogenic cells in suspension (Fig. 5.).

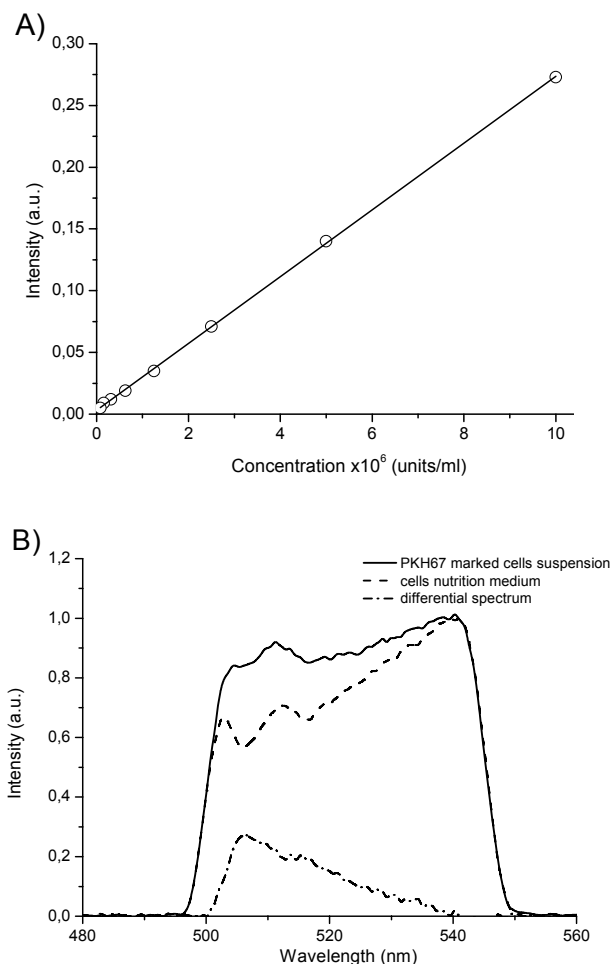


Fig. 5. Plot of measured fluorescence signal at 506 nm vs concentration of the PKH67 stained myogenic cells in suspension (A). Fluorescence spectra of stained myogenic cells, nutrition medium and the obtained differential spectrum (B). All spectra are normalized to 540 nm.

As the native fiber probe background signal has dominant peak near 540 nm, all measured spectra were normalized to it and the differential spectra were calculated for elimination of the influence of the probe. For the fluorescence signal measurements in the model layered specimen we used three gelatine-milk slices and put one drop of cells nutrition medium after first upper gelatine-milk slice and one drop of suspended PKH67 stained cells (at a concentration of $5 \cdot 10^5$ cells per ml) after the second gelatine-milk slice (Fig. 6).

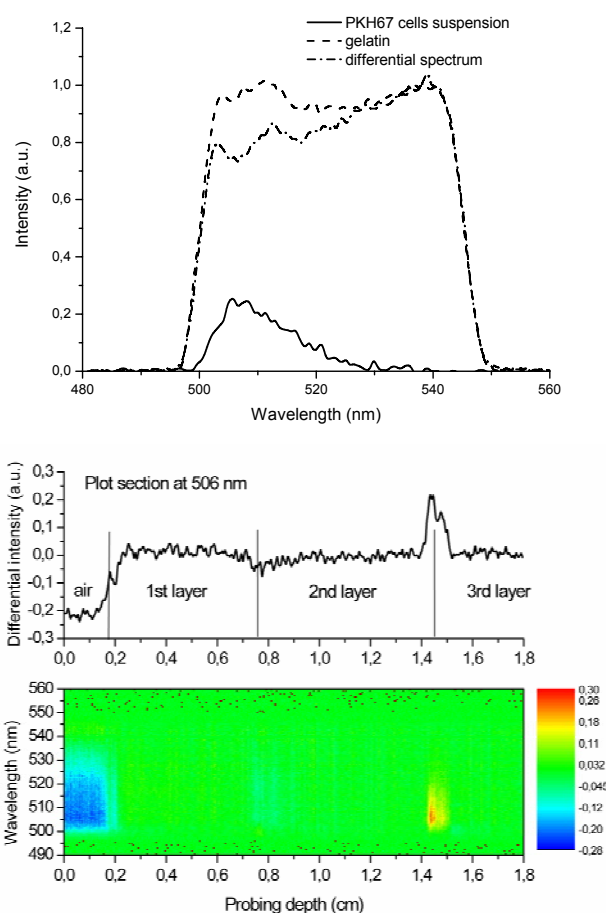


Fig. 6. Fluorescence spectra of stained myogenic cells, a slice of gelatine and obtained differential spectrum (upper plot). Spectra are normalized to 540 nm. Set of fluorescence intensity of PKH67 stained cells in layered specimen collected at different probing depths of a fiber tip (bottom view, bottom plot). A plot (bottom view, the upper section plot) represents the distribution of the fluorescence intensity of the marker registered at 506 nm along the layered specimen.

The difference in fluorescence intensity value at 506 nm represents the ability to localize and to evaluate the spatial localization of the PKH 67 stained fluorescing myogenic cells in light scattering environment.

4. Conclusions

The constructed portable unit for fluorescence measurements could provide the real-time monitoring of fluorescing objects in biological tissue at various probing depths. The facility for accurate targeting of the position of the stained cells, which has been demonstrated within scattering layered environment, may improve the performance of fiber-probe based equipment as a diagnostic tool, utilizing the fluorescence spectroscopy method for the detection of labelled cells in biological tissue in real time regimen.

5. Acknowledgement

This study has been supported by the Lithuanian State Science and Studies Foundation, the grant No. B-07041.

6. References

1. Utzinger U., Richards-Kortum R., "Fiber optic probes for biomedical optical spectroscopy", *J. Bio. Opt.* 8, 2003. p. 121-147.
2. Pfefer T.J., Schomacker K.T. etc., „Light Propagation in tissue during fluorescence spectroscopy with single-fiber probes”, *IEEE J. Select. Top. Quant. Electr.* 7(6), 2001. p. 1004-1012.
3. Kaškelytė D., Čiburys A., Bagdonas S., Streckytė G., Rotomskis R., Gadonas R., Fiber-optics based laser system for 2-D fluorescence detection and optical biopsy, *Med Physics in Baltic States: Proceedings of the 6th International conference on medical physics*, 10-11 October, Kaunas 2008, p. 12-14.

CdTe QUANTUM DOTS STABILIZATION BY PROTEIN IN AQUEOUS SOLUTION

Vilius PODERYS * **, Deividas MOTEKAITIS**, Ričardas ROTOMSKIS* **

* Institute of Oncology Vilnius University, Laboratory of Biomedical Physics;

**Vilnius University, Physics Faculty, Quantum Electronics Department, Biophotonics laboratory

Abstract: Quantum dots – semiconductor fluorescent nanoparticles are very promising fluorescent markers due to their unique properties. It is very important to know bioeffects of quantum dots before using them in medicine, however it is still very little known about interaction of quantum dots with biomolecules. In this work we investigated stability and spectral properties of CdTe quantum dots in aqueous media and effect of quantum dot – protein interaction on these properties. We showed that BSA stabilizes CdTe quantum dots.

Keywords: Quantum dots, bovine serum albumin, fluorescence spectroscopy, quantum dot – protein interaction

1. Introduction

Since the first time fluorescent semiconductor nanoparticles (quantum dots) were synthesized, they are widely explored due to their possible applications in many fields, including medicine. Tunable emission wavelength, broad absorption and sharp emission spectra, high quantum yield (QY), resistance to chemical degradation and photobleaching, versatility in surface modification makes quantum dots very promising fluorescent markers [1].

Quantum dots can be used for live cell labelling *ex vivo*, detection and imaging of cancer cells *ex vivo* [2], as a specific marker for healthy and diseased tissues labelling [3], for labelling healthy and cancerous cells *in vivo* [4], and for treatment of cancer using photodynamic therapy [5]. Despite all unique photophysical properties, some problems must be solved before quantum dots can be successfully applied in medicine. Quantum dots usually are water insoluble and made of materials that are toxic for biological objects (Cd, Se). To make them suitable for application in medicine surface of quantum dots has to be modified to make them water-soluble and resistant to biological media. After injection of quantum dots to live organisms they are exposed to various biomolecules (ions, proteins, blood cells, etc.). This could lead to degradation of quantum dot coating or quantum dot itself. In this case toxic Cd²⁺ ions are released and can cause damage to cells or even cell death. It is very important to know the bioeffects of quantum dots before using them in medicine. Till now

it is still very little known about the interaction of quantum dots with biomolecules. Recently the interaction of quantum dots with biomolecules attracted much interest and is studied using various methods, such as atomic force microscopy, gel electrophoresis, dynamic light scattering, size-exclusion high-performance liquid chromatography, circular dichroism spectroscopy and fluorescence correlation spectroscopy [6-9].

In this work we investigated stability and spectral properties of water-soluble CdTe quantum dots coated with thioglycolic acid in aqueous solutions (deionized water and saline) and in model media (deionized water and saline with bovine serum albumin).

2. Materials and methods

Quantum dots solutions were prepared by dissolving CdTe-TGA quantum dots ($\lambda = (550 \pm 5)$ nm, PlasmaChem GmbH, Germany) in deionized water or saline (0.9%), and diluting further till required concentration. Prepared solution was divided in two parts. A small amount of concentrated bovine serum albumin (BSA) (BSA, V fraction, $M = 69000$ g/mol, Sigma, Germany) solution (in deionized water or saline) was added to one solution and equal amount of solvent was added to another. Deionized water was prepared using two stage water cleaning system (distiller GFL 2008, Germany and deionizer MicroPure, TKA, Germany). pH values of solvents were 6 and 5.6 for deionized water and saline respectively.

Spectral measurements were performed immediately after preparation of solutions. Absorbance spectra were measured with Varian Cary Win UV (Varian Inc., Australia) absorption spectrometer. Photoluminescence

spectra were measured with Varian Cary Eclipse (Varian Inc., Australia) and PerkinElmer LS 50B (PerkinElmer, USA) fluorimeters. Photoluminescence excitation wavelength was 405 nm, excitation slits were 5nm, and emission slits 5nm and 4 nm for Varian Cary Eclipse and PerkinElmer LS 50B, respectively. Measurements were done in 1 cm path length quartz cells (Hellma, Germany). Cells were hermetically sealed and between measurements kept in dark at room temperature.

Photoluminescence decay was measured with FLS920 (Edinburgh instruments, UK) using time correlated single photon counting technique. EPL-405 (Edinburgh instruments, UK) laser, emission wavelength 405nm and pulse repetition rate 500 kHz was used for excitation. Photoluminescence decay was measured at peak of photoluminescence band (550 nm).

Samples for atomic force microscopy measurements were prepared by casting a drop (40 μm) of solution on freshly cleaved V-1 grade muscovite mica (SPI supplies, USA) spinning at 1000 rpm. Commercially available atomic force microscope (AFM) diInnova (Veeco instruments inc., USA) was used to take 3-dimensional (3-D) images of quantum dots. RTESP cantilevers (Veeco instruments inc., USA) with a tip curvature of >10 nm and a nominal spring constant of 40 Newton/meter (N/m) were used. Measurements were performed in tapping mode in air. All images were acquired at a scan rate of 1 Hz per line with a 512 pixel x 512 pixel image definition. Image processing included flattening (2nd order) to remove the background slope caused by the irregularities of the piezoelectric scanner. The analysis was performed using the SpmLabAnalysis software (Veeco instruments inc., USA).

3. Results

We investigated dynamics of quantum dots spectral properties (photoluminescence intensity, position of photoluminescence maximum and width of photoluminescence band) in aqueous solutions. Dynamics of quantum dots photoluminescence properties are presented in Fig. 1. As can be seen from Fig.1 A photoluminescence intensity of quantum dots dissolved in deionized water increases from 556 a.u. just after preparation, till 937 a.u. after 88 hours. At this stage photoluminescence intensity increases to 168 % of initial value, but photoluminescence band maximum position and width at half maximum remains constant, respectively 548 nm and 53 nm. After 88th hour photoluminescence intensity begins to decrease and decreases slowly till 142nd hour (805 a.u.,143% of initial photoluminescence intensity). When photoluminescence intensity begins to decrease (after 88 hours) photoluminescence band (maximum at 548 nm) starts to shift to longer wavelength region and shifts by 26 nm to 574 nm(at 182nd hour), but width of photoluminescence band still remains constant till 112th hour. From 112th hour photoluminescence band starts getting narrower and width of

photoluminescence band decreases from 53 nm (112th hour) to 45 nm (142nd hour) and later width of band remains constant. After 142 hours photoluminescence intensity starts to drop quite fast and 230 hours after preparation of solution photoluminescence disappears (intensity is 25 a.u.). Fig. 1 B shows absorbance band intensity dependence on time.

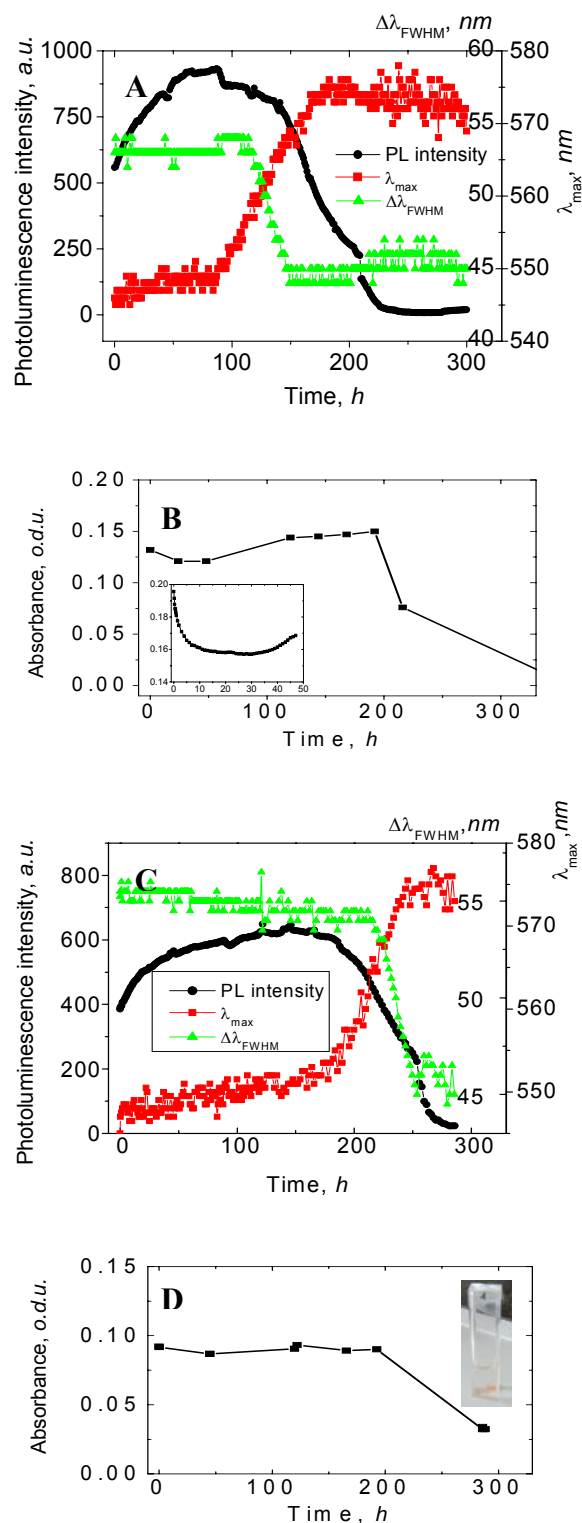


Fig. 1. CdTe QD spectral properties dependence on time. Photoluminescence band intensity, position and width dynamics: A - in deionized water, C – in saline. Quantum dot

absorption band intensity dynamics: B- in deionized water (insert shows initial absorption change 0-48 h), D – in saline, (concentration of quantum dots, $c=3,84 \cdot 10^{-7}$ mol/l).

Quantum dots absorbance is decreased after 24 hours but later it slowly increases till 192nd hour. After 192nd hour precipitate starts forming and absorbance intensity decreases.

In case when saline is used instead of deionized water, one can see similar changes of CdTe quantum dots photoluminescence properties like described above. During first stage photoluminescence intensity increases, and photoluminescence band maximum position and width at half maximum remains constant, respectively 548 nm and 53 nm. At this stage photoluminescence intensity increases to 166 % of initial value (from 389 a.u. to 648 a.u.) at 144th hour. Later photoluminescence intensity starts to decrease and 274 hours after preparation of solution is close to zero (40 a.u.). During this stage, when photoluminescence intensity is decreasing, photoluminescence band starts to shift bathochromically (163th hour) and shifts by 25 nm from 550 nm to 575 nm (at 244 hour). Width of photoluminescence band starts to decrease 226 hours after solution preparation and narrows by 9 nm (from 54 nm to 45 nm at 253 hour). Absorbance band intensity dependence on time is presented in Fig. 1D. Quantum dots absorbance in saline remains constant till 192nd hour. After 192nd hour precipitate starts forming and absorbance intensity decreases (Fig. 1 D insert). All these changes are very similar to changes that appear when quantum dots are dissolved in deionized water. Intensity increase, shift of photoluminescence band and decrease of band width in both cases are very similar: intensity increases by 168% (deionized water) and 166% (saline), band shifts by 26 nm (deionized water) and 25 nm (saline), band narrows by 8 nm (deionized water) and 9 nm (saline). Despite all these similarities one difference can also be observed: phase of photoluminescence growth is longer in case of quantum dots in saline (144 hours compared to 88 hours).

These results show that presence of Na^+ and Cl^- ions doesn't make big influence on spectral properties of CdTe quantum dots in aqueous media.

In biological objects quantum dots are exposed to various ions and biomolecules. In circulatory system quantum dots starts to interact with serum proteins. Freshly prepared CdTe quantum dots solution ($V=2$ ml) was titrated with BSA solution ($c=10^{-4}$ mol/l). Fig. 2 shows, that adding BSA to CdTe quantum dots solution increases their photoluminescence intensity up to certain concentration of BSA. Saturation is achieved when concentration of protein is $c=10^{-5}$ mol/l. Further titration leads to photoluminescence decrease (Fig. 2 line A). Change of photoluminescence intensity is caused by two processes: interaction of quantum dots with proteins and dilution effect. Graph of reference solution (titrated with saline) is presented in Fig. 2 (line B). Difference between photoluminescence

intensity of solution titrated with BSA and photoluminescence of solution titrated with saline gives photoluminescence change caused by interaction between CdTe quantum dots and BSA (Fig.2 line C). This line reaches its maximum value at $c=1.05 \cdot 10^{-5}$ mol/l.

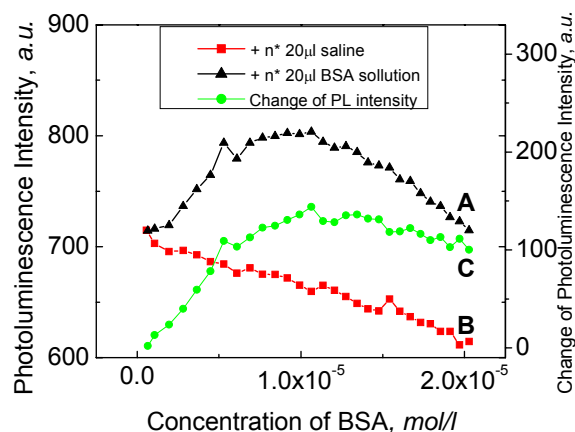


Fig. 2 CdTe quantum dots ($\text{CdTe } c = 4,8 \cdot 10^{-7}$ mol/l, $V = 2$ ml) photo photoluminescence intensity:

A – during titration with BSA solution ($c = 10^{-4}$ mol/l), B – titration with saline, C – change of photoluminescence intensity caused by BSA (dilution effect is eliminated).

For further investigations we chose $c = 1.5 \cdot 10^{-5}$ mol/l concentration of albumin. We decided to use 1.5 time bigger concentration, than concentration giving biggest photoluminescence increase, to ensure that all quantum dots are interacting with BSA. Photoluminescence spectral properties and absorption band intensity dynamics of CdTe quantum dots aqueous solutions with BSA is presented in Fig. 3. After the addition of protein photoluminescence of quantum dots suddenly increases (by 27% and 68% a.u. for saline and deionized water solutions, respectively). After jump, photoluminescence intensity further increases for approximately 40 hours and reaches 157% of initial value for saline and 184 % of initial value for deionized water solution. Later photoluminescence intensity starts decreasing, but decrease of intensity is quite slow and at longer time scale becomes negligible. This shows that BSA stabilizes CdTe quantum dots in aqueous media.

Even after two months quantum dots remain in solution and precipitates don't appear (Fig.3 D insert). Photoluminescence of quantum dots solutions with protein remains more intense than 50% of initial value. Absence of precipitate and quite intense photoluminescence of quantum dots solutions shows that BSA prevents quantum dots from aggregation. AFM measurements of long kept solutions confirm this idea. In Fig. 4 D CdTe quantum dots, deposited from saline solution after precipitate was formed, is presented. Large layered structures are seen on the surface. Height of these images is 70nm – 130 nm. Phase image (insert of Fig. 4 D) clearly shows that these large structures are formed from layers. Height of one layer is approximately equal to 3.5nm - 4 nm. Diameter of CdTe quantum dots that

have photoluminescence band at 600 nm is 3.5 nm [10]. It is approximately equal to height of one layer. This confirms idea, that precipitate formed in solution is large aggregates formed of CdTe quantum dots. Measurements of quantum dots deposited from freshly prepared solutions (Fig. 4 A-C) also shows, that quantum dots forms aggregates. AFM image of quantum dots, deposited from solution that was kept for 40 min., is presented in Fig. 4 A. A lot of small round structures are present on the surface. These structures are 2 nm – 3 nm in height and 20 nm – 30 nm in width.

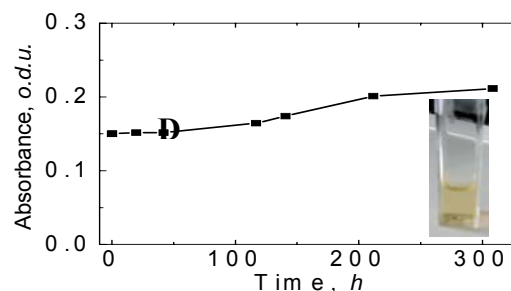
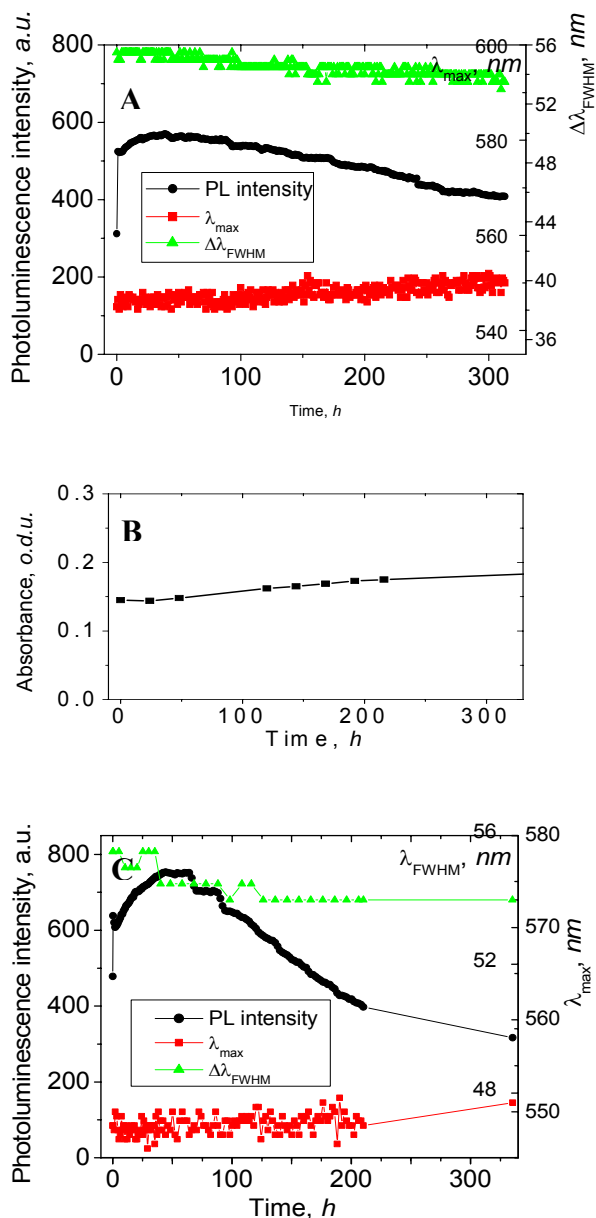


Fig. 3. CdTe QD spectral properties dependence on time in the presence of BSA. Photoluminescence band intensity, position and width dynamics: A – in deionized water with BSA, C – in saline with BSA. Quantum dot absorption band intensity dynamics: B – in deionized water with BSA, D – in saline with BSA. (Concentration of quantum dots $c=3,84 \cdot 10^{-7}$ mol/l, concentration of BSA $c=3 \cdot 10^{-5}$ mol/l).

Height of these structures is approximately equal to height of single quantum dot. Shape of colloidal quantum dots should be close to spherical. Structures seen on the surface have much bigger width than height. This can be explained by AFM imaging artefact called “tip imaging”. It is also possible that that these small structures are not single quantum dots but few quantum dots that are attached to each other. AFM image of quantum dots deposited from solution that was kept for 5 hours shows larger structures (fig. 4 B). After 5 hours height and width of structures varies in broader range. Some small structures (height - 3 nm, width – 20 nm) can be seen but also bigger structures (up to 9 nm in height and up to 70 nm in width) appear.

Image of sample prepared from solution that was kept for 24 hours (Fig. 4 C) shows that sizes of these structures increase even more. All these samples were prepared under the same conditions, so changes in the images are caused by changes in the quantum dot solution. Fig. 4 A–C shows that after dissolving quantum dots in deionized water, quantum dots start to aggregate and after some time precipitate of large aggregates appear. In case of quantum dots solutions with BSA, precipitate does not appear even after long time. Image of samples prepared from quantum dots in saline with BSA taken 1 month after solution preparation (Fig. 4 E) shows that there are no large structures that could form precipitate, but there are plenty of round structures that are 9 nm – 20 nm in height and 40nm – 60 nm in width. This result confirms that protein stabilizes quantum dots in aqueous solution and prevents quantum dots from aggregation.

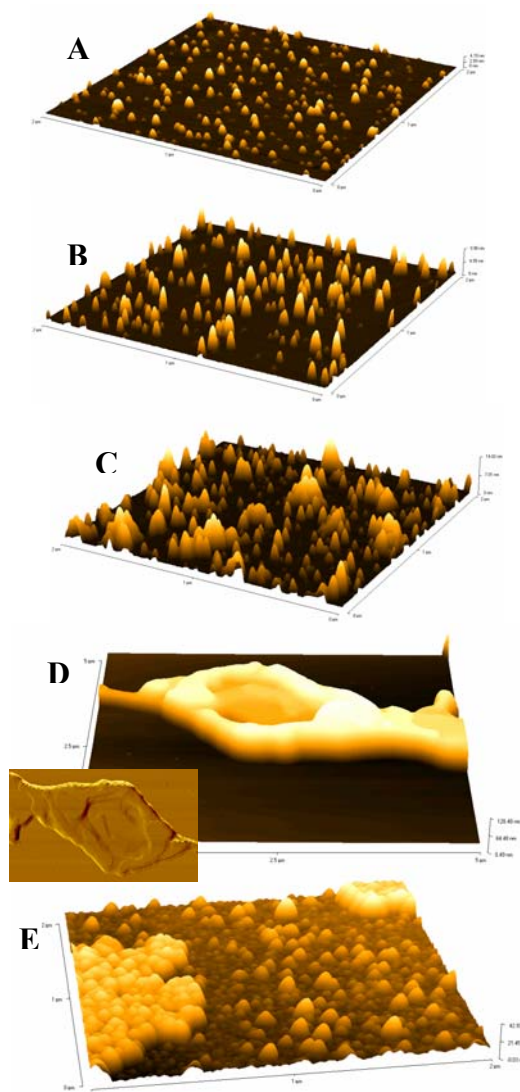


Fig. 4 AFM images of CdTe quantum dots (A-D) and CdTe quantum dots with BSA on mica. CdTe quantum dots deposited from solution in deionized water: A – 40 minutes after preparation, B – 5 hours after preparation, C – 24 hours after preparation. D – CdTe quantum dots deposited from saline solution after precipitate was formed (insert – phase image). E – CdTe quantum dots with BSA deposited from saline solution 1 month after preparation of solution. (A–C and E images are 2 μm x 2 μm , image D – 5 μm x 5 μm).

We also measured photoluminescence kinetics of quantum dots solution in deionized water with and without BSA. Photoluminescence decay of both samples is presented in Fig. 5. Photoluminescence of quantum dots without protein decays faster (Fig. 5 line A) and four photoluminescence decay lifetimes are needed to get good decay fit (reduced $\chi^2=1.018$). These lifetimes are: $\tau_1=3.4\text{ns}$, $\tau_2=14.1\text{ns}$, $\tau_3=30\text{ns}$, $\tau_4=88.2\text{ns}$. Fitting with three exponents doesn't give good results – $\chi^2=1.268$. In case of quantum dots solutions with BSA, three exponents are enough to get good fitting results ($\chi^2=1.063$, life times - $\tau_1=10.5\text{ns}$, $\tau_2=29.6\text{ns}$, $\tau_3=78.9\text{ns}$).

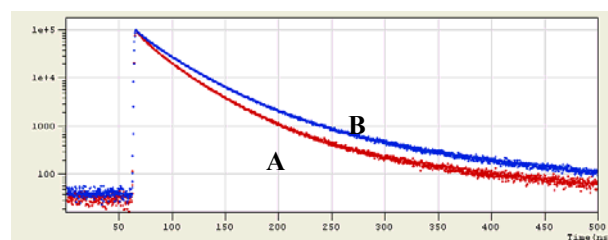


Fig. 5. Photoluminescence decay kinetics of CdTe quantum dots in deionized water (measured 48 h after preparation): line A – without BSA, line B – with BSA.

4. Discussion

Dynamics of absorption and photoluminescence properties of investigated solutions (presented in Fig. 1 and Fig. 3) shows two phases – growth of photoluminescence and decrease of photoluminescence. In the first phase photoluminescence of quantum dots increased in all investigated solutions. Despite quite large increase in photoluminescence spectra, changes in absorption spectrum are very small even a small decrease of absorption band can be seen after 24 hours. After that absorption of quantum dots solutions starts slowly increasing. During this phase photoluminescence band peak position and width remain constant. These changes indicate that core of quantum dot remains intact. Core degradation would cause blue shift of photoluminescence band; aggregation of quantum dots would cause a red shift. Change of photoluminescence intensity indicates, that properties of quantum dots coating (or coating itself) is changing: molecules coating core of quantum dot are rearranging, being replaced by other molecules or being washed-out. Theoretically increase of quantum dots photoluminescence intensity is explained by decrease of nonradiative transitions or their speeds. Decrease of defects on quantum dots surface would give this effect [11]. Another process that can change intensity of quantum dots photoluminescence is aggregation. Aggregation of quantum dots decreases photoluminescence quantum yield. Slow dissolution (monomerisation) of quantum dots powder (aggregates) could cause increasing photoluminescence intensity due to increased photoluminescence quantum yield of monomeric quantum dots compared with aggregated form. More detail investigation of absorption spectrum dynamics during first two days after preparation of solution (Fig. 1 B insert) contradicts to this explanation. Absorption of quantum dots dissolved in deionized water decreases during first day. This decrease can be explained by aggregation of quantum dots. Aggregation of quantum dots leads to decrease of absorption intensity, red shift, broadening and intensity decrease of photoluminescence band. But in first phase width and wavelength of photoluminescence band doesn't change, photoluminescence intensity increases. So these changes are caused not by aggregation of quantum dots but by changes in quantum dot coating. CdTe-TGA quantum dots are fluorescent nanoparticles composed of CdTe core and TGA coating. Rearrangement of quantum dot

coating leads to decrease of defects on quantum dot surface and increase of photoluminescence quantum yield. Sudden increase of quantum dots photoluminescence band, after adding BSA to solution, shows that interaction of quantum dots with BSA strongly increases photoluminescence quantum yield. Photoluminescence decay measurements confirm this result. Photoluminescence decay of quantum dots with BSA is tri-exponential while photoluminescence decay of quantum dots is described with four exponents. This shows that addition of protein eliminates one excitation relaxation path. Photoluminescence lifetime analysis shows that fastest relaxation component ($\tau_1=3.4\text{ns}$) disappears. Fastest relaxation component is caused by defects of quantum dots [12]. Elimination of this component leads to increase of quantum dots photoluminescence quantum yield. So rearrangement of TGA coating or formation of additional BSA layer is responsible for fluorescence increase in the first phase.

In the second phase photoluminescence of quantum dots starts to decrease. TGA molecules are not covalently bound to CdTe core and probably are washing out slowly. This process increases number of defects on quantum dots surface and leads to decrease of photoluminescence quantum yield. AFM images (Fig. 4 A–D) show that quantum dots in aqueous media starts to aggregate immediately after preparation of solution. Effects of aggregation are not seen in the first phase, but can be clearly seen in second phase. TGA coating makes CdTe quantum dots water-soluble. Washing out of coating decreases water-solubility of quantum dots and increases aggregation speed. In the second phase effects of aggregation (decrease and red shift of photoluminescence) are seen in both quantum dots solution without protein (Fig. 1 A, C). Decrease of photoluminescence band width is related to increase of monodispersity of quantum dots. Increase of monodispersity (at second phase) is caused by precipitation of large aggregates. Precipitation stage is also visible in absorbance spectrum (Fig. 1 B, D). Formation of precipitate decreases quantum dots concentration in the solution, so absorbance of solution decreases.

Second phase is different for solutions with protein. In this case photoluminescence decreases slowly and after some time stabilizes. Width and position of photoluminescence band doesn't change during this phase. This shows that quantum dots in the presence of protein don't aggregate, protein prevents degradation of quantum dots coating by replacing TGA molecules of forming additional BSA coating layer.

5. Conclusions

This study showed that water-soluble CdTe-TGA quantum dots in aqueous solutions are not stable. AFM study showed that quantum dots aggregates in solution and 9 days after preparation of solution precipitates. Na^+ and Cl^- ions don't make much influence on stability of CdTe-TGA quantum dots in aqueous

solution. BSA interacts with CdTe-TGA quantum dots, prevents their aggregation increases photoluminescence quantum yield and makes them stable. This effect is achieved by forming a new or additional layer of quantum dot coating.

Acknowledgements This study has been supported by the European Structural funds, the grant No BPD2004-ERPF-1.5.0-12-05/0035 / BPD-222.

6. References

1. Rotomskis R., Streckytė G., Karabanovas V.. Nanodariniai diagnostikai ir gydymui: nanomedicinos link. Medicina, Kaunas, 2006. 42 (7) p. 542-558.
2. Nida DL., Rahman MS., Carlson KD., et. al. Fluorescent nanocrystals for use in early cervical cancer detection. Gynecologic Oncology, 2005. p. 89-94.
3. Rotomskis R. Optical biopsy of cancer: nanotechnological aspects, Tumori. 94. 2008. p. 200-205.
4. Gao X., Cui Y., Levenson R.M., Chung L., Nie S.. In vivo cancer targeting and imaging with semiconductor quantum dots, Nature Biotechnology 22, 2004. p. 969 – 976.
5. Bakalova R., Ohba H., Zhelev Z., et. al. Quantum dots as photosensitizers?, Nature Biotechnology , 11, 2004. p. 1360-1361.
6. Shao L., Dong C., Sang F. Et. al.. Studies on interaction of CdTe quantum dots with bovine serum albumin using fluorescence correlation spectroscopy. Journal of Fluorescence 1(19), 2009. p. 151-157.
7. Ipe BI., Shukla A., Lu H. Et. al.. Dynamic light-scattering analysis of the electrostatic interaction of hexahistidine-tagged cytochrome P450 enzyme with semiconductor quantum dots. Chem Phys Chem 7(1), 2006. p. 1–8.
8. Pons T., Uyeda HT., Medintz IL., Mattoussi H.. Hydrodynamic dimensions, electrophoretic mobility, and stability of hydrophilic quantum dots. J Phys Chem B, 110(41), 2006. p. 20308– 20316.
9. Nehilla BJ., Vu TQ., Desai TA.. Stoichiometry-dependent formation of quantum dot-antibody bioconjugates: a complementary atomic force microscopy and agarose gel electrophoresis study. J Phys Chem B, 109(44), 2005. p. 20724–20730.
10. Zhang. Y., He J., Wang P., et. al.. Time-Dependent Photoluminescence Blue Shift of the Quantum Dots in Living Cells: Effect of Oxidation by Singlet Oxygen. J. AM. CHEM. SOC., 128, 2006. p. 13396-13401.
11. Stephen J., Byrne, Serena A., et. al.. Optimisation of the synthesis and modification of CdTe quantum dots for enhanced live cell imaging., J. Mater. Chem., 16, 2006. p. 2896–2902.
12. Jeong S., Achermann M., Nanda J., et al.. Effect of the thiol–thiolate equilibrium on the photophysical properties of aqueous CdSe/ZnS nanocrystal quantum dots. J. Am. Chem. Soc., 127(29), 2005. p. 10126-10127.

NANODIAMONDS AS CELL BIOMARKERS

Augustinas KULBICKAS

Liquid Crystals Laboratory, Faculty of Physics and Technology, Vilnius Pedagogical University, Studentu 39,
LT-08106 Vilnius, Lithuania.

Email: augustinask@yahoo.com

Abstract: Optical microscopy and Raman spectroscopy of (N-V) defected nanodiamonds were performed at 300K and 77K. Molecules of 5CB LC demonstrating good anchoring with diamond surface and expose external defects of diamonds. Internal (N-V) defects of diamonds possess fluorescence and spin manipulation at room temperature and could be used as cell biomarkers.

Keywords: Nanodiamonds, (N-V) defects, Raman spectroscopy, fluorescence

1. Introduction

Diamond nanomaterials are good candidates for various applications in physics, chemistry and biology. In the biology one of the key avenues to understanding how biological systems function at the molecular level is to probe biomolecules individually and observe how they interact with each other directly *in vivo*. Laser-induced fluorescence is a technique widely adopted for this purpose owing to its ultrahigh sensitivity and capabilities of performing multiple-probe detection [1]. However, in applying this technique to imaging and tracking a single molecule or particle in a biological cell, progress is often hampered by the presence of ubiquitous endogenous components such as flavins, nicotinamide adenine dinucleotides, collagens and porphyrins [2a,b,c,d, e] that produce high fluorescence background signals. These biomolecules typically absorb light at wavelengths in the range of 300–500 nm and fluoresce at 400–550 nm [3]. To avoid such interference, a good biological fluorescent probe should absorb light at a wavelength longer than 500 nm and emit light at a wavelength longer than 600 nm, at which the emission has a long penetration depth through cells and tissues. Organic dyes and fluorescent proteins are two types of molecules often used to meet such a requirement; however, the detrimental photo physical properties of these molecules, such as photo bleaching and blinking, inevitably restrict their applications for long-term *in vitro* or *in vivo* observations. Fluorescent semiconductor nanocrystals (or quantum dots), on the other hand, have gained considerable attention in recent years because they hold a number of advantageous features including high photo bleaching thresholds and broad excitation but narrow emission spectra well suited for multicolor labelling and detection. Unfortunately, most nanomaterials are toxic, and hence reduction of

cytotoxicity and human toxicity through surface modification plays a pivotal role in successful application of quantum dots to *in vivo* labelling, imaging, and diagnosis. Type Ib diamonds emit bright fluorescence at 550–800 nm from nitrogen-vacancy point defects, (N-V)⁰ and (N-V)⁻, produced by high-energy ion beam irradiation and subsequent thermal annealing. The emission, together with non cytotoxicity and easiness of surface functionalization, makes nano-sized diamonds a promising fluorescent probe for single-particle tracking in heterogeneous environments [1]. In particular, the designs of various biomarker systems based on the Raman and fluorescent properties of nanoparticles hold much promise, as opposed to conventional organic fluorophores which suffer from poor photo stability, narrow absorption spectra, and broad emission features [4]. Their unique optical properties strongly depend on (N-V) defects in diamond. Nitrogen-vacancy (N-V) defect are responsible for the red/near-infrared fluorescence of diamonds. Nanodiamonds with (N-V) centers can be one of smallest cell markers being limited to the range of tens of nanometers [1]. Now for diamond synthesis are developed wide variety techniques: chemical vapor deposition (CVD) [5], high pressure and high temperature (HPHT) [6]. CVD technique is very inefficient for creating N-V defects in nanodiamonds [7]. Stable and bright fluorescent (N-V)-rich nanodiamonds can be fabricated by irradiation and annealing in vacuum of type Ib high pressure high temperature (HPHT) diamonds grown from metal catalysts in a few minutes [8].

In this manuscript are reporting structural, Raman and fluorescence study of nanodiamonds properties to find the possibility to use these nanodiamonds as cell biomarkers.

possesses spin, which is the quantum form of magnetism.

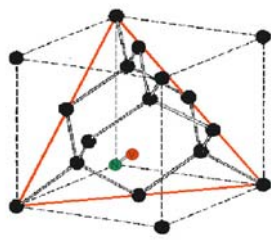


Fig. 7. Nitrogen - vacancy defect in the diamond structure.

In essence, spins are analogous to the tiny bar magnets and can code and store information by pointing in different directions. In practice, its spin can be manipulated using optical or magnetic techniques and the defect can be made to emit a single photon of light which has the characteristic of being “spin-up” or “spin-down”. This in itself is not unique as many other materials have similar defects that can be used in the same way. The real advantage is that the properties of diamond mean that it can work at room temperature while other technologies being explored require very low temperatures. Surprising the (N-V) centre possesses spin at room temperature, which can be manipulated by illumination and the defect can be made to emit a single photon of light which has the characteristic of being ‘spin-up’ or ‘spin-down’ [14]. The Raman spectra at 300 K and 77K are plotted in (Fig.8a,b,c,d). In the (Fig.8b) the diamond spectra are weak at 637 nm and displaying small amount of (N-V) defects. After irradiation the line at 637 nm is stronger as result formation more (N-V) defects (Fig.8a). The (N-V) defects have formed strong optical transitions with zero-phonon lines (ZPL) at 575 nm and 637 nm respectively (Fig.8 a,b,c,d). The ZPL peak at 575nm .is due the electronic transition of the neutral defect center (N-V)⁰, and the 637 nm ZPL peak corresponds to the ³A→³E transition of the negatively charged defect center (N-V)⁻ [15–18]. Negatively charged nitrogen-vacancy (N-V)⁻ centers in diamond have attracted much attention recently due to their unique properties, such as very long spin lifetimes at room temperature and their suitability for single photon sources [19].

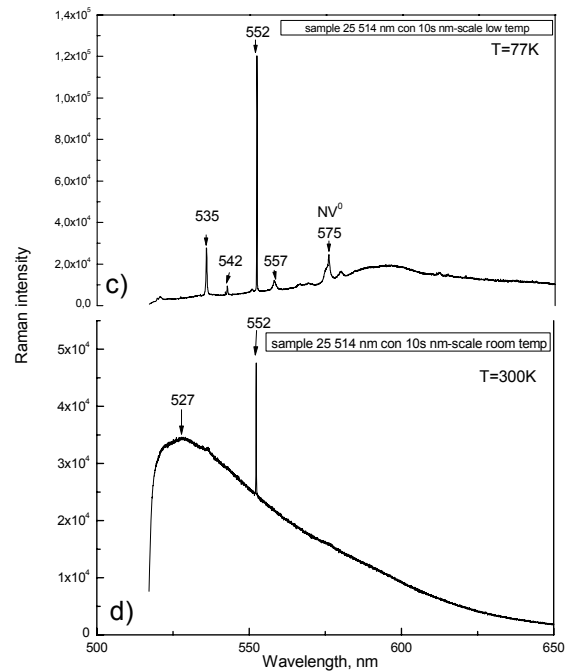
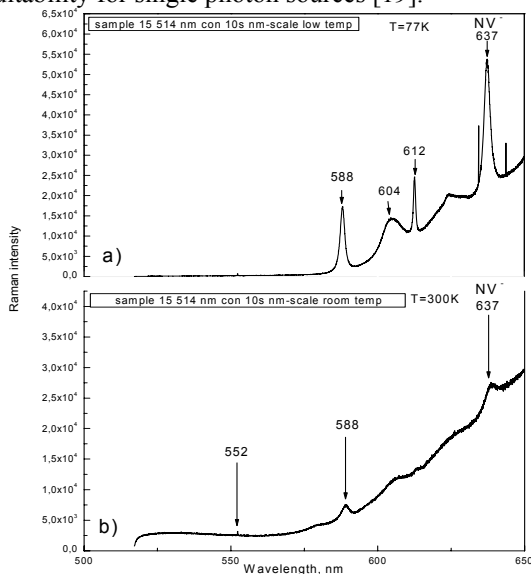


Fig. 8. The intensity of Raman spectra of different (a, b) and (c, d) diamonds at the 77 K and 300 K temperatures

3. Conclusion

The nitrogen defected diamonds possesses several unique properties: good fluorescence stability and spin manipulation at room temperature of the (N-V) defects. It is shown the possibility to use the (N-V) defects of nanodiamonds as cell biomarkers.

Defected. nanodiamonds with (N-V) defects located close to the cell in tens nanometers distance to get information from neighbouring cells.

Acknowledgements Support COST MP0803, COST P-19 and COST TD 08002 is gratefully acknowledged. Author thanks prof. R. Vaišnoras for helpful discussions.

4. References

1. Chi-Cheng Fu, et all, Characterization and application of single fluorescent nanodiamonds as cellular biomarkers, Proc Natl Acad Sci USA 104, 2007. p.727-732.
2. (a) J. Sabataityte, I. Simkiene, G.-J. Babonas, A. Reza, A. Suchodolskis, M. Baran, R. Szymczak, R. Vaisnoras, L. Rasteniene, V. Golubev, et all, Modification of photonic properties in porphyrin-infiltrated opal crystals, Photonics and Nanostructures - Fundamentals and Applications, 5, 2007. p. 125-128. (b) J. Sabataityte, I. Simkiene, G.-J. Babonas, A. Reza, M. Baran, R. Szymczak, R. Vaisnoras, L. Rasteniene, V. Golubev and D. Kurdyukov, Physical studies of porphyrin-infiltrated opal crystals, Materials Science and Engineering: C, 27, 2007. p. 985-989. (c) I.Simkiene, J. Sabataityte, A. Reza, G.J. Babonas, V. Golubev, D. Kurdyukov, Hybrid system of iron porphyrin or aminosilanized c-Si, Photonics and Nanostructures- Fundamentals and Applications 5,

- (2007) p. 129-135. (d) J. Sabataityte, I. Simkiene, G.-J. Babonas, A. Reza, A. Suchodolskis, M. Baran, R. Szymczak, R. Vaisnoras, L. Rasteniene, V. Golubev, D. Kurdyukov Modification of photonic properties of porphyrin-infiltrated opal crystals, *Photonics and Nanostructures-Fundamentals and Applications* 5, 2007. p. 125-128.(e) J. Sabataityte, I. Simkiene, A. Reza, G.-J. Babonas, R. Vaisnoras, L. Rasteniene, D. Kurdyukov, V. Golubev Studies of opal crystals with iron porphyrin, *Superlat. Microstr* 44, 2008. p. 664-669.
3. I Minevičiūtė, V. Gulbinas, M. Franckevičius, R. Vaišnoras, M. Marcos, J.L. Serrano, Exciton migration and quenching in poly(propylene imine) dendrimers, *Chemical Physics* 359 (2009) p. 65-70
 4. K. W. Sun, J. Y. Wang, and T. Y. Ko, Raman spectroscopy of single nanodiamond: Phonon-confinement effects, *Appl Phys Lett*, 92, 2008. p. 153115-3.
 5. Stacey A, Aharonovich I, Praver S and Butler J E Controlled synthesis of high quality micro/nano-diamonds by microwave plasma chemical vapor deposition *Diamond Relat. Mater.* 18, 2009. p. 51-55.
 6. R.Z. Yu, H.A. Ma, Z.Z. Liang, W.Q. Liu, Y.J. Zheng, X. Jia, HPHT synthesis of diamond with high concentration nitrogen using powder catalyst with additive $Ba(N_3)_2$ *Diamond Relat. Mater.* 17, 2008. p. 180-184.
 7. Kennedy T A, Colton J S, Butler J E, Linares R C and Doering P J, Long coherence times at 300 K for nitrogen-vacancy center spins in diamond grown by chemical vapour deposition *Appl. Phys. Lett.* 83, 2003. p. 4190-4192.
 8. P. Boudoul et al, High yield fabrication of fluorescent nanodiamonds, *Nanotechnology* 20, 2009. 235602 (11pp).
 9. H. Yokoyama, *Handbook of Liquid Crystal Research* (Oxford University Press, New York, 1997), Chap.6./ B. Jerome, Surface effects and anchoring in liquid crystals, *Rep.Prog.Phys.* 54, 1991. p. 391-451.
 10. K. Kočevar, R. Blinc, and I. Muševič, Atomic force microscope evidence for the existence of smecticlike surface layers in the isotropic phase of a nematic liquid crystal, *Phys.Rev. E* 62, 2000. p. R3055-R3058.
 11. K. Kočevar, A. Borštnik, I. Muševič, and S. Žumer, Capillary Condensation of a Nematic Liquid Crystal Observed by Force Spectroscopy, *Phys.Rev.Lett.* 86, 2001. p. 5914-5917.
 12. B. Zalar, S. Žumer and D. Finotello, Deuteron NMR Study of Monolayer Thick Films of Nematogenic Molecules, *Phys.Rev.Lett.* 84, 2000. p. 4866-4869.
 13. A.V.Zakharov and R.Dong, Surface polarization and effective anchoring energy in liquid crystals, *Phys.Rev. E* 64, 2001. p. 042701-4.
 14. G.Balasubramanian, P.Neumann, D.Twitchen, M.Markham, R.Kolesov, N.Mizuochi, J.Isoya, J.Achard, J.Beck, J.Tissler, V.Jacques V, PR.Hemmer, F.Jelezko, J.Wrachtrup, Ultralong spin coherence time in isotopically engineered diamond, *Nat Mater* 8, 2009. p. 383-387.
 15. G.Davies, M.F. Hamer, Optical Studies of the 1.945 eV Vibronic Band in Diamond *Proc. R. Soc. Lond. A* 348, 1976. p. 285-298.
 16. A.Gruber, A.Drābenstedt, C.Tietz, L.Fleury, J.Wrachtrup, C.von Borczyskowski, *Science* 276, 1997. p. 2012-2014.
 17. F.Jelezko, C.Tietz, A.Gruber I.Popa, A.Nizovtsev, S.Kilin, J. Wrachtrup, Spectroscopy of Single N-V Centers in Diamond, *Single Mol.* 2, 2001. p. 255-260.
 18. F.Treussart, V.Jacques, E.Wu, T.Gacoin, P.Grangier, J.F.Roch, Photoluminescence of single colour defects in 50nm diamond nanocrystals, *Physica B* 376, 2006. p. 926-929.
 19. A.D.Greentree, B.A.Fairchild, F.M.Hossain, S.Praver, *Diamond integrated quantum photonics, Materials today* 11, 2008. p. 22-31.

PPI DENDRIMERS ENCAPSULATED WITH SILVER NANOPARTICLES AS CARRIERS FOR MEDICAL APPLICATIONS

Marius FRANCKEVIČIUS

Liquid Crystals Laboratory, Faculty of Physics and Technology, Vilnius Pedagogical University, Studentu 39, LT-08106 Vilnius, Lithuania.

Email: marius.franckevicius@yahoo.com

Abstract: Poly(propylene-imine) PPI dendrimers incorporated with silver nanoparticles were studied. Optical spectra of fourth generation liquid crystalline poly(propylene-imine) PPI dendrimer with antimicrobial silver nanoparticles in chloroform solution were investigated. Shift of plasmon resonance peak towards to IR region about 20 nm in the liquid crystalline poly(propylene-imine) PPI-silvernanoparticle system was observed.

Keywords: liquid crystalline dendrimers, encapsulated dendrimers, silver nanoparticles, absorption

1. Introduction

Nanoparticles have distinguished possibility to be applied for diagnostics and targeted therapy. There exist many nanostructures with possible applications for targeting into cell, but in this study we orient on to dendrimers, which are soft polymeric nanostructures that offer structural flexibility and possibility to incorporate nanoparticles [1].

Dendrimers are perfect biofriendly, non-toxic, monodisperse organics macromolecules, with highly branched, and well defined chemical structure [2]. Dendrimers are a relatively new group of polymeric macromolecules, and have considerable interest to biomedical researchers because of their desired properties manipulation possibility during the synthesis. All bonds in dendrimers emerge radially from a central core to which monomers are attached. For the synthesis of dendrimers divergent and convergent strategy can be applied, therefore periphery and interior of dendrimer can distinguish big differences in features. Chemical and physical properties of dendrimers can be varied and optimized, therefore they show potential for medical applications. Typical size of these compounds varies from 1 to about 10nm [3] that it's possible to diffuse dendrimers through biological membranes [4]. Comparing lower generation dendrimers with higher generations tend to adopt spherical surface containing empty spaces in the interior. The empty spaces could host a guest molecules, drugs or nanoparticles [5]. This feature is very important when we talk about dendrimers as drug carriers, templates for nanoparticles synthesis and possible holders in wide range of nanosized materials. Drugs can be covalently coupled to the

dendrimer surface or complexed within the interior because there are many terminal groups to which drug molecules can be conjugated. Encapsulation of drugs inside dendrimers offer potential benefits such as prolonging the circulation time in the blood, protecting unstable drugs from the environment, enhancing the solubility of poorly soluble drugs, achieving controlled release and tissue targeting.

It's also known that silver is efficient antimicrobial agent [6, 7]. Therefore usefulness of these low toxic, noble metal nanoparticles is very important for medical applications. On other hand silver nanoparticles exhibit the highest efficiency of plasmon resonance of all other known metal nanoparticles. Optical properties of metal nanoparticles originate from collective oscillations of conductor electrons, which are termed surface plasmon polariton resonances after excitation by electromagnetics radiation [8]. There exist many works in which optical properties of silver nanoparticles were studied [9, 10].

Recently were demonstrated, dendrimers are an effective polymeric cage for the preparation noble metal nanoparticles – referred as dendrimer metal nanocomposites [11]. Metal nanoparticles can be formed in the dendrimer interior or on periphery, it's depending on the metal which is used to the synthesis, the type of reaction core and on the peripheral functional groups of the dendrimer [12].

In some cases hybrid systems when they are composed from organic-organic or organic-inorganic composites are very interesting for many applications: in membrane technology, drug delivery, sensors technology and etc. [13]. Synthesis of these hybrid systems were described and characterized by some groups for different

applications [12, 14]. Suppose dendrimers and silver nanoparticles can compose fluorescent, biocompatible and highly photostable dendrimer nanocomposite that may be used for cell labelling [15].

In this work optical properties of liquid crystalline (LC) poly(propylene-imine) (PPI) dendrimers of fourth generation with encapsulated silver nanoparticles were investigated for medical applications.

2. Experiment

Liquid crystalline PPI dendrimer of fourth generation with $-OC_5H_{11}$ terminal mesogenics units and Ag silver nanoparticles were used. Synthesis of liquid crystalline PPI dendrimers were described in detail in ref. [16] by condensation of 4-(40-ethoxybenzoyloxy) salicylaldehyde with the terminal amino groups of the $G = 4$ of poly(propylene imine) (PPI-(NH₂)₃₂) using a method previously described [17]. For small silver nanoparticles preparation briefly 200 mL 0.1 mM AgNO₃ solution was reduced with 2 mL 0.5 mM NaBH₄ in the presence of tri-sodium citrate (0.3 mM) under gentle stirring. Immediately after injection of the reducing agent, 2 mL of a 5 wt% aqueous solution of PVP was added [18].

Incorporation of silver nanoparticles in dendrimers was involved by using concentrations of the same molar ratios of both materials in chloroform solution. Firstly liquid crystalline dendrimers were dissolved in chlorophorm solution. Aqueous solution of silver nanoparticles was evaporated and then nanoparticles were mixed with dendrimer chloroform solution.

Encapsulated LC PPI dendrimers with silver nanoparticles were characterized by optical absorption spectroscopy. Optical spectra were recorded by double-beam spectrophotometer Perkin Elmer Lambda 19. More information of purity of dendrimers was described in ref. [16]. Structural and optical characteristics of used silver nanoparticles were described by Bastys et al. [18].

3. Results

Structure of liquid crystalline PPI dendrimers of fourth generation is presented in Fig. 1. Also silver nanoparticles a few nanometer in size in the liquid crystalline PPI dendrimer were encapsulated.

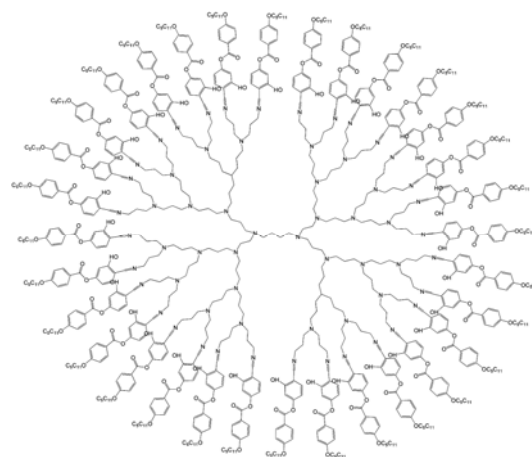


Fig.1. Fourth-generation PPI-[C2]32 liquid crystalline dendrimer

Figure 2 shows modeled liquid crystalline PPI dendrimer like-structure consisting of four terminal flexible chains on periphery were demonstrating empty spaces inside branching units. In this empty spaces could be hosted silver nanoparticles. Calculations of the same dendrimers structures composed of six and eight terminal chains show occupation of empty spaces are 1 to 3nm² in square.

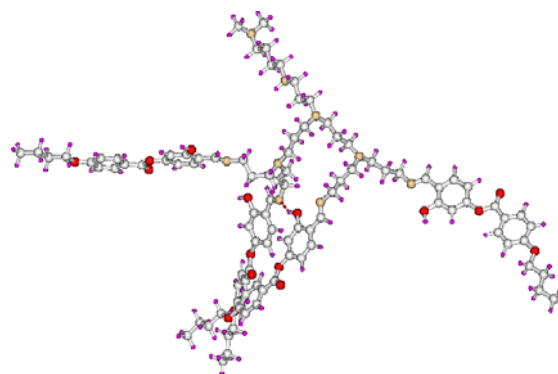


Fig.2. The calculated periphery of the PPI dendrimer structures composed of 4 terminal flexible chains displaying empty spaces between chains

These empty spaces can be used as containers or holders for silver nanoparticles or drugs. According calculations size of encapsulated silver nanoparticles in to dendrimer couldn't be bigger than these calculated sizes.

Figure 3 shows transmission electron microscope images (TEM) of silver nanoparticles. Background of the image shows initial nanoparticles, whose are used for incorporation into liquid crystalline PPI dendrimer.

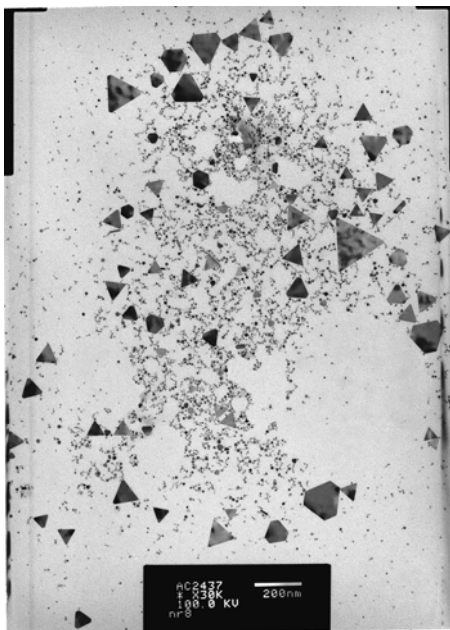


Fig.3. TEM image of silver nanoparticles in size $\sim 2\text{-}3\text{nm}$ and $\sim 100\text{nm}$.

The steady state normalized absorption spectrum of pure LC PPI G4 dendrimer in chloroform solution presented in fig. 4, where three absorption bands at 260 nm, 315 nm and 375 nm were recorded.

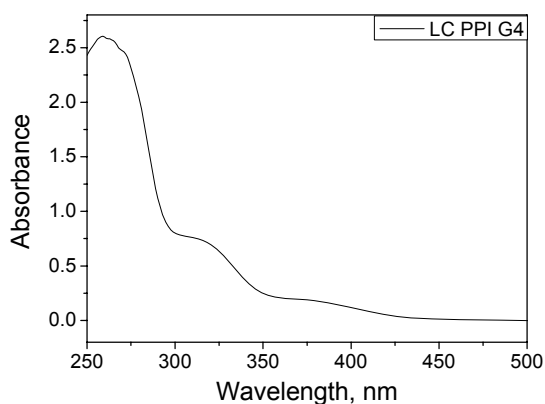


Fig.4. Absorption spectra of liquid crystalline PPI G4 dendrimer First two absorption bands situated in lower wavelengths interval are related with dendrimer central core and interior. Therefore low intensity absorption band near 375nm is related with dendrimers periphery

More accurate analysis of these LC dendrimers of various generations in different concentrations in chloroform was described in our previous work [19]. Absorption band dislocated at longer wavelengths expect major advertence, because flexible liquid crystalline periphery of dendrimer could interact with silver nanoparticles. Bands maximum position of liquid crystalline dendrimers depends on generation and corresponded functional units. By increasing dendrimer size, extinction maximum position moves to longer wavelengths, while for first two bands they are almost stationar in the same wavelength position in UV region. Band shift also depends and from length of used mesogenics units on periphery. When mesogens are bigger, shift dependence from generation is wider. Therefore for these studies we have used family of dendrimers with bigger mesigenic units.

Optical spectra changes corresponded with terminal units and could tell us about possible interactions between dendrimer and nanoparticle. In fig. 5a and fig. 5b there are shown of silver nanoparticles plasmon resonance band in aqueous and chloroform solutions, and absorption spectra of liquid crystalline PPI dendrimer encapsulated with silver nanoparticles in fig. 5c. It's known, that the dipole absorption maximum of the silver nanoparticle rapidly shifts to longer wavelengths by increasing particle size [9] and indistinctly by the used environment. Also absorption bands markedly changes depending on environment. In our case intensity of absorption bands of these Ag nanoparticles differs for two different media. In chloroform solution, absorption maximum of silver nanoparticles decreases in about 10 times comparing with that in aqueous solution. Therefore position of bands for these different solvents was almost nonchanged. Similar results of silver nanoparticles were obtained and in distilled water, acetone and ethanol solutions by Tilaki et. all. [10].

In figure 5c plotted normalized absorption spectra of liquid crystalline dendrimer interacting with silver nanoparticles. In comparison with below plotted spectra, absorption maximum is shifted to towards longer wavelength region about 20 nm. This shift of absorption band emerges from dendrimers interaction with silver nanoparticle.

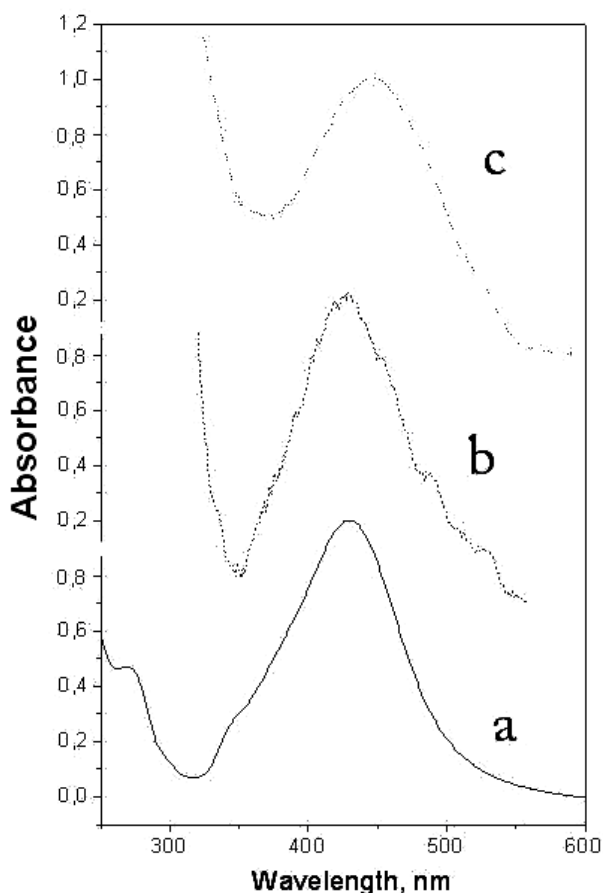


Fig.5. Optical spectra of silver nanoparticles in aqueous solution (a), silver nanoparticles in chloroform solution (b) and silver nanoparticles encapsulated liquid crystalline dendrimer (c)

4. Conclusions

Optical spectra of fourth generation liquid crystalline poly(propylene-imine) PPI dendrimer with antimicrobial silver nanoparticles in chloroform solution were investigated. Shift of plasmon resonance peak towards to IR region about 20 nm in the PPI-Ag system was observed in comparison with pure silver nanoparticles in chloroform and silver nanoparticles in distilled water.

Acknowledgements Thank the Lithuanian State Science and Studies Foundation. Projects COST P19, COST TD0802 and COST MP0803. Also I'm thankful prof. Rimantas Vaisnoras and dr. E. Tamuliene for discussions from experimental and theoretical points of view.

5. References

1. Prasad P.N. Nanophotonics, Wiley, 2004. (chapter 13).
2. Thomalia A.D.. Birth of a New Macromolecular Architecture: Dendrimers as Quantized Building

- Blocks for Nanoscale Synthetic Organic Chemistry. *Aldrichimica Acta* 37, 2004. p. 39.
3. Frechet J.M.J.. Dendrimers and Other Dendritic Macromolecules: From Building Blocks to Functional Assemblies in Nanoscience and Nanotechnology. *Journal of Polymer Science:Part A: Polymer Chemistry* 41, 2003. p. 3713.
4. Balogh L., Swanson D.R., Tomalia D.A., Hagnauer G.L. and McManus A.T.. Dendrimer-Silver complexes and Nanocomposites as Antimicrobial Agents. *Nano Lett.* 1, 2001.p. 18.
5. Vogtle F.. *Dendrimers II: Architecture, Nanostructure and Supramolecular Chemistry*, Springer, 2000. (chapter 3).
6. Ip M., Lui S.L., Poon V.K.M, Lung I. and Burd A.. Antimicrobial Activities of Silver Dreesings: an *in vitro* Comparision. *Journal of Medical Microbiology* 55, 2006. p. 59.
7. Furno F., Morley S.K., Wong B., Sharp B.L., Arnold P.L., Howdle S.M., Bayston R., Brown P.D., Winship P.D., and Reid H.J..Silver Nanoparticles and Polymeric Medical Devices: a New Approach to Prevention of Infection. *Journal of Antimicrobial Chemotherapy* 54, 2004. p. 1019.
8. Kreibig U., Vollmer M.. *Optical Properties of Metal Clusters*, Springer, 1995. (chapter 1).
9. Evanoff Ir D.D. and Chumanov G.. Synthesis and Optical properties of Silver nanoparticles and Arrays. *Chem.Phys.Chem.* 6, 2005. p. 1221.
10. Tilaki R.M., Iraj Zad A., and Mahdavi S.M.. Stability, Size and Optical Properties of Silver Nanoparticles Prepared by Laser Ablation in Different Carried Media. *Applied Physics A* 84, 2006. p. 215.
11. Esumi K., Hosoya T., Suzuki A., and Torigoe K.. Formation of Gold and Silver Nanoparticles in Aqueous Solution of Sugar-Perstituted Poly(amidoamine) Dendrimers. *Journal of Colloidal Science* 226, 2000. p. 346.
12. Stofik M., Stryhal Z. And Maly J.. Dendrimer-encapsulated Silver Nanoparticles as Novel Electrochemical Label for Sensitive Immunosensors. *Biosensors and Bioelectronics* 24, 2009. p. 1918.
13. Vogtle F., Richardt G. and Werner N. *Dendrimer Chemistry Concepts, Synthesis, Properties, Application*, Wiley, 2009. (chapter 8).
14. Jin L., Yang S.P., Wu H.X., Huang W.W., Tian Q.W.. Preparation and Characterization of Silver Nanoparticles with Dendrimers as Templates. *Journal of Applied Polymer Science* 108, 2008. p. 4023.
15. Lesniak W., Shi X., Bielinska A., Janczak K., Sun K., Baker J. R., Balogh L. P.. Labelling Cells with Silver/Dendrimers Nanocomposites. *Mater. Res. Soc. Symp. Proc.* 845, 2005. AA5.37.1.
16. Pastor L., Barberá J., Kenna M., Marcos M., Martín-Rapún R., Serrano J. L., Luckhurst G. R. and Mainal A.. End-on and Side-on Nematic Liquid Crystal Dendrimers. *Macromolecules* 37, 2004. p. 9386.

17. Barberá J., Marcos M. and Serrano J.L.. Dendromesogens: liquid crystal organizations versus star burst structures. *Chem. Eur. J.* 5, 1999. p. 1834.
18. Bastys V., Pastoriza-Santos I., Rodriguez-Gonzalez B., Vaisnoras R. And Liz-Marzan L. M.. Formation of Silver Nanoprisms with Surface Plasmons at Communication Wavelengths. *Adv. Funct. Mater.* 16, 2006. p. 766.
19. Kulbitskas A., Tamuliene E., Rasteniene L., Franckevicius M., Vaisnoras R., Marcos M., Serrano J.L., Jaskorzynska R., Wosinski L.. Optical Study and Structure Modelling of PPI Liquid Crystalline dendrimer derivatives. *Photonics and Nanostructures – Fundamentals and Applications* 5, 2007. p. 178.

INVESTIGATIONS OF SILVER NANOPARTICLES FOR UV PERSONAL DOSIMETERS

Judita PUIŠO*^{**}, Asta Guobienė*^{***}, Igoris PROSYČEVAS^{**}

*Department of Physics, Kaunas University of Technology, Studentų g. 50, LT - 51368, Kaunas, Lithuania

** Institute of Physical Electronics, Kaunas University of Technology Savanorių pr. 271, LT-50131, Kaunas, Lithuania

*** International Studies Centre, Kaunas University of Technology, Mickevičiaus g. 37, LT - 44244, Kaunas, Lithuania

Abstract People are exposed to natural or artificial UV radiation in different ways; unintentionally or intentionally, as at their workplace or on their spare time. The effects of UV on health can be harmful – as in its effect on skin cancer rates, or beneficial – as in the case of its effect on vitamin D status. A personal dosimetry is necessary in order to quantify the amount of individual UV exposure. Silver nanocomposites layers as possible personal UV dosimeters were investigated. Silver nanocomposites layers were fabricated using spin coating and UV irradiation on glass substrate. Ag/PVP nanocomposites were investigated by UV-VIS and AFM.

Keywords: Silver, nanoparticles, PVP, UV irradiation, UV-VIS, AFM

1. Introduction

People are exposed to natural or artificial UV radiation in different ways; unintentionally or intentionally, at their workplace on their spare time. UV radiation contributes to the aging of the skin and, in different ways, to the generation of skin cancers [1-5]. Primarily because of behavioral changes resulting in higher UV-exposure of the skin to UV the incidence rates of skin cancer have increased dramatically in many industrialized countries with a larger Caucasian population. Currently, for example, the annual incidence rate for basalioma and squamous cell carcinoma in Germany is about 70 per 100,000 population (it was 15 in 1970) and for melanoma 14 per 100,000 citizens (3 in 1970). The corresponding data for melanoma currently is 19 cases per 100,000 citizens in USA. The risk for melanoma in the USA was about six times lower in 1960s. Part of the increase in incidences of skin cancers certainly can be ascribed to a longer life expectancy and also to a higher skin cancer awareness amongst physicians and consequently an increased diagnosis rate. Besides these factors, UV-exposure as a result of both UV radiation levels and behavior plays an important role [2]. Solar UV-A (320 to 400 nm) and the higher-energy and the shorter wavelength UV-B (290 to 320 nm) penetrate the Earth's atmosphere, and chronic exposures have been linked to melanoma, the most fatal form of skin cancer. UV-C (100 to 290 nm) has the highest energy but is blocked by the ozone layer [3].

However, UV-C exposures are possible from artificial sources, including germicidal lamps, arc welding equipment, and mercury arc lamps in older tanning beds [1]. There is widespread public interest in the relationships between UV radiation and health. The effects of UV on health can be harmful – as in its effect on skin cancer rates, or beneficial – as in the case of its effect on vitamin D status. In the past, researchers have attempted to determine these relationships as functions of ambient UV radiation. However, the UV doses that humans are typically received are less than 5% of that available UV [1, 2]. A personal dosimetry is necessary to quantify the amount of individual UV exposure. In practical use dosimeters are based on polysulphone and on polyphenylene oxide (PPO), polymers undergoing changes in its optical properties upon irradiation with UV [4-5]. Other systems determine the UV dose by quantifying damage induced in *Bacillus subtilis* spores upon UV exposure [3].

In our days silver nanostructures hold great interest due to their unique properties and potential application in nanoelectronics, magnetic, biosensors, data storage, catalysis, surface enhanced Raman scattering and excellent antibacterial properties. Silver nanostructures are particularly interesting due to their size- and shape – dependent plasmonic properties. Plasmonic properties of silver nanoparticles are very sensitive to UV and gamma irradiation and structural changes [6-10].

The results of UV effect on morphology and plasmonic properties of silver nanocomposites are presented. Silver/PVP nanocomposites layers are

presented there also. The possible formation mechanism of Ag nanostructures the effect of molar ratio of PVP to silver nitrate, UV exposure time are discussed based on experimental results obtained by UV-VIS, AFM and FTIR.

2. Experimental

Silver nitrate (AgNO₃ analytical reagent) and poly(N)- vinyl pyrrolidone (PVP) (average MW=10 000) and sodium dodecyl sulfate (SDS) (MW=288.38) were obtained from Sigma Aldrich. Deionised water was prepared with a Milipore water purification system. In a typical experiment 250 mg of AgNO₃ were added to 4 ml of aqua's PVP (30 wt%) solution. Ag-PVP films were produced on the pre-treated glass substrates from the colloidal silver solution in PVP by spin coating. The glass substrates were pretreated for 10 min sonically in acetone and were dried in air stream. Ag/PVP films were spin-coated with "DYNAPERT PRECIMA" centrifuge. The spin speed was above 1800 rpm and spinning time was 30 s. UV source (Hibridas Exposure Unit MA4, power 1200 W, wavelength 300-400 nm, and exposure time from 1 to min.) were used for UV irradiation. The Ag/PVP layers were aged in the "black box" for 3 months. Samples were placed on the table as a patient and irradiated by UV source under atmospheric pressure and ambient temperature. The formation of silver nanoparticles in PVP solution and thin Ag/PVP films were confirmed by recording absorbance by UV-VIS (UV/VIS/NIR AvaSpec-2048) spectrometers. The morphology properties of the silver polymer nanocomposites (Ag/PVP) were investigated by atomic force microscope NT- 206 (AFM). V type noncontact silicon cantilever NSC11/15 silicon probe (constant force 3 N/m, resonant frequency 65 Hz) was used for AFM measurements. Image processing and analysis of the scanning probe microscopy data were performed with a program "Surface View version 2.0".

3. Results and discussion

Absorbance spectra of Ag/PVP thin films after UV irradiation on glass and 3 months ageing is presented in Fig. 1.

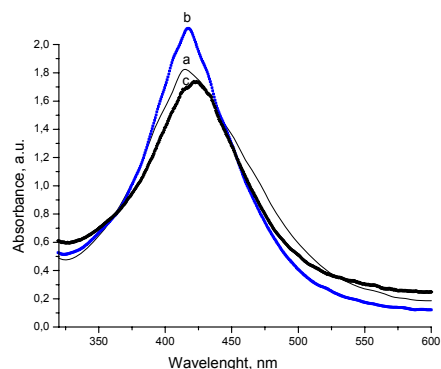


Fig. 1. Absorbance spectra of Ag/PVP films after primary UV irradiation and aging: a) 1 min, b) 20 min, and c) 180 s

The surface plasmon (SPR) peak in UV-VIS spectra at 415-419 nm, indicated plasmonic properties of silver nanoparticles. According [6-9] we produce spherical silver nanoparticles with 20 nm size in polymer [7-9]. Using Chumanov's calculations [10] we find that size of silver nanoparticles is about 40 nm. According "Mieplot" calculations results, the size of spherical silver nanoparticles is 30-35 nm. The intensity of SPR peak dependences (position, halfwidth and cording adsorbance) on UV exposure time, irradiation induces the redshift of SPR peak from 415 nm to 420 nm, increasing half-width of peak. UV irradiations induce silver nanoparticles aggregation. Absorbance of Ag/PVP layers after the secondary UV irradiation is presented in Fig 2.

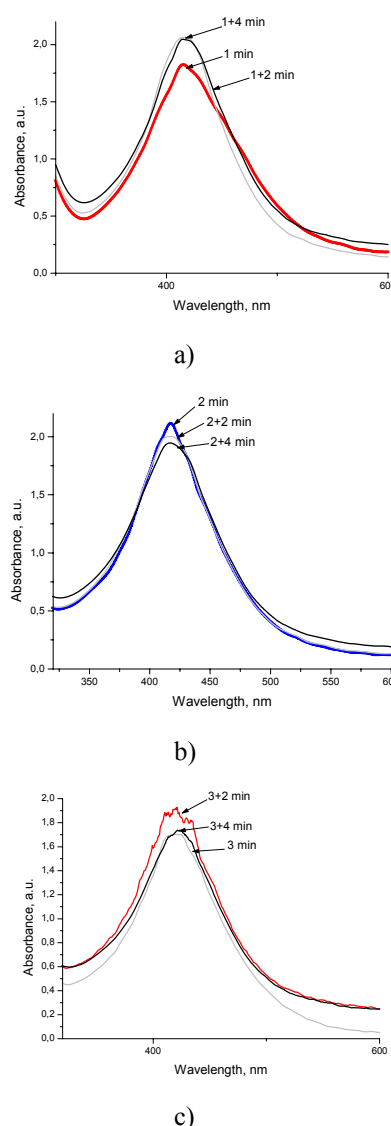
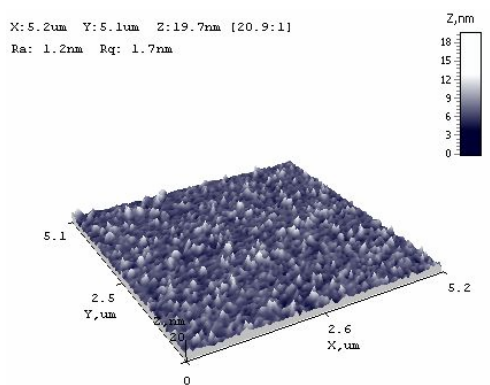
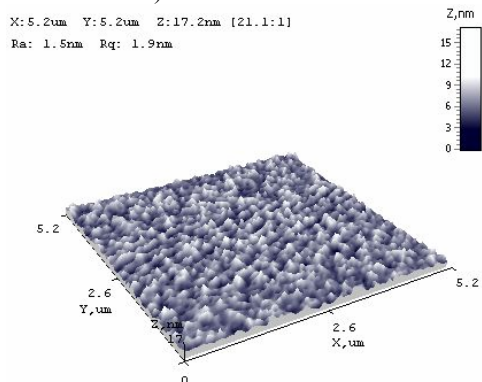


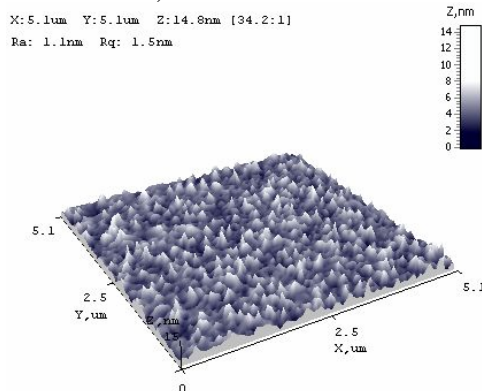
Fig. 2. Absorbance spectra of Ag/PVP films after secondary UV irradiation a) 1 min, b) 20 min, and c) 180 s



a)



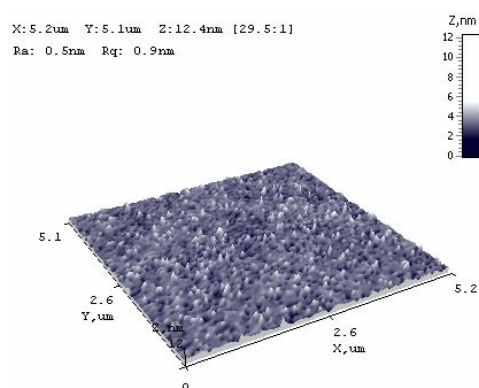
b)



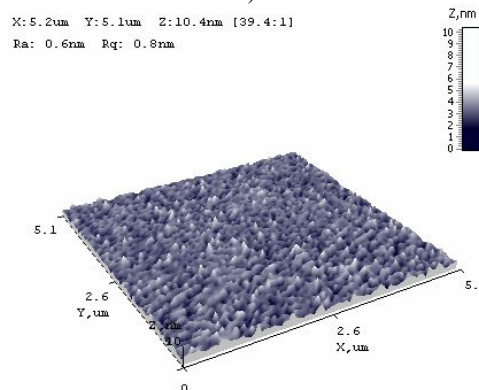
c)

Fig. 3. Morphology of Ag/PVP nanocomposites after UV irradiation a) 1 min, b) 1+2 min and c) 1+4 min.

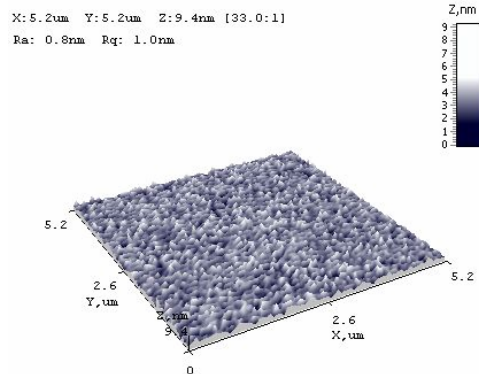
According to [9] results, surface plasmonic properties (SPR resonance peak position, intensity in UV spectra) are dependent on the UV irradiation time of Ag/PVP layer. We found that the plasmonic properties of Ag/PVP layer after secondary UV are dependent on the sample's history (as previous UV irradiation). The secondary UV irradiation induced the change of absorbance from 1.82 to 2.04 a.u. when the Ag/PVP



a)



b)

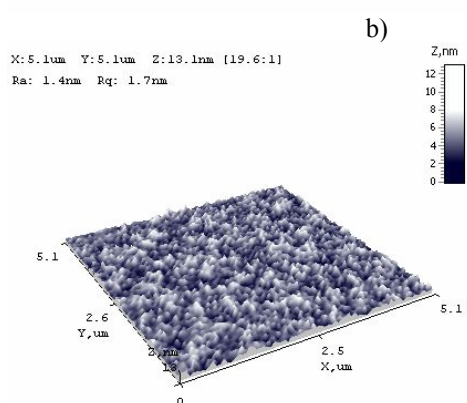
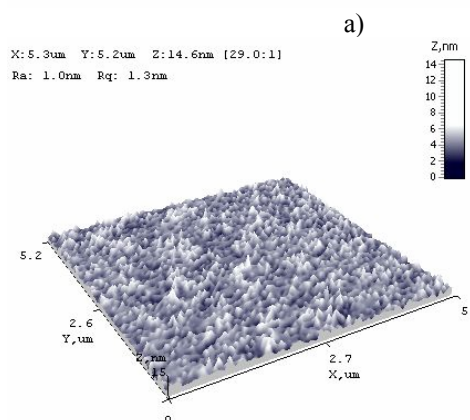
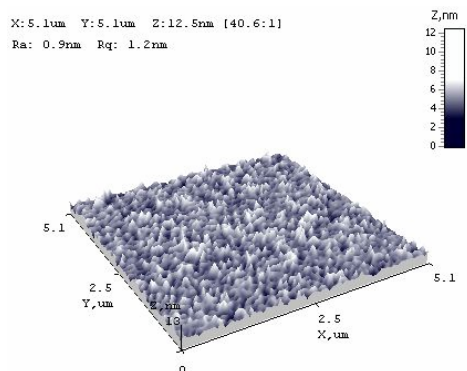


c)

Fig. 4. Morphology of Ag/PVP nanocomposites after UV irradiation a) 2 min, b) 2+2 min and c) 2+4 min.

layer was irradiating for 1 min. It could be mentioned that when the Ag/PVP layer was irradiated for 2 min the secondary UV irradiation induced the change of absorbance from 2.11 to 1.94 a.u. Redshift of SPR peak from 419 nm to 423 nm in UV-VIS spectra was induced by the secondary UV irradiation. It was observed only for the larger particles which were produced by primary UV exposure. We can say that at the first case (primary

UV exposure was 1min) changes of absorbance were induced by silver photoreduction, at the second (primary UV exposure was 2 min) – by photodegradation of polymer and the third case (primary UV exposure was 3 min) – by silver nanoparticles agglomeration and polymer degradation. Morphology of Ag/PVP nanocomposites is presented in Fig 3 and Fig. 4 and Fig. 5.



c)

Fig. 5. Morphology of Ag/PVP nanocomposites after UV irradiation a) 4 min, b) 4+2 min and c) 4+4 min.

We found that the main Ag/PVP nanocomposite layers structure is very flat 3D (islands) structure. Roughness (Rq) of these layers after primary UV irradiation varied

from 1.56 nm to 0.87 nm. The secondary UV irradiation induced changes in roughness and Ag/PVP morphology was very weak (0.2-0.4 nm).

4. Conclusions

The influence of UV to plasmonic properties and morphology of Ag/PVP nanocomposites was absorbed at very short UV irradiation time from 1 min to 7 min. Intensity and position of the surface plasmon resonance of Ag/PVP are dependent on the UV irradiation time also on type of UV irradiation (primary or secondary). Changes of plasmonic properties of Ag/PVP layers are challenge for new personal UV dosimeters. We suggest that detectors based on surface plasmon resonance become a useful tool in both clinical and scientific areas.

5 Acknowledgements

The Lithuanian Science and Study Foundation and COST action MP0803 have supported this work.

6. References

1. S. T. Durant, K. Paffet, M. Shrivastav, G. S. Timmins, W. F. Morgan, and J. A. Nickoloff, UV Radiation Induces Delayed Hyperrecombination Associated with Hypermutation in Human cells,- *Molecular and cellular biology* **26**, No 16, 2006, 6047-6055p.
2. P. Hoeppe, A. Oppenrieder, C. Erianto, K. Koepke, J. Reuder, M. Seefeldner, D. Nowak, Visualization of UV exposure of the human body based on data from a scanning UV- measuring system, *Int. J. Biometerol* **49**, 2004, 18-25 p.
3. Y. Furusawa, K. Suzuki and M. Sasaki, Biological and Physical deosimeters for monitoring Solar UV-B light, *J. Radiat. Res.* **31**, 1990, 189-206 p.
4. Parisi, A.V., Wong, C.F., Galea, V. A study of the total ultraviolet exposure to all the leaves for small plant growth. *J. Photochem. Photobiol. B: Biol.*, **45**, 1998, 36-42 p.
5. Parisi, A.V., Kimlin, M.G, Personal solar UV exposure measurements employing polysulphone with an extended dynamic range. *Photochem. Photobiol.*, **79**, 2004, 411-416p. .
6. Stepanov, A.L. Quantitative analysis of surface plasmon interaction with silver nanoparticles.- *Optics Letters* **30**, No. 12, 2005, 1524-1526 p.
7. Choi N.K., Seo D. S., Lee J.K, Preparation and stabilization of silver colloids protected by surfactant.- *Materials forum*, **29**, 2005, 394-397 p.
8. Carotenuto G., Pepe G.P., and Nicolais L., Preparation and characterization of nano-sized Ag/PVP composites for optical applications.- *Eur. Phys. J.* **B16**, 2006 11-17 p.
9. Yang X., Lu Y., Preparation of polypyrrole-coated silver nanoparticles by one-step UV-induced polymerization *Materials Letters*, **59** 2005: pp. 2484-2487p.
10. Evanoff Jr D.D., Chumanov G. Synthesis and optical properties of silver nanoparticles and arrays. *J. Phys. Chem* **108** 2004 13948-13956p.

PRESCRIBING, RECORDING, AND REPORTING EXTERNAL BEAM THERAPY A SUMMARY OF ICRU REPORTS Nos 29, 50, 62 AND 71

Torsten LANDBERG*, Per NILSSON**

*Oncology Malmö, Lund University, Malmö University Hospital, SE-205 02 Malmö;

**Radiation Sciences, Umeå University, Umeå University Hospital, SE-901 85 Umeå, Sweden

Abstract: This presentation is a summary and a discussion of the ICRU Reports Nos 29, 50, 62 and 71.

Keywords: Radiotherapy, external, ICRU, prescribing, recording, reporting, QA, QC.

Volumes

The process of determining the volumes for the treatment of a patient with malignant disease consists of several distinct steps, during which different tissues, organs, and volumes are defined three-dimensionally. They will be considered here as volumes. These volumes are, or represent (Fig. 1):

Gross Tumor Volume (GTV), Clinical Target Volume (CTV), Internal Target Volume (ITV), Planning Target Volume (PTV), Organ at Risk (OR), Planning Organ at Risk Volume (PRV), Treated Volume, and Irradiated Volume.

It should be noted that only GTV, CTV, and OR represent tissues, whereas the other ones are purely geometric concepts, which do not strictly represent tissue- or organ borders.

Gross Tumor Volume (GTV)

The Gross Tumor Volume (GTV) is the gross palpable or visible/demonstrable extent and location of the malignant growth. The GTV may consist of primary tumor ("GTV-T"), metastatic lymphadenopathy ("GTV-N"), or other metastases. The GTV corresponds almost always to those parts of the malignant growth where the tumor cell density is the largest. Due to the high density of the cancer cells in the GTV, an adequate dose must be delivered to the whole GTV in order to obtain local tumor control in radical treatments. No GTV can be defined if the tumor has been completely removed *e.g.* by previous surgery. The shape, size, and location of a GTV may be determined by means of different methods such as clinical examination (*e.g.* inspection, palpation, endoscopy), and various imaging techniques (*e.g.* X-ray, CT, Digital

Radiography, Ultrasonography, MRI, and radionuclide methods). The methods used to determine the GTV should meet the requirements for staging the tumor according to the clinical TNM (UICC International Union against Cancer 1997, 2002) and AJCCS (American Joint Committee on Cancer, 1997, 2002) systems, and the definition of the GTV is then in full agreement with the criteria used for the TNM-classification. The GTV (primary tumor, metastatic lymphadenopathy, other metastases), may seemingly be different in size and shape, sometimes significantly, depending on what examination technique that is used for evaluation (*e.g.* palpation versus mammography for breast tumors, and CT versus MRI for some brain tumors). The radiation oncologists should in each case therefore indicate which method has been used for evaluation and for the definition of the GTV.

The Gross Tumor Volume should be described in standard topographical or anatomical terms, *e.g.* "18

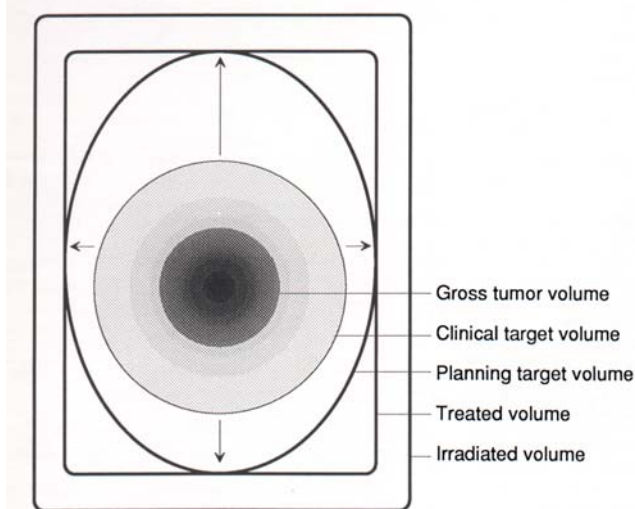


Fig. 1. Schematic representation of some of the volumes.

mm tumor in the left lobe of the prostate adjacent to but not breaching the capsule". In many situations, a verbal description might be too cumbersome and also, for the purpose of data recording and analysis, a classification system is needed. Several systems are proposed for coding the anatomical description; some of them are mentioned in ICRU Report No. 50. A GTV may be confined to only part of an organ (e.g. a T1 breast cancer), or involve a whole organ (e.g. in multiple metastases to the brain). The GTV may or may not extend outside the normal borders of the organ or tissue involved.

Clinical Target Volume (CTV).

The Clinical Target Volume (CTV) is a tissue volume that contains a demonstrable GTV and/or is considered to contain microscopic, subclinical extensions at a certain probability level. This volume thus has to be treated adequately in order to achieve cure. For the treatment of subclinical disease, two situations may be defined as below, and as illustrated in Fig. 2. In this situation the prescription is based on the assumption that in some anatomically definable tissues/organs, there may be cancer cells at a given probability level, even though they with present day techniques cannot be detected; they are subclinical. The level of probability is based on clinical experience from adequately documented treatments and follow-up. For the purpose of prescription of treatment, it can usually be described in terms of frequency of risk for later detectable manifestations, when not treated adequately in the subclinical situation.

Prescription of treatment of subclinical extensions adjacent to a GTV.

Clinical experience indicates that around a GTV (Fig. 2, a & b) (primary tumor; GTV-T, or metastatic lymphadenopathy; GTV-N) there is generally subclinical involvement, *i.e.* individual malignant cells, small cell clusters, or microextensions, which cannot be detected by the staging procedures. The GTV together with this surrounding volume of local subclinical involvement can be defined as a Clinical Target Volume (CTV-T for primary tumor, and CTV-N for metastatic lymphadenopathy, etc). If the same dose is prescribed for two such CTVs, they can be labelled CTV-TN. If different doses are prescribed, there will be one CTV-T, and one CTV-N, respectively. If the GTV has been removed by seemingly radical surgery, but it is still felt that radiotherapy is needed for the tissues that remain close to the site of the removed GTV, this volume is also usually designated as CTV-T.

Prescription of treatment of subclinical extension at a distance from a GTV.

Additional volumes (CTVs) with presumed subclinical spread (Fig. 2 c&d) (e.g. regional lymph nodes, N0) may also be considered for therapy. They are also defined as Clinical Target Volumes, and may topographically be designed CTV-N I, CTV-N II, etc. In order to stress that in such cases subclinical disease is treated "electively", it may be useful to add also "E", e.g. CTV-EN. It may also be useful to differ between "high-risk" CTVs and "low-risk" CTVs. A precise description of the terminology used should be available in the treatment protocol. If different doses are prescribed, different CTVs have to be prescribed for treatment planning. Thus, for any given situation there is often more than one CTV. One situation can be illustrated by considering a primary tumor and its regional lymphatics separately (e.g. in breast saving procedures) where the primary tumor and its regional lymphatics are separated anatomically. In other situations the aim is to treat two or more CTVs to different dose levels. One common example of this is "boost" therapy, where often the "high-dose" volume (often containing the GTV or GTVs) is located inside the "low-dose" volume. One has to stress that the prescription of the GTV(s) and CTV(s) are based on general oncological principles, and are not specific to the field of radiation therapy. For instance, in surgery, a safety margin is taken around the Gross Tumor Volume according to clinical judgment, and this implies the same use of the Clinical Target Volume concept as in external beam radiation treatments. Also in brachytherapy, volumes to be treated are defined, and thus the concept of CTV is valid. The definition of GTV(s) and CTV(s) thus constitute the basic prescription of treatment, and must precede the subsequent treatment planning.

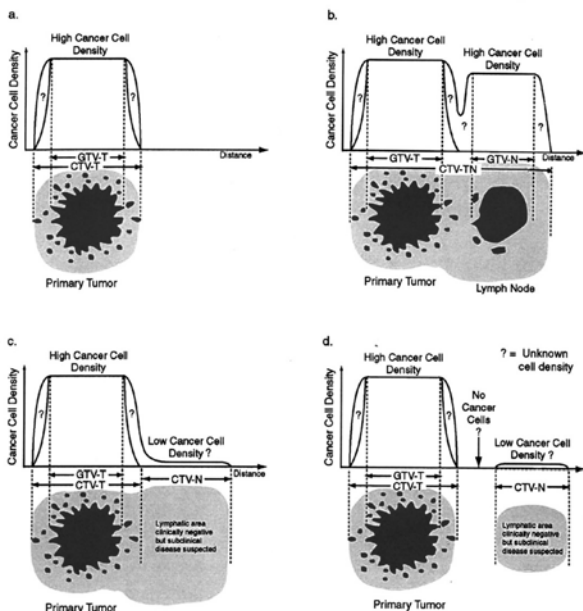


Fig. 2. Schematic illustrations of the relations between GTV(s) and CTV(s), in different clinical situations.

Planning Target Volume (PTV)

Margins for geometric variations and uncertainties.

Once the CTV(s) have been defined, then in external beam radiation treatment, a suitable arrangement of beam(s) will have to be selected in order to achieve a dose distribution that can be accepted. To-day this calculation can only be done for a static representation, whereas in fact there are variations and uncertainties in the positions, sizes and shapes, and orientations of both the tissues, patient, and the beams in relation to the common coordinate system. This will be seen both during a single session and from one session to another. The variations and errors may be either random or systematic. Such variations and uncertainties may also occur when information for the decision making is obtained (e.g. by CT-scanning), and also between this part of the procedure and the first treatment. Different geometric variations and uncertainties to be considered when defining the PTV (see below) are given in Figs. 4 & 5. This creates a situation where the dose distribution is being calculated for a static situation which does not reflect the real mobile situation. If no margins are added, some of the tissues will for part of the treatment move out of the therapeutic beam, and this will result in underdosage. Other parts of the tissues may move around in a dose gradient, and then it will hardly be possible to state the exact dose received by each part of the tissues. If margins are too large, this will result in unnecessary morbidity. We are facing a situation, for which there is no ideal solution. Rather one has to agree on acceptable compromises. In order to assure that the CTV(s) really receive a dose that does not deviate significantly from the prescribed and planned dose, one has to take into account and add margins to the CTV(s) for dose planning purpose for variations in tissue positions, sizes, and shapes, as well as for variations in patient position and the beam geometries, both intrafractionally and interfractionally. This leads to the concept of Planning Target Volume (PTV). Figs. 4, 5 & 6 illustrate schematically the different Volumes and Margins, that will be discussed in detail below. For the final treatment planning (definition of beam sizes etc.), all the different variations and uncertainties will have to be considered, and their overall effect defines a static volume (Planning Target Volume [PTV]), that will be used for treatment planning and for basic reporting of doses, then considered to be representative for the corresponding CTV(s).

The need for such additional margins, included in the PTV, thus results from a number of geometrical variations and uncertainties in relation to the reference points and coordinate systems. Examples are given below.

Internal Margin (IM).

An Internal Margin (IM) has to be added to the CTV to compensate for expected physiologic variations in size, shape, and position of the CTV during therapy in relation to an Internal Reference Point and its corresponding Coordinate System. The Internal Margin, commonly asymmetric around the CTV, compensates

for movements and variations in site, size and shape of the tissues which contain or are adjacent to the CTV, resulting from e.g.: respiration, different fillings of the bladder, different fillings of the rectum, swallowing, heart beat, movements of the bowel.

These internal variations are thus basically physiological ones, and they result in changes in site, size, and shape of the CTV. They can usually not be influenced easily. They do not depend on external uncertainties in patient day-to-day set-up or beam geometry.

The Internal Target Volume (ITV).

The Internal Target Volume (ITV) is the volume encompassing the CTV, that takes into account the fact that the CTV varies in position, shape and size.

The Internal Target Volume (ITV) is defined by the Internal Margin (IM), as described above, and is referred to the patient coordinate system.

Set-up Margin (SM).

To account specifically for uncertainties and variability in the reproducibility of patient positioning and inaccuracies in the alignment of the therapeutic beams during treatment planning and treatment through all treatment sessions, a Set-up Margin (SM) for each beam is needed. The uncertainties to be compensated for may vary with different anatomical directions, and thus the size of such margins depends on the selection of beam geometries. The inaccuracies depend on such factors as: variations in patient positioning, lack of reproducibility of the equipment (worn bearings causing e.g. sagging of gantry, collimators, and couch), human factors (e.g. experience and precision of the radiographers/radiotherapists).

They may also vary from center to center, and within a given center from machine to machine. The use of patient immobilization devices, the application of quality assurance programs for *i.a.* the physical aspects of the treatment equipment, and the skill and experience of the radiographers/radiotherapists are important factors which have to be taken into account. The use of different record and verify systems (in real time or not) may also be important, and may significantly reduce the size of the needed set-up margins. It is useful for a center to evaluate their own set-up margins, at least for frequent treatment techniques, thus allowing for potential standardizations. The net effect from combining an Internal Margin (referenced in the patient coordinate system) and a Set-up Margin (referenced to the external coordinate system) to the CTV leads to the concept of Planning Target Volume (PTV). The Planning Target Volume (PTV) is a geometrical concept, used for treatment planning, and it is defined to select appropriate beam sizes and beam arrangements, to ensure that the prescribed dose is actually delivered to the CTV. Thus the border of the PTV has to be clearly defined on charts or in files for treatment planning purposes. For the purpose of dose

specification for reporting, the margin that defines the PTV will have to be a closed line, even if this may not be necessary for the proper selection of beam parameters. It may be advantageous, but is probably often not feasible for different reasons, to display also the borders of the Internal Target Volume.

Note that in some cases, the Internal Margin approaches a very low value, (e.g. with brain tumors), and in other cases the Set-up Margin may be very small (e.g. with on-line correction for the different set-up errors and variations).

Ideally, the size of the margins should be determined in an iterative way during the selection of an optimal beam arrangement, e.g. in beam's eye view (as when planning both co-planar or non-coplanar conformal therapy). In practice this may not always be feasible, and as a compromise one can specify the margins for uncertainty in such a way, that they can be used for different types of beam arrangement (e.g. one beam, two opposed beams, box technique, orthogonal beams, moving beam). In daily clinical use, this is probably the most feasible way to go when defining the PTV for treatment planning and for basic dose specification for reporting, and is the approach recommended in ICRU Report # 50, 1993.

Depending on the clinical situation (e.g. patient condition and site of the CTV), and the chosen technique, the PTV could be very similar to the CTV (e.g. small skin tumors, pituitary tumors), or by contrast much larger (e.g. lung tumors). Since the PTV is a purely geometric concept, but has to be related to the basic anatomical description, it may surpass normal anatomical borders (e.g. include parts of clinically unaffected bony structures), or even extend outside the patient (e.g. in a case of tangential irradiation of the breast [Fig. 4]) if the basic anatomy is presented in a static way (which for the moment seems in general to be the only realistic method). The problem is of course a fundamental one: how can one combine a static dose calculation with a moving CTV? One has to accept the use of rather artificial methods, and in a situation as described above, it is recommended that, for the purpose of treatment planning (dose calculation in air will of course not be meaningful) and for evaluation of the dose distribution to add "constructed tissue" (see Fig. 6) to the static, "frozen" reference situation (e.g. to a transverse section). As a compromise, the width (thickness) of this slice of "constructed tissue" can be chosen to agree with the average of the position of PTV with different degrees of variations and uncertainties (e.g. different phases of respiration). It may not be necessary to add all uncertainties due to the movements and spatial variations linearly (Fig. 4 & 5). Some of the movements and variations previously listed could deviate systematically at the time of the irradiation compared to the planning process. Other uncertainties may vary at random. If the random uncertainties are normally distributed and the systematic uncertainties are estimated by their standard deviations, the combined effect can be estimated. The total standard deviation is then the root of the square sum of random and systematic uncertainties. It should be realized that the different variations and

uncertainties may be either symmetric or anisotropic, and they may be independent, counter-variate, or co-variate. The size may differ for different parts of a CTV (e.g. base versus apex of the bladder and prostate), and the temporal conditions may vary (e.g. with the respiratory cycle). The situation may be quite different for a single patient from that for a random patient population.

The PTV is thus the volume that is used for dose calculation, and the dose distribution to the PTV has to be considered to be representative of the dose distribution to the corresponding CTV. Since the Planning Target Volume is a static, geometrical concept, used for treatment planning, it does not in fact represent defined tissues or tissue borders. Actually, the tissues contained geometrically within the PTV may not truly receive the planned dose distribution; at least not in some parts close to its border. This is due to the variation in position of the CTV within the boundaries of the PTV during a course of treatment. When delineating the PTV, consideration should also be given to the presence of any radiosensitive normal tissue (Organs at Risk, see below). This may lead to the choice of alternative beam arrangements and/or shapes as part of an optimization procedure. In some cases it may be necessary to change the prescription (for volumes and/or doses), and then accept a smaller benefit. When, for radical treatments, the probability of benefit approaches a low value, then the aim of therapy may shift from radical to palliative.

Note that the definition of the Planning Target Volume (PTV) in Reports # 62, and #71 (ICRU 1999, and 2004) is identical to that in the previous Report # 29 ICRU 1978, and Report # 50 ICRU 1993 definition of "Target Volume". The two concepts are thus synonymous.

Penumbra and Dose Gradients.

The penumbra is not included in the PTV. The beam aperture has to be increased in order to compensate for the penumbra.

Organs at Risk (OR) ("Critical Normal Structures").

Organs at risk are normal tissues whose radiation sensitivity may significantly influence treatment planning and/or prescribed dose (e.g. spinal cord). The dose-volume response of normal tissues is a complex and gradual process. It depends on earlier effects induced long before depletion of stem cells or differentiated cells that in addition may have a complex structural and functional organization. For the analysis of volume-dependence of the dose-response parameters, it has been suggested that the tissues of an Organ At Risk can be considered to be organized in "Functional Sub Units, (FSUs), and the concepts of "serial", "parallel", and "serial-parallel" organizations of the normal structures (Fig. 3) has been suggested. For example, the spinal cord has a

high “relative seriality”, implying that a dose above tolerance limit to even a small volume of the Organ at Risk may be deleterious, whereas the lung usually has a low “relative seriality”, meaning that it may be the relative size of the volume that is irradiated above tolerance level that is the most important parameter.

As an example can be mentioned late effects from mantle treatment for Hodgkin’s disease. The late effects from the (partial) irradiation of the lungs (a parallel tissue) were much less serious than those from the heart (a combined serial [coronary arteries] and parallel [myocardium] tissue).

For the moment the model has not been tested enough to allow for firm recommendations, but indeed it highlights an important problem.

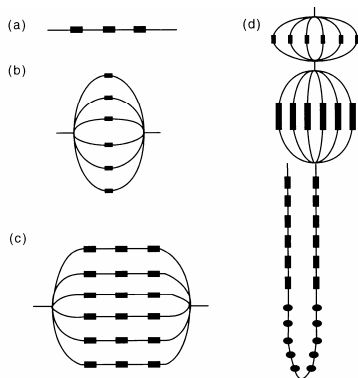


Fig. 3. Schematic examples of tissue organization structures in the parallel-serial model.

- a) a serial string of subunits (e.g., the spinal cord),
- b) a parallel string of subunits (e.g., the lungs),
- c) a serial-parallel string of subunits (e.g., the heart),
- d) a combination of parallel and serial structures (e.g., a nephron).

Modified from Withers et al., (1988) and Källman et al., (1992).

It may be useful to state whether the Organ at Risk is considered to be arranged mainly Serially (“Se”), mainly in Parallel (“Pa”), or mainly in a serial-parallel mixed fashion (“Mi”).

Planning Organ at Risk Volume (PRV)

As is the case with the Planning Target Volume, any movements of the Organ(s) at Risk during treatment, as well as uncertainties in the set-up during the whole treatment course must be considered. An integrated margin has to be added to the OR to compensate for these variations and uncertainties, using the same principles of Internal and Set-up Margins as for the PTV. This leads, in analogy with the PTV, to the concept of Planning Organ at Risk Volume (PRV). Note that a PTV and a PRV may overlap.

Treated Volume.

Due to the limitations of the irradiation techniques and in some specific clinical situations, the volume receiving the prescribed dose may not match accurately the PTV; it may be larger (sometimes much larger) and in general

of a simpler shape. This leads to the concept of Treated Volume. It is defined when the treatment planning procedure is completed and the beam arrangement as well as all the other irradiation parameters have been selected. The Treated Volume is the tissue volume which (according to the approved treatment plan) is planned to receive at least a dose selected and specified by the radiation oncologist as being appropriate to achieve the purpose of the treatment, e.g. tumor eradication, or palliation. The treated volume is thus a volume enclosed by the isodose surface corresponding to that dose level. For example, if the prescribed dose is 60 Gy, and the

minimum dose (considered to be adequate) was 5 % below the central dose (which was normalized to 100 %), the treated volume is then enclosed by the 57 Gy isodose surface. Normally, in the patient, the tissue volume which actually receives that dose level (i.e. “actual” treated volume) should match the “planned” treated volume (“Conformal Therapy”). It is important to identify the Treated Volume and its shape, size, and position in relation to the PTV for different reasons. One is to evaluate causes for local recurrences (“in-field” [=too low dose] versus “marginal” [=too small volume] ones). Another is to evaluate complications in normal tissues encountered outside the PTV but within the Treated Volume. The comparison of the Treated Volume and the PTV for different beam arrangements can be used as part of the optimization procedure (“conformity index”).

Irradiated Volume

The Irradiated Volume is the tissue volume which receives a dose that is considered significant in relation to normal tissue tolerance. If the Irradiated Volume is reported, the significant dose must be expressed either in absolute values (in Gy) or relative to the specified dose to the PTV. The Irradiated Volume depends on the treatment technique used.

Probability of Benefit versus Risk of Complications

It is recognized that the linear addition of the margins for all types of uncertainties would generally lead to an excessively large PTV. This could result in exceeding the patient tolerance and fail to reflect the actual clinical consequences.

The risk of missing part of the cancer cell population must be balanced against the reduction of the risk of severe and serious normal tissue complications. The balance between disease control and risk of complications often dictates acceptance of reduced probability of cure in order to avoid severe and serious treatment-related complications.

Therefore, the selection of a composite margin and the delineation of the border of the PTV involve a compromise that relies upon the experience and the judgment of the radiation-oncology team.

Colour Code.

For each volume defined, a color code is proposed to assure clarity of interpretation.

- GTV: Gross Tumor Volume (dark red)
- CTV: Clinical Target Volume (pink)
- ITV: Internal Target Volume (dark blue)
- PTV: Planning Target Volume (light blue)
- OR: Organ at Risk (dark green)
- PRV: Planning Organ at Risk Volume (light green)
- Landmarks (black)

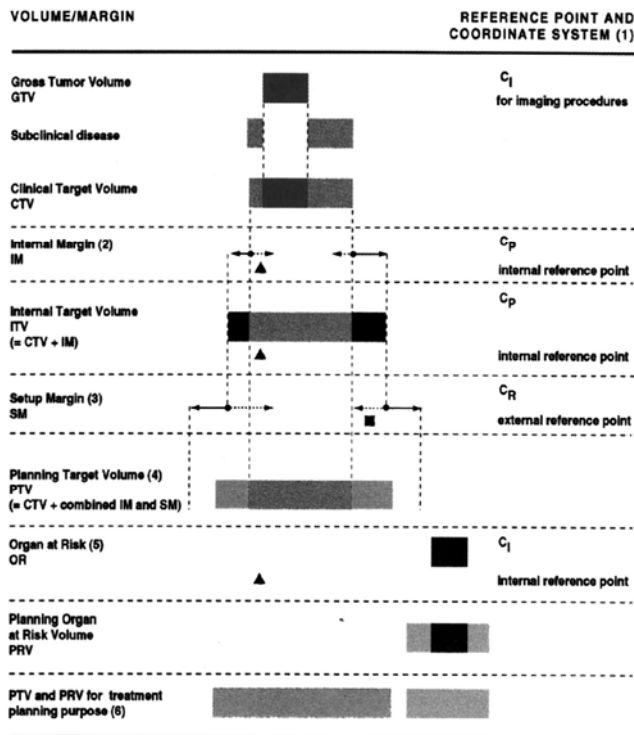


Fig. 4. Schematic representation of the different volumes/margins.

Note:

- (1) The Internal Margin may be asymmetrical.
 - (2) Like the Internal Margin, the Set-up Margin may also be asymmetrical.
 - (3) To delineate the PTV, the IM and SM are not added linearly (since this could result in an excessively large PTV), but are combined (for explanation, see text). The PTV is thus smaller than if one would simply have added the IM and SM linearly.
 - (4) For Organs at Risk (OR), margins are added in the same way as for the PTV.
 - (5) The PTV and PRV may or may not overlap.
- Note that when the Treated Volume is made smaller by use of many beams (e.g. in IMRT) the Irradiated Volume gets larger.

Scenario A.

A margin is added around the Gross Tumor Volume (GTV) to take into account potential “subclinical” invasion. The GTV and this margin define the Clinical Target Volume (CTV).

In external beam therapy, to ensure that all parts of the CTV receive the prescribed dose, additional safety margins for geometric variations and uncertainties must be considered.

An Internal Margin (IM) is added for the variations in position and/or shape and size of the CTV. This defines the Internal Target Volume.

A Set-up Margin (SM) is added to take into account all the variations/uncertainties in patient-beam positioning.

The CTV combined with the IM and the SM define the Planning Target Volume (PTV) on which the selection of beam size and arrangement is based.

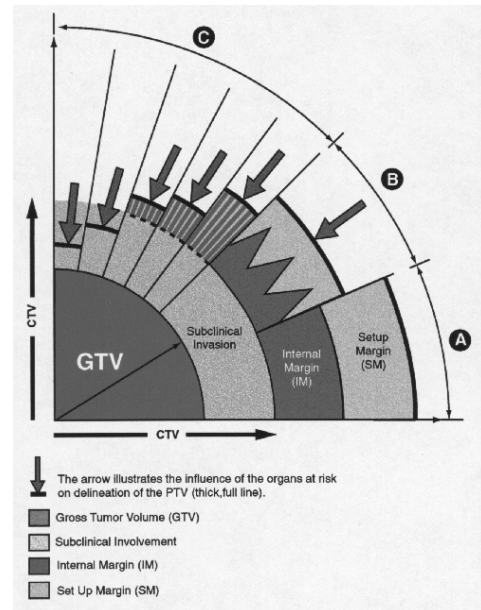


Fig. 5. Schematic representations of the relations between the different volumes (GTV, CTV, PTV, and PRV) in different clinical scenarios.

Scenario B.

The simple (linear) addition of all factors of geometric uncertainty, as indicated in scenario A, often leads to an excessively large PTV, which would be incompatible with the tolerance of the surrounding normal tissues.

In such instances, instead of adding linearly the Internal Margin and the Set Up Margin, compromise combinations are used, e.g., $\sqrt{\sum \sigma^2}$ formalism. This quantitative evaluation is only relevant if all uncertainties, and their σ , are known, i.e. in a few sophisticated protocols.

Scenario C.

In the majority of the clinical situations, a “global” safety margin is adopted. In some cases, the presence of Organs at Risk dramatically reduces the width of the acceptable safety margin (e.g., presence of the spinal cord, optical nerve, etc.). In other situations, larger safety margins may be accepted.

Since the incidence of subclinical invasion may decrease with distance from the GTV, a reduction of the margin for subclinical invasion may still be compatible with chance for cure, albeit at a lower probability rate.

It is important to stress that the thickness of the different safety margins may vary with the angle from which one looks at the PTV (e.g., bony structures or

fibrotic tissue may prevent, at least temporarily, malignant cell dissemination). **(Note that if an adequate dose cannot be given to the whole GTV, the whole aim of therapy shifts from radical to palliative).**

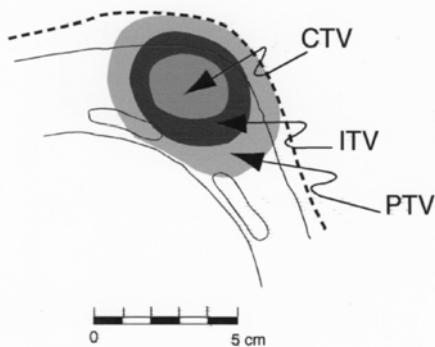
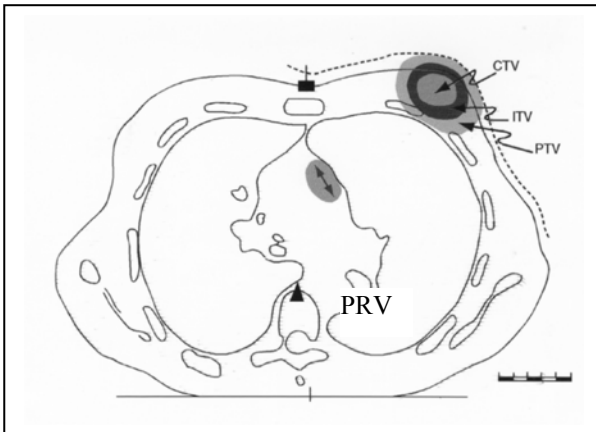


Fig. 6. Patient with cancer of the left breast after lumpectomy (no GTV present) considered for postoperative radiotherapy to the whole breast (not shown here), and a boost (shown here) to the tumor bed. The relations between the different volumes and margins are shown in one planar section. The internal and external reference points are indicated. Due to respiratory movements, the PTV extends outside the average position of the body contour.

Central circle = CTV (Clinical Target Volume), Dark grey = ITV (Internal Target Volume), Light grey(outer circle) = PTV (Planning Target Volume), \longleftrightarrow = OR (Organ at Risk, in this case the Left Anterior Descending Coronary Artery, shown here as projected onto the section), PRV (Planning Organ at Risk Volume), ————— = Average position of the contour and tissues, - - - - - = Extreme position of the normal tissues, \blacktriangle = Internal Reference Point, \blacksquare = External Reference Point.

Central dose

As a general principle, the present system of recommendations for reporting doses is based on the

selection of a point within the PTV, which is referred to as the ICRU Reference Point. The ICRU Reference Point shall be selected according to the following general criteria: 1) the dose at the point should be clinically relevant and representative of the dose throughout the Planning Target Volume (PTV); 2) the point should be easy to define in a clear and unambiguous way; 3) the point should be selected where the dose can be accurately determined (physical accuracy); 4) the point should be in a region where there is no steep dose gradient.

These recommendations will be fulfilled if the ICRU Reference Point is located:

- firstly (always) at the center (or in a central part) of the PTV, and
- secondly (when possible) on (or near) the central axis of the beam(s).

The dose at the ICRU Reference Point is the ICRU Reference Dose, and shall always be reported.

The dose variation throughout the CTV.

The dose variation in the CTV is the relevant information. It can generally be estimated from the dose variation in the PTV, but is always confined within the dose limits for the PTV. A certain degree of inhomogeneity of the absorbed dose throughout the PTV can never be avoided in radiation therapy (*i.e.* the dose varies from the maximum dose value (Note the volume restriction for maximum dose) to the minimum dose value). As a basic requirement, the maximum dose and the minimum dose to the PTV shall be reported together with the dose at the ICRU Reference Point. These three dose values then indicate the dose profile to the PTV.

Following ICRU Report # 50 (1993), it is recommended to keep the dose variation in the PTV within + 7 % and - 5 % of the prescribed CTV-dose.

The three levels of dose evaluation for reporting.

The level of completeness and accuracy of reporting therapeutic irradiation depends to a large extent on the situation in the department and on the aim of the treatment. For different clinical and practical considerations, different levels of ambition for dose evaluation can be identified. Three levels have been selected for reasons given below, but it is recognized that intermediate levels could also be identified.

In the following paragraphs, only the basic, minimal requirements at the three levels are listed. However, as a general rule, it is recommended to report any additional available information considered to be clinically relevant.

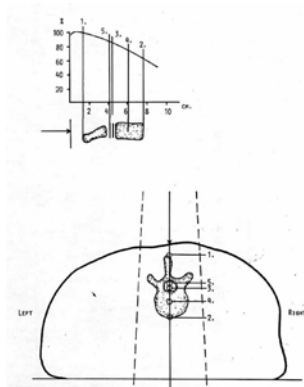


Fig. 7.

Level 1:

The requirements should be followed in all centers, for all patients. They constitute the standards below which safe and accurate radiotherapy cannot be performed. At this level, it is assumed that the dose at the ICRU Reference Point can be accurately determined as well as an estimate of the maximum and minimum doses to the PTV, using at least central-axis depth dose tables and standard isodose charts.

Level 2:

The standards of dose planning at this level allow the exchange of more complete and relevant information between different centers. At this level, it is assumed that the GTV, CTV, OR, PTV, and PRV can be defined using reliable patient data acquisition tools, and/or modern imaging techniques under reliable conditions (e.g., a series of CT and/or MRI sections). It is also assumed that complete dose distributions are available in planes or volumes, with inhomogeneity corrections, when appropriate. There must be a full quality assurance program covering the whole procedure.

Level 3:

Level 3 includes the development of new techniques for which reporting criteria are not yet established (e.g.

BNCT, intensity modulation, etc.). Some procedures which are now at level 3 can become level 2 with the development of techniques, equipment and standards.

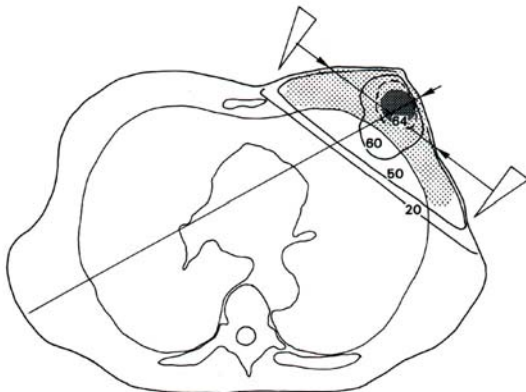


Fig 8.

At any level, the dose at the ICRU Reference Point and the best estimation of the maximum and the minimum dose to the PTV should be reported. Furthermore, any additional relevant information should be given, when available, e.g. Dose-Volume-Histograms (DVHs). The absorbed doses to the Organs at Risk should also be given.

Reporting Doses in a Series of Patients.

ICRU Reports 29, 50, 62 & 71 dealt with reporting dose in external beam therapy in an individual patient. Different issues are encountered when reporting treatments for a series of patients.

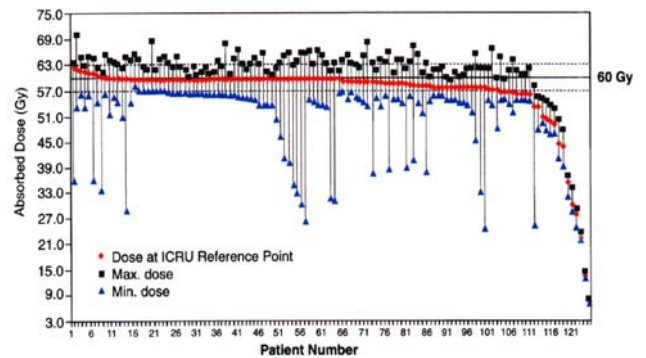


Fig. 9.

Diagram showing the dose delivered to 125 patients in a non-small cell lung cancer trial. The prescribed dose was 60 Gy \pm 5% at the ICRU Reference Point. The patients are sorted in descending order of 1.) dose at the ICRU point, and 2.) minimum dose. The dotted lines indicate the permissible dose variation of \pm 5% from the prescribed dose. As regards dose to the ICRU point, 102 patients fulfilled the criteria; whereas, 23 patients received higher or lower doses to the ICRU Reference Point. (Courtesy of Ann-Margret Engström, RN, Oncological Centre, Lund, Sweden).

Graph showing the proportion of a series of patients receiving an absorbed dose within three defined deviations from the prescribed dose in the protocol (same patient material as in Fig. 9.).

Upper: dose at ICRU point.

Lower: minimum dose to the PTV.

(Courtesy of Ann-Margret Engström, RN, Oncological Centre, Lund, Sweden).

First, the treatment prescription or protocol should be described in detail, including the volumes, absorbed dose levels, and fractionation. The treatments should be reported following the above recommendations, and the deviations from the prescription should be stated. In particular, the proportion of patients in whom the dose variation is less than \pm 5%, \pm 5-10%, and more than \pm 10% of the prescribed dose at the ICRU

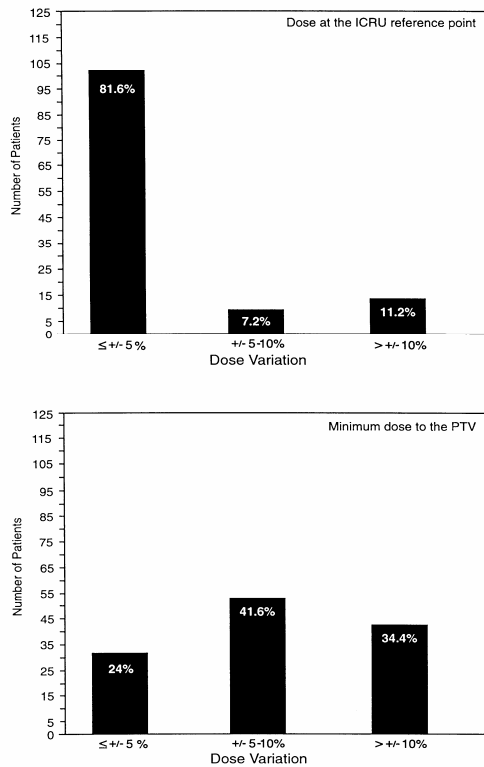


Fig. 10.

Reference Point should be reported. When reporting the treatments in scientific journals, it is recommended that the prescribed CTV and PTV and corresponding doses be illustrated in an isodose distribution chart, giving the total absorbed doses in Gy.

References

1. ICRU. (1978) International Commission on Radiation Units and Measurements. Dose Specification for Reporting External Beam Therapy with Photons and Electrons. ICRU Report 29 (Bethesda, MD: ICRU).
2. ICRU. (1993) International Commission on Radiation Units and Measurements. *Prescribing, Recording, and Reporting Photon Beam Therapy*. ICRU Report 50 (Bethesda, MD: ICRU).
3. ICRU. (1999) International Commission on Radiation Units and Measurements. *Prescribing, Recording, and Reporting Photon Beam Therapy, Supplement to ICRU Report No. 50*. ICRU Report 62 (Bethesda, MD: ICRU).
4. ICRU. (2004) International Commission on Radiation Units and Measurements. *Prescribing, Recording, and Reporting Electron Beam Therapy*. ICRU Report 71 (Bethesda, MD: ICRU).

MODELING OF THE RESPONSE OF IONIZATION CHAMBERS IN RADIOTHERAPY FIELDS WITH DINAMIC INTENSITY MODULATION

Sandija PLAUDE*, Sergey POPOV*, Arturs MEIJERS*, Albert MILLER**, Yuri DEKHTYAR***
*Latvian Oncology Centre of Riga Eastern Clinical University Hospital, Riga, Latvia
**Vilnius University Oncology Institute, Vilnius, Lithuania
***Riga Technical University, Riga, Latvia

Abstract: Ionization chamber (IC) is the most common and trusted radiation detector in Radiotherapy (RT) dosimetry. However, due to its finite size detector volume have an impact on point dose measurements especially in a penumbra and regions of high dose gradients inside Intensity Modulated Radiotherapy (IMRT) fields. The aim of this work is to make a comparison of measured and modeled point doses in the case of dynamic radiotherapy using IC's of different active volumes, to evaluate magnitude of the chamber volume effect on the discrepancy between the calculated and the measured dose.

Keywords: Point dose measurements, ionization chamber, IMRT

1. Introduction

Although there are many different radiation detectors used in IMRT dosimetry, the IC is still the gold standard in point dose measurements [1]. In three-dimensional (3D) conformal radiotherapy and in IMRT beam's central axis (CAX) is usually used for absolute dose measurements. In the case of conformal radiotherapy usually there is a uniform dose distribution and low dose gradients inside the field, while in the intensity modulated field there could be a region of a high dose gradient as well as areas of low dose.

Moran et al. within the framework of their study created a dose-gradient analysis tool for IMRT quality assurance (QA) that helps to avoid dose measurements in high dose gradients and low dose regions [2]. However in the case of IMRT there are low dose regions and high dose gradients inside the radiation field moreover inside the Planning Target Volume (PTV), so it is very important to check the dose also in these areas. Many authors suggest that in case of IC over – responses or under – responses this effect will smooth out when all treatment fields are analyzed together [3]. Although in the previously mentioned study in almost all situations when IC over or under – responses were identified, this can be used only to understand a behaviour of IC in certain treatment conditions but not to analyze a treatment plan for the patient.

One of the most common sources of errors in dose

determination in case of IMRT is the variation of the measurement conditions from the reference ones [4, 5]. Sánchez – Doblado et al. found a general correlation between the IC position relative to a segment and the derived correction factor, c , that indicate the difference between reference and measurement conditions.

Almost in all studies about IMRT dosimetry Monte – Carlo (MC) simulation is used as a model for theoretical dose calculation. From the other hand there are attempts to introduce in clinical routine methods of absolute dosimetry in IMRT fields, employing simple chamber volume Dose-Volume Histogram based correction, in that way correcting chamber volume effect [6].

Aim of present study is to verify correctness of dose modelling using simple geometrical model for evaluation of the chamber volume effect.

2. Material and Methods

2.1. Accelerator and collimator

Measurements were performed on linear accelerator Clinac 2100C/D (Varian Medical Systems, USA). This is a dual photon energies accelerator equipped with a multileaf collimator (MLC). The MLC has 40 opposed leaf pairs. Each MLC leaf is 6 cm thick made from wolfram with leaf transmission 1.5% - 2.0% for 6MV photon energy. A width of each MLC leaf is 1 cm at the level of the isocenter.

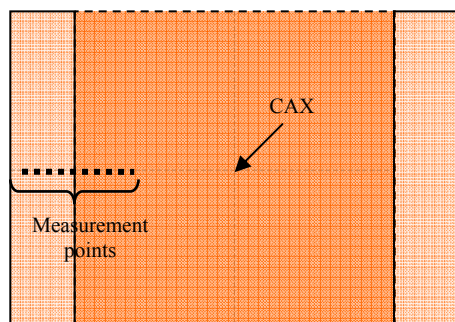


Fig.1. Test field configuration.

2.2. Test field configuration

Intensity modulated test field is made so that 10 cm width symmetrical to the CAX the dose is high and uniform, but 5-7 cm from the CAX there is low dose region (Fig.1).

A desired fluency was obtained using dynamic MLC. In the middle part of the test field a speed of leaves is 0,4 cm/s, but at the edge of the field MLC leaves move at 2,0 cm/s. A gap between opposite leaves is 3 mm. Measured points were chosen so that they cover the high dose region as well as low dose region. Dose was measured in 10 points with 1 mm interval between them. There is a high dose gradient between two dose levels.

2.3. Ionization chambers

Three radiation detectors were used. PTW 30006 “Farmer” type chamber with its active volume 0.6 cm^3 ; PTW 31002 “Semiflex” type IC 0.125 cm^3 ; Scanditronix Wellöfer semiconductor p-type diode model PFD^{3G} (Fig.2.). Diameter of active area of the detectors was 6.1 mm, 5.5 mm and 2.0 mm respectively [7].

Detectors were positioned with their longitudinal axis perpendicular to the beam axis. Measurements were made in a depth of 5 cm with SSD (Source – Skin Distance) =95 cm and SAD (Source – Axis Distance) =100cm.

Dose profiles for dynamic field were acquired using film dosimetry. Films were irradiated in water equivalent phantom at a depth of 5 cm at the isocenter plane. Kodak[®] X-Omat films were used for the measurements.

2.4. Dose modeling

A simple model using Microsoft Excel software was developed to calculate the integrated dose in arbitrary units inside volume of IC. Employed model was using chamber volume as only parameter to model chamber response to the photon fluency delivered by means of moving leaf gap. This model allows to estimate the response of the IC depending of the velocity of MLC leaves and the gap between opposite leaves. It was also possible to take into account a diameter of IC cross-

section, which is the main parameter of our interest.



Fig.2. Radiation detectors: a) PTW 30006 “Farmer”; b) PTW 31002 “Semiflex”; Scanditronix Wellöfer semiconductor p-type diode

3. Results and Discussion

Figure 3 shows calculated profiles in high gradient region of test field with dynamic IM for Farmer and Semiflex ICs. Figure 4 shows measured profiles in the same high dose gradient region of test field. Dose profile acquired by semiconductor detector and film are shown as reference to illustrate actual dose gradient in region of interest.

Figure 5 shows ratio of Farmer and Semiflex chamber responses in region of interest – modelled using only volume effect and derived from measured data. Additional points show difference of the variation of modelled and measured responses of the chambers. One can see that simple use of volume effect of the chamber gives discrepancy up to 19% with measurement results. Results of measurements and modelling have shown that volume effect of the chamber is important factor to take into account during measurements in dynamic fields. However, it is not possible to introduce only volume based correction factor to arrive to agreement with measured data. Variations of central electrode effect, recombination, and polarisation in dynamically modulated photon fields are important factors to consider.

Additional modelling and measurements are needed to take into account all important factors affecting ionization chamber response in radiotherapy fields with dynamically modulated intensity.

4. Conclusions

Using simple volume based modeling of chamber response in dynamically IM radiotherapy fields is not possible to predict with sufficient accuracy response of the large volume ionization chamber in high dose gradient regions of the field.

Results of such a model have differences up to 20% with experimental results. It is not possible to evaluate chamber response in the high dose gradient of the IM field using chamber volume DVH based correction factor. Additional modeling is needed to evaluate chamber response in dynamically IM fields.

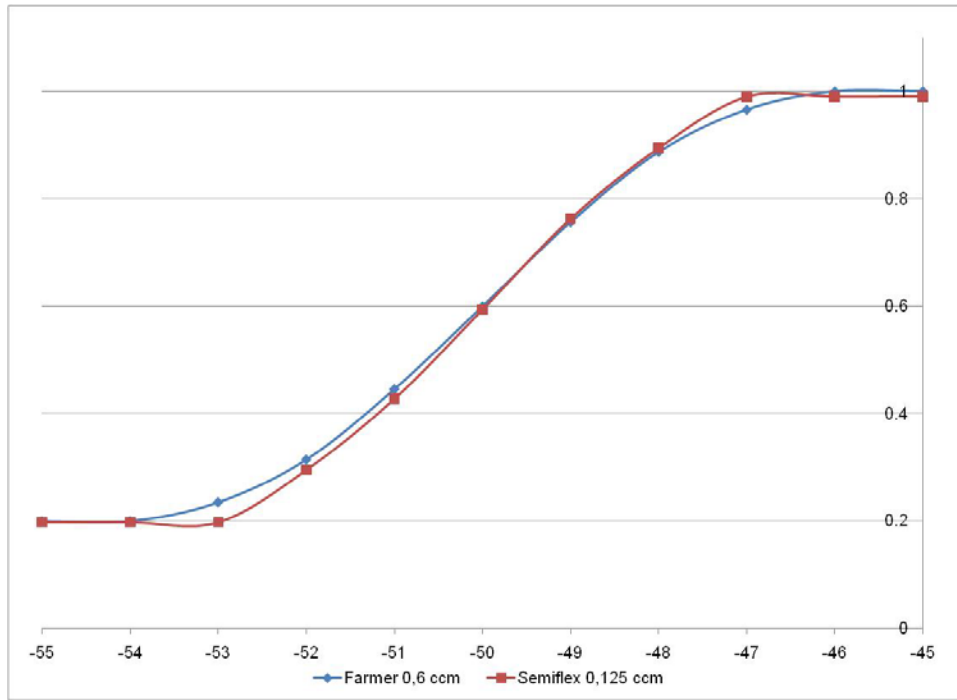


Fig.3. Calculated profiles in high gradient region of test field with dynamic intensity modulation.

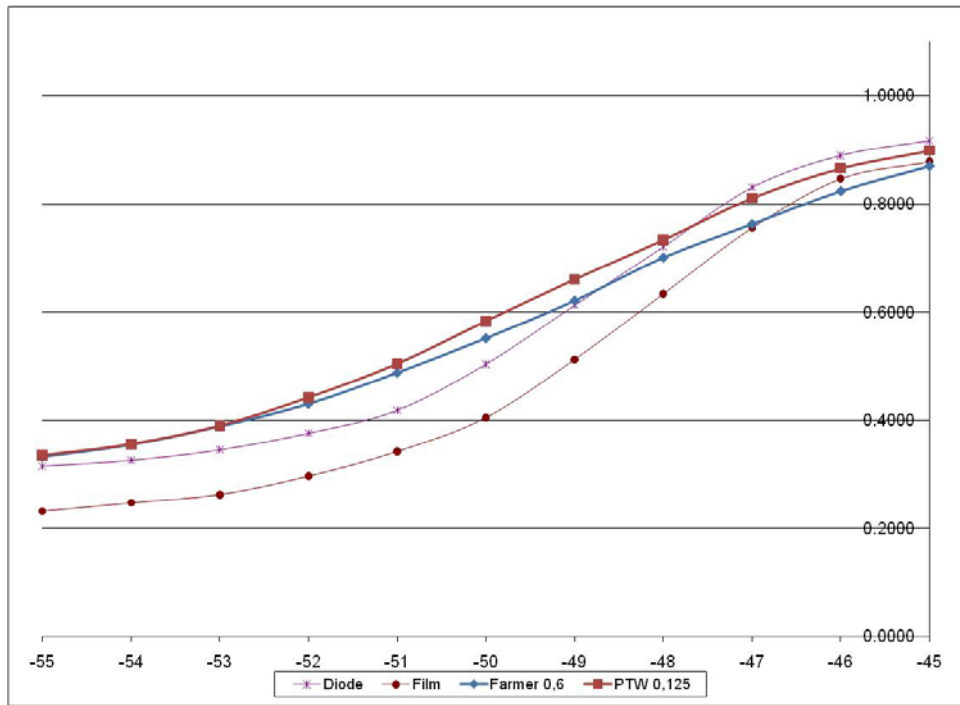


Fig.4. Measured profiles in high gradient region of test field with dynamic intensity modulation.

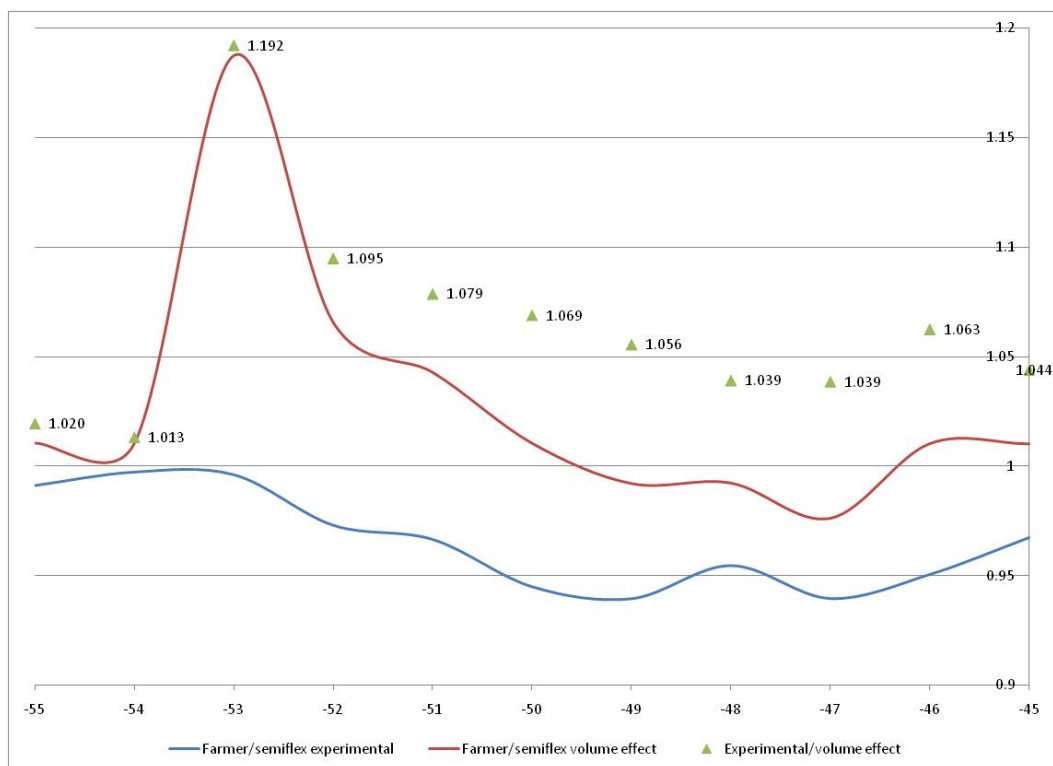


Fig. 5. Comparison of Farmer and Semiflex chamber responses.

5. References

1. Escude L., Linero D., Molla M. et al. Quality assurance for radiotherapy in prostate cancer: point dose measurements in intensity modulated fields with large dose gradients. *Int J Radiat Oncol Biol Phys*, 66, 2006. p. 136 – 140.
2. Moran J. M., Radawski J., Fraass B. A. A dose -gradient analysis tool for IMRT QA. *J of Applied Clin Med Phys*, Vol. 6, No. 2, 2005. p. 62 – 73
3. González – Castaño D., Pena J., Sánchez – Doblado F. et al. The change of response of ionization chambers in the penumbra and transmission regions: impact for IMRT verification. *Med Biol comput.* 46, 2008. p. 373 – 380.
4. Sánchez Doblado F., Hartmann G. H, Pena J. et al. Uncertainty estimation in intensity – modulated radiotherapy absolute dosimetry verification. *Int. J. Radiation Oncology Biol. Phys.*, Vol. 68, No 1, 2007. p. 301 – 310.
5. Sánchez – Doblado F., Capote R., Rosello J. V. et al. Micro ionisation chamber dosimetry in IMRT verification: Clinical implications of dosimetric errors in the PTV. *Radiat Oncol*, 75, 2005. p. 324 – 348.
6. Kawamorita R., Iwai K., Takeushi Y. et al. Examination of Dose Verification in Intensity Modulated Radiation Therapy (IMRT) Treatment Planning Using Averaging Dose in Chamber Volume. *Jpn J Radiol Technol* 58 (6), 2002. p. 783-792.
7. Technical Data, PTW – Ionization chambers, PTW Freiburg.

MODELING OF FIELD PARAMETERS FOR DOSE VERIFICATION IN EXTERNAL BEAM RADIOTHERAPY

Arturs MEIJERS*, Sergey POPOV*

* Latvian Oncology Centre, Riga Eastern Clinical University Hospital, Riga, Latvia, LV1079

Abstract: In radiation therapy it is necessary to perform manual dose verification for each treatment plan. Several dosimetric parameters are dependent on treatment field size, however usually they are measured only for square fields. Therefore method allowing approximation of irregularly shaped field with equivalent square is necessary.

Methods: Spreadsheet based equivalent square calculation tool based on Clarkson integration method was developed.

Results: Basic verification tests suggested that by using developed method equivalent square can be determined with 1.32 % error; such error would result in calculation of treatment field monitor units with 0.042 % error.

Conclusions: Developed tool is easy to implement and use for manual treatment plan verifications.

Keywords: equivalent square; manual dose verification

1. Introduction

According to international approach and recommendations, it is necessary to perform manual treatment plan verification for each patient. Manual monitor units (MU) verifications most commonly are done by using point dose calculation methods, such as isocentric method, SSD method, Clarkson's method etc. For example, SSD method allows calculating point dose by following equation [1]:

$$MU = \frac{TD \times 100}{K \times (\%PDD)_c \times S_c(r_c) \times S_p(r) \times (SSD \text{ factor})} \quad (1)$$

where:

K – calibration index of accelerator

r_c – collimator field size

S_c – collimator scatter factor

S_p – phantom scatter factor

TD – tumor dose

Parameters of linear accelerator (linac) are mostly dependant on beam energy, field size and depth. Parameters dependant on field size are usually acquired for square fields, however such fields are rarely used for treatment delivery. More significant are irregularly shaped fields. However, since beam parameters are acquired for square fields, it is necessary to approximate irregularly shaped fields with square field. Therefore concept of equivalent square (EQSQ) was introduced. Development of simple and easy-to-use EQSQ calculation method is significant for manual treatment plan verification. Since previously widely used dose calculation algorithms, such as pencil beam convolution

algorithm or PBC, had implemented EQSQ concept, it was possible to acquire this parameter directly from treatment planning system (TPS) reports, however analytical algorithms, such as anisotropic analytical algorithm or AAA, do not use EQSQ for dose calculation. Therefore, to perform manual plan verifications alternative EQSQ calculation method is necessary.

2. Methodology

EQSQ can be defined by geometric or dosimetric approach. Dosimetric approach takes into account physical characteristics of the beam, therefore it is considered more precise. Let us consider square field equivalent to irregularly shaped field if percentage depth dose (PDD) of square field at reference depth is equivalent to the PDD of irregular field.

EQSQ calculation method is based on Clarkson's integration method. However Clarkson's method is based on use of parameters such as scatter air ratio (SAR) and tissue air ratio (TAR). Since acquisition of these parameters require additional measurements, scatter maximum ratio (SMR) and tissue maximum ratio (TMR), which are special cases of scatter phantom ratio (SPR) and tissue phantom ratio (TPR) respectively, were used instead. SMR and TMR can be calculated from depth dose (PDD) curves by method described in *British Journal of Radiology, 1996, Supplement No. 25* [2]. Calculation is done by using peak scatter factor (PSF).

Total SMR of irregularly shaped field can be determined by following steps:

1. From freely chosen point vector is drawn to field edge.
2. Intersection point of vector and field edge is found.
3. Length of vector from starting point to intersection point is determined.
4. Determined vector is considered as radius of circular field.
5. SMR for such circular field is determined.
6. Previous five steps are repeated until whole field is covered. Angle between vectors is chosen constant (to ease calculation).
7. SMR for all circular fields is summed.
8. As mentioned above, angle between vectors is constant. Therefore contribution of all circular fields towards SMR of irregular field is considered equal. SMR of irregularly shaped field is determined as average of SMR sum of circular fields.
9. Square field with the same SMR as SMR of irregular field is determined. This square field is considered equivalent square.

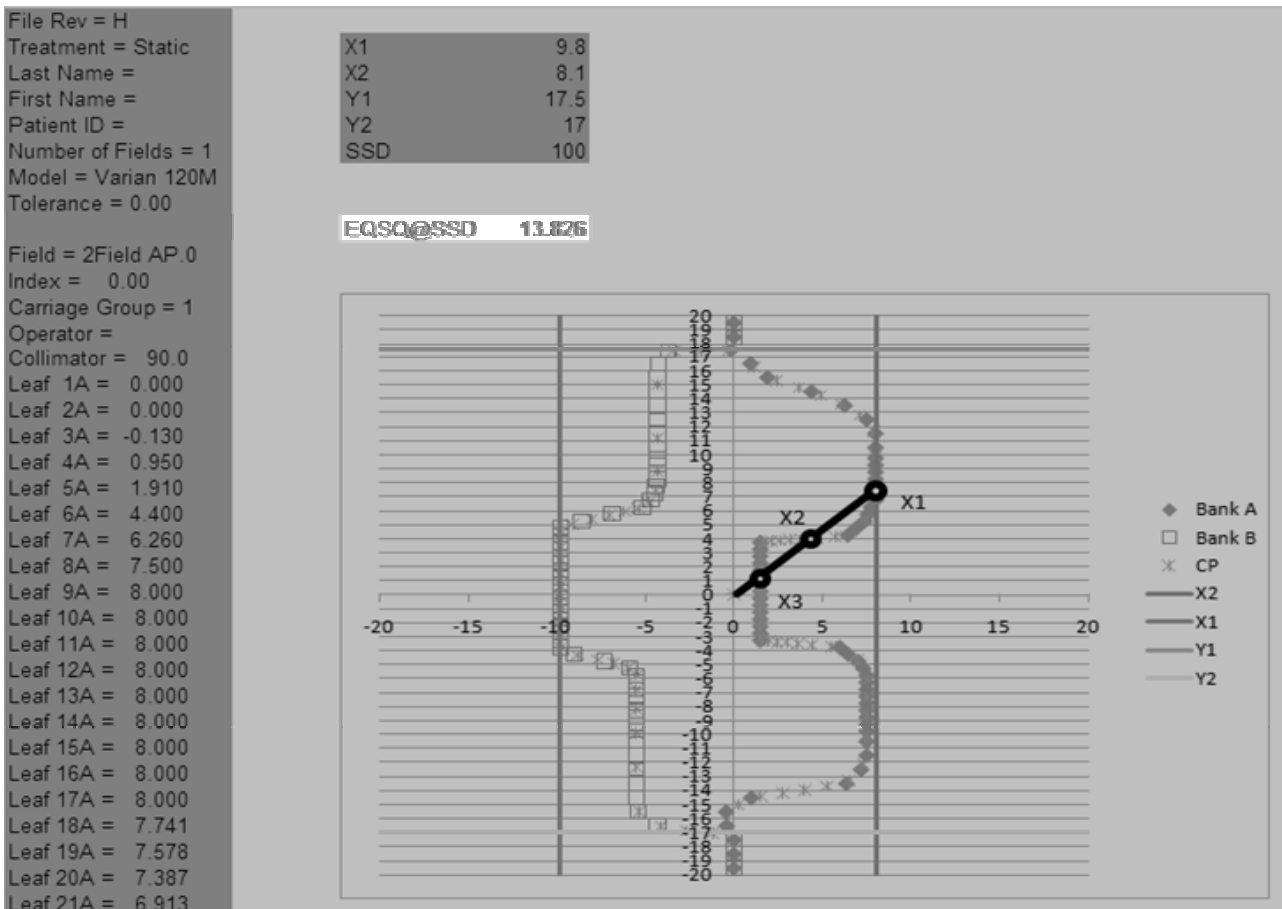


Fig. 1. EQSQ calculation tool

In case any vector intersects field edge more than once due to irregular field shape, the vector is divided on several parts as shown in figure 1. Total SMR for such vector is determined by following equation:

$$SMR_V = SMR_{X1} - SMR_{X2} + SMR_{X3} \quad (2)$$

Algorithm as described above was fulfilled in Microsoft Excel spreadsheet, to make it easy accessible and usable. To calculate EQSQ it is necessary to import file from TPS with MLC positions and enter collimator jaw positions as well as SSD. Figure 1 shows example of the calculation.

3. Analysis and results

It is important to determine optimal number of vectors. As a result calculation will be less time consuming. Statistical evaluation was used to find optimal number of vectors. EQSQ was calculated for 32 randomly chosen irregular fields using different number of vectors. Calculated EQSQs for single field were normalized to maximal value, allowing comparing results of different fields. Confidence level was chosen 95%. Results are shown in Table 1.

Table 1. Optimization of number of vectors

vectors	average	CI	error
2	0.900	0.029	3.20%
4	0.930	0.026	2.80%
6	0.964	0.030	3.10%
12	0.963	0.030	3.10%
18	0.963	0.029	3.10%
24	0.962	0.029	3.10%
36	0.962	0.029	3.00%
72	0.963	0.029	3.10%

According to Chart 1, it is not necessary to use more than 24 vectors, since the calculated result does not change significantly if the number of vectors is further increased.

To evaluate error of EQSQ calculation method, two tests were performed. Firstly EQSQ were determined for square fields with size from 4 to 35 cm. EQSQ for square field is square of the same size as given field. Acquired results are shown in Table 2. Maximal error for determined EQSQ is 2.2 %.

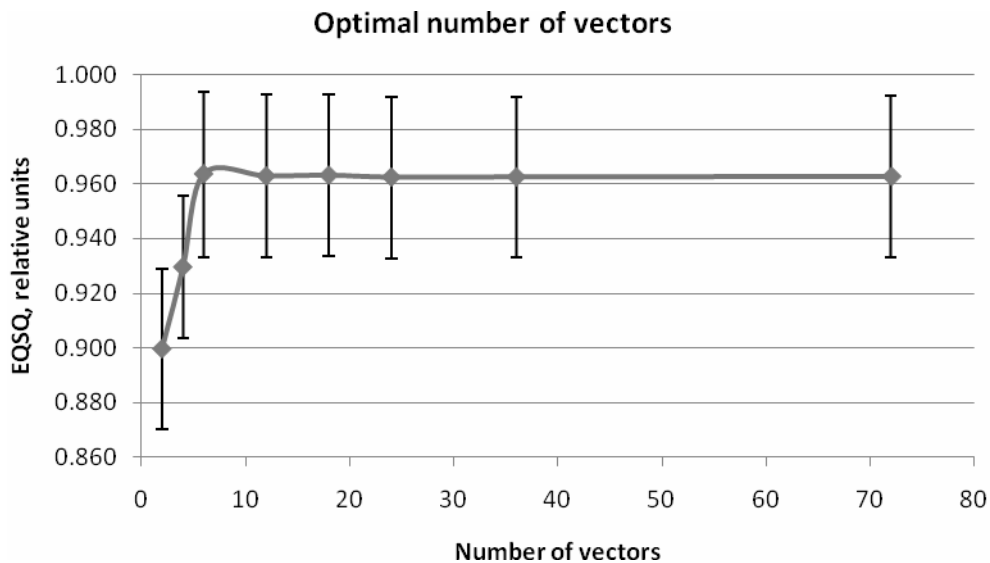


Chart 1 Optimal number of vectors

Secondly EQSQ were determined for 25 randomly chosen irregular fields. Same fields were calculated by using Varian TPS Eclipse 6.0 with PBC dose calculation algorithm. Both results were compared. The difference between EQSQ acquired by both methods was 1.83 ± 0.85 % (with confidence level 0.95).

Before using described EQSQ calculation tool for manual MU verification, it was necessary to verify the significance of EQSQ error contribution towards calculated MU. By using SSD method (equation 1) necessary MUs were determined to deliver 1 Gy in water, in depth 10 mm, SSD set to 1000 mm. Beam data of Varian Clinac 2100 for 6 MeV were used. Calculation was performed for square fields with the same size as shown in Table 2 using precise EQSQ values. Afterwards MU calculation was repeated using determined EQSQ as shown in Table 2. Test showed that EQSQ values which were determined by developed tool (1.32 ± 0.52 %) introduced error for calculated MU 0.042 ± 0.021 % (confidence level 0.95).

Table 2. EQSQ determination errors

		EQSQ, cm	Error
Square field size, cm	4	3.97	0.80%
	6	6.00	0.10%
	8	7.83	2.20%
	10	9.97	0.30%
	12	11.85	1.20%
	15	14.76	1.60%
	20	19.58	2.10%
	25	24.55	1.80%
	30	29.60	1.30%
35	34.33	1.90%	

4. Conclusions

Developed tool is easy usable and appropriate for EQSQ calculation of irregularly shaped fields, which can be used for manual MU verification. It is easy adjustable for different machines and beam energies.

Statistically it was determined that optimal number of vectors for EQSQ calculation is 24. Basic verification of tool showed that EQSQ can be determined with error 1.32 ± 0.52 %. Such EQSQ error would result in calculated MU error 0.042 ± 0.021 %.

EQSQ values calculated by developed tool were compared with values calculated by TPS system with PBC dose calculation algorithm. Difference between both results was 1.83 ± 0.85 %.

To successfully implement this tool qualitative SMR data are necessary. If SMR are calculated from PDD data, it is suggested to measure PDD for 0×0 cm field. For further verification of the tool, it would be necessary to carry out measurements to determine whether actual PDD of square field as calculated by the tool is the same as for given irregularly shaped field.

5. References

1. Khan F. M., *The Physics of Radiation Therapy*, Lippincott Williams & Wilkins, Philadelphia, 2003. p. 511.
2. *British Journal of Radiology*, 1996, Supplement No. 25.

QUALITY ASSURANCE PROGRAMS FOR A LINEAR ACCELERATOR

Carl MAGNUS NILSSON

Medical Radiation Physics Malmö, Lund University, Malmö University Hospital, SE-205 02 Malmö, Sweden

Abstract: Quality Assurance (QA) is a comprehensive method for evaluation of an accelerator's performance. It involves tools aiming at getting a correct absorbed dose to the patient and a good uptime. Daily, weekly, monthly and yearly checks of an accelerator are needed for a good surveillance of the accelerator. An acceptance test is done to check that the accelerator at delivery is within specified limits. The parameters are later checked within different timeframes to see if the values keep within a specified limit, and if not then corrected. The QA and Quality Control (QC) of the accelerators at Malmö University Hospital are described.

Keywords: Quality Assurance, Quality Control, Acceptance Test, Clinical Linear Accelerator

1. Introduction

Linear accelerators has undergone a tremendous development since their introduction in the 1950s, and are now equipped with multiple interlocks, automatic change between photon and electron mode, multileaf collimators (MLC), moving collimators, etc. The QC has to check all parts of the system. It is the responsibility of a clinical physicist to coordinate the QC work. Some work can be delegated to e.g. radiographers since they are regular users of the accelerator. This paper will give an introduction to QA and QC at Malmö University Hospital and the following points will relate to different aspects of QC and the responsible personnel.

2. Quality Control

Acceptance Test [1]

During the installation of an accelerator the medical physicist must assure that the facility is properly prepared. This may include: (1) installing the proper warning signs, (2) assuring that the appropriate audio and video equipment is installed to monitor the patients, (3) assuring that the appropriate door interlocks are in place and connected properly and assuring that the emergency power failure illumination is installed or available (e.g. flashlights).

As soon as the accelerator can deliver radiation, a beam safety tests should be the first thing on the agenda and to perform tests of the safety interlocks, determination of radiation exposure levels outside barriers and determination of exposure levels in the occupied areas during beam-on.

Initial checking of mechanical and radiation systems is to commence after this. Alignment of collimator axis

and collimator jaws has to be made. The collimator axis, the light localizer axis and cross hairs must all be congruent and follow the same axis and this must be checked for all ranges of motions. When this is within the specified limits, the light field and radiation field congruence and coincidence must be verified. This can be done by exposing two films with collimators rotated 180°. Congruence and symmetry must be verified over the full range of both collimator and gantry positions. The mechanical and radiation isocenter location should then be determined to be within the specified limits. Other mechanical system tests must also be performed. The patient support system (couch) must be tested to assure that it's flex, both with and without load is within the specified limits and that the couch is able to take the maximum weight, that the couch stops at the right positions and hold the position and the coordinates of the table are within specified limits.

At commissioning of an accelerator it is necessary to establish that the beam profile conforms to the accelerator's specifications. This should be done in a water phantom making measurements at least close to maximum and at 10 cm deep, and other specification depths at which the profile is specified.

Variation of output with different field sizes is also a parameter that is required at commissioning. Depth doses and profiles are also measured for different field sizes.

The manufacturers often have documents with tests to perform, and the documents should be reviewed to see which additional tests are needed.

After the acceptance test, the commissioning can commence which includes beam data acquisition, entry

of beam data into a radiotherapy treatment planning system, development of operational procedures and training of all users in the operation of the accelerator.

Daily QC

Each day a routine output check with a phantom (see Fig. 1) is performed by nurses at the accelerator.



Fig. 1. A polystyrene phantom with an RK-chamber inside.

If a deviation appears, a physicist is summoned to do more accurate measurements. The data from the daily check is put into a homemade Excel sheet to be plotted. The phantom consists of a block of solid water, where an ion-chamber [RK chamber] is placed inside. The phantom is then placed on the treatment table and SSD, field size, alignment etc are set, and then the phantom is irradiated three times with a predetermined number of monitor units (MU). The value is then corrected for pressure and temperature and compared to a reference value. The reference value is obtained by a physicist when the RK chamber is calibrated, and when the output from the accelerator is well determined and at zero deviation. Daily QC is performed for all photon energies as well as for one electron energy. Laser and light field check is also done daily to see if the lasers begin to drift and to see if a standard field (10 cm x 10 cm) still is the same.

Weekly QC

A weekly measurement with a phantom from IBA, called StarTrack (see Fig. 2), is performed on each accelerator.



Fig. 2. Phantom from IBA, with ion chambers. Used for weekly checks of accelerators.

This check includes measurements of profiles, hard/dynamic wedge, energy and output for both photons and electrons. The calibration here is very important, and it should be done together with a more accurate measurement of the absolute dose.

Monthly/Annual Service

This is a more extensive service where the medical physicist together with an engineer works on the machine for half a day. First the engineer does a mechanical integrity check/service of the machine, checking everything from imaging plate, and MLC, to lubricants, breaks, etc. A visual inspection is done of water hoses, couplings and manifolds for leakage and wear. All fans are checked for proper function. Water- and gas-pressure and water temperature are checked and water is refilled if need be.

The table is also inspected: Table movements and brakes, emergency lowering of table, and there are more specific tests for Varian and Electa tables. The coordinate system and iso-rotation is checked.

The way the MLCs are checked depends on its construction. In general the movement of the MLC is checked with different field sizes, and also with asymmetric fields. There are also some parameters to have in mind as a physicist when thinking of the MLC QC. The leaves must go to the required position, which has three aspects: The independent motion of each leaf, the leakage through and between leaves, the weight of the collimator may cause the alignment of the leaves to be different at different gantry angles and that the relationship between the optical field and the radiation field may differ.

On an Electa machine where the position of the MLC leaves are positioned via reflectors, the intensity and position of the reflectors are checked. On Varian, the MLC is initialized, fans to MLC driver card is checked and visual inspection of MLCs is done.

Gantry and collimator angle readout is checked with a water level device. Isocenter check is important, especially when IGRT is involved. A related parameter is the mechanical and optical distance indicator.

Alignment of radiation field with field light is done with Gafchromic film.

Lasers are checked and aligned if need. Lasers are also compared to the position of the light field and together with a phantom.

Dose rate for the different energies, default dose rate value and PLS server are checked.

The imaging system is checked: Anti Collision switches, full detector calibration and imaging with a PTW phantom and analyses in software is performed, (applies for both EPID and cone-beam CT).

After the mechanical check the physicist and engineer together goes through each energy and looks at the profiles, i.e. flatness and symmetry. The energy for the electrons is also checked. When that is done and – if needed - corrected, the physicist measures absolute dose for the photons in an in house built water phantom (see Fig. 3) and if the need arises corrects the output if variations are larger than 1%. This is always done

together with another medical physicist to minimize the risks for mistakes.



Fig. 3. In house built water phantom for measurements of absolute dose. Room for an ion-chamber is also seen.

In the larger annual services that lasts a week, a large water tank (see Fig. 4) is used to take up dose profiles and depth doses. These are compared with the results of previous measurements of absorbed dose in the water tank and also the profiles taken up previously.

Depth dose and profiles for open and wedge fields, absolute dose, TMR^{20}_{10} , and R_{50} are measured. These services also include preventive exchanges on the accelerators for example if one sees a MLC leaf beginning to falter, one exchanges it beforehand, or lubricates etc, all to keep the accelerator working properly.

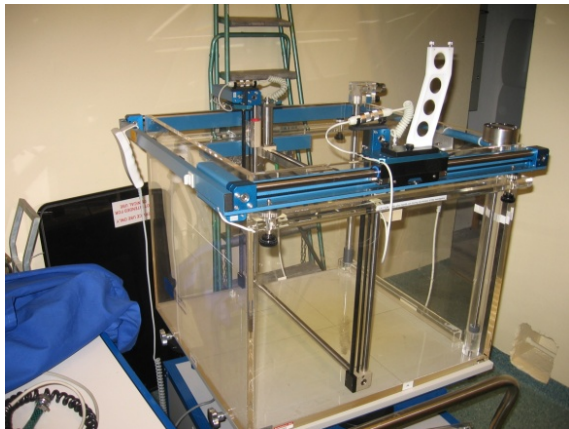


Fig. 4. Water tank from IBA, where an electrometer, diode, computer etc. is connected.

Patient Specific QC

IMRT QC

QC of IMRT is performed before each patient starts his/her treatment. The plan is exported and calculated on a phantom, IBA MatriXX (see Fig. 5).



Fig. 5. IMRT phantom from IBA, with MULTICube polystyrene.

The phantom is then irradiated in two ways. One series of irradiations where the phantom is irradiated in gantry and collimator 0° which is to check the fluence from the accelerator. The second irradiation is performed as if the phantom was the patient, and then each field is summed up to give a view of the complete dose to the patient/phantom. Then the measured and calculated dose distribution on the phantom is compared using γ evaluation and a visual comparison of the profiles. We use the criteria 3% and 3mm in our γ evaluation.

In vivo QC

For an *in vivo* system it is important to check initially that the system is stable and constant over time. This can be made that one irradiates the diodes 10-15 times and the spread should be within 0.5%. The measurements should be remade at different days for 1-2 weeks to see that the diodes are constant.

3. Results

We have an uptime of 97-98%. Using the in house made Excel sheet the physicist can follow the output from the daily QA check as can be seen in Fig. 6 for 4 MV photons and in Fig. 7 for 10 MV photons.

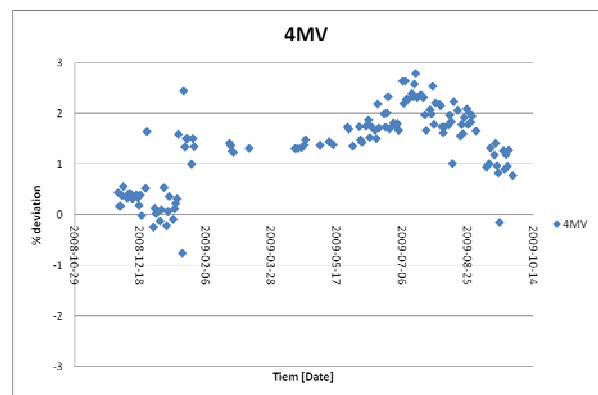


Fig. 6. Per cent deviation from reference output in the daily morning QA for 4 MV photons.

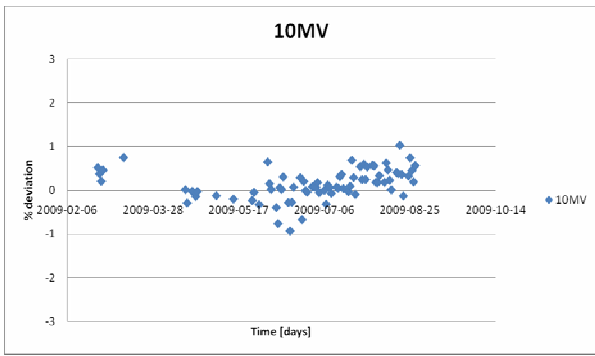


Fig. 7. Percent deviation from reference output in the daily morning QA for 10 MV photons.

4. Conclusions

A good QA program that can overlook the essential parameters of an accelerator, and a good collaboration

between different categories of workers such as engineers, physicists, nurses etc. helps to keep a high uptime of the accelerator. Tools for the physicist to keep an overview of how the accelerator is behaving may either be an Excel sheet or software from a manufacturer etc. and is also an important part of the QA/QC. All of these different parts of QC are important parts of the QA and ways of maintaining a high uptime and a good quality of the beam delivered to the patient.

5. References

1. Nath et al.: AAPM code of practice for radiotherapy accelerators; Medical Physics, Vol. 21, No. 7, July 1994.
2. QC checks come from internal documents at UMAS.

**BRIEF DESCRIPTION OF TECHNICAL FEATURES AND APPLICATIONS
OF MEDICAL EQUIPMENT AND MEDICAL DEVICES DEVELOPED IN THE
"ATOMMED" CENTER**

Alexander Kuznetsov

Atommed center, 115 230, Moscow, Varshavskoye shausse, 46, 115 230, Russia

1. Automated set of equipment designed to produce a solution of Tc-99

The solution of technetium is the main diagnostic radiopharmaceutical used in the radiochemical laboratories for the determination of cancer tumors. Its consumption is steadily increasing each year.

However, there is a number of objective reasons, which make it difficult to obtain this solution and to use it in medical institutions. Mo-99 is traditionally used to obtain a solution of Tc-99, but Mo-99 in turn is obtained by dividing the U-235 in a nuclear reactor. Reactors all over the world including Russia have annually stops because they work out their resource exploitation. In addition preventive work within two months is carried out on each reactor. All this leads to disruption of supply of feedstock, to noticeable rise in the cost of raw materials, and as a result to impossibility of carrying out diagnostic procedures. It is also worth noting that the solution of Tc-99, obtained by traditional method is of low quality, and 20% of researches conducted with its use are not informative.

The proposed methodology and a set of equipment have several advantages, as a feedstock uses natural MoO₃ (Molybdenum Oxide), which has no restrictions for its holdings and use. This allows:

- to minimize the dependence of the production of Tc-99 solution from the supply of Mo-99 from nuclear reactors (i.e. from the technological breaks and annual stops of the reactors, from the steady decrease in the number of operating reactors, etc.)
- to ensure a stable operation of the medical units
- to make the process of obtaining a solution of Tc-99 cheaper

Proposed set of equipment can be installed in any radiochemical laboratory of medical institution covering about 30 square meters. From this center it is also possible to supply clinics located at a distance of 50-100 km with prepared solution of Tc-99 with a given activity for specific diagnostic studies.

The quality of the resulting solution of Tc-99 is fully consistent with international standards for pH, specific activity, the content of Mo-99, impurities, etc.

2. High energy micro source based on Ytterbium-169.

The project declares the development of isotope production for medical use in brachytherapy of breast cancer. Used high energy micro source is a titanium capsule containing a radioisotope Yb-169.

The most widespread method of cancer therapy in Russia and all around the world is surgical removal of the tumor and surrounding tissue (usually the entire organ) followed by a course of radio / chemotherapy.

Special value of high energy micro source application lies in the possibility of cancer treatment, which saves organs (primarily breast cancer). Combined treatment using high energy micro source allows to preserve organs, and it is critical for patients.

The main advantages of the proposed high energy micro source based on Yb-169 are:

3. • softer emission spectrum (63-217 keV), compared to the possible source of Ir-172 or Co-60
4. • the possibility of using high energy micro source for the treatment of superficial cancers, as well as for the treatment of cancers of "head-neck" area.

It is necessary to solve the question on the adaption of domestic equipment to use new sources and/or evaluate the possibility of using foreign equipment for the same purpose.

OSL IN HOUSEHOLD SALT (NaCl) FOR ENVIRONMENTAL, OCCUPATIONAL AND MEDICAL DOSIMETRY

Christian BERNHARDSSON*, Maria CHRISTIANSSON*, Christopher RÄÄF*, Sören MATTSSON*,
*Medical Radiation Physics, Department of Clinical Sciences, Malmö, Lund University, Malmö University Hospital,
SE-205 02, Malmö, Sweden

Abstract: The recent progress in our work to implement salt (NaCl) as a dosimeter is presented. Laboratory investigations have indicated a linear dose response from 1 mGy to about 100 mGy and detection limits down to 0.1 mGy. Investigations in the clinic comparing TL-dosimetry in LiF and OSL in NaCl have indicated a similar dose response for the two dosimeters at different photon energies. Field studies with stationary dosimeter kits containing TLDs (LiF) and NaCl suggests that salt is also a good candidate for environmental monitoring of radiation.

Keywords: OSLD, TLD, NaCl, LiF, dosimetry

1. Introduction

Today there are no direct dosimeter for the general public in case of an accident involving external exposure from ionising radiation. There are however methods for assessing collective, and to some extent also individual, doses in such cases [1, 2]. The drawback with many of the retrospective methods for individual dose estimations is that they are complicated and have a relatively high dose threshold under which they are unreliable. In our search of finding methods and materials for individual dose assessments we have focused on optically stimulated luminescence (OSL) in household salt (NaCl). This particular dosimeter can be found almost everywhere and it has shown several promising dosimetric properties [3, 4] and e.g. a linear dose response between 0.1 mGy to 100 mGy and a low limit of detection, down to 0.1 mGy for some brands of salt [5].

The use of OSL in NaCl is not limited to retrospective dosimetry. Preliminary investigations carried out in different radiation environments in a hospital, shows a similar response for LiF and NaCl for absorbed dose measurements at different photon energies. NaCl dosimeters can also be used as a cheap alternative for environmental dosimetry. Studies that have been carried out in a highly ¹³⁷Cs-contaminated village in Belarus during the summer of 2008, suggests that NaCl dosimeters are as good indicators of absorbed dose and its variation, as the particular LiF (TLD-100) dosimeters used in the same village.

2. Material and methods

To investigate salt as a dosimeter in different radiation situations, special dosimeter kits have been designed containing NaCl and LiF. These "twin" dosimeter kits were normally assembled with two sections of 30-50 mg NaCl and two chips of LiF (TLD-100, Harshaw). Before the dosimeter kits were assembled, which was carried out the night before the distribution, the salt was exposed to sunlight (bleached) for a few days, in order to get a low background luminescence. The chips and the salt were placed between two 4 mm thick layers of PMMA, this forming a dosimeter kit of two different luminescent materials. To avoid bleaching of the OSL signal, all dosimeter kits were covered with a light tight adhesive tape. Additionally, the environmental dosimeters were placed in plastic bags filled with silica gel, to protect the dosimeters from rain and moist during the measurement period.

After the kits were collected, the TLDs were read out using a TOLEDO TLD reader (VINTEN Instruments, England). The signal in the NaCl dosimeters was assessed using a TL/OSL reader (TL/OSL DA 15; Risø National Laboratory, Roskilde, Denmark) which is an automated equipment that can manage 48 samples (or aliquots) per run. The salt from each dosimeter kit was carefully mixed and divided onto five, or more, different aliquots. To assess the stored signal in the salt, it was optically stimulated by blue light ($\lambda = 470 \pm 30$ nm) for 40 – 100 s. The average signal, OSL_{signal} (counts mg^{-1}), for a dosimeter kit was defined as:

$$OSL_{sample} = \frac{\sum_{i=1}^n \left(\frac{S_i}{m_i} \right)}{n} \quad (1)$$

where S_i is the integrated signal, in the beginning of the stimulation, from aliquot i with mass m_i and n is the number of aliquots (normally $n = 5$). Similarly, an OSL background, OSL_{bkg} (counts mg^{-1}) was estimated as the integrated signal during the late phase of the stimulation time. The absorbed dose, D_{sample} (mGy), to the salt was thereafter estimated by applying a calibration coefficient, $c_{specific}$ (counts $mGy^{-1} mg^{-1}$) to the net signal:

$$D_{sample} = \frac{1}{c_{specific}} \cdot (OSL_{sample} - OSL_{bkg}) \quad (2)$$

Details on the read out protocol and on the calibration coefficients are described in more detail by Bernhardsson et al. [5] and in [6].

2.1 Occupational and medical exposures

To test salt as a personal dosimeter and at different photon energies, four staff members working in the radiology and nuclear medicine departments at Malmö University Hospital (UMAS) carried the dosimeter kits during one month. The salt used for the personal dosimeters was Falsalt fint havssalt (Hansson and Möhring, Halmstad, Sweden), a naturally fine grained sea salt consisting of $NaCl \geq 99.6\%$. The kits were attached to the investigated persons regular TLD (LiF: Mg, Ti) and the TL-readings from these were used for the NaCl/LiF comparison. Similar dosimeter kits were also attached to TLDs that were positioned on the inside walls of a nuclear medicine investigation room. A few other dosimeter kits were placed in the primary radiation field from a mammography X-ray unit and in the primary beam of a ^{60}Co therapy unit. At the ^{60}Co unit the dosimeter were given eight successively increasing doses in the range from 1.4 mGy to 4.1 Gy.

2.2 Environmental exposure

To test the salt (Falsalt fint bergsalt, Hansson and Möhring, Halmstad, Sweden) during normal environmental conditions, dosimeter kits were positioned in a highly ^{137}Cs -contaminated village in Belarus, during the summer of 2008. Between 5 and 14 kits were attached to the inside- and outside walls of each one of the 7 houses included in the study. After 2.5 months the dosimeters were re-collected and brought back to Sweden for the read-out. During the distribution and collection of the dosimeters a special radiation protection instrument, GR-110 (NaI(Tl)-detector; Exploranium, Canada) was used to directly determine the dose rate *in situ*. A mean value from these measurements was used to include the GR-110 readings in the comparison between NaCl and LiF.

A few TLDs and direct measurements, using various radiation protection instruments (e.g. SRV-2000; RADOS, Finland), were used during transport and

storage to estimate the dose accumulated when the dosimeters were not in position in the village.

3. Results and discussion

3.1. Occupational and medical exposures

The relation between the OSL-signal in NaCl and the absorbed dose as measured by LiF for measurements on the personnel in diagnostic radiology and nuclear medicine as well as in the primary beam of a mammography X-ray unit is shown in: Fig. 1. The same relation is also shown for similar measurements in a ^{60}Co beam. At low photon energies (mammography), the OSL-measurements indicate a somewhat higher response relative to the LiF-TL dosimeters. The effect may be attributed to the somewhat higher atomic number of NaCl ($Z = 11; 17$) compared to LiF ($Z = 3; 9$).

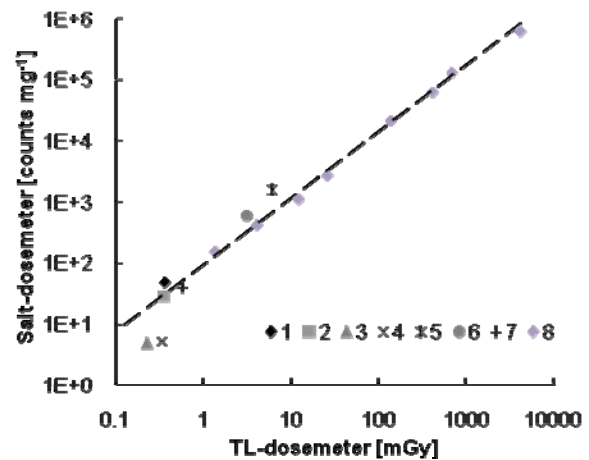


Fig. 1. The OSL signal from NaCl as a function of absorbed dose measured by LiF (TLD) for ten "twin" dosimeter kits (OSL and TL) positioned at the following locations; *i.*) on individual staff members in diagnostic radiology (no 1 and 2), *ii.*) on individuals at the nuclear medicine department (no 3 and 4), *iii.*) in the mammography primary radiation field (no 5 and 6), *iv.*) on the interior walls of a nuclear medicine laboratory (no 7). The OSL response vs. absorbed dose determined by LiF-TL dosimeters placed in a ^{60}Co beam is shown for comparison (no 8).

Although these results are based on a small number of NaCl/LiF dosimeters, the salt shows a similar dose response at different photon energies, compared to ordinary TLDs.

3.2. Environmental exposure

The total absorbed dose accumulated under field-conditions in the Belarusian village, between resetting of the luminescence and the read-out in Sweden, is presented in: Fig. 2. The absorbed dose to 54 dosimeter kits as determined by OSL in NaCl is plotted as a function of the corresponding value for TL in LiF. In view of the low signals there is a fairly good correlation ($r^2 = 0.55$) between the two types of dosimeters. There is however a systematic difference, where the NaCl dosimeters on average, show a 0.16 mGy higher absorbed dose compared with the TLDs. This might

indicate a too small background subtraction in the NaCl batches or a too high background subtraction in the LiF chips. It could also be an effect of a variation in the sensitivity of the LiF chips during the measuring period, i.e. between calibration and read-out. Another explanation could be that the fading of the signal is more rapid in the LiF chips compared to NaCl, at least during the first 2 – 3 months.

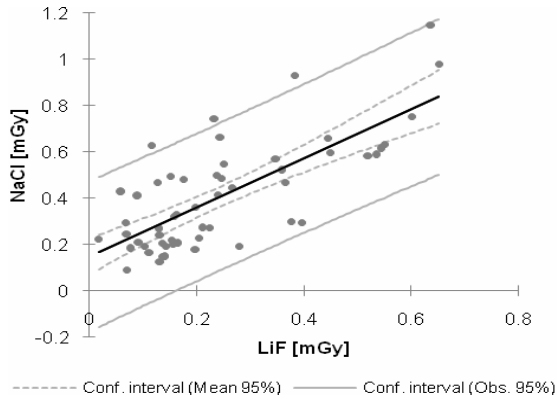


Fig. 2. Absorbed dose as determined by OSL in NaCl vs. the absorbed dose as determined by TL in LiF.

In Fig. 3 and 4, is the absorbed dose as determined by LiF and NaCl, respectively, plotted as a function of the corresponding dose obtained from the GR-110 measurements at each position of the luminescent dosimeters. The GR-110 values refer to the average value of the dose rate at the outset and the collection of the luminescent dosimeters minus an estimated background ($0.11 \mu\text{Sv h}^{-1}$ and $0.17 \mu\text{Sv h}^{-1}$ for the indoor and outdoor measurements, respectively). Different colors have been used to distinguish the dosimeters that were positioned inside from dosimeters outside the buildings. The regression line is however fitted to all dosimeter readings. The correlation in terms of Pearson's r^2 was higher for the outdoor measurements compared to those inside. The better correlation found for the outdoor dosimeters is probably due to the higher absorbed dose which provide a better signal to noise ratio.

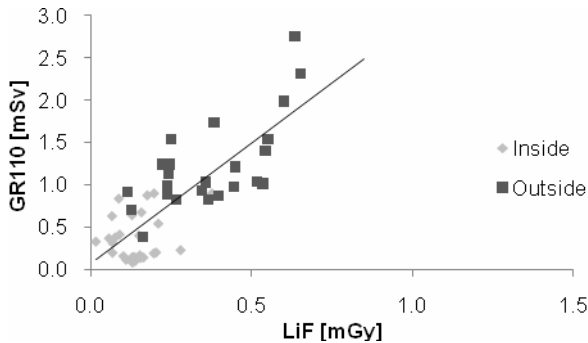


Fig. 3. The average effective dose as measured with GR-110 (on outset and collection) as a function of the absorbed dose in LiF at the same position, inside and outside the houses.

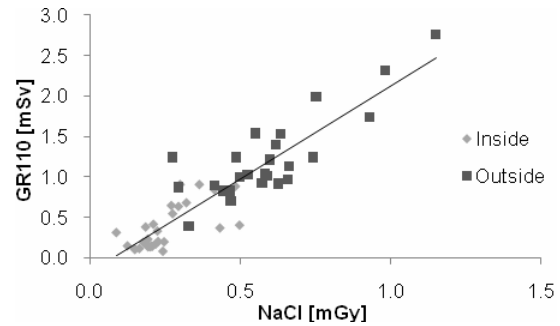


Fig. 4. The average effective dose as measured with GR-110 (on outset and collection) as a function of the absorbed dose in NaCl at the same position, inside and outside the houses.

Generally, the estimated dose rate indoors were rather low ($\bar{D}_{\text{NaCl}} = 0.14$; $\bar{D}_{\text{LiF}} = 0.07 \mu\text{Gy h}^{-1}$) or comparable to the normal background radiation level in many European countries. Nevertheless, there is a moderately or good correlation between the three dosimeters. The best correlation is observed between GR-110 and NaCl readings ($r^2 = 0.82$), compared to GR-110 and LiF ($r^2 = 0.55$). This may partly reflect the similar responses between NaI(Tl) and NaCl for the photon energies studied. It is however apparent that some of the specific LiF chips used in this study show a larger variation in sensitivity than originally stated by the manufacturer. This might have had a negative influence on the 0.01 mGy detection limit, as specified by the manufacturer, and should be taken into consideration when looking at the indoor measurements where the dose rate was relatively low.

A new expedition to the same village was carried out during the summer of 2009, with the same purpose as in 2008. Then additionally 10 houses (including 72 dosimeter kits) were investigated and the information from these dosimeters will bring more light to the usefulness of salt as a dosimeter for the environment.

4. Summary and conclusions

It has been shown that household salt can be used to measure absorbed doses down to a few tens of mGy. Measurements also indicate a slightly higher response in NaCl- relative to LiF dosimeters at lower photon energies. The effect may be attributed to the higher atomic number of NaCl compared to LiF, and differences in directional dependence in sensitivity. More studies on salt are required to fully understand the dose response at different photon energies.

It has also been shown that household salt can be used as a dosimeter at absorbed doses from a few tenths of mGy and during field conditions. Even though the detection limit of OSL in salt, as stated in [5], is not yet as low as for the best TL systems using LiF, the use of salt instead of LiF would reduce the cost in both preparation and in read out time, as well as in the cost of manufacturing the dosimeters. The drawback is that the salt must be kept sealed from light and that it is sensitive to moisture. However, the risk of those factors can easily be reduced by a different design of the dosimeter casings.

Hence, both laboratory and field studies demonstrate that household salt is a useful tool for retrospective dosimetry and a good candidate for environmental monitoring. Still, there are some properties that must be investigated and improved before it can be fully used as a dosimeter e.g.

- long- and short term fading properties when exposed to monochromatic light sources and in darkness,
- comprehensive study of the dose response at different radiation qualities from low energy to high energy photons in hospitals and from photons to neutrons in the nuclear industry,
- develop a protocol for individual calibration of each salt sample,
- develop more rigid dosimeter holders.

5. References

1. ICRU (2002) Retrospective Assessment of exposures to ionising radiation. ICRU Report 68. Nuclear Technology Publishing, Ashford, United Kingdom
2. Clemic A.K., Bailey P.D., Miller K.M. and Monetti M.A. External dosimetry in the aftermath of a radiological terrorist event. *Radiat Prot Dosim*, 120, 2006. p. 242-249.
3. Thomsen K.J., Bøtter-Jensen L. and Murray A.S. Household and workplace chemicals as retrospective luminescence dosimeters. *Radiat Prot Dosim*, 101, 2002. p. 515–518.
4. Zacharias N., Stuhec M., Knezevic Z., Fountoukidia E., Michael C.T. and Bassiakos Y. Low-dose environmental dosimetry using thermo- and optically stimulated luminescence. *Nucl Inst Meth Phys Res*, 580, 2007. p. 698–701.
5. Bernhardsson C., Christiansson M., Mattsson S. and Rääf C.L. Household salt as a retrospective dosimeter using optically stimulated luminescence. *Radiat Environ Biophys*, 48(1), 2009.p. 21-28.
6. Christiansson M., Bernhardsson C., Mattsson S. and Rääf C.L. Optimization of read-out sequences for optically stimulated luminescence (OSL) of household salt for retrospective dosimetry. *Proceeding: International conference on radioecology and environmental radioactivity*, Bergen, Norway, 15 – 20 June 2008.

ULTRAVIOLET RADIATION INFLUENCES WETTABILITY AND BIOLOGICAL PROPERTIES OF PMMA SURFACE

Yuri DEKHTYAR¹, Linda LANCERE¹, Nataliya POLAYKA¹, Alexander RAPOPORT², Anna RUSAKOVA²,
Alexander SUDNIKOVICH², Valdis VALTERS³

¹Riga Technical university, ²University of Latvia, ³Valter's Prosthetic laboratory, ltd.

Abstract: PMMA (poly-methyl metha acrylate) material is widely used for eye prostheses. During its exploitation the material is under sun radiation, ultraviolet (UV) being the component. Therefore the properties of PMMA influenced by UV could affect biocompatibility of the prostheses. The present article is targeted to explore influence of UV on wettability and biological properties of PMMA

Keywords: PMMA, ultraviolet radiation, sun radiation, eye prostheses

1. Introduction.

The tear liquid should moisten the PMMA eye prosthesis during its exploitation. This could be disturbed by sun ultraviolet, strong radiation destroying molecular couples of the PMMA [1, 3, 5, 6]. Currently there are not experimental data on the soft Sun UV influence on PMMA wettability properties.

The article is targeted to explore influence of the simulating sun UV radiation on the PMMA wettability.

The latter could be influenced because of the chemical alteration induced by UV [1, 3, 5, 6] or just because of the escaping electrons from the surface layer (photoemission). As the result the surface should acquire an electrical charge. To verify this, the electron work function of the radiated specimens was measured.

Disturbance/damage/reconstruction of chemical couples at the PMMA surface could have a negative influence on the cell behaviour. Taking this into account, the viability of the yeast eukaryotic cells deposited on the radiated specimens was tested too.

2. Methods and materials.

2.1. Radiation

For physical simulation process, samples from commercial material "Stoma" (*Ctoma*) were taken with size of $\sim 1 \times 1 \text{ cm}^2$, thickness about 2-4mm.

The UV irradiation was supplied from the Hamamatsu Spot Light Source equipped with Hg-Xe lamp (intensity at the source exit was 3500 mW/cm^2 at wavelength 365nm), the specimens were placed at 0,4 m distance from the source exit. The room air was the environment

for the specimens. The room temperature was $+20^{\circ}\text{C} \pm 2^{\circ}\text{C}$ and humidity $39 \pm 7 \text{ mmHg}$.

The temperature at the specimen's surface during the radiation was not higher as in the room.

Before radiation each specimen was cleaned with 96% ethanol.

2.1. Measurements of wettability

Wettability was tested by the modified Axisymmetric Drop Shape Analysis-Profile (ADSA-P) drop method before and after the UV exposure. The physiological solution was used as the testing liquid. The drop with diameter $\sim 10 \text{ mm}$ was measured using the optical microscope MMI-2 (*MMI-2*). The image of the drop was projected via CCD camera (Imaging Source) to the PC screen. The contact angle was measured from images applying in the Photoshop software CS3 version. Before measurements each sample was cleaned with 96% ethanol. The above described sequence was repeated 15 times for each sample to collect statistics.

2.2. Electron work function.

The electron work function (ϕ) was determined as the result of the pre-threshold photoelectron emission measurements. For this each specimen was positioned in the hand made spectrometer [8] and photoelectron emission current was detected in dependence on the photon energy in a range 4-6 eV. The duration (exposure) of the experiment was several times less in contrast to the above radiation of the specimens.

2.3. Biological test.

To verify the UV influence on chemical couples behaviour at the surface of PMMA, non-irradiated and irradiated samples were compared. On both yeast cultivation *sacharomyces cerevisiac 14* was deposited and left for 4 days. Then the dried and coloured cells showing differently living and dead cells were counted with Olympus CX31 microscope and results compared (Fig.4).

3. Results

UV radiation increased the contact angle, i.e. wettability of the PMMA became worse in the exposure range until 90 minutes, however was directed to the native condition at 160 minutes (Fig. 1) This could be connected with deposition of the electrical charge since the electron work function increases and positively correlates to the contact angle at least in the range until 90 minutes of exposure (Fig. 2). The increase of the work function value evidences that the surface acquired the negative charge. Because of the UV radiation could induce photoemission electrons should leave the specimen, the latter inducing the positive charge of the PMMA surface. However the experiment demonstrated the reversible result. This could be explained that UV reconstructed chemical couples of PMMA. The charged surface relaxed during 2-2.5 months (Fig. 3). The biological test demonstrated that yeast cell viability on the radiated surface falls down (Fig 4).

4. Conclusions.

1. UV radiation has a non monotonic influence on the wettability of the PMMA surface: the surface changed to the hydrophilic until 90 minutes of radiation and turned back to the native state, when the exposure was increased to 160 minutes.
2. Alteration of wettability is probably connected with reconstruction of chemical PMMA couples.
3. The alteration of PMMA properties induced by UV radiation decreases viability of the yeast cells positioned on the PMMA surface.

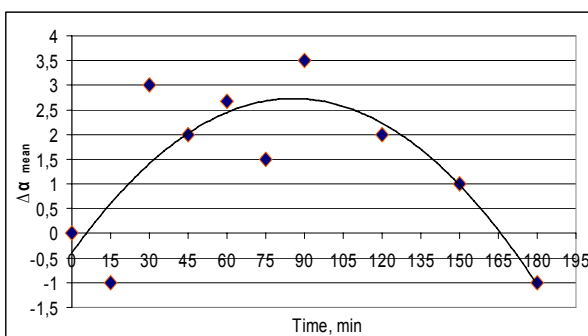


Fig.1. Contact angle (mean) increment after different irradiation exposures.

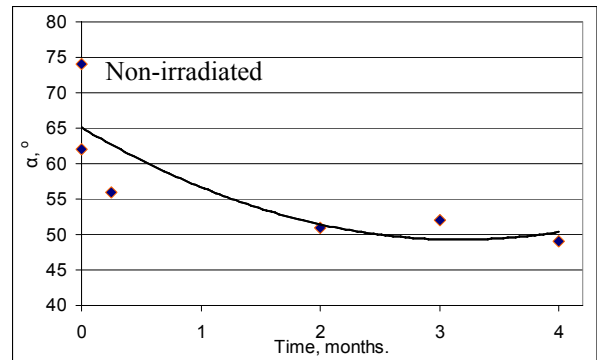


Fig.2. Irradiated 2 h. Mean contact angle dependence from time.

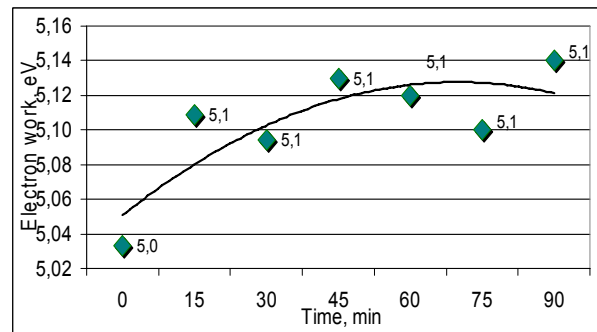


Fig.3. Electron work dependence on exposure time.

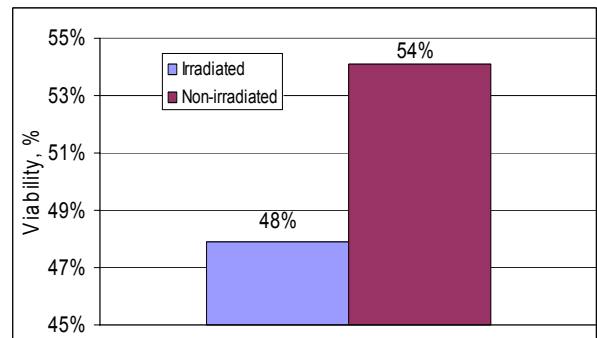


Fig.4. Eukaryotic yeast cell viability on PMMA surface. Irradiated 90min.

5. References.

1. Ratner B.D., Hoffman A.S, Schoen F.J., Lemons J.E. Biomaterial science. Academic press., New York, 484, 1996.
2. Dekhtyar Yu., Polyaka N., Sammons R. Electrically charged hydroxyapatite enhances immobilization and proliferation of osteoblasts. *IFMBE proc.* Springer , 20, 2008. p. 357-360.
3. Ranby J, Rabek JF. Photodegradation, Photo-oxidation and Photostabilization of Polymers. London: John Wiley, 156, 1975.
4. Wunderlich B., Pyda M., Encyclopedia of Polymer Science and Technology\Vol.12, Thermodynamic Properties of Polymers, University of Tennessee, Chemical Sciences Division of Oak Ridge National Laboratory, 165, 2002.
5. Caykara T., Guven O., UV degradation of poly(methyl methacrylate) and its

- vinyltriethoxysilane containing copolymers, Department of Chemistry, Faculty of Art and Science, Gazi University, Hacettepe University, Ankara, Turkey, 1999. p. 225-229.
6. Lican Lu, Nianfa Yang, Yuanli Cai, Well-controlled reversible addition-fragmentation chain transfer radical polymerisation under ultraviolet radiation at ambient temperature. College of Chemistry, Xiangtan University, Xiangtan, Hunan, China, 2005. p. 5287-5288.
 7. Kaariainen T.O., Cameron D.C., Improving the adhesion of sputtered coatings on PMMA using ALD interlayers, Advanced Surface Technology Research laboratory, Lapeenranta University of Technology, Mikkeli, Finland, 23, 2009.
 8. Akmene R.J., Balodis, A. Dekhtyar J.D., Markelova G.N., Matvejev J.V., Polyaka N., Rozenfeld L.B., Sagalovich G.L., Samrnov J.S., Tolkaov A.A., Uprish A.I. Exoelectron emission spectrometer complete set of surface local investigation. Surface. Physics, mechanics, chemistry. N 8, 1993. p. 125 - 128.

TOTAL AND SCATTER DOSE MODELLING IN PHOTON IRRADIATED Si SAMPLES, COVERED BY PROTECTIVE COATINGS

Inga CIBULSKAITĖ*, Diana ADLIENĖ*

*Kaunas University of Technology

Abstract: Total and scatter doses due 25-32 keV X-ray beam irradiation of Si samples, covered by different materials protective coatings, calculated by Monte Carlo based modelling code EGSnrc are presented in this paper.

Keywords: dose, scatter, modelling, Monte Carlo

1. Introduction

Through low energy (25-32) keV X-ray photon interactions (the photoelectric effect, the Compton effect) with material, the photon radiation transfers energy to it. This transfer is considered as a dose.

The energy transport during the X-ray photons interaction with different materials, that are used for radiation registration, processes could be analysed in detail experimentally or by modelling. In constructions of up-to-date detectors new perspective composite materials (crystal, polycrystalline) are used, the active volume of the most detectors is protected by protective coating (polymers, amorphous materials), defending it from mechanical, aggressive atmospheric and ionising radiation damage.

It is difficult to test each construction practically, so the results obtained by mathematical modelling of the photon interaction process could be used for this purposes. and after this, by choosing the most perspective constructions – examine their characteristic practically.

The scattered radiation, that is due to X-ray interaction with material, could reach the active volume again and that negatively influence on the registration of the useful signal.

By varying detector's geometry, construction and materials composition according to selected criterion it is possible to find the optimal version for detector with less influence of scatter to the signal recorded by detector. The selection of such criterion let us prognosticate new constructions, to compare its characteristic to characteristics of detectors used in praxis. As the criterion for the scatter process estimation in radiation sensitive material could be calculated according to lower scatter dose to total dose ratio. By application of this criterion it is possible to compare indirectly the efficiency of the registration of all configurations detectors also those that are under construction.

Si is one of the materials sensitive to ionising radiation and applied in many solid state detectors. Not considering the detective properties of this material, the calculation of the total and scatter dose by Monte Carlo based code in Si samples, was done to investigate the influence of the different protective coatings applied to Si samples, for the doses results.

2. Instruments and methods

Interactions of low energy (25-32) keV polyenergetic X-ray photons with matter were simulated using simulation code based on Monte Carlo method (EGSnrc Code system) [1] Investigation of interaction effects in Si samples was performed using adapted the real exposure conditions, representing mammography examinations of patients.

Assuming that Si sample without and with coating was placed at a central position on the top of 45 mm polymethylmethacrylate PMMA phantom, representing "standard" compressed female breast that was used instead of patient for the simulation of the real irradiation conditions, Monte Carlo simulations were performed within cylindrical geometry, virtually dividing the X-ray exposed space between compression paddle and breast support table into zones, corresponding to the different densities and compositions of presented materials.

Individual photon histories were simulated and the history of each photon was followed until either all of its energy was transferred to electrons or it was absorbed locally due to the scattering events in material. It was assumed that 10^8 or 10^9 photons having in 1 keV increments increasing energy from the range of 1 keV to 35 keV interact with samples. Considering small sample size (mm range) as compared to exposure area (12 x 18) cm, it was assumed that X-ray photons beam is parallel to Z-axis in the central zone of interaction and there was no X-ray beam distortion.

Total and scattering doses in uncoated and coated samples were calculated using modified user code

DOSnrc (EGSnrc) [2] in each region of interest. Estimated relative statistical uncertainty of calculated doses was 0.8% in the case when 10^8 photon histories were taken for the simulation, and 0.2% - for 10^9 photon histories.

The spectra of the X-ray beam, entered to the code system for interaction modelling, were generated for different X-ray tube potentials from the range of (25 - 32) kV when the tilting angle of the Mo anode was 16° . Generated X-rays were attenuated by 1 mm Be window of the X-ray tube, 0.03 mm thick Mo filter and 3 mm thick polymethylmethacrylic compression paddle of mammography unit.

Additional filtration of the photons with the energies below 10 keV and above 20 keV was undertaken due to the fact, that Mo is characterized by K lines at the energies: 17.38 keV ($K_{\alpha 2}$), 17.49 keV ($K_{\alpha 1}$), 19.61 keV ($K_{\beta 1}$) and 19.96 keV ($K_{\beta 2}$) [3]. X-ray photon spectra were calculated using IPEM Spectrum Processor [4] and average photon energies for the applied X-ray tubes potentials were estimated taking into account the special geometry of the irradiation.

3. Results

Adapted for specific geometry EGSnrc code was used for X-ray photon interaction with physical object modelling. The main characteristic that was chosen was radiation dose, that reflects information about energy transfer, absorption and scatter in every segment of the complex object irradiated by X-ray photons. The result of modelling are total and scatter doses in selected objects. It was considered that the total dose represents the energy, transferred to the target and the scatter dose is defined as a dose, which can be traced back to the photons that have been scattered in Compton and Rayleigh effects and to the photons that were created through relaxation processes after Compton and photoelectric effect.

Modelling of low energy (25-32) keV X-ray induced processes was performed for the constructions consisting of Si wafer (active volume) protected by different coating materials which are commonly used in radiation detector constructions. Some characteristics of the investigated coatings are provided in Table 1.

X-ray interaction effects in the detector construction are dependent on X-ray attenuation and scattering processes in the coating material, which are influenced at least by the coating structure (polycrystalline, amorphous, polymer-like), coating density and thickness, and the construction of the layered structure (with or without chemical bonding between detector and coating material).

A thin air gap existing between the coating and detector material was inserted into modelling geometry in the case of free standing polymeric foils. Nanoscale interlayer structure between bulk material and coating was considered for the modelling of the structures

having direct deposited or grown coating layers on the top of the active volume.

The thickness of Si target in investigated constructions varied within the range of 0.1 mm – 3.0 mm, the thickness of protective coatings was from the interval of 100 nm - 1.0 mm.

Table 1. Coating materials

Coating type	Coating material	Z_{eff}	Density, g/cm^3
Free standing polymeric foils	Polyethylene H – 14 %, C – 85 %	5.68	0.93
	Mylar, Polyethylenetereftalate H – 4 %, C – 62 %, O – 33 %	6.71	1.38
	Rubber H – 11%, C – 88%	5.75	0.92
Direct deposited / grown layers	Carbon fibre	6.10	1.75
	SiO_2	11.5	2.32
	DLC film synthesized from C_2H_2 : H – (24 % to 38%)	diverse	1.60 2.12
	SiOx-containing DLC film, synthesized from HMDSO: main components, O and Si (17% - 24%)	diverse	1.87 2.20

Comparing the modelling results, radiation induced scatter dose of X-ray photons was higher in all coated Si specimens of different thickness, as compared to uncoated ones, while the total dose was less, due to the photon energy absorption in coating material. Increasing for scatter dose and decreasing for the total dose tendency was observed with the increasing density of coating material within the whole energy range of mammography examinations, when the thickness of coating was kept constant.

Some variations of calculated scatter doses in Si targets of different thickness coated by different coating materials of the same thickness, representing results of the investigation are shown in Fig. 1. Lines in this figure indicate the highest and lowest scatter doses corresponding to the coating material, which were evaluated within the group of coated samples, having the same Si target thickness. A broadening of the range between the highest and lowest scatter dose within the group indicates the influence of coating material (increased density) on scatter dose in coated Si when the thickness of the active Si volume is decreased. The highest scatter dose was estimated for Si-DLC film containing SiO_x combination, which represented the highest density (2.2 kg/m^3) of all investigated coatings. Scatter doses calculated for Si coated by nanoscale DLC film were included in Fig 1 for the comparison of the results.

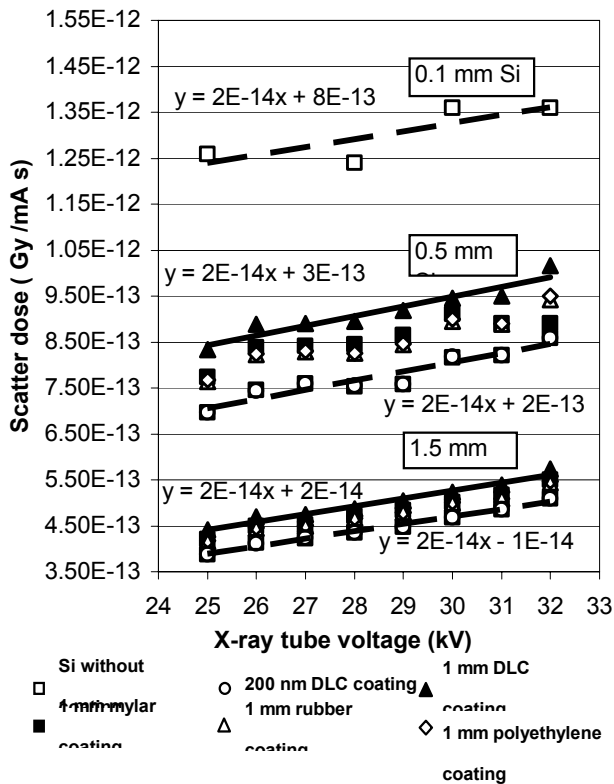


Fig. 1. Simulated scatter doses in Si samples of different thickness coated by different coatings of the same thickness. Detector thicknesses are indicated.

Three possible cases were investigated for the estimation of the influence of the coating thickness on the X-ray attenuation processes in irradiated detector constructions: 1) coating thickness h is of the same order as the thickness of the active layer d ($h \approx d$); 2) $h/d \leq 0.1$; and 3) $h \ll d$. Calculations of total, scatter and scatter to total dose ratio were performed for different combinations of Si and coating material thicknesses, covering the whole range mentioned above and for all possible photon energies. Most appropriate total and scatter dose calculation results obtained for 30 keV X-ray irradiated samples, which correspond to the commonly used coating thicknesses are presented in Fig 2 and 3 respectively and results of the scatter to the total dose ratio, presented in figure 4. The ratio of the doses for the planar sample case is presented for the comparison.

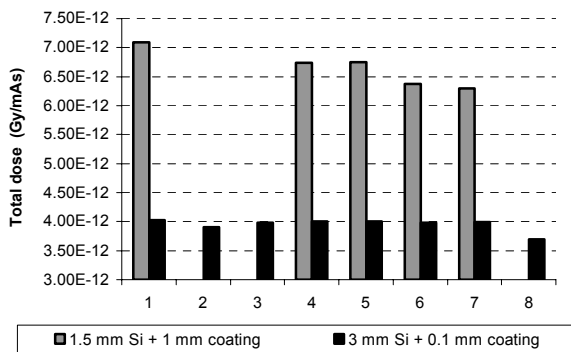


Fig 2. Total dose variation in Si samples coated by different materials: 1 – uncoated Si, 2 – Si coated by DLC containing SiOx; 3- Si coated by a-C:H coating, 4 - Si coated

by rubber, 5 - Si coated by polyethylene, 6 – Si coated by mylar; 7 – Si coated by carbon fibre, 8 – Si coated by SiO₂

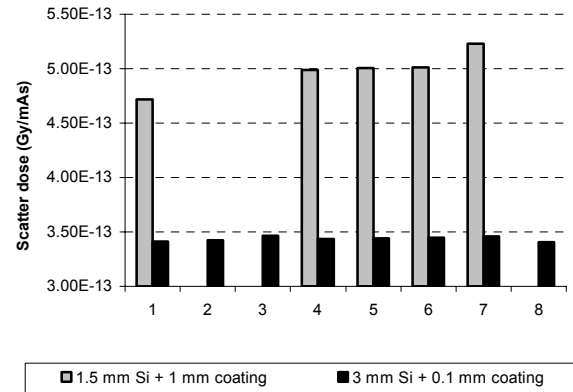


Fig 3. Scatter dose variation in Si samples coated by different materials: 1 – uncoated Si, 2 – Si coated by DLC containing SiOx; 3- Si coated by a-C:H coating, 4 - Si coated by rubber, 5 - Si coated by polyethylene, 6 – Si coated by mylar; 7 – Si coated by carbon fibre, 8 – Si coated by SiO₂.

The highest dose ratios were found in the case of $h/d \leq 0.1$. The influence of the coating to X-ray scattering processes within detector material was negligible, when the thickness of the protective layer was extremely small as compared to Si thickness $h \ll d$. This characteristic for bulk and planar Si sample cases (Table2).

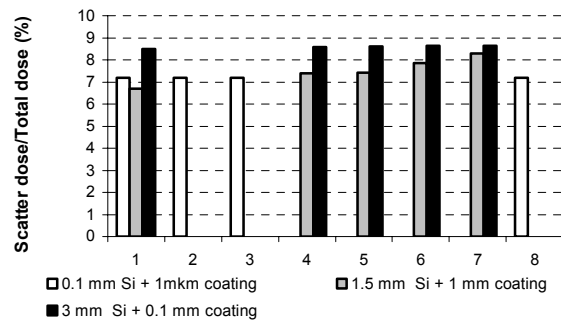


Fig 4. Variations of the scatter to total dose ratio in Si samples coated by different materials: 1 – uncoated Si, 2 – Si coated by DLC containing SiOx; 3- Si coated by a-C:H coating, 4 - Si coated by rubber, 5 - Si coated by polyethylene, 6 – Si coated by mylar; 7 – Si coated by carbon fibre, 8 – Si coated by SiO₂

As it could be seen from figure 4, such cases are Si samples coated by thin DLC coating containing SiOx, Si coated by a-C:H coating and Si coated by SiO₂.

As was mentioned before, scatter influence negatively to registered signal and scatter dose contributes to the registered signal to noise ratio, so it seems to be possible to reduce the number of scattering events in irradiated detector material performing the optimization of the coating thickness, when appropriate material is chosen for the coating. From the obtained modelling results, considering that criterion for the scatter process estimation in radiation sensitive material could be calculated according to lower scatter dose to total dose ratio, nanothick coatings deposited or grown on detector surface, are the best candidates to have lowest influence of the scatter to active volume.

Table 2 Scatter dose in planar Si volume

Construction	Scatter dose, Gy (mA s) ⁻¹		
	25 kV	28 kV	30 kV
0.1 mm Si, without coating	1,258*10 ⁻¹²	1,236*10 ⁻¹²	1,356*10 ⁻¹²
0.1 mm Si with 0.001 mm SiO ₂ coating	1,259*10 ⁻¹²	1,239*10 ⁻¹²	1,359*10 ⁻¹²
0.1 mm Si with 0.001 mm a-C:H coating	1,260*10 ⁻¹²	1,238*10 ⁻¹²	1,361*10 ⁻¹²
0.1 mm Si with 0.001mm carbon coating, containing SiO _x	1,260*10 ⁻¹²	1,238*10 ⁻¹²	1,360*10 ⁻¹²
0.1mm Si with 0.1 mm carbon coating, containing SiO _x	1,272*10 ⁻¹²	1,288*10 ⁻¹²	1,413*10 ⁻¹²

However these coatings also have to provide almost the same or better protective properties as the often used relative thick free standing polymeric foils do.

4. Conclusions

The calculation of the total and scatter doses in Si samples coated by protective coatings were performed using Monte Carlo based modeling code EGSnrc. The modeling of (25-32) keV the X-ray photons interaction processes with mentioned material allowed to investigate the scatter contribution to the registered dose thought obtained total and scattered doses results. The

criterion of the scatter contribution is scatter to total dose ratio. Combination of the scatter modelling results obtained from Monte Carlo calculations with the manufacturing technological parameters of the experimental coatings, allows to get coatings that have good protective features, with possibly low scatter dose to total dose ratio and in this way to optimise the construction of ionising radiation detector that are suitable for low energy X-ray photon doses recording. As the modelling results shows, the influence of the thin (< 1 µm) DLC coatings containing SiO_x, to X-ray scattering processes within detector material was negligible.

5. References

1. Kawrakow I.; Rogers D.W.O. The EGSnrc Code System. Monte Carlo Simulation of Electron and Photon Transport. National Research Council of Canada. 2003. <http://www.irs.inms.nrc.ca>
2. Rogers D.W.O., Kawrakow I., Seuntjens J.P., Walters B.R.B., Mainegra-Hing E. *NRC User Codes for EGSnrc*. NRCC Report PIRS-702, 2005.
3. Dosimetric Aspects of Mammography. Report 6 of the Netherlands Commission on Radiation Dosimetry, 1993.
4. Cranley B. J. Gilmore, G. W. A. Fogarty, and L. Desponds, IPEM Report 78. Catalogue of Diagnostic X-Ray Spectra and other Data. The Institute of Physics and Engineering in Medicine IPEM; CD-Rom Edition 1997. Electronic Version prepared by D. Sutmond, 1997.

**APPLICATION OF A SYNTHETIC DIAMOND DETECTOR FOR THE
MEASUREMENT OF RELATIVE DOSE DISTRIBUTIONS IN RADIOTHERAPY**

N. KAZUCHITS*, M. RUSSETSKYI*, A. SHULENKOV**, V. KUKUSHKIN***,
S. MARTYNOV***, V. KHRUNOV***, J. TUZOV***,
G. GATSKEVICH****, D. KANDYBOVICH****

* Belarussian State University, 220030 Minsk, Belarus;

** UP Minskii NII Radiomaterialov 220024 Minsk, Belarus;

*** Institute in Physical and Technical Problems 141980 Dubna, Moscow Region;

**** N.N. Alexandrov National Cancer Centre of Belarus Minsk, Belarus

Abstract: The suitability of a synthetic diamond for the measurement of relative dose distributions in selected radiotherapy applications was studied. The performance of the synthetic diamond detector was analyzed by comparison with that of natural diamond detector produced by a Physikalisch-Technische Werkstätten (Freiburg, Germany) (PTW). The synthetic diamond detector is concluded to be suitable for relative dose measurements, especially when high response and high spatial resolution are required.

Keywords: Diamond, detector, sensitivity, γ -rays, dose rate

1. Introduction

Diamond is the attractive material for radiation detectors fabrication. The main advantage of this material is its radiation hardness. For application of diamond detectors in radiotherapy it is necessary to note two additional features – chemical inertness and "tissue equivalence". The last feature is due to atomic number of the carbon ($Z=6$) is similar to the effective atomic number of the human soft tissue ($Z=7,4$). At present time natural diamond radiation detectors for radiotherapy are under the commercial production [1]. However, such detectors are rather expensive because of only a small part of natural diamond crystals is suitable for dosimetry application.

Another material for radiation detectors production is high-pressure high-temperature (HPHT) synthetic diamond [2, 3]. Both natural and HPHT synthetic diamonds have practically the same physical properties [4]. The electronic applications of the HPHT material are restricted by a high concentration of the nitrogen and inhomogeneity of the crystals. Nevertheless, the improvement of the HPHT technology enables to consider synthetic diamond detectors as a future commercial product. In general, both natural and HPHT synthetic diamonds require a complex selection for dosimetry application.

The purpose of this work is to compare characteristics of HPHT synthetic diamond detector with PTW natural diamond detector. Sensitivity, temporal current

stability and current linearity with dose rate were measured in high-energy photon beam.

2. Details of experiment

The HPHT synthetic diamond crystals produced by "Adamas-BSU" company (Minsk, Belarus) were used in our experiments. Diamond plates 0,3 mm thickness were cut from as-grown crystals. After pre-selection by UV-photoconductivity method the detector structures were fabricated on the diamond plates. For this purpose it was performed an ion implantation of boron into both surfaces of diamond followed by high temperature (1400 °C) annealing in vacuum. Finally, the Ti+Au contacts were deposited on both boron-doped layers.

Prepared structures were tested using calibrated ^{137}Cs irradiation source of Federal State Unitary enterprise «Institute in Physical and Technical Problems» (Dubna, Russia). Leakage current, sensitivity, pre-irradiation dose, stability and linearity of current with dose rate were measured.

The best samples were hermetically sealed in plastic cases for certification in Basic laboratory of metrological service of the Russian centre of science of radiology and surgical technologies (St. Petersburg). Certification was carried out while γ -rays ^{60}Co irradiated detectors were submerged in the water phantom.

Experimental results are related to the best synthetic diamond detector.

3. Results and discussion

Temporal dependence of current for several γ -rays ^{137}Cs dose rates for the synthetic diamond detector is shown in figure 1a. For comparison, the similar characteristic for IIA-type natural diamond detector is shown in figure 1b. For both detectors maximum irradiation dose rate is equal 6,02 cGy/s and bias voltage is 30 V.

As shown in figure 1, both detectors require pre-irradiation dose about 10 Gy for current stabilization. Requirement of pre-irradiation is character feature of all types of diamond detectors and related to trapping of charge carriers on the local states in the band gap of material. It is necessary to note that sensitivity of synthetic diamond is about 20 times higher than that of natural diamond. Nevertheless, the synthetic diamond detector current fluctuations are higher and reach the value about 3%.

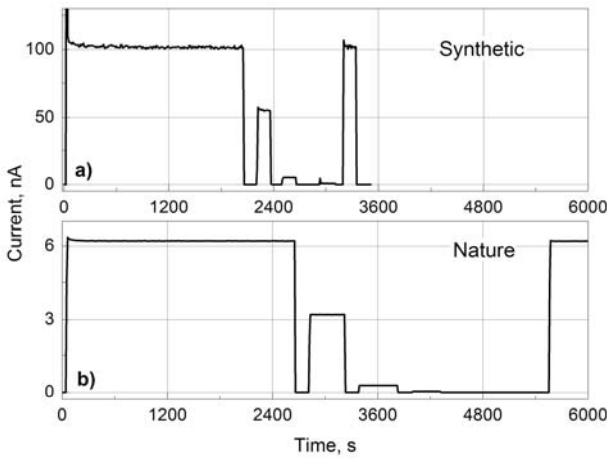


Fig. 1. Temporal dependence of current for several γ -rays ^{137}Cs dose rates for synthetic (a) and natural (b) diamond detectors

Knowledge of the detector dose rate response is of importance for accurate dosimetry. Figure 2 shows such dependences for both types of detectors under the γ -rays irradiation of ^{137}Cs source.

For natural and synthetic diamond detectors this dependence is close to linear and can be approximated by the equation [5]:

$$i = i_0 + RD^\Delta, \quad (1)$$

where i - detector current, i_0 - detector current without irradiation (dark current), D - the dose rate, R - sensitivity, and Δ - linearity index.

Fit of the dependences in figure 2 with expression (1) with fitting parameters R and Δ gives $\Delta = 1,011$, $R = 0,1 \mu\text{C}/\text{Gy}$, and $\Delta = 0,978$, $R = 1,7 \mu\text{C}/\text{Gy}$ for natural and synthetic diamond respectively.

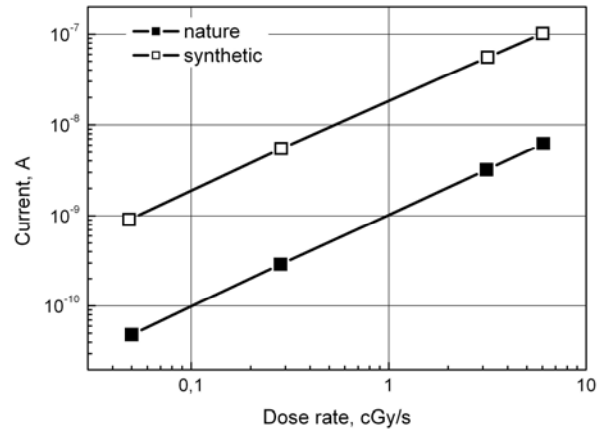


Fig. 2. Dose rate dependence of current for natural and synthetic diamond detectors under γ -rays ^{137}Cs source exposure

The suitability of the synthetic diamond detector for γ -rays registration was investigated by measuring depth-dose curves and profiles in 6 and 18 MeV scanning photon beam of "Varian" linear accelerator. Relative dose rate distribution measurements by both PTW natural diamond and synthetic diamond detectors were carried out in water phantom. Detectors were placed perpendicular to the beam axis.

Depth-dose curve of a 6 MeV photon beam measured by the PTW natural diamond detector is presented in figure 3.

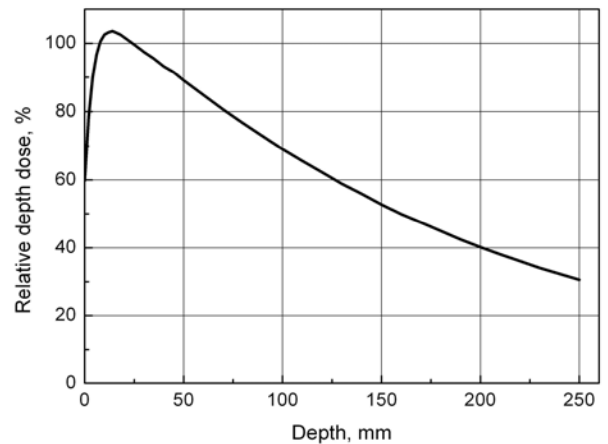


Fig. 3. Depth-dose curve of a 6 MeV photon beam measured by PTW natural diamond detector

It was not possible to obtain such dependence for synthetic diamond detector because of its current exceeds maximum threshold of used PTW registration equipment.

For this reason further dose rate distribution measurements were carried out while detectors were submerged in water phantom on depth of 150 mm.

Radiation field distribution is shown in figures 4 and 5 for natural and synthetic diamond detectors respectively. Parameters of registered radiation field are presented in table 1. As shown in figure 5, synthetic diamond detector measurements with integration time of 0,5 s are characterized by higher signal fluctuations in comparison with natural diamond detector. Such

results are in good agreement with mentioned above signal fluctuations. The same-measurements carried out with integration time of 4,5 s correspond to the reference measurements with natural diamond detector.

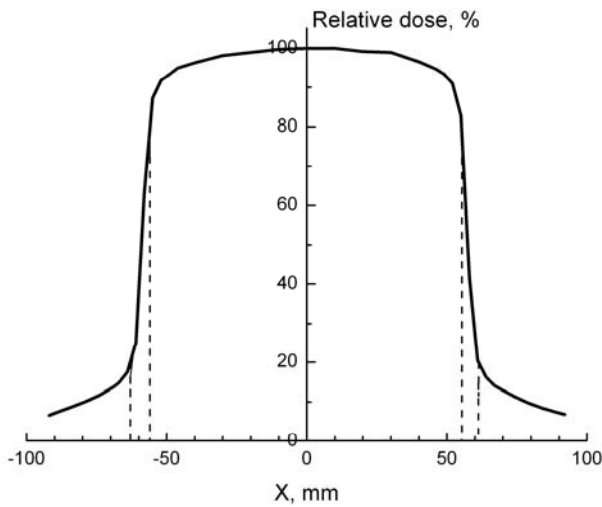


Fig. 4. Profile of a narrow 6 MeV photon beam measured by the PTW natural diamond detector. Integration time is 0,5 s. Field size is 10 cm×10 cm. Depth is 150 mm.

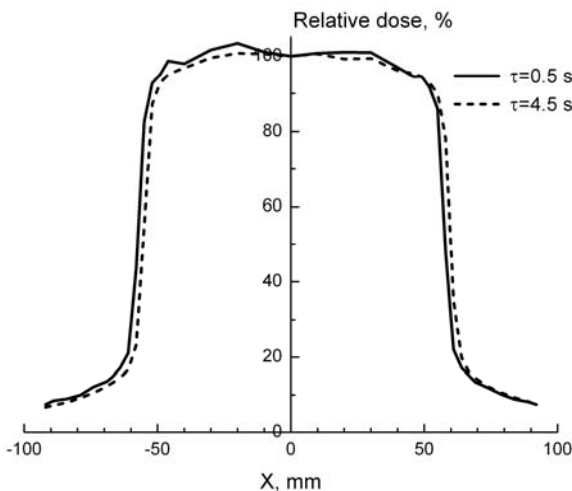


Fig. 5. Profile of a narrow 6 MeV photon beam measured by synthetic diamond detector with integration time of 0,5 s and 4,5 s. Field size is 10 cm×10 cm. Depth is 150 mm.

Table 1. Parameters of a 6 and 18 MeV photon beam measured by both type diamond detectors with various integration time. Field size is 10 cm×10 cm. Depth is 150 mm.

Parameter	γ-rays 6 MeV			γ-rays 18 MeV		
	PTW	Synth		PTW	Synth	
Integr. time, s	0,5	0,5	4,5	0,5	0,5	4,5
Left pen, mm	6,96	6,63	6,82	8,06	8,36	7,71
Right pen, mm	6,83	6,81	6,48	8,37	8,22	8,09
Field width (on 50%), cm	11,49	11,53	11,54	11,5	11,53	11,55
Field heterogeneity, %	3,89	4,51	3,14	2,07	2,76	2,53

Other parameters of a radiating field, such as the field size and penumbras sizes (i.e. the distance between relative dose levels of 80 % and 20 %) have close values for both tested diamond detectors.

4. Conclusion

The presented results indicate that the synthetic diamond detector is comparable with PTW natural diamond detector and can be used for accurate measurements of dose rate distributions with a high dose gradient in high-energy photon beam for a wide variety of applications, especially when high response and high spatial resolution are required.

5. References

1. <http://www.ptw.de>.
2. Marczewska B., Nowak T., Olko p., Gajewski W., Pal'yanov Yu., Kupriyanov I., and Waligorski M.. Synthetic diamonds as active detectors of ionizing radiation. *Diamond and Related Materials*, V. 13, 2004. p. 918-922.
3. Descamps C., Tromson D., Mer C., Nesladek M., Bergonzo P., and Benabdesselam M.. Synthetic diamond devices for radio-oncology applications. *Phys. Stat. Sol. (a)*, V. 203, 2006. p. 3161-3166.
4. The properties of natural and synthetic diamond. Edited by J.E. Field, Academic press, 1992. p. 710.
5. Laub W., Kaulich T. and Nusslin F.. A diamond detector in the dosimetry of high-energy electron and photon beams. *Phys. Med. Biol.*, V. 44, 1999. p. 2183-2192.

CHANGES OF SWIMMER’S BODY TEMPERATURE OBTAINED BY THERMOVISION METHOD

Virgilijus Minialga*, Birutė Statkevičienė**

*Kaunas University of Technology; **Lithuanian Academy of Physical Education

Abstract: The temperature of swimmer’s body changes when he swims certain distance. It can correlate with sportsman’s state. It is essential in cold water and can influence the results of competition. Fast non-contact method for temperature measurement was used for the research. The temperature was measured by thermovision device. It enables to obtain surface temperature in several seconds. The method is based on warm body thermal radiation. The temperature was measured after swimmer covered several distances. Changes of temperature in different parts were different.

Keywords: thermal radiation, temperature measurement, thermovision, body temperature

1. Background of measurements

The temperature of human body can be measured by non-contact method according to the changes of infrared radiation of heated bodies [1].

The total power emitted per unit area R from the body surface depends on temperature T and for black body it can be calculated by equation defined as Stefan – Boltzmann Law [2]:

$$R = \sigma T^4, \quad (1)$$

where σ is called the Stefan – Boltzmann constant is given by $\sigma = 5,67 \cdot 10^{-8} \text{ W m}^{-2} \text{ K}^{-4}$.

According to this law the observed spectral distribution function $R(\lambda)$ of emitted power increases with the increase of temperature.

The total emissive power from a gray (not black) body is smaller than from black body and can be calculated by empirical law [2]

$$R = e \sigma T^4, \quad (2)$$

where $e < 1$ is called the emissivity of gray body. It is particular for every different body and should be measured or evaluated for every different surface.

The power radiated from the body under the investigation in a thermovision device is evaluated according the above mentioned laws. It calculates the temperature of remote body and shows it on the device monitor. The newest devices show the temperature distribution in different colors according to the temperature-color scale.

2. Measurements of human temperature

The device Flir i5 was used for investigation the temperature of swimmer’s body. Infrared radiation images are shown on the device’s monitor. These photos can be transformed to the computer for the further usage.

They are colored in artificial colors for better comprehension. The colors in different photos mean the different temperature values, e.g. red color in the first photo can mean 23°C and the same red color can mean 30°C in the second photo. Therefore color-temperature accordance in the bottom of monitor should be observed. The temperature of central part of image is written in the upper left corner. The error of device is 0.1°C . However one must know that human body is not a black body. The emissivity e in equation (2) should be taken into account.

The situation during measurements is shown in Fig. 1.

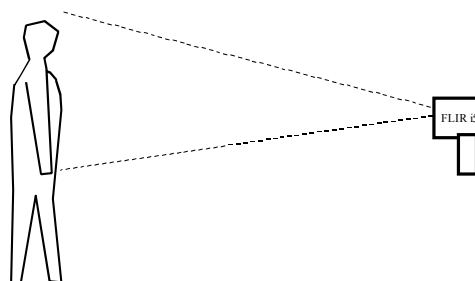


Fig. 1. Scheme of taking humans body infrared images

3. Conditions for infrared images

Water is not transparent for infrared radiation, the same is for window glasses. Therefore there is no possibility

to take infrared photo of person during swimming. Some additional errors are in case of wet bodies. Several series of thermal images were taken for investigation of temperature changes on the swimmer's body. All photos were taken of persons in bathing suits. Skins in images were dry in some photos and wet in the others.

4. Temperature measurement results

The experiment of some load influence was carried out. The first set of infrared photos was taken of dry swimmer before the start. One can see that the highest temperatures according to the temperature lines in each image are in front of the upper part (36°C). The lowest temperature is in legs region (34°C). Fig. 2 represents swimmer ready to the start, the glasses seem to be cool. This is because they are not transparent for infrared radiation.

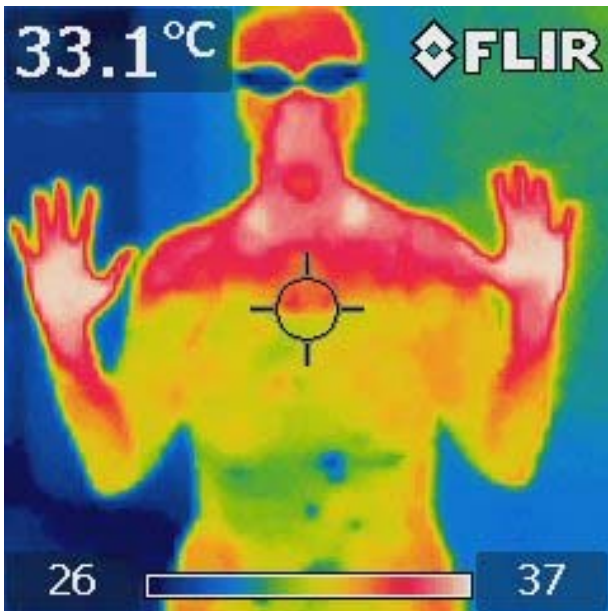


Fig. 2. Swimmer is ready for the start; glasses are not transparent for infrared radiation and seem as being cool (dark in the image).

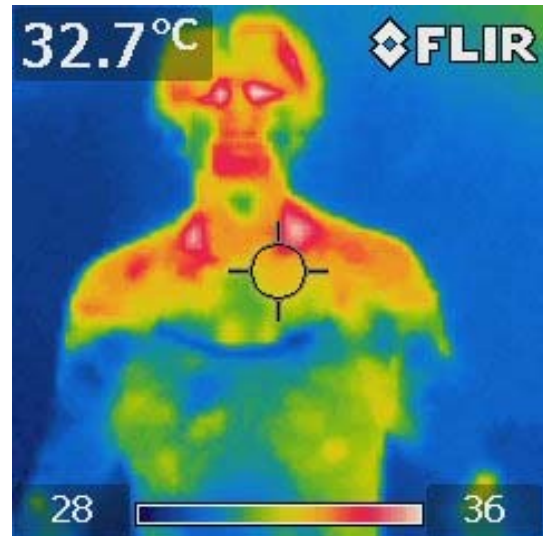
Infrared photos of swimmers body before the start in front of the person and in back of the person are shown in Fig. 3. Measurements of the temperature were carried out using the above mentioned photos.

Photos taken after 50 m of swimming distance show that skin temperature is reduced (Fig.4). Measured temperatures of swimmers body are lower than in the first case by 1°C – 2°C. Photos taken after 200 m of swimming distance show that measured temperatures of swimmers body are lower than in the first case by 1°C – 2°C.

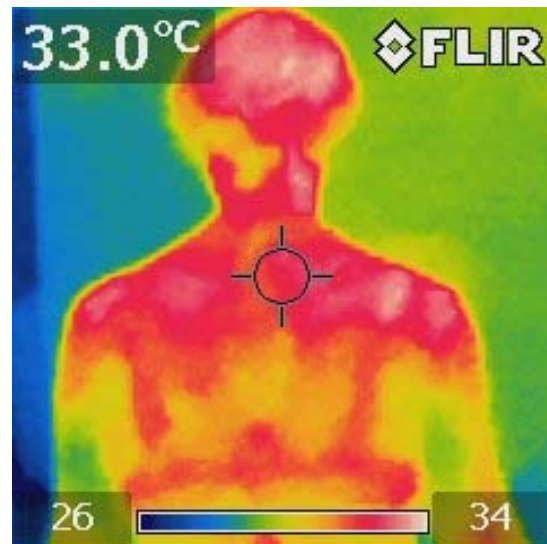
The research of infrared pictures allow to conclude that the temperature distribution on the surface of body after 200 of swimming distance is of higher contrast (Fig.5). This means that only narrow regions of human body have comparatively high temperature. Temperature of those places does not change considerably, it reduces only by several degrees. The

highest temperature after swimming remains on the head, on the shoulders, on the spine, on the knee, on the shin's surfaces.

Graphs in Fig.6 show that the main decrease of the temperature with distance is on the upper part of the swimmers body. The temperature on the biceps surface

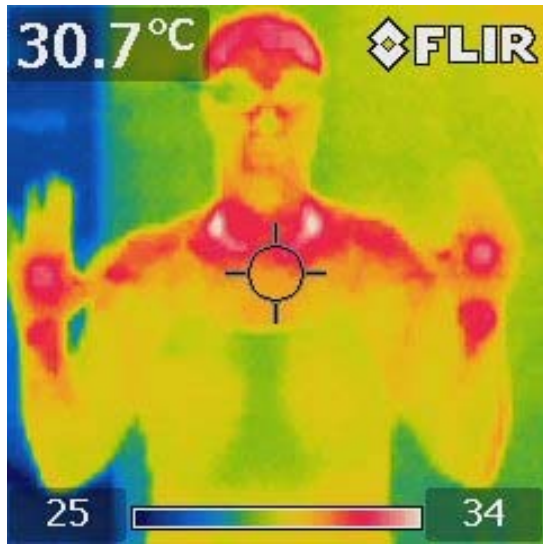


a)

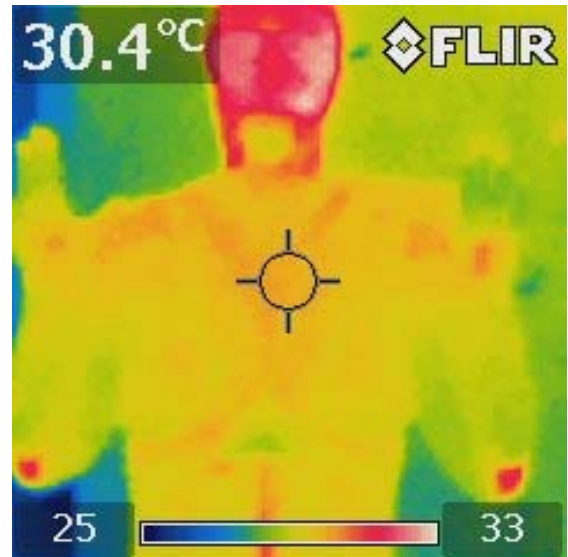


b)

Fig. 3. Infrared photos the upper part of the swimmer's body before the start; a) the front of the person; b) the back of the person.

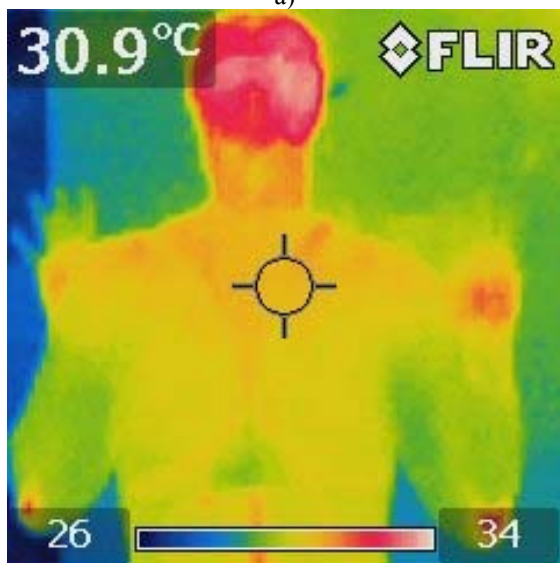


a)



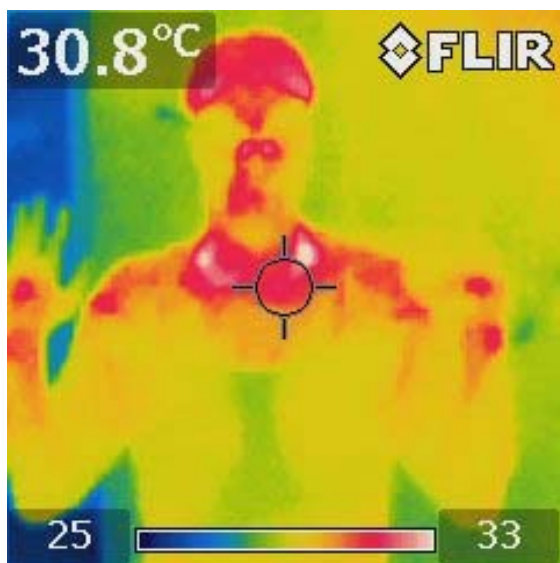
b)

Fig. 5. Infrared images of the upper part of the swimmer's body's after 200 m distance.



b)

Fig. 4. Infrared images of the upper part of the swimmer's body's after 50 m distance



a)

is approximately constant, the nose and chin surface temperature decreases relatively considerably after 50 m distance and increases slightly after 200 m distance. Graphs in Fig.7 show that temperature on the lower part of swimmers body is approximately constant after swimming distance. The temperature on the surface of thigh slightly increases, on the surface of shin slightly decreases and on the surface of knees is several degrees higher and slightly decreases. Graphs in Fig.8 show that temperature on the central part of swimmers body is approximately constant with distance. E.g., this is true for abdomen. The temperature on the surface of spine decreases with distance permanently and on the surface of buttocks a bit increases.

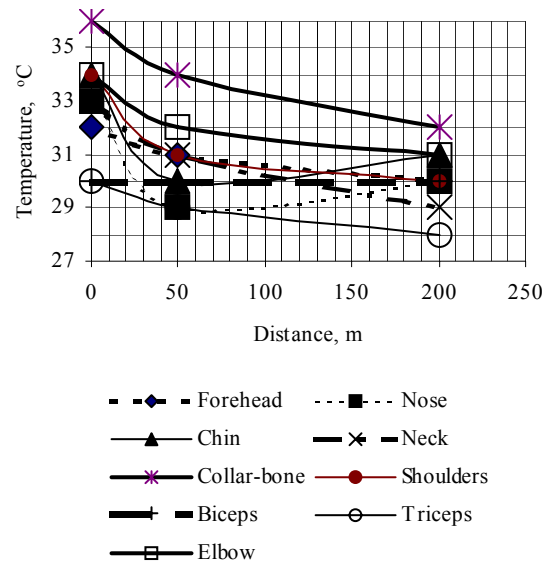


Fig. 6. Changes of the temperature on the upper part of the swimmer's body

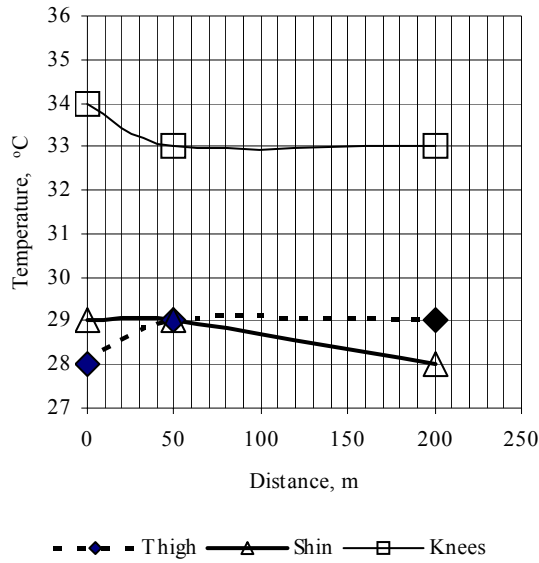


Fig. 7. Changes of the temperature on the lower part of the swimmer's body

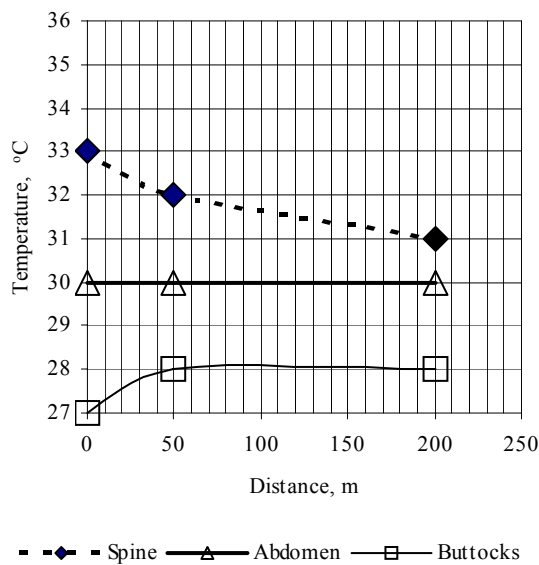


Fig. 8. Changes of the temperature on the central part of the swimmer's body

5. Conclusions

Temperature of swimmer's body surface falls by several degrees after swimming in swimming pool for short distances (e.g. 50 m). It changes not significantly for the longer distances.

Reduction of temperature is observed on the upper part of swimmer's body after swimming in swimming pool. The temperature changes slightly on the surface of the central part and the lower part. At some points it seems that the temperature increases after physical load or remains the same.

The temperature distribution becomes of higher contrast after longer distances, the regions of higher temperature include smaller area.

The head, shoulders, spine, knee and shin's surfaces have the highest temperature after swimming.

Water layer and covers of glass sheets change emission of infrared radiation and can cause errors in temperature measurements.

6. References

1. Coh M., Sirok B. Use of thermovision method in sport training. *Facta Universitatis; Series: Physical Education and Sport*, Vol.5, N 1, 2007, p. 85-94.
2. Bransden B.H. and Joachain C.J.. *Physics of atoms and molecules*. 2nd ed., Harlow, Pearson Education Limited, ISBN 0582 35629 X, 2003, p. 9-10.

IGNALINA NUCLEAR POWER PLANT DOSE MONITORING SYSTEM

, Oleg Klepalov, Kęstutis Gediminskas *, Romas VILKAS *, Mindaugas ZIKAS *, Gediminas ADLYS *
* Kaunas University of Technology
**Ignalina Nuclear Power Plant

Abstract: The occupational exposure control is one of the important problem ensuring safety of personnel during operation of nuclear power plant.

The TLD-system RADOS was set into operation in December of 1994. The software of this system ensured data interface between new system and existing database of INPP and provided a multi-user mode of data access.

As a next step for the upgrading of the personal dosimetry system and preventing the overexposure of personnel in NPP a new electronic dosimetry system using RAD-80 and RAD-51 dosimeters was implemented in 1997. Moreover the dynamic exchange of personal exposure from the electronic dosimetry data allowed planning the dose budget more exactly during implementation of different kinds of activities (especially during maintenance period).

Analysis and comparison of data obtained using both dosimetry systems has shown that in general the parallel application of the TLD-system and electronic dosimetry system allowed to improve the quality of dose reduction measures, which represented the effectiveness of the implementation of ALARA program in NPP.

Keywords: personal dosimetry system, TLD, dose monitoring, ALARA

1. Introduction

The first unit of Ignalina NPP went into service at the end of 1983, the second unit was set into operation in 1987. Their design lifetime was projected out to 2010 - 2015. A total of four units were originally planned on this site.

The Ignalina NPP contains two RBMK-1500 reactors. This is the most advanced version of the RBMK reactor design series. Compared to the Chernobyl NPP, the Ignalina NPP is more powerful (1500 MW versus 1000 MW), and is provided with an improved ACS (Accident Confinement System).

Data base of Ignalina NPP consists of data on about 3500 persons, therefore the problem of duly and correct record-keeping of the personnel occupational exposure data and management of personal doses is one of the important problems ensuring safety of personnel during operation of the plant.

During first years of the INPP operation film dosimeters of type IFKU were used for the monitoring of personnel occupational exposures. However the old system had several essential imperfections, such as:

- low range of measurement (0.5 – 20 mSv);
- special conditions for processing the dosimeters were required;
- possibility to lose data if the film is spoiled by light or by heat;

- automatic registration and transmission of the data was not provided etc.

It was clear that some measures to improve the existing personal dosimetry system have to be considered taking into account the growing strictness of requirements and international recommendations that occupational concerning personnel exposure.

The first step for improving the personal dosimetry system at INPP was made in 1989. In this year INPP started to use new type of TL dosimeters with Al₂O₃ detectors. These dosimeters had a number of advantages as compared to film dosimeters:

- wider range of measurement (0.1-10⁴ mSv);
- stable sensitivity;
- mechanical durability.

Besides after modernization of the dosimeter processing unit the possibility to transfer data from the measurement unit to a computer was provided, that made the creation of the exposure database for NPP workers possible. However this system had some weaknesses too: very high photosensitivity of detectors, manual processing were the main problems using this system.

To overcome the above mentioned problems the project for the developing and improvement of the personal dosimetry system in INPP was initiated in 1994 within the framework of the "Bilateral Technical Assistance Program between Sweden and Lithuania in order to enhance the radiation protection safety at Ignalina NPP".

2. Personal dosimetry system

The TLDs most commonly used in medical applications are LiF:Mg,Ti, LiF:Mg,Cu,P and Li₂B₄O₇:Mn, because of their tissue equivalence. Other TLDs, which are used because of their high sensitivity, are CaSO₄:Dy, Al₂O₃:C and CaF₂:Mn.

TLDs are available in various forms (e.g. powder, chips, rods and ribbons).

A basic TLD reader system consists of a planchet for placing and heating the TLD, a PMT to detect the thermoluminescence light emission and convert it into an electrical signal linearly proportional to the detected photon fluence and an electrometer for recording the PMT signal as a charge or current. A basic schematic diagram of a TLD reader is shown in Fig. 1. TLD-system which is used at Ignalina NPP is presented in Fig.2.

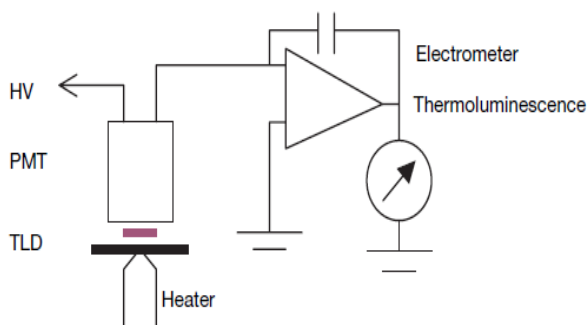


Fig.1. TLD reader.

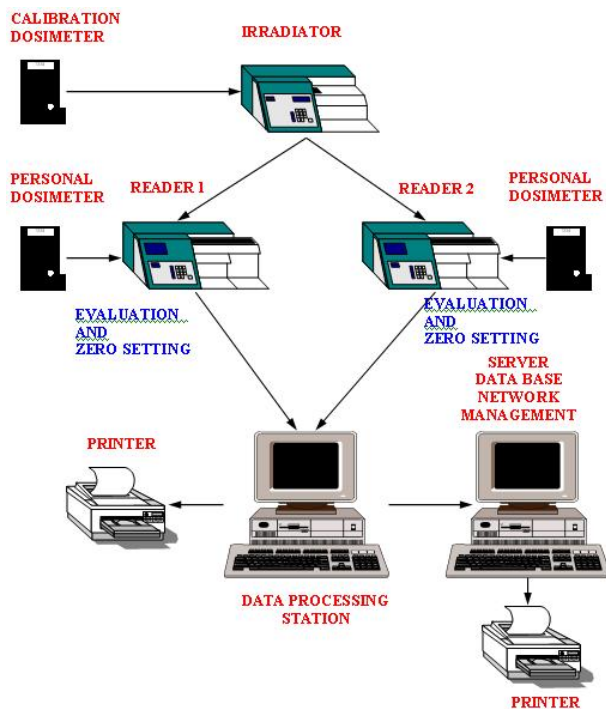


Fig.2. Schematic diagram of the TLD system "RADOS" in Ignalina NPP.

External exposure of personnel in the reference year was controlled once a month using thermoluminescent dosimeters.

Control of the external exposure of personnel working under hazardous conditions was performed using both: thermoluminescent and electronic RAD dosimeters at the same time. The staff was allowed to work in a controlled area, presuming a dose of 0.2 mSv per day if, the difference between the collected individual dose and annual dose limit did not exceed 5.0 mSv after the work. If the difference between the collected individual dose and the annual dose level did not exceed 3.0 mSv, the staff was allowed to work under hazardous conditions, accounting 0.05 mSv per day.

In 2008 individual dosimetric control was carried out for 3599 workers. 2320 workers of the NPP staff and 1279 workers from contractor's organization staff (CO).

3. Results

The average individual dose of 0.91 mSv was estimated to CO + INPP personnel in 2008: 0.96 mSv for NPP personnel and 0.83 mSv for the personnel from contract organizations (Fig.3). Maximum individual dose for INPP staff was 18.09 mSv, maximum dose to sole worker from the contractor organization was 19.98 mSv.

Data on the number of investigated workers and received collective doses are provided: for 2008 - in Table1; for the whole period of operation of Ignalina NPP -in Fig.4.

1. Table. 2008 Ignalina NPP and contractor's organization personnel irradiance indicators.

Doze range, mSv	INPP		INPP + RO	
	The number of people, people.	Collective dose, people·mSv	The number of people, people.	Collective dose, people·mSv
0,0 - 0,5	1824	85,34	2973	117,70
0,5 - 1,0	91	65,44	120	87,23
1,0 - 5,0	266	678,91	302	743,88
5,0 - 10,0	79	535,91	88	607,55
10,0 - 15,0	33	405,51	54	664,17
15,0 - 17,0	18	286,20	32	512,48
17,0 - 18,0	7	122,76	14	246,30
18,0 - 20,0	2	36,10	16	307,89
20,0 - 25,0	-	-	-	-
25,0 - 50,0	-	-	-	-
Controlled the number of employees, people..	2320		3599	
The collective dose value, sq·MSV	2216,17		3287,20	
Average dose, mSv	0,96		0,91	
The maximum dose value, mSv	18,09		19,98	

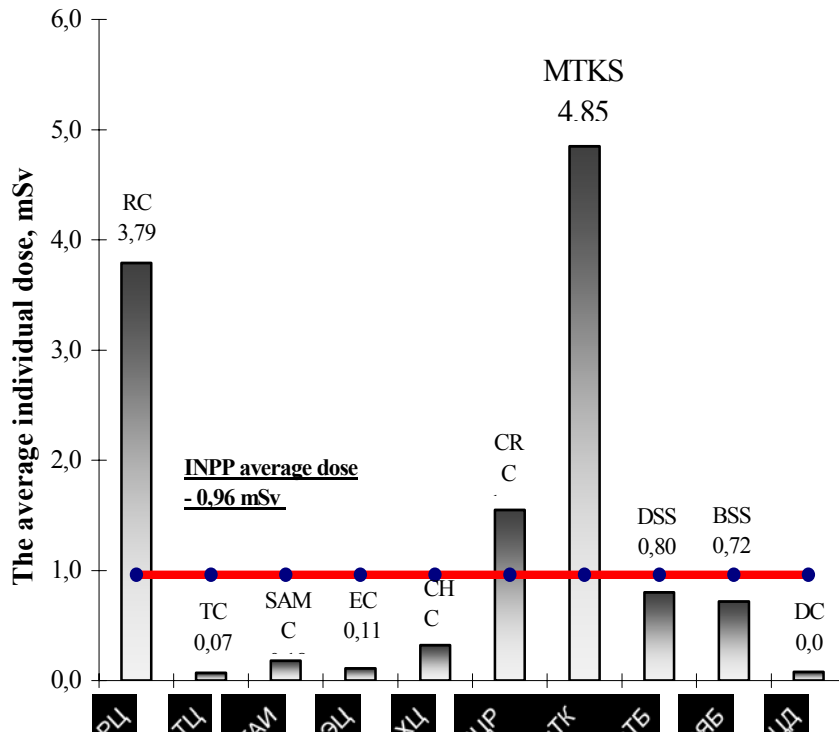


Fig. 3. Average individual doses in INPP in 2008.

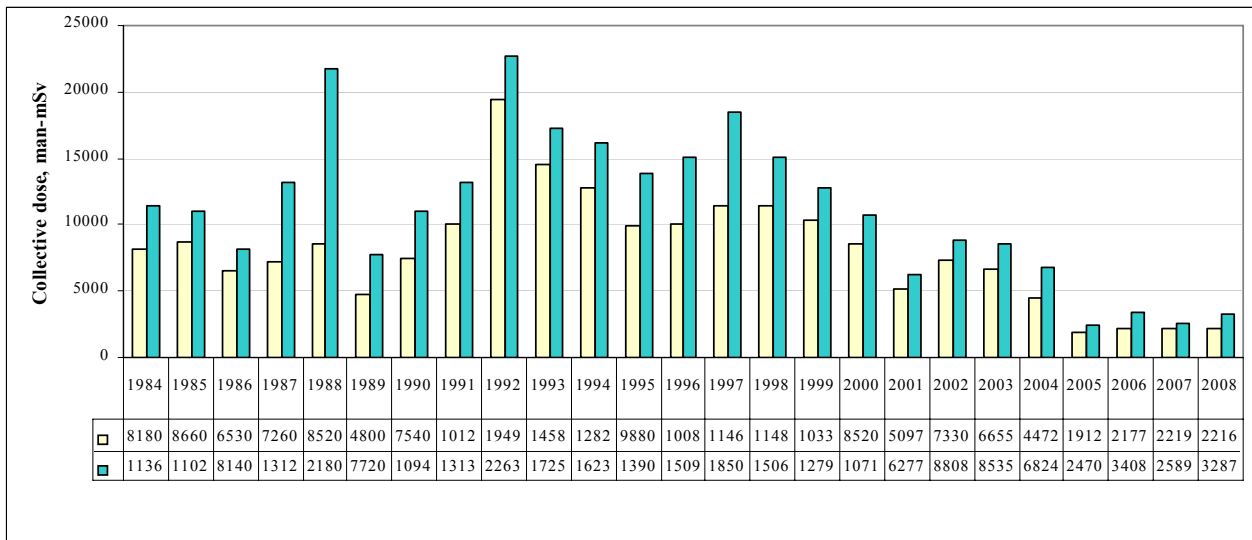


Fig. 4. Annual collective doses to workers of the Ignalina NPP.

4. Conclusions

The installation of two described dosimetry systems allowed to improve the quality of measures that have to be considered implementing ALARA program. Performance measures which were undertaken within ALARA program in Ignalina NPP allowed to achieve 3287.2 man-mSv collective dose to the INPP + CO staff in 2008. This represents 74% of planned annual dose: Collective dose to the INPP staff was 2216.2

man-mSv, instead of planned 3327 man-mSv in 2008 Planned. Collective dose to the staff from contractor organization was 1071.0 man-mSv as compared to the planned 1100 man-mSv.

4. References

1. K. Almenas, A. Kaliatka, E.Ušpuras. Ignalina RBMK-1500. A Source Book. 1998.

APPLICATION OF NEUTRONS IN RADIOTHERAPY

Gediminas ADLYS
Kaunas University of Technology

Abstract: An overview of neutron application for medical purposes from technological and physical point of view is presented in this article. It discusses the features of fast neutron therapy, neutron capture therapy and production of radionuclides by means of neutron activation and analyzes the requirements for neutron beams which are produced using different sources (nuclear reactors, accelerator driven systems neutron spallation sources).

Keywords: neutron therapy, neutron sources, reactors, spallation sources

1. Introduction

Advance of science and technology continually find its place in medicine practice. Soon after X-rays discovery it was used for diagnostics and therapy and it continues until now. Improvements in radiotherapy results were noted with each technological advance. The field of radiation therapy began to grow after discovery of the radioactive elements polonium and radium. Radium was used until the cobalt and caesium teletherapy machines came into use. Nowadays, these units are being replaced by linear accelerators, working without radioactive sources, which makes them safer in the radiological point of view.

With invention of computed tomography three-dimensional planning became a possibility. It allows more accurate determination of the dose distribution using images of the patient's anatomy.

Construction of superconducting magnets and progress in cryogenic technique was applied developing nuclear magnetic resonance equipment for new imaging modalities. Advance in nuclear and particle physics technologies was basis for the positron emission tomography.

The development of high power compact accelerators such as radiofrequency quadrupole linacs or cyclotrons creates the possibility to use neutron related techniques in medicine at reasonable cost. In proton accelerators accelerated protons could be used for proton therapy or for the bombardment of the proper target, which releases neutrons of sufficient energy to treat tumors at the modest tissue depths.

Additionally, research nuclear reactors are used as neutron sources for producing radionuclides for medicine and for direct neutron therapy as a part of radiation therapy.

Recently attention of radiotherapists is paid to the new developing branch of nuclear physics and technology – nuclear spallation neutron sources.

2. The place of neutrons in radiotherapy

Radiation therapy is the medical use of ionizing radiation primarily in the treatment of malignant tumor.

The biological response of a cancer cells to ionizing radiation is described by its radiosensitivity. The types of cancer are classified as "radioresistant"; if tumors do not respond well to low LET radiation [1]. Highly sensitive cancer cells are rapidly killed by modest doses of radiation while radioresistant cancer cells require much higher doses for radical cure than may be safe in hospital practice. The majority of epithelial cancers are only moderately radiosensitive, which require 60-70 Gy dose of radiation to achieve a radical cure.

Radiation therapy of cancer is based upon the basic effect of ionizing radiation to destroy the ability of cells to divide and grow by damaging their DNA strands. The damage is caused by a photon, electron, proton, neutron or ion beam. It is done directly or indirectly ionizing the atoms of the DNA chain. For photon, electron and proton beam the damage is caused as a result of atomic interactions. It entails primarily the ionization of water, forming free radicals, notably hydroxyl radicals, which then damage the DNA. With neutron radiation the damage is caused by nuclear interactions. Cells have mechanisms for repairing DNA damage. If radiation is delivered in small sessions, normal tissue will have time to repair itself. Tumor cells typically lack effective repair mechanisms compared to most healthy cells and are generally less efficient in repair between fractions. It is one of reasons why the total dose is spread out over time or fractionated. Accumulating damage to the cancer cells causes them to die or reproduce more slowly.

Photon, electron and proton radiation are called low linear-energy-transfer (LET) radiation. Neutrons are high LET radiation. If radioresistant tumor cell is damaged by low LET radiation it has a good possibility

to repair itself and continue to grow. With high LET radiation such as neutron radiation, the probability for a damaged tumor cell to repair itself is very small. This difference is quantified by the relative biological effectiveness (RBE). For neutrons it is the ratio of the doses of a reference radiation, usually X-rays and neutron radiation required to produce the same biological effect.

For radiation protection purposes, the International Commission on Radiological Protection, ICRP, has described the biological effectiveness of radiations by a series of Quality Factors (ICRP 1977) and by a series of radiation weighting factors (ICRP 1991). The Commission chose a value of 1 for all radiations having low LET, including X-rays and gamma radiations of all energies. According to the existing ICRP system, the radiation weighting factors for neutrons are from 5 to 20 in dependence on neutron energy. In medical practice radiation weighting factor of 3 is used [2] for neutrons. It means that using neutrons required tumor dose is about one-third the dose required for photons or electron treatment. A full course of fast neutron therapy is delivered in only 10 to 12 treatments, compared to 30-40 treatments needed for low LET radiation.

It was discovered, that radiations with a high linear energy transfer (LET) including fast neutrons are less dependent than X-rays on the presence of oxygen to produce cell death [3]. It is so-called oxygen effect. Low LET radiation damage is caused mostly by indirect biochemical action, formatting of free radicals that damage the DNA. The presence of free oxygen is required to facilitate this radiation damage. In the absence of oxygen the effect of indirect action is limited [4]. Proliferating tumor cells can reduce the blood supply to the centre of large tumors. It is reason way many tumor contained zones have a very low oxygen tension. Cells that lack oxygen are therefore resistant to low LET radiations. It causes radio-resistance of cancer and failure of treatment when conventional radiation therapy with X-rays is used. To overcome this problem, high pressure oxygen (HPO) is used in experimental radiotherapy. Gray and his associates made the observation in 1953 [3], that the radiation effect on living cells in anoxia rapidly increases with oxygenation until it reaches a near maximum effect (40 mm Hg in normal capillaries and tissues). Further increase in oxygenation does not appreciably increase the radiation effect in normal tissues. The influence of oxygen on radio-sensitivity is expressed as the ratio of the dose needed to produce a given degree of damage when cells are anoxic at the time of irradiation to that which suffices to produce the same damage when cells have ample oxygen available [4]. The most practical method of raising oxygen tension in malignant cells was to raise the partial pressure of oxygen in the respired air. This proved difficult to administer because patients had to be placed for long durations within HPO tanks and reduced choice of angular beam arrangements. Alternative to HPO was to use high LET radiations such as fast neutrons. It was realized using cyclotrons to accelerate protons onto beryllium targets to produce fast neutrons

of 7-10 MeV energy. The main therapeutical effect was achieved due to the recoiling protons and heavier recoiling nuclei, which increased number of ionization events along their tracks.

3. The fast neutron therapy

The fast neutron therapy is based on fast neutron ability to penetrate deeply in to the tissue. More than 20 neutron therapy centers in the world apply these techniques for treating oncology patients [5].

The dose distribution of high energy neutrons is similar to those of high energy X ray beams [4]. An additional advantage of fast neutron therapy lies in the overall treatment time. When damage to cell is minimal, the cell can recover following removal of the damaging stimulus (sub-lethal cell damage). Neutron therapy can be delivered in much fewer fractions and sub-lethal damage can be reduced.

Fast neutron beam therapy is more effective in soft tissue and bone sarcomas [6] and is superior to photons in high-grade, locally advanced prostate cancer treatment. Side effects for fast neutron therapy are similar to those of low LET therapy. Careful, computerized treatment planning minimizes effects on normal tissues. Most of the acute side effects are temporary and normal tissue recovery occurs with time. Promising development for neutrons is neutron capture therapy (NCT).

4. The neutron capture therapy

The neutron therapy is presently realized in two versions: fast neutron therapy and neutron capture therapy (NCT) [2]. NCT idea was proposed in 1936, 4 years later after neutron discovery. Radionuclide with a large absorption cross-section for thermal neutrons is introduced into the patient's body mainly through the blood. Reaction products created during neutron irradiation of patient are affecting tumor cells.

The nuclides used for a neutron capture therapy are boron and gadolinium at present time.

Naturally occurring stable isotopes of boron are ^{10}B (19.9 %) and ^{11}B (80.1 %). Gadolinium has 7 naturally occurring stable isotopes. The isotope mass distribution is shown in Fig. 1.

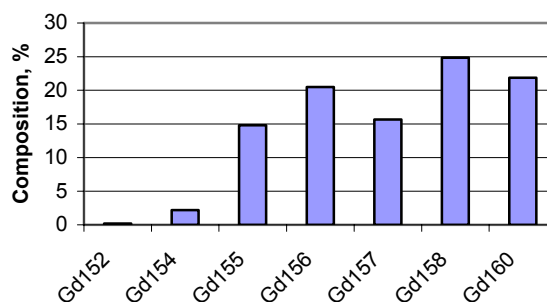


Fig.1. Composition of naturally occurring gadolinium isotopes

The values of total cross-section for stable boron and gadolinium nuclides corresponding to three different neutron energies are presented in Table 1.

Table1. Total cross-section values, barns (1 b = 1·10⁻²⁴ cm²)

Nuclide	Thermal neutrons 0.025 eV	Fission neutrons	Fusion neutrons, 14 MeV
B10	3840	2.638	1.467
B11	5.05	2.425	1.415
Gd152	1070	7.003	5.699
Gd154	92.35	6.981	5.697
Gd155	60948	6.981	5.694
Gd156	6.995	6.983	5.694
Gd157	255085	6.979	5.696
Gd158	6.354	6.978	5.694
Gd160	4.904	6.983	5.699

It is clearly seen that the biggest neutron interaction cross-section is for thermal neutrons (first column) interacting with nuclides ¹⁰B, ¹⁵⁵Gd, ¹⁵⁷Gd.

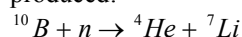
The reaction products are gamma photons, protons, alpha particles. The corresponding reactions are (n,γ), (n,p), (n,α). The values of above-mentioned reactions cross-sections for thermal neutrons are presented in Table 2.

Table2. Reaction cross-section (0.025 eV), barns

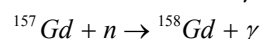
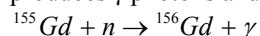
Reaction	B10	Gd155	Gd157
(n,γ)	5.00E-03	60889	254078
(n,α)	3.84E+03	8.18E-05	4.78E-04
(n, p)	3.00E-03	0	0

Analysis of reaction cross-section values and comparison with values of total cross-section shows that for ¹⁰B nucleus alpha particle emission has 99.9 % probability and very small gamma photon and proton emission probability.

During the neutron capture reaction nucleus of Boron ¹⁰B absorbs neutron and two charged particles are produced:



Inverse situation is for thermal neutron capture by Gadolinium reaction. Probability of alpha emission during reaction with neutrons is very small. Almost all reactions are radiative neutron absorption which produces γ photons and higher gadolinium isotopes:



New reaction products ¹⁵⁶Gd and ¹⁵⁸Gd are stable.

At present, the most studied and used in clinical practice is Boron neutron capture therapy (BNCT). This method is based on the radiation damage produced by high LET particles (α and ⁷Li) emitted in the ¹⁰B neutron capture reaction: ¹⁰B(n,α)⁷Li. The total kinetic energy of charged particles produced is approximately 2,4 MeV. A range of these charged particles in a tissue is

approximately of the order of the size of tumor cell. These high linear energy transfer particles dissipate their kinetic energy in the cell. As a result, the cell comprising ¹⁰B during neutron irradiation is effectively destroyed. Because of higher concentration of ¹⁰B isotope in the tumor cells mainly the cancer cells are destroyed. Thus, the basic idea of BNCT is that a neutron „finds“ out the tumor cells and destroys them [4]. Therefore, selective delivery of boron and high accumulation into tumor tissue achieving the range of 20-35 μg g⁻¹ are the most important requirements for efficient neutron capture therapy of cancer [7]. It could be realized using specific borated compounds. ¹⁰B isotope compose only one fifth from total naturally occurring boron mass. Therefore the boron containing compounds are ¹⁰B enriched and synthesized. If introduces into the patient's blood this compound produces ¹⁰B isotope in the tumor cell with a concentration of 30 μg g⁻¹ while the concentration of boron in surrounding normal tissue cells is approximately 10 μg g⁻¹ [2].

5. The requirement for the neutron beam for neutron therapy

The use of boron neutron capture therapy (BNCT) for the treatment of deep-sealed tumors requires neutron beams of suitable energy and intensity [8].

The thermal neutrons are most intensively absorbed by ¹⁰B, but they weakly penetrate the tissue and therefore produce the major radiation load on the surface layers, primarily on the skin. If the cancer tumor is located under the normal tissue at the depth of 30-70 mm, neutron energy should be ranged from 1 eV to a few tens of keV [8]. This is the energy range of epithermal neutrons, just above thermal. Epithermal neutrons passing through the normal tissue layers are slowing down, gradually establishing thermal equilibrium with a tissue. It results in the peak of the thermal neutron flux in the deep tissue and could provide the maximum of absorbed dose in the irradiated deep scatter tumors.

Fast neutrons as compared to epithermal neutrons produce radiation effects in the tissue by recoiling protons and have no selective character.

The required absorbed radiation dose in a single treatment and desirable exposition duration are the factors for choosing of the intensity of a neutron beam. It was shown [8] that for 10 min exposition, for attaining an absorbed dose of 20 Gy in the tumor with the ¹⁰B concentration of 30 μg g⁻¹ the required epithermal neutron flux has to be from the range of (0,5-1)·10¹⁰ cm⁻² s⁻¹. If neutron flux is reduced than to attain the same absorbed dose it is possible by an increase in ¹⁰B concentration in the tumor or by the extension of the irradiation time. However it is to point out, that the absorbed dose produced by fast neutrons and by accompanying gamma-rays should non exceed 10 % of the therapeutical dose, i.e. 2 Gy.

The neutron spectrum for fast neutron therapy should be similar to the neutron spectrum of uranium fission [2]. In this case a fraction of neutrons with the energy over

100 keV in the beam would be 90 %, the neutron flux on the collimator output - approximately $1 \times 10^9 \text{ cm}^{-2} \text{ s}^{-1}$. The dose produced by an accompanying gamma radiation could reach 50 % - level of the total dose [2].

6. The neutron sources for therapy

In clinical practice, basically powerful cyclotrons or nuclear reactors are used as neutron sources. Wide utilization of such facilities is limited by high construction and maintenance expenses and nuclear safety reasons.

The initial clinical studies in boron neutron capture therapy were carried out with fission reactor produced neutron beam of thermal neutrons [9].

The nuclear reactor is the most powerful stationary source of neutrons. At 1 MW heat power in the reactor core, approximately 10^{17} neutrons s^{-1} are produced. It is quite natural that the beams of the reactor neutrons have been used for the NCT and FNT purposes. There are still some active operating therapeutical beams produced in nuclear reactors of various kinds and powers in the world.

Another approach to using fission reactors has been based upon the use of a fission converter which converts a reactor's thermal neutron to fission neutron beams. This approach could be especially useful for the adaptation of the existing medium power multipurpose reactors for neutron capture therapy.

Modification of existing reactors, new reactors designed specially for BNCT and accelerator based sources would all have to be considered to meet the increased need for neutron therapy.

The MTR reactor designed for medical research has a power of 10 MW. Some other reactors developed as sources of neutrons for NCT have a power ranging from 5 to 20 MW.

A BNCT treatment facility is in use at the VTT Chemical Technology's FiR-1 research reactor facility (250 kW Triga reactor) in Espoo, Finland [10]. The neutron beam from the reactor is moderated into the epithermal (0.5-10 keV) energy range in the aluminiumfluoride-aluminium layers.

Despite the nuclear reactor in its stationary regime of operation has a constant power level and the beam composition thereby providing standard expositions, a powerful reactor is a very complex and expensive facility whose maintenance demands quite strong requirements for nuclear safety. With quite a rare exception, the cancer therapy centers and clinics are usually remote from the physics centers having nuclear reactors.

The development of accelerator based neutron sources (ABNS) has been of interest for almost three decades [11]. The main goal of all the investigations was and is to create ABNS that will produce epithermal beams with a sufficient flux of neutrons and energy spectrum as those produced by nuclear reactors and to secure more clinically friendly environment for the treatment of patients than the environment at a nuclear reactor facility is.

Nuclear reactions on light nuclei are supposed to be used for the production of neutrons. In some clinics neutron generators based on $T(d,n)^4\text{He}$ fast neutron sources are used [12]. However wide use of neutron generators is limited due to a strong regulation on high-activity tritium target application.

Experimental results specifying neutron yield data from thick target on accelerator-based neutron source show that the most prospective reactions considered for the fast neutron therapy are: ${}^7\text{Li}(p,n){}^7\text{Be}$, ${}^7\text{Li}(d,n)2{}^4\text{He}$ and ${}^9\text{Be}(d,n){}^{10}\text{B}$.

Protons or deuterons with energies up to 2-2.5 MeV are needed for the obtaining of neutrons.

Accelerator driven system (ADS) is one of the most promising concepts under development [13].

Initial goal of this concept is nuclear waste transmutation and energy amplification, but the progress in this research field will be useful also for medical purposes, especially looking for new neutron sources.

Energy amplifiers are subcritical systems, driven by a proton accelerator for energy extraction from components of spent nuclear fuel. The high energy protons from the accelerator hit the spallation target and generate some 20-40 neutrons per proton by spallation phenomena. The generated spallation neutrons drive the reactor to produce power under sub-critical conditions.

The power of such a hybrid system is regulated via the proton current intensity of the accelerator. Studies by Nobel Laureate Carlo Rubbia and his co-workers have shown that using investigated experimental hybrid systems it would be possible to achieve reactor power of 1500 MW, if an accelerator which is able to accelerate protons to 1 GeV (1000 MeV) and generate a proton current intensity of 10-20 mA would be in operation [14]. Even higher proton current intensities (100 mA and more) are pointed out by the other designer groups, [15].

ADS consist of three main components: the accelerator, the spallation target and the subcritical reactor.

Usually spallation target as a neutron source and a promising tool for medical applications represents a heavy material of high atomic number (Z) or high (N/Z) ratio, like a lead or lead bismuth eutectic (LBE).

In medicine, radioactive elements are increasingly used for diagnosis, therapy and pain relieving [16]. These elements can be produced through neutron capture on stable elements in an accelerator driven activator, as an alternative to reactor production exploiting the process called Adiabatic Resonance Crossing (ARC). The ARC concept was first proposed by Carlo Rubbia for the transmutation by neutron capture of long-lived nuclear waste, and for radioisotope production for nuclear medicine applications [17]. The ARC effect is based on the fact that elements to be activated have large capture resonances at energies of a few eV. Another factor is that the high energy neutrons in a medium with high atomic number, low absorption cross-section and high elastic scattering cross-section are slowed down through a sequence of a large number of elastic collisions and with low energy loss per collision. In this way most fast neutrons reach the epithermal region. The epithermal

neutrons effectively reaches the energy range containing the neutron capture resonances of target nuclide and have a high probability to be captured by the materials to be activated. This phenomenon is converse to neutron slowing down physics in nuclear fission reactor. The strong interest is induced by perspectives of European spallation source in Sweden [18]. It can be good possibility for collaboration in neutron therapy too.

5. References

1. B. Jones, R. G. Dale, A. Carabe-Fernandez. Charged particle therapy for cancer. *Applied Radiation and Isotopes* 67 (2009) p. 371-377.
2. B.F. Bayanov, V.P.Belov et al., Accelerator based neutron source for the neutron-capture and fast neutron therapy in hospitals. *Nuclear Instruments and Methods in Physics Research A* 413 (1998) 392-426.
3. J.B. McEwen. Clinical trial of radiotherapy and high pressure oxygen. *Annals of The Royal College of Surgeons of England*. 1996. September, 39 (3) 168-171
4. D.T.L. Jones, A. Wambersie. Radiation therapy with fast neutrons. A review. *Nuclear instruments and methods in physics research A* 580 (2007) 522-525.
5. V.N. Kononov, M.V. Bokhovko et al., Accelerator-based fast neutron sources for neutron therapy. *Nuclear Instruments and Methods in Physics Research A* 564 (2006) 525-531
6. www.neutrontherapy.niu.edu/
7. H. Nakamura, M.Ueno et al., Development of boron nanocapsules for neutron capture therapy. *Applied Radiation and Isotopes*. 67 (2009) S84-S87.
8. E. Bisceglie, P.Colangelo et al., Production of epithermal neutron beams for BNCT. *Nuclear Instruments and Methods in Physics Research A* 476 (2002) 123-126.
9. O. Harling. Fission reactor based epithermal neutron irradiation facilities for routine clinical application in BNCT. *Applied Radiation and Isotopes* 67 (2009) p. S7-S11.
10. V.Tanner, I.Auterinen, J.Helin et al. On-line neutron beam monitoring of the Finnish BNCT facility. *Nuclear Instruments and Methods in Physics Research A* 422 (1999) 101-105
11. R.F.Barth. Boron neutron capture therapy at the crossroads: Challenges and opportunities. *Applied Radiation and Isotopes* 67 (2009) 53-56.
12. V.N. Kononov, M.V. Bokhovko et al., Accelerator-based fast neutron sources for neutron therapy. *Nuclear Instruments and Methods in Physics Research A* 564 (2006) 525-531.
13. A.Lafuente, A.Abanades et al. Dynamic response of an accelerator driven system to accelerator beam interruptions for criticality. *Nuclear Instruments and Methods in Physics Research A* 591 (2008) 327-337.
14. C.H.M. Broeders, I Broeders. Neutron physics analysis of accelerator-driven subcritical assemblies. *Nuclear Engineering and Design* 202 (2000) 209-218
15. P.Ausset, D. Gardès. Beam diagnostics for high intensity hadron accelerators. *Nuclear instruments and methods in physics research A* 577 (2007) 161-167.
16. H. Arnould, C.A.Bompas et al. Experimental verification of neutron phenomenology in lead and transmutation by adiabatic resonance crossing in accelerator driven systems. *Physics Letters B* 458 (1999) 167-180.
17. K.Abbas, S. Buono et al., Development of an accelerator driven neutron activator for medical radioisotope production. *Nuclear instruments and methods in physics research A* 601 (2009) 223-228].
18. Ch. Vettier, C.J.Carlile, P. Carlsson. Progress for the European spallation source in Scandinavia. *Nuclear instruments and methods in physics research A* 601 (2009) 223-228.
19. F.M.Wagner, P.Kneschaurek and all. The Munich fission neutron therapy facility MEDAPP at the research reactor FRM II. *Strahlentherapie und Onkologie*. Vol. 184, Nr 12/December 2008, 643-646.
20. H. Kumawat, D. Dutta et al. Heat deposition in thick targets due to interaction of high energy protons and thermal hydraulics analysis. *Nuclear instruments and methods in physics research B* 266 (2008) 604-612.
21. M. Salvators, I. Slessarev et al. Long-lived radioactive waste transmutation and the role of accelerator driven (hybrid) systems. *Nuclear instruments and methods in physics research A* 414 (1998) 5-20.



KOMPELKSINIAI SPRENDIMAI RADIACINEI SAUGAI MEDICINOJE

Darius Mikšys, Andrej Rožkov,
UAB „Lokmis“

UAB „Lokmis“ yra viena pirmaujančių šiuolaikinės matavimo įrangos ir matavimo sprendimų tiekėjų Lietuvos rinkai. Kompanija siūlo kompleksines radiologinės saugos, metrologinių, elektros, fizikinių matavimų, cheminės analizės ir telekomunikacijų sistemas, jų projektavimo, kalibravimo, įdiegimo ir aptarnavimo paslaugas.

Kompanijos Radiometrijos padalinys nuolatos plečia savo veiklos sritis ir koncentruojasi ne tik į pavienių produktų pasiūlą, bet ir į kompleksinius sprendimus branduolinei energetikai, aplinkos apsaugai, moksliniams tyrimams, fizinei saugai, pramonei, branduolinei medicinai.

Medicinoje srityse, kuriose naudojami jonizuojančiosios spinduliuotės šaltiniai, svarbiausia yra užtikrinti pacientų ir personalo, bei aplinkos radiacinę saugą. UAB „Lokmis“ siūlo kompleksinius sprendimus bei priemones šiam tikslui įgyvendinti.

Radiologinė sauga

Tam, kad pacientui būtų patikimai parinkta tiksli radioaktyvaus preparato dozė, būtina naudoti patikimus ir aprobuotus dozės kalibravimo prietaisus. Siūlome dozės kalibratorius, kuriuose integruotos funkcijos patenkins pačius didžiausius Jūsų, kaip profesionalų, lūkesčius. Saugiam preparatų pernešimui ir transportavimui siūlome švininės ar volframinės švirkštų apsaugas, ekranuotus švirkštų laikiklius, specialius transportavimo konteinerius (įvairaus tūrio švirkštams su apsaugomis transportuoti), bei pincetus, skirtus saugiam ampulių paėmimui, adatų nuėmimui ar kitų radioaktyvių medžiagų ir atliekų tvarkymui.

Taip pat galime pasiūlyti kalibracinius įvairaus tipo radioaktyviuosius šaltinius, skirtus dozės kalibratorių ar jonizuojančiosios spinduliuotės detektorių darbiniams parametrų tikrinti.

Radioaktyviosioms branduolinėje medicinoje susidarančioms atliekoms šalinti bei laikyti siūlome nerūdijančio plieno švinuotus konteinerius su specialiais keičiamais įdėklais.



Aplinkos stebėseną

Patalpų radiacinei stebėsenai naudojami skaitmeniniai zonos monitoriai su prijungiamais išoriniais detektoriais. Detektoriai gali būti skirti skirtingo tipo – alfa, beta, gama ar rentgeno jonizuojančiajai spinduliuotei registruoti. Galimi įvairūs sistemų variantai. Pavyzdžiui, skaitmeninis zonos monitorius su vietiniu ekranu ir pavojaus signalizacijos įrenginiu bei išoriniu detektoriumi. Šiuo atveju, detektorius bus tvirtinamas kontroliuojamoje patalpoje, o monitorius, tarkime, gretimose patalpoje. Taip pat galima sistema, kai vienu metu į tinklą sujungiama iki 16 detektorių ir jie išdėstomi keliose patalpose. Tokiu atveju detektorių parodymai stebimi ir kontrolė vykdoma centralizuotai – iš nutolusioje patalpoje esančio kompiuterio su specialia programine įranga.



Paviršinės taršos matavimas.

Paviršinės taršos matavimų pasirinkimas taip pat priklauso nuo registruojamos spinduliuotės tipo. Jei laboratorijoje planuojama veikla su alfa ar beta šaltiniais, rekomenduojame pasirinkti matuoklius, su

ksnenonu užpildytais detektoriais. Beta, beta/gama paviršinės taršos matavimams dažniausiai naudojami butanu pildomi detektoriai. Pastarųjų detektorių trūkumas – detektorius reikia nuolatos papildyti butano dujomis. Alternatyva, nors kiek ir brangesnė – scintiliaciniai detektoriai, kurie nereikalauja specialios priežiūros ar sąnaudinių medžiagų, be to, scintiliaciniais detektoriais registruojamos visų trijų tipų jonizuojančiosios dalelės – alfa, beta ir gama. Taip pat galime pasiūlyti matuoklį, kuris ne tik registruoja paviršinę alfa, beta ir gama dalelių taršą, bet kartu yra ir dozės galios matavimo įrenginys. Rankų kojų paviršinės taršos matavimams taip pat galima pasirinkti matuoklius tiek su dujomis užpildytais, tiek scintiliaciniais detektoriais.

Dozimetrija ir radiometrija.

Medicinos personalo apšvita registruojama termoluminescenciniais dozimetrais, tačiau jais sukaupta dozė nepateikia duomenų apie tam tikru metu gautą apšvitą. Nešiojamieji asmeniniai dozimetrai išsprendžia šią problemą – personalas, dirbantis su jonizuojančiosios spinduliuotės šaltiniais visada bus tikras, kad jo gaunama apšvita neviršija nustatytų lygių. Radiometrai naudojami tuomet, kai nereikia pastoviai sekti jonizuojančiosios spinduliuotės lygio ir pakanka jį patikrinti prieš ar po darbo. Tačiau jie puikiai tinka ir nuolatinei stebėsenai vykdyti, o dėl plataus išorinių daviklių pasirinkimo, ne veltui vadinami universaliais jonizuojančiosios spinduliuotės matuokliais.



Fizinė sauga

Pacientų ir personalo fizinei radiacinei saugai užtikrinti siūlome įvairių modelių švinines apsaugas – prijuostes, apsiaustus, apykakles, širmas, mobilius apsauginius ekranus. Klientas pagal poreikį gali užsisakyti norimos spalvos ar dydžio priemones, taip pat galima suprojektuoti gaminį pagal kliento pageidavimą.



Rentgeno spinduliuotės kokybės parametrų tyrimas

Švedų kompanija RTI Electronics AB gamina patikimus ir novatoriškus rentgeno spinduliuotės prietaisus (įprastiniai rentgeno aparatai, mamografai, kompiuteriniai tomografai) kokybinių parametrų matuoklius Barracuda ir Piranha. Barracuda – tai mažas, tačiau galingas matavimo modulių įrenginys, prie kurio prijungiami reikiami detektoriai. Modulių rinkinį galima bet kada pakeisti ar papildyti naujais – priklausomai nuo Jūsų poreikių. Renkantis Piranha matuoklį patartina iš anksto numatyti, kokio tipo rentgeno aparatai bus tikrinami – prietaisas parenkamas pagal tikrinamų prietaisų tipą.



UAB „Lokmis“ siūlo standartinius ir nestandartinius, reikalaujančius atskiro įdirbio, sprendimus radiologinei saugai užtikrinti (mobilios laboratorijos, specialūs pramonės įmonių užsakymai). Mūsų specialistai visuomet suteiks profesionalias konsultacijas bei patars, kuris sprendimas labiausiai atitinka Jūsų poreikius.

Jūsų patikimas partneris:

UAB „Lokmis“
 Visorių g. 2, LT-08300 Vilnius
 Tel.: 8 5 215 18 95
 Faks.: 8 5 215 46 17
 el. paštas: office@lokmis.lt



Mes atstovaujame:



PRELIMINARY PATIENT DOSE ESTIMATION FOR CT EXAMINATIONS IN LITHUANIA

Leonid KRYNKE*, Julius ZILIUKAS*
*Radiation protection centre in Lithuania

Abstract: During period of 2007-2008 by specialists of Radiation Protection Centre in Lithuania was collected data about patient doses in diagnostic computed tomography from 16 Lithuanian medicine centers for 420 CT procedures. The main purpose of this work was – to set diagnostic reference levels (DRLs) in this area. The method for DRLs estimation is based on the 3rd quartile of the dose distribution for standard-sized patients [1]. Proposed DRLs have been approved by director of Radiation Protection Centre for head, spine, abdomen, pelvis and chest examinations in the units of dose length product (DLP, $mGy \times cm$). During 2009 was collected additional data, which covered 21 medicine centers and 23 CT units. New data estimation in relation with approved DRLs values was performed. All dose values were registered from CT scanner console, which are provided by manufacturer of CT equipment. With each CT machine were performed computed tomography dose index (CTDI, mGy) measurements, using calibrated 100 mm pencil Ion chamber, dedicated for CT and Barracuda Cabinet equipment to compare measured dose value and displayed value on CT scanner console. New Lithuanian DRLs were compared with European countries proposed DRLs.

Keywords: Diagnostic Reference Levels (DRLs), Computed Tomography (CT), Computed Tomography Dose Index (CTDI), Dose Length Product (DLP)

1. Introduction

The number of CT scanners in Lithuania in a last five years was significantly grown and now CT examinations are very popular and widely accessible. There were 32 CT units in 2005s and at this moment there are 48 CT units in operation. It's known, that CT procedures provide up to 40% of whole diagnostic medical exposure in developed country [2]. It is often documented, that patient doses are higher than necessary and the image quality in CT often exceeds the level, needed for confident diagnosis. One of the opportunities to decrease individual CT doses is to implement diagnostic reference levels (DRLs). By the medical exposure directive [4], Member States of the EU are obliged to adopt the diagnostic reference levels into national legislation and regulations concerning radiation protection. The aim of this study is to investigate the situation in computed tomography about patient doses and assess it in relation with proposed CT reference levels by different EU countries.

2. Method and Equipment

During period of 2007-2008 specialists of Radiation Protection Centre in Lithuania collected data about patient dose in diagnostic computed tomography from

16 Lithuanian medicine centers for 420 CT procedures. After the data had been collected, was performed its processing and evaluation. For list of chosen CT procedures were calculated DRLs, based on 3rd quartile of the dose distribution in each hospital for standard-sized patients. DRLs for head, spine, abdomen, pelvis and chest procedures in units of dose length product (DLP, $mGy \times cm$) were proposed. During 2009s was collected additional data, which covered 21 medicine centers with 23 CT units. New data estimation in relation with approved DRLs was performed.

In this work one-slice and multi-slice scanners of different manufacturers were checked. Dose values, displayed on machine console during CT procedure – CTDI, DLP and additional important procedure parameters, as voltage [kVp], current [mA], rotation time [s], pitch, slice width [mm], number of slice, scan distance [cm] etc. were recorded. One of the problems for part of scanners was that they have no saved information about dose in patient protocols. It mainly refers to older scanner with older software. For newer versions this problem is solved. For results reliability with each scanner was registered the data of at least 10 patient of each procedure.

The deviation for CTDI, displayed on CT console for each CT unit was evaluated. Head (16cm) and body (32cm) phantoms with calibrated 100 mm pencil Ion chamber, dedicated for CT and Barracuda Cabinet equipment were used for measurements. Method fully explained in [3] source. Measurements with head (16

cm) and body (32 cm) phantoms were performed for evaluation of deviations between measured and displayed CTDI values.

3. Results and discussion

Estimated deviation of measured and displayed dose values for different CT units was in range of 13% (Table 1).

Results of table 1 show, that CTDI values displayed by CT scanners is quite correct and it lets us use them for further statistical evaluation of patient doses through CT examination.

Table 1. Types of CT scanner and deviation between CTDI values measured and displayed on CT console

CT unit	slice	Head, CTDI, mGy		Deviation %
		Measured	Displayed	
Philips Brilliance	16	28	27,7	-1,08
Philips Brilliance	16	70	62,3	-12,36
Philips Brilliance	16	31	30,4	-1,97
Philips MX Duo	2	68,5	65,5	-4,58
Philips MX 8000 QUAD	4	36,7	32,5	-12,92
Siemens Emotion	16	58,8	59,37	0,96
Siemens Emotion	6	66,2	59,9	-10,52
Siemens Somatom Balance	1	53,6	53,2	-0,75
Siemens Somatom Emotion	1	55,9	59,2	5,57
Siemens Somatom Emotion Duo	2	54,6	59,17	7,72
Siemens Somatom Emotion Duo	2	53,8	59,7	9,88
Siemens Somatom Esprit +	1	63	59,3	-6,24
Siemens Somatom Sensation	16	73,5	71,68	-2,54
Siemens Somatom Esprit	1	49,9	48,6	-2,67
Siemens Somatom Esprit	1	53,4	56,7	5,82
Toshiba Asteion	1	68	63,3	-7,42
Toshiba Asteion	4	74,3	67,7	-9,75
Toshiba Asteion	64	45,6	40,4	-12,87

As result of data evaluation, DRLs, based on 3rd quartile of the dose distribution in each hospital for standard-sized patients for head, spine, chest, abdomen and pelvis examinations were proposed (Table 2).

Table 2. Proposed DRLs for basic CT examinations

Examination	Average DLP, mGy x cm	Standard deviation	DRLs, mGy x cm
Head	819,1	196,5	950
Spine	464,0	452,7	300
Chest	454,7	229,3	650
Abdomen	957,4	611,3	1200
Pelvis	434,8	250,4	550

In comparison with different European countries Lithuanian DRLs basically are very close to them (Table 3).

Table 3. Lithuanian DRLs in comparison with different countries established DRLs

Examination	LT 2008 DRLs	German ⁵ 1999 DRLs	British ⁶ 2000 DRLs	Italy/ 2000 DRLs	EC ² 1999 DRLs
Head	950	1050	1050	1050	1050
Spine	300	280			
Chest	650	650	650	650	650
Abdomen	1200	1500	800	800	780
Pelvis	550	750	600	800	570

To perform more confident evaluation during 2009 has been collected additional data, which covered more medicine centers and CT units. After evaluation additional data a comparison of new results and established DRLs was performed.

Head examination

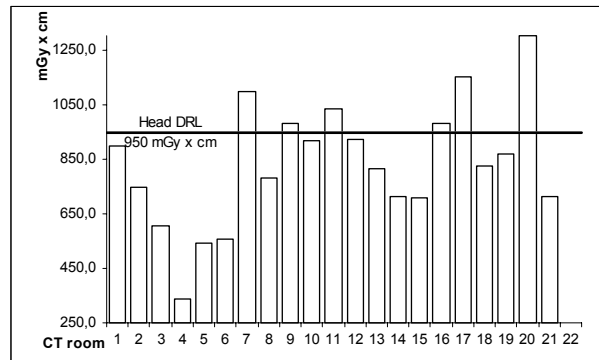


Fig. 1 Average DLP values in comparison with head DRL value – 950 mGy x cm

Average values for head examination for 6 medicine centers (or 28%) are above DRL value (950 mGy x cm). Average max/min DLP values – 1304/339 mGy x cm. Variation of main parameter of head examination between CT rooms was in range: 120-140 kV; 200-500 mAs;

Chest examination

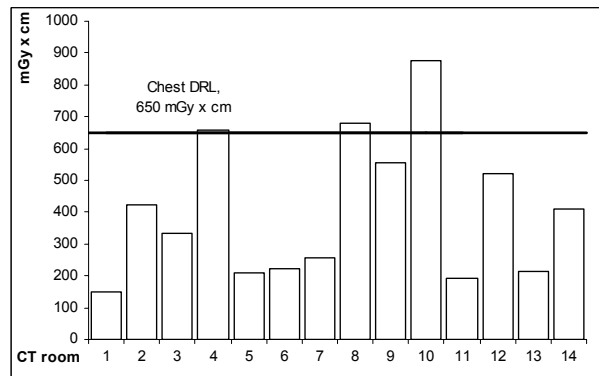


Fig. 2 Average DLP values in comparison with Chest DRL value – 650 mGy x cm

Average values for chest examination for 3 medicine centers (or 21%) are above DRL value (650 mGy x cm).

Average max/min DLP values – 875/148 $mGy \times cm$. Variation of kV and mA parameters for chest examination between CT rooms - 110-130 kV ; 200-500 mA ;

Spine examination

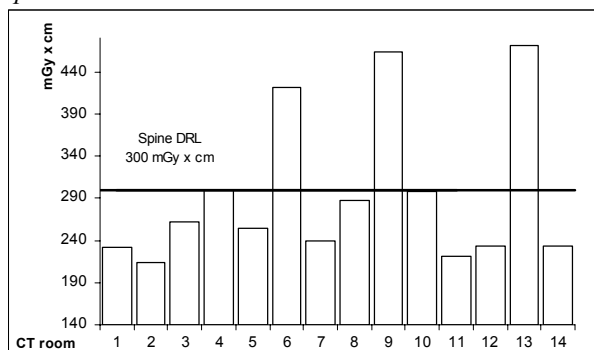


Fig. 3 Average DLP values in comparison with spine DRL value – 300 $mGy \times cm$

Average values for spine examination for 3 of medicine centers (or 21%) are above DRL value (300 $mGy \times cm$). Average max/min DLP values – 471/214 $mGy \times cm$. Variation of kV and mA parameters for spine examination between CT rooms – 120-140 kV and 200-600 mA ;

For pelvis and abdomen examination the data is being collected still to evaluate situation more confidently.

For head, chest and spine examinations was found compliance to established DRLs for these examinations. Wide variation of parameters for the same examination, but different CT units and medicine centers could be a reason of variation of dose values. The relation between exceeded dose values and type of CT unit was not found. Observing the data, were spotted 2 medicine centers, with enlarged average DLP values for all established DRLs in CT. 2 medicine centers were found exceeding DRLs for 2 of examinations and remainder centers exceeds DRLs for 1 of examinations.

4. Conclusions

In this study were made first steps for establishment DRLs in computed tomography in Lithuania. First-new DRLs values in units of dose length product ($mGy \times cm$) were proposed and approved by director of Radiation Protection Centre. Second - by evaluating

additional data, were found several medicine centers, within average dose values are above proposed reference levels. Additional data collection and evaluation from medicine centers with exceeded average DLP values is intended in a short term future. During further investigation of situation in computed tomography, there is intention to settle DRLs for more detailed examination (cervical spine, thoracic spine, lumbar spine; different phase of abdomen examination etc.).

After national DRLs establishment it is essential for all medicine centers not exceed these levels. For this reason regular local compliance checking with DRLs is necessary. Medicine physicist availability, performing these procedures, should bring essential help. At this moment medicine physicists are involved only in big medicine centers activity.

5. References

1. Guidance on the establishment and use of diagnostic reference levels for medical X-Ray examination, Institute of Physics and Engineering in Medicine, Report 88, York 2004.
2. European guidelines on quality criteria for computed tomography. Report EUR16262. European Community, Brussels, Belgium, 1998.
3. Dosimetry in diagnostic radiology: an international code of practice technical reports series No 457, p. 188-196.
4. COUNCIL OF EUROPEAN UNION (1997): 'Council Directive 97/43/EURATOM of 30 June 1997 on health protection of individuals against the dangers of ionizing radiation in relation to medical exposure
5. Publication of diagnostic reference levels for radiological and nuclear medical examinations Diagnostic reference levels, 2003, p. 3, (Available on <http://www.bfs.de/en/ion/medizin/referenzwerte01.pdf>), Accessed on 25 September 2009.
6. J. Clarke, K. Cranley, J. Robinson, H. S. Smith, A. Workman, Application of draft European Commission reference levels to a regional CT dose survey, The British Journal of Radiology, 73, 2000. p. 43-50.
7. Decreto legislativo 26 maggio 2000, n. 187, p.15, (Available on http://www.ifinmed.it/download/Dlgs187_00.pdf), Accessed on 25 September 2009.

INFRARED SPECTROSCOPICAL STUDIES OF DISTRIBUTION OF CHEMICAL COMPONENTS IN URINARY STONES

Milda PUČETAITĖ*, Valdas ŠABLINSKAS*, Vaiva HEDRIXSON**, Zita KUČINSKIENĖ**, Arūnas ŽELVYS***, Feliksas JANKEVIČIUS***

*Dept. of General Physics and Spectroscopy, Faculty of Physics, Vilnius University; ** Dept. of Physiology, Biochemistry and Laboratory Medicine, Faculty of Medicine, Vilnius University; ***Centre of Urology, Vilniaus University Hospital Santariskių klinikos, Faculty of Medicine, Vilnius University

Abstract: Kidney diseases which cause the occurrence of urinary stones are frequent in human pathology. The formation process of the stones is not fully understood therefore the studies of chemical composition and structure are of great importance. The means of Fourier transform infrared spectroscopy (FTIR) were used to determine the composition of the stones while FTIR microscopy was used to create chemical maps of cross-sectioned stones. The data from the study were used to analyze the formation process of the stones.

Keywords: urinary stones, FTIR, microspectroscopic surface reflectance imaging

1. Introduction

The composition and structure of urinary stones is complex and depend on a variety of factors which include diet, sex, environment, metabolism, etc. The identification of the components and structure of the stone enables to find out the underlying cause of the disease, prescribe treatment and prevent recurrences [1].

The qualitative and quantitative analysis of urinary calculi is challenging because of their usually small size, fragility, heterogeneous composition. Fourier transform infrared spectroscopy (FTIR) is easy and rapid method to obtain quantitative and qualitative information about chemical composition of the calculi even from small amount of the substance. In addition, this method enables to distinguish such similar components in the stones as calcium oxalate mono- and dihydrate. Microspectroscopic surface reflectance imaging is an informative method for analyzing morphology of cross-sectioned stones [2].

2. Experimental

Urinary stones for this study were surgically removed from patients in Vilnius University hospital Santariskių klinikos. 2 mg of homogenized sample was finely grounded with potassium bromide (KBr) powder of spectroscopic purity and converted into a pellet using manually operated hydraulic press "Specac" exerting a pressure of 10 tons. The pellet was placed in the sample compartment of "Vertex 70" spectrometer from "Bruker" in the path of infrared radiation emitted by

"glowbar" light source. The spectrum was obtained using liquid nitrogen cooled MCT (mercury cadmium telluride) detector with 4 cm^{-1} spectral resolution. The spectrum was then matched against library spectra to identify various stone components.

The cross-sectioned stones were fixed on glass microscope slides using two-component epoxidic glue and polished. Spectra were obtained using FTIR microscope "Hyperion 3000" from "Bruker" with single element MCT detector. The resolution of the spectrometer was set to 2 cm^{-1} . False-colour images representing the distribution of different chemical components in the urinary stones were obtained by integrating the area under the spectral band of specific chemical component. OPUS software was used for this purpose.

3. Results and discussions

In this study, the components found in the stones were: calcium oxalate (mono- and dihydrate), phosphates (carapatite and brushite), uric acid and struvite. The majority of stones (~78%) are constituted from calcium oxalate with phosphate deposits. Some of the stones (~17%) are constituted from pure uric acid (Fig. 1) and the others (~5%) – from three components: calcium oxalate, phosphate and struvite (Fig. 2).

FTIR spectroscopy allows distinguish two very similar substances: calcium oxalate monohydrate and calcium oxalate dihydrate [3]. Such analysis in this work was based on the position of C-O stretching spectral band. This band shifts from 1317 cm^{-1} for calcium oxalate

monohydrate to 1324 cm^{-1} for calcium oxalate dihydrate (Fig. 3).

The second issue in this study is related to distribution of chemical components in the cross-section of the stone. FTIR microscope was used for capturing of infrared image of cross-sectioned stones. The spectra from small areas of the cross section ($100\times 100\mu\text{m}$) were used for constructing false-colour images.

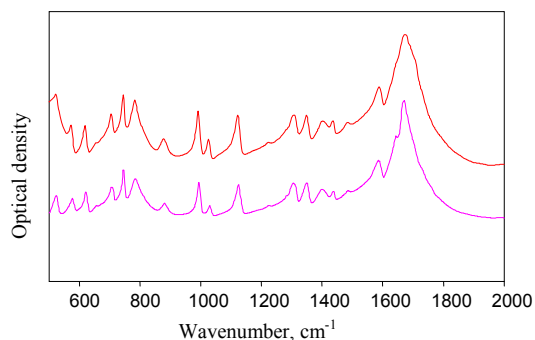


Fig. 1. Spectrum of pure uric acid stone (top) compared with spectrum of uric acid from the library (bottom).

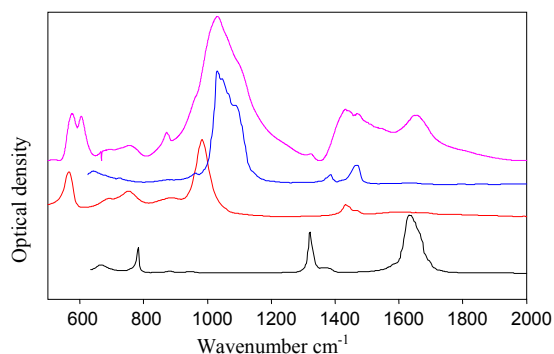


Fig. 2. Spectrum of urinary stone (top) constituted from calcium oxalate (black curve), carbapatite (blue curve) and struvite (red curve).

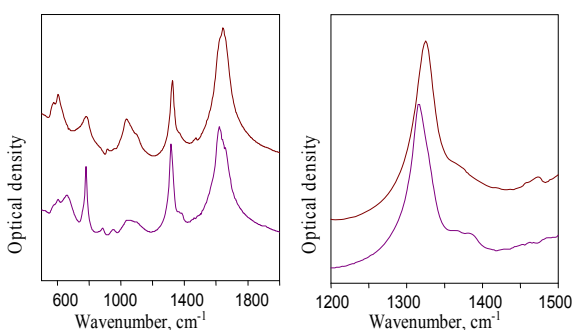


Fig. 3. Spectra of stones containing calcium oxalate monohydrate (bottom) and calcium oxalate dihydrate (top). The band of the latter is shifted to the side of higher wavenumbers.

The images were obtained by integrating area under specific spectral band. Having analyzed the data obtained, we divided the stones into two groups: the ones with some ordered distribution of chemical components and the others without any organized structure. One of the stones constituted of calcium oxalate and calcium phosphate (brushite) is shown in figure 4. Optical and false-colour images of this stone

are presented in figure 6. The false-colour image in the middle shows how calcium oxalate is distributed in the cross-section of the stone. Red colour corresponds the areas where the concentration of calcium oxalate is high and blue colour – where the concentration is low. The bottom image represents distribution of brushite. Having these images in mind, we can assume that the stone was induced by small deposit of brushite on the epithelium and the layer of calcium oxalate formed on it through time.



Fig. 4. A photo of the stone constituted from calcium oxalate and calcium phosphate (brushite).

A photo of another stone, constituted from calcium oxalate and calcium phosphate (carbapatite), is presented in figure 5. False-colour and optical images of this stone are shown in figure 6. Here we cannot see an organized structure, and the chemical compounds are distributed randomly in the cross-section of the stone.



Fig. 5. A photo of the stone constituted of calcium oxalate and calcium phosphate (carbapatite).

From this data, we can assume that both chemical components are distributed in the stone evenly what is resulted by simultaneous crystallization. In addition, there is no evidence that the stone formed on epithelium before it became loose. Most likely, the stone formed from oversaturated solution of the compounds.

4. Conclusions

Conventional infrared spectroscopy, enhanced by KBr pellet technique, can be used to the qualitative and quantitative analysis of urinary stones. Even chemically rather similar components such as calcium oxalate monohydrate and calcium oxalate dehydrate give rise to very specific infrared absorption spectra. Accuracy of determination of relative concentration of some chemical component in the stone depends on abundance of the component. In case of major component (relative concentration more than 50%)

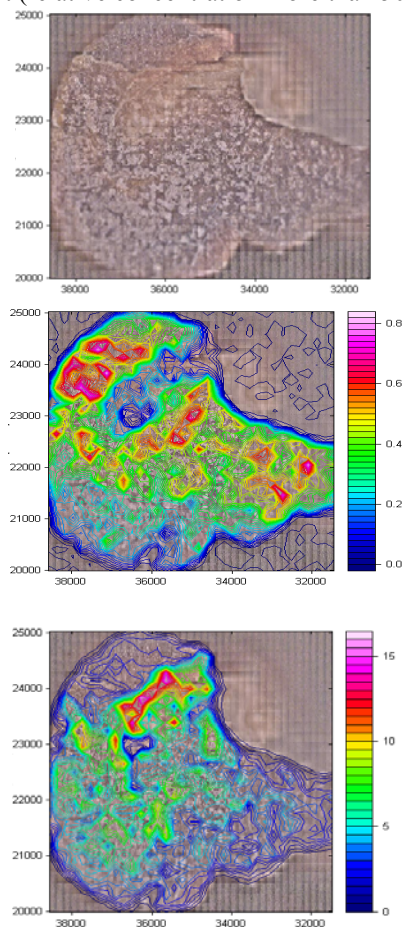


Fig. 6. Optical (top image) and false-color images of the stone constituted from calcium oxalate (middle image) and brushite (bottom image). Red color represents areas with high concentration of the chemical component and blue color – areas with low concentration or lack of the corresponding component.

of the stone, the concentration can be defined with accuracy of 3%, while in case of minor component (relative concentration less than 5%) accuracy can be as low as 10%.

Infrared spectroscopical mapping can be efficiently used for elucidating the distribution of chemical components in the stones. Due to disability to prepare urinary stone samples suitable for infrared transmission measurements, only reflection spectra can be used for the infrared mapping. One has two options here - either to use diffuse reflection spectroscopy or specular reflection spectroscopy. Our experience is that

diffusion reflection is difficult to use due to technical problems. Imaging by mapping requires using mapping stage incorporated to the diffusion sphere needed for such experiments. Such technical arrangement is hardly possible. Specular reflection measurements do not require the diffusion sphere and can be performed for the kidney stones fixed on mapping stage. Unfortunately the surface of polished kidney stone is rather porous what results to very weak signal of specularly reflected infrared light. Intensity of the signal depends on the size of illuminated area of the stone surface.

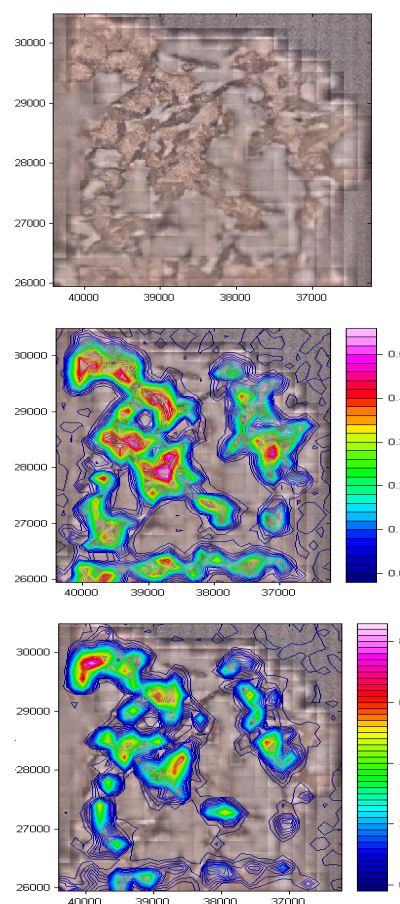


Fig. 7. Optical (top image) and false-color images of the stone constituted from calcium oxalate (middle image) and carapatite (bottom image). Red color represents areas with high concentration of the chemical component and blue color – areas with low concentration or lack of the corresponding component.

Theoretically, infrared microscopy allows diminish this area almost to diffraction limit - $10 \times 10 \mu\text{m}$. In practice, due to weakness of the signal of specular reflection from polished kidney stones this area cannot be smaller than $100 \times 100 \mu\text{m}$. This limitation seems not to be critical for studies of distribution of chemical components in urinary stones. Chemical images obtained in this work show that in case of ordered structure of the stones the components have domain structure and the domains are big enough to be characterized by infrared specular reflection microscopical technique. Spectra collected by specular

reflection technique exhibit absorptions resembling the first-derivative of a conventional absorption spectrum. The bands of such spectra are called restrahlen bands and their intensity grows proportionally to the absorption.

For the first time in this work it is shown that there can be two types of mixed calcium oxalate and calcium phosphate stones. The stones of the first type do not have any domain structure, while the stones of the second type have one domain of calcium phosphate located close to the edge of the stone surrounded by calcium oxalate. This finding brings to conclusion that the stones with calcium oxalate as a main component can be formed in two ways: (I) loose calcium oxalate stone grows in urinary system from oversaturated salt solution without fixation to the walls of the system (II) calcium oxalate stone, which was initiated on the walls. In this case the grow starts from formation of calcium phosphate crystal on the wall of the system. Later this crystal is covered by calcium oxalate.

We believe, that having larger set of calcium oxalate/calcium phosphate mixed stones we will be able to clarify if covering of calcium phosphate crystal by calcium oxalate takes place on the walls of urinary system, or the process starts when calcium phosphate for some reason (naturally, with aid of medicines or ultrasound treatment) will become loose. Such studies are now underway in our laboratory

5. References

1. Laurence Estepa, Michel Daudon. Contribution of Fourier Transform Infrared Spectroscopy to the Identification of Urinary Stones and Kidney Crystal Deposits. John Wiley & Sons, Inc. Biospectroscopy 3, 1997. p. 347-369.
2. Jennifer C. Anderson, James C. Williams Jr., Andrew P. Evan, Keith W. Condon, Andre J. Sommer. Analysis of Urinary Calculi Using an Infrared Microspectroscopic Surface Reflectance Imaging Technique. Urol Res., 35, 2007. p. 41-48.
3. C. Paluszkiwicz, M. Galka, W. Kwiatek, A. Parczewski, S. Walas. Renal Stone Studies Using Vibrational Spectroscopy and Trace Element Analysis. John Wiley & Sons, Inc. Biospectroscopy 3, 1997. p. 403-407.
4. Iqbal Singh. Renal Geology (Quantitative Renal Stone Analysis) by 'Fourier Transform Infrared Spectroscopy'. Int Urol Nephrol, 40, 2008. p. 595-602.
5. V. Hendrixson, V. Šablinskas, D. Leščiūtė, A. Želvys, F. Jankevičius, Z. Kučinskienė. Infrared spectroscoplcal approach in kidney stones research // Laboratorinė medicina. t. 10, nr. 2, 2008. p. 99-105.

HEALTH PHYSICS ASPECTS OF TRITIUM IN NUCLEAR SECTOR

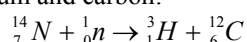
Irma GAJAUSKAITĖ*, Tatjana ZYK**, Gediminas ADLYS*, Edvardas KIELIUS*
*Kaunas University of Technology, **Ignalina Nuclear Power Plant

Abstract: Radiological effects of tritium are discussed, characterization of natural and manmade sources of tritium including nuclear sector is provided, dependence of tritium discharges upon reactor type is analyzed and tritium monitoring system in Ignalina NPP is presented in this article.

Keywords: environmental radioactivity, tritium, nuclear reactors, RBMK reactor, liquid scintillation counter

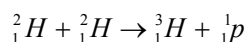
1. Introduction

Tritium is a radioactive form of hydrogen, which is found naturally in air and water. Naturally occurring tritium is produced in the upper atmosphere by interaction of cosmic rays with the nuclei of the atmospheric gases, principally by induced reactions. Maximum contribution has the interaction between a fast neutron and atmospheric nitrogen. Products of this reaction are tritium and carbon:



Very small fraction of natural tritium is produced by neutron capture by 6Li in the earth's crust [1].

The third way is cosmic deuterium reaction with deuterium



These are primarily interactions that happen in the upper atmosphere and the tritium falls to earth as rain.

The man made tritium is released into environment by different sources.

A large source was the stratosphere that accumulated tritium from the past thermonuclear testing [2]. Because of the atmospheric nuclear test conducted from 1945 until 1963, natural levels of 3H in environmental samples were enhanced. After stoppage of atmosphere nuclear weapon tests at 1963 the released activity of 3H has decayed with a half-life of 12.33 year. At present, the level of tritium in the atmosphere is close to natural origin before the nuclear tests [3].

The main source of the released tritium to-day are nuclear reactors and uranium fuel reprocessing plants. Other possible sources include consumer products and medical wastes [2].

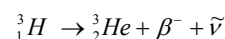
New tritium sources are research units for nuclear fusion and neutrons generation.

At present, natural tritium production remains far higher than manmade sources.

2. Radiological effects of tritium

The tritium nucleus has extra neutrons, deficit in protons and excess amount of energy to be stable.

Because of this phenomenon the nucleus 3H will undergo a nuclear transformation (radioactive decay) and one neutron converts to proton. This reduces the energy in the nucleus and new helium nucleus is left more stable. During transformation tritium nucleus emits a beta minus particle and antineutrino.



The antineutrino $\bar{\nu}$ has no biological significance because it practically does not interact with matter.

The maximum energy of emitted beta particle is of 18,6 keV with an average energy is of 5,7 keV. This is low energy beta radiation compared to most naturally occurring radioactive beta emitters. It is considered that relative biological effectiveness (RBE) of tritium is the same as of standard X-ray or gamma radiation. In this case, radiation weighting factor equal to 1 is applied to all Low Energy Transfer radiation (LET). The justification is that in general the greater values may not apply to cancer induction in humans (ICRP, 2007).

Tritium is pure beta emitter of low energy. The maximum energy of 18,6 keV corresponds to maximum range of 6 μm in water or biological tissue. For comparison, the thickness of the epidermis and dermis of human skin is 20-100 μm and 1-3 mm respectively [1]. So the outer layer of skin is enough to stop external beta radiation of tritium. For this reason tritium could produce most internal exposure if it is taken into the body. It can happen by two main ways: inhalation and ingestion. The three major forms of tritium are present in the environment: tritiated water vapor (HTO), molecular tritium (HT) and tritiated methane (CH_3T) [4]. These can be incorporated as a tissue free-water tritium into living organisms as organically bound tritium (OBT).

Organically bound tritium has longer retention time in body than tritiated water. In the case of tritiated water tritium is expelled with a biological half life of approximately 10 days. For organic tritium inside the body the half life is approximately 30 days [1].

3. Tritium sources in nuclear sector

At present, it is considered, that the main source of manmade tritium is a nuclear fuel cycle (nuclear power stations and nuclear fuel reprocessing plants).

The new sources of tritium are tritium production plants for nuclear fusion technology and tritium release during fusion experiments. Tritium release from nuclear power plant depends on the reactor type. The nuclear power stations using light water reactors (PWR - pressurized water reactor and BWR – boiling water reactor) have rather low discharge of tritium as compared to others types of reactors used in European Union (GCR- gas cooled reactor and AGR- advanced gas cooled reactor). Annual normalized discharge of airborne tritium activities from different reactor types used in EU [5] are presented in Figure 1 and of the liquid tritium – in Figure 2.

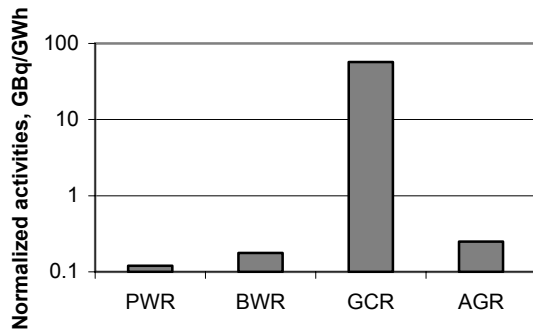


Fig1. Normalized annual releases (GBq/GWh) by reactor type for airborne tritium

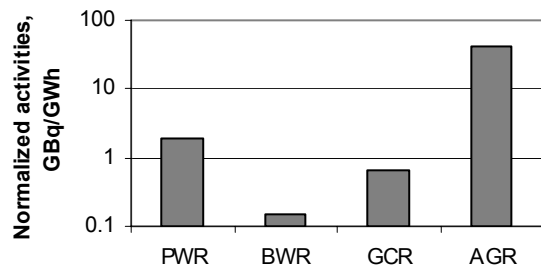


Fig2. Normalized annual discharges by reactor type for liquid tritium

In heavy water reactors annual airborne tritium releases ranges from 0,1 PBq to 1 PBq and liquid tritium releases from 0,1 PBq to 0,5 PBq [1]. Most significant contribution is due to reprocessing plants.

4. Determination of tritium activity in Ignalina NPP

Article 35 of the Euratom Treaty requires that each Member State shall establish nuclear facilities necessary to carry out continuous monitoring of the levels of radioactivity in air, water and soil and to ensure compliance with the basic safety standards.

The World Health Organization set the annual effective dose limit of 0,1 mSv for daily consumption of tritiated

water. Besides that, in keeping with the philosophy of ALARA, internal exposure should be kept as low as practical. In that connection, tritium is one of several radioactive nuclides routinely monitored in and around nuclear power plants.

Measurements of the released to the atmosphere tritium in Ignalina nuclear power plant are performed using combined T-¹⁴C unit, produced by ATOMKI (the accredited Institute of Nuclear Research of the Hungarian Academy of Sciences) [6]. Unit consists of absorption vapor samplers, based on the fact that vapor can be bound and collected with the hygroscopic agent. The bound water can be recovered in the laboratory and the tritium concentration of the water can be measured. The activity of tritium is measured by liquid scintillation method. The limit of measurement is 7 mBk/m³. Specific activity of tritium releases to the cooling water channel from RBMK reactor for 2008 is shown in the Fig.3.

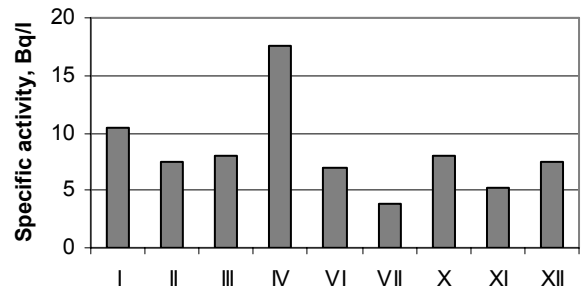


Fig. 3 Specific activity of liquid tritium releases from RBMK reactor during 2008.

5. References

1. C.Boyer, L.Vichot et all. Tritium in plants: A review of current knowledge. *Environmental and Experimental Botany* 67 (2009) 34-51
2. C.Varlam, I.Stefanescui et all., Applying direct liquid scintillation counting to low level tritium measurement. *Applied Radiation and Isotopes* 67 (2009) 812-816
3. M.Villa, G. Manjon. Low-level measurements of tritium in water. *Applied Radiation and Isotopes* 61 (2004) 319-323.
4. L. Vichot, C. Boyer et all. Organically bound tritium (OBT) for various plants in the vicinity of a continuous atmospheric tritium release. *Journal of Environmental Radioactivity* 99 (2008) 1636-1643.
5. S. Van der Stricht., A, Jensens. Radioactive effluents from nuclear power stations and nuclear fuel reprocessing plants in the European Union, 1995-1999. *Radiation protection* 127, European Commission Directorate-General Environment. 2001.
6. G. Vodila, M.Molnar et all., Mapping of tritium emissions using absorption vapor samplers. *Journal of Environmental Radioactivity* 100 (2009) 120-124

**INVESTIGATION OF TIME AND LOCATION DEPENDENT
ELECTROMAGNETIC FIELD RADIATION OF MOBILE PHONES**

Dainius BERNATAVIČIUS, Vladas ZALESKAS, Darius KYBARTAS
Kaunas University of Technology

Abstract: Mobile phone is an electromagnetic wave transmitter. Most of mobile phones in European Union are connected to GSM network which uses 900 MHz and 1800 MHz frequency. This means propagation of high frequency and short length electromagnetic waves. Mobile phone users feel irradiation of electromagnetic field. The phone radiates electromagnetic waves differently in different mode of operation. Analysis of irradiation from mobile phone is necessary evaluating negative effects of low frequency electromagnetic fields and their impact on a human body. Results of mobile phone wave power measurements are presented in this article and field strength changes of the electromagnetic field related to the measurement's location and distance from the transmitter tower are discussed.

Keywords: Mobile phone; radiation; electromagnetic field

**1. Effects of low intensity electromagnetic radiation
on human health**

Despite the fact that ICNIRP produces guidelines for recommended limits on low intensity electromagnetic exposure (Table 1) [1] and concerns regarding the health effects of low-intensity electromagnetic radiation from sources such as power lines, base stations and mobile phones are being brought to daylight, still there are little reliable data, because it is difficult to find a way to determine what effects are caused by electromagnetic radiation and one can find contradictory articles over the subject.

Table 1. Recommended limits of low intensity electromagnetic exposure

	European power frequency	Mobile phone base station frequency		Microwave frequency
Frequency	50 Hz	900 MHz	1.8 GHz	2.45 GHz
	Electric field (V/m)	Power density (W/m ²)	Power density (W/m ²)	Power density (W/m ²)
Public exposure limits	5 000	4.5	9	10
Occupational exposure limits	10 000	22.5	45	

Many studies deny short term effects on physical human condition, like the one done by Inonu University, Turkey [2]. The study was planned to determine impact of mobile phone electromagnetic fields on baseline foetal heart rate, acceleration and deceleration. 40 pregnant women were holding the MP on standby mode and on dialling mode, each for 5 min. Similar recordings were taken while there were no phones around for 10 min. No surprise, that there were seen no change in test subjects from such short exposure.

Nevertheless, it is possible to measure short term effects in certain cases. When 20 healthy subjects were divided into two groups and exposed to typical mobile phone signal (902,4MHz) before and during electroencephalogram (EEG), recording results differs from baseline and sham conditions' EEGs. Difference was even greater if exposed during, rather than before recording the EEGs. Conclusion was made that pulsed high frequency electromagnetic fields can affect normal brain functioning for some time. [3]

However the most important question is about the association between long-term mobile phone usage and the risk of developing a brain tumour. This question is based on the fact that the exposure of the brain depends on the type of phone and position of the antenna. Exposure tends to be highest in the temporal lobe and insular region and overlying skull, scalp, and parotid gland tissues. This exposure appears to be even higher in children owing thinner scalps and skulls, increased water content of their brain, and lower brain volume. Following the completion of multinational feasibility studies in the late 1990s, the IARC (WHO), commenced the INTERPHONE study. The primary objective of this study, involving 13 nations, was to

assess whether radiofrequency radiation exposure from mobile phones is associated with tumour risk, specifically, risk of glioma, meningioma, acoustic neuroma and parotid gland tumours. [2]

Despite the fact that the study has been started in year 2004 collective INTERPHONE results are not published yet. Researches claim that using a mobile phone for ≥ 10 years approximately doubles the risk of being diagnosed with a brain tumour on the same side of the head as that preferred for cell phone use. [4]

2. Experimental

Measurements of field strength were performed using portable wide band electric field meter **Chauvin Arnoux C.A 43**. (Table 2).

Table 2. Main specifications of field meter

Bandwidth	Electric field
100 kHz	0,1 V/m
to 2,5 GHz	to 200 V/m

Measurement's location and distances from the transmitter tower were identified using GPS navigation system **Acme NS-351**. Mobile phone **Nokia 6500c** was used in all measurements.

Measurements were performed for four mobile phone modes in each location, indicated in Fig.1. These modes were: 1.swich on; 2.dialling and calling; 3.ringing and answering; 4.sending SMS. Considering the fact that there is a natural background of electromagnetic radiation, it was not necessary to measure electric field for a long time. The first and the fourth modes required up to 10 seconds for one measurement, however the second and the third modes required up to 30 seconds for one measurement.



Fig. 1. Locations of measurement points

All measurements were performed holding the phone at a distance of ~ 20 cm to antenna of field meter. This distance is about the same as diameter of human head. Locations of measurements were selected along the road 5 to 10 meters outside from the road and were

marked on the map. Locations outside of the road were selected to ensure independency of the experiment on the traffic (It was possible that vehicles are equipped with radio transmitters).

3. Results

Collected data was grouped and analysed. Only mostly typical data for different locations are presented in this paper.

Only small variations from 1 V/m to 2 V/m. of the background electric field were found during the investigation. Do to this reason, no compensation measures were undertaken.

It is easily seen in Fig.2 that the field strength increases during the first second to maximum and then drops down step by step. The curves for switch on and sending SMS are approximately the same, but the curve representing calling-mode is different: it drops down when the conversation starts, but remains higher than the background level until the end of conversation.

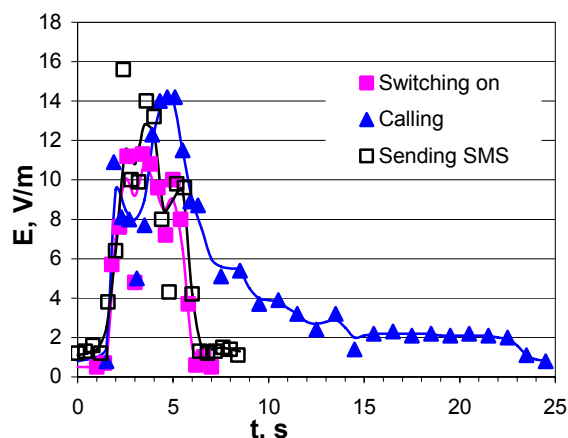


Fig. 2. Changes of electric field strength for different modes of phone operation

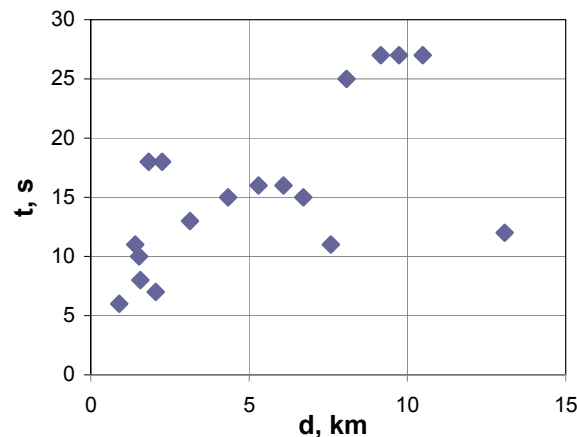


Fig. 3. Time span which is needed for drop down of the electric field strength in call mode of phone

Fig.3 shows time dependence of the signal quality: time span, which is needed to drop down field strength, is bigger when the distance between operating phone and transmitter tower is longer. If the signal quality is high enough, it takes less time to drop down the field strength (Fig.4)

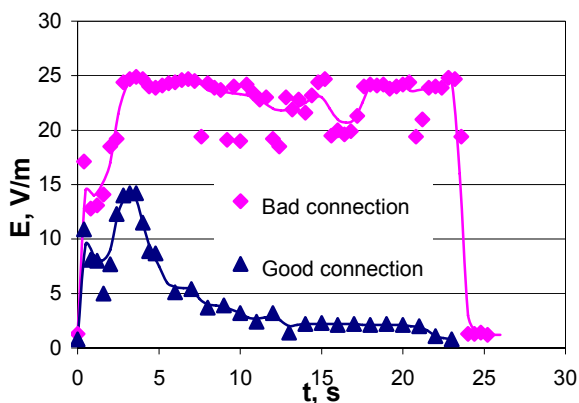


Fig. 4. The influence of signal quality for calling mode

We were trying to get clear relationship between electric field strength and the distance to the transmitter tower. Unfortunately it was not possible because of the influence of other factors like uneven terrain. The trends for different modes of phone operation are presented in Fig. 5-8.

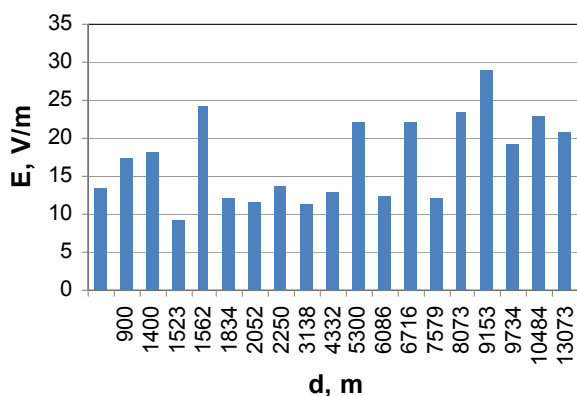


Fig. 5. Field strength distribution along the road for a switch on mode

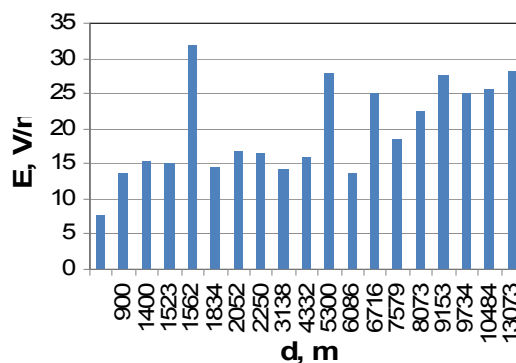


Fig. 6. Field strength distribution along the road for a calling mode

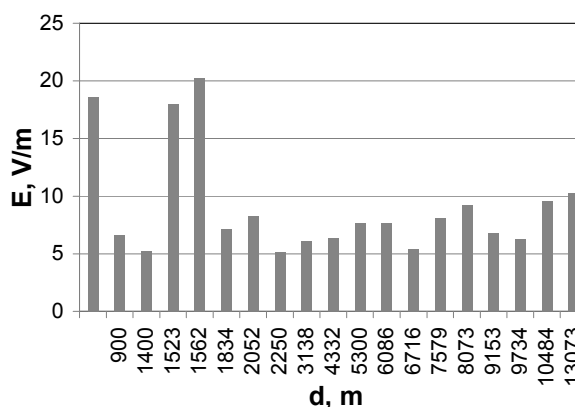


Fig. 7. Field strength distribution along the road for a conversation mode

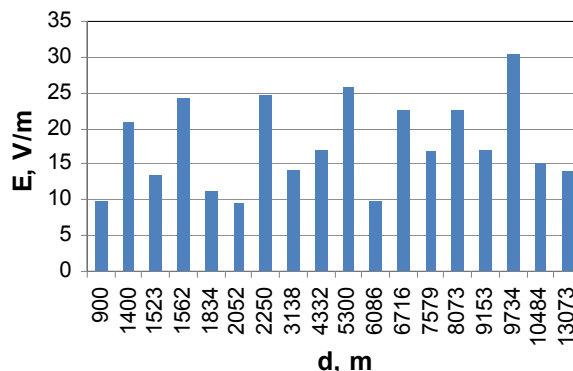


Fig. 8. Field strength distribution along the road for a sending SMS mode.

4. Conclusions

Radiated electromagnetic waves are most intensive at the beginning of the connection. Then intensity decreases gradually to certain magnitude, which is only enough to sustain the connection. This settled electric field value might be hardly distinguishable from background radiation if the connection is of good

quality, or it might be similar to peak value if there is an obstacle between cell phone and tower. Electric field strength is approximately the same for both waiting for answer or conversation modes.

Meanwhile sending SMS and switching on the phone emits similar signal in magnitude, shape and duration, which is around 5s.

Intensity of the signal doesn't depend on a distance from the tower in the highly populated areas, where towers are close to each other and cover all territory uniformly.

Considering obtained data it is to conclude, that keeping mobile phone at the distance from the body when sending SMS, switching on the phone and waiting for the answer it is possible to avoid most of radiation dose.

5. References

1. <http://www.who.int/peh-emf/about/WhatisEMF/en/index4.html>
2. Celik O., Hascalik S. Effect of electromagnetic field emitted by cellular phones on fetal heart rate patterns. *European Journal of Obstetrics & Gynecology and Reproductive Biology* 112 (2004) 55–56
3. Curcio G., Ferrara M., Moroni F. D'Inzeo G., Bertini M. De Gennaro L. Is the brain influenced by a phone call? An EEG study of resting wakefulness. *Neuroscience Research* 53 (2005) 265–270
4. Khurana V, Teo Ch., Kundi M., Hardell L, Carlberg M. Cell phones and brain tumors: a review including the long-term epidemiologic data. *Surgical Neurology* 72 (2009) 205–215

ELECTROMAGNETIC RADIATION AT COMPUTERIZED WORKPLACES AND THE IMPACT OF ELECTROMAGNETIC FIELD ON THE HUMAN HEALTH

Pranas KANAPECKAS*, Stasys MACIULEVIČIUS*, Alfredas OTAS*, Algis VALYS, Vytautas PETRAUSKAS*,
Neringa VAIČIŪNAITĖ*
*Kaunas University of Technology

Abstract: Increasing amount of electrical equipment at the work places and at home causes increasing impact of electrical and magnetic fields on human health. Although the impact of low frequency electromagnetic fields over human health remains not properly explored and comprehensive evaluated, surrounding electromagnetic fields in the office environment do not contribute to the well fare being of the office workers.

The impact of electromagnetic fields over human health is discussed in this investigation. Special attention is paid to industrial frequency electromagnetic field and its harming influence.

Keywords: Electromagnetic field, health problems, Video Display Units

1. Introduction

The statistics shows rapid growth of the computers number in Lithuania. Also the amount of persons working with computer is growing too. According to the data of LIKS (Lithuania Computer Society) there were approximately 230.000 computers installed in Lithuania at the beginning of new millennium. The number of hours spent on computer is tremendous – it is approximately 65.000 hours per career. Hours under lightness, limited work space and insufficient ventilation in some cases could cause serious health problems.

Analysis of recent publications concerning electromagnetic field impact over human body shows that the surrounding electromagnetic field could be a significant problem and extra attention should be paid to this.

Industrial frequency harming effects were investigated very carefully in offices, workplaces and at home. Results of electromagnetic fields measurements at computerized workplaces are presented in Table 1[1].

The results of measurements show that metallic constructions such as, metal pipes and steel frameworks makes a big influence to intensity of magnetic field. Engineers and network administrators should pay attention to these effects by reducing electromagnetic field as much as possible and creating safe and comfortable workplaces.

World Health Organization (WHO) published the information about the influence of low frequency fields on human body in the report “Electromagnetic fields and public health”[2]. It was shown that industrial frequency magnetic fields having magnetic flux density higher than 0,3- 0,4 μ T could become a cancerogenic factor for workers during the long working hours [2].

Table 1. Results of measuring of the electromagnetic filed measurements [1]

Sources of electromagnetic radiation	Percentage in workplaces (%)	Magnetic flux (50Hz) density (μT)
Network cables	47,4	53,3
Comutators (switch)	22,8	33,6
Steel frames	15,6	15,2
Transformers	8,4	8,8
Electricity network	3,5	1,2
Direct curent sources	1,3	3,0

According to the opinion of the World Health Organization, cancer, Alzheimer’s disease, Parcinson’s disease, mental problems even the growing number of suicides are caused by electromagnetic field harming influence. Due to the possible health risks it is highly recommended to reduce electromagnetic field radiation at all human living spaces. Another publication [3] revealed that the magnetic field of industrial frequency (50 Hz) having flux density 0,2 -0,4 μ T could be the main factor causing the appearance of the blood cancer. Besides, the risk is twice higher for a young people and children.

Permissible levels of electromagnetic irradiation from the industrial electromagnetic field (50 Hz) are presented in a Table 2.

Table 2. Permissible levels of electromagnetic irradiation from industrial electromagnetic fields

Country or organization	Inhabitants Electric field, kV/m	Workers Electric field, kV/m	Inhabitants Magnetic field, mT	Workers Magnetic field, mT
ICNIRP (1998)	4,16	6,33	0,0833	0,4166
ACGIH (1996)		25,0		1,0
CENEL EC (1995)	8,33 3	25,0	0,53 3	1,33 3
NRPB (1993)	10,0	10,0	1,33 3	1,33 3
NH&MRC (1989)	5,0	10,0	0,1	0,5
Germany (1989)	20,6	20,6	5,0	5,0
Russia (1985)		5,0		1,76
Poland (1980)		15,0		
Lithuania (2001)		25-5,3*		0,7-4,0*

* - depends on working hours

ICNIRP – International Commission on Non – Ionizing Radiation Protection;
 ACGIH – Amerikan Conference of Governmentel Industrial Hygienist;
 CENELEC – Comite Europeen de Normalization ELECTrotechnique;
 NRPB – National Radiological Protection Board;
 NH&MRC – National Health & Medical Research Council (Sante nationale et Conseil de recherches medicales).

Permissible electric and magnetic field intensities were investigated using the results of experimental investigation, mathematical modelling and extrapolation.

It was assumed that a human body has homogeneous and isotropic electrical conductivity. The sine equation of time and Faraday law was used for the evaluation of the induced current intensity:

$$J = \pi R f \sigma B,$$

Where B is magnetic flux density; R is a radius of loop of the induced current..

Elliptic model was used for the estimation of the current density in the body. Assuming, that the homogeneous conductivity of the body is 0,2 S/m and the magnetic flux density is 100 μT, the resulting current density of 0,2-2mA/m² in a human body was calculated [CRP 1997]. The highest values of current density were found in the head-neck region. If an electric field vector is parallel to the axis of human

body, the 5kV/m field induces 2mA/m² current at in the head and neck area of human's body [ILO 1994].

2. Measurement of electromagnetic radiation

Measurements of electromagnetic radiation were performed using equipment and methodology of the Computer equipment testing laboratory (CETL) at Kaunas University of Technology (KTU). CETL is accredited at the Lithuanian National Accreditation Office as the electromagnetic radiation of computer displays exploring institution (www.kompirsveikata.lt). Electromagnetic radiation limits for video display units (VDUs) are set in „TN01:1998. Displays. Permissible levels of electromagnetic radiation“, which corresponds to international standard MPR II. These limits are presented in Table 3.

Table 3. Permissible levels of electric field strengths and magnetic flux densities [4].

Field	Frequency range	MPR II, TN01:1998	TCO
Electric	0 Hz	500 V	500 V
	5 – 2 kHz	25 V/m	10 V/m
	2 – 400 kHz	2.5 V/m	1.0 V/m
Magnetic	5 – 2 kHz	250 nT	200 nT
	2 – 400 kHz	25 nT	25 nT

*according to MPR II, measuring device should be located in 50 cm in front of the VDU; according to TCO - in 30 cm in front of the VDU and at 50 cm around the VDU.

Hygiene requirements for the computerized working place environment and equipment are regulated by Lithuanian Hygiene Norm HN-32:2004 „Working at video terminals. Safety and health requirements“. However the levels of electromagnetic radiation emitted by modern VDUs are lower than those from natural sources, and are not are not considered to be harmful to the human's health [5].

3. Results

Measurements of VLF electric and magnetic fields at 124 workplaces in 42 rooms of Kaunas University of Technology have been performed. The results of measurements are presented in the Table 4.

It was found that Hygiene Norm (HN) levels of electric field strength were exceeded at 13 places and were twice as high as recommended at 3 workplaces, when measurements were performed for the electric field frequency of 2 to 5Hz. Also, the magnetic field levels were higher than recommended at 19 workplaces and were twice as high as recommended at 7 places for the frequency range 2 - 5Hz.

Measurements performed in Student's hostel No.2 (3 rooms, 7 workplaces) have shown twice enhanced level of the electric field strength as compared to the recommended level at all investigated work places. It is to point out, that in many cases the overexposure was registered for the 5Hz-2kHz frequency range of the measured electromagnetic fields.

Table 4. Measured electric field strengths and magnetic flux densities

Sub division	Measurements were done in		Number of workplaces where HN levels were exceeded*			
	No of rooms	No of work places	Electric field		Magnetic field	
			5- 2 kHz	2 - 400 kHz	5 - 2 kHz	2 - 400 kHz
Central building of KTU	17	41	13 (3)	1	19 (7)	4 (1)
Gymnasium o KTU	1	14	1	-	-	5
IT Institute	5	16	3 (3)	-	8	-
Hostel No.2	3	7	7 (7)	-	-	-
SC "Vibro Technika"	5	6	3 (2)	-	-	1
Faculty of Informatics	3	23	-	-	-	-
Faculty of Management	8	17	6 (2)	-	2	-
Total	42	124	33 (17)	1	29 (7)	10 (1)

* Number in parenthesis indicates the number of workplaces where measured electromagnetic radiation

was more than twice higher as compared to the HN levels.

4. Conclusions

Electromagnetic fields could be reduced by:

- using proper installation of power network in room,
- using computer equipment satisfying requirements of international standards,
- moving part of computer equipment and various electric devices farther from work desk,
- regular measurement of electromagnetic fields.

This enables to decrease the negative and possibly dangerous influence of electromagnetic radiation in the case when it exceeds internationally recognized norms. Periodically performed measurement of electric field strength and magnetic flux density at the computerized workplaces should ensure that the recommended HN levels are not exceeded.

5. References

1. Electro-Magnetic Pollution and Health in the Workplace. <http://www.powerdome.ie/research/The%20Facts/EM%20in%20the%20Workplace.htm>
2. EMF Exposure Standards & Guidelines. <http://www.lessemf.com/standard.html>
3. **WHO.** Establishing a dialogue on risks from electromagnetic fields. WHO, 2002, 68 p
4. IEEE standards for safety levels. <http://www.lessemf.com/book4.html#631>
5. TCO'03 Displays. CRT Displays Ver. 3.0. TCO Development, 2005, 100 p.
6. TFT versus CRT: A comparison of advantages and disadvantages. http://www.necdisplaysolutions.com/coremedia/generator/index.realm=Monitoring_BGArticle_Details,spec=x_uk_en,solutionId=,docId=56396
7. 8. Wim van Eric. Electromagnetic radiation from Video Display Units: <http://jya.com/emr.pdf>
8. Marcus G. Kuhn. Electromagnetic eavesdropping risk of flat-plain displays <http://www.cl.cam.ac.uk/~mgk25/pet2004-fpd.pdf>
9. Electromagnetic Radiation Standards Committee <http://www.sae.org/standardsdev/groundvehicle/emr.htm>

EDUCATION OF MEDICAL PHYSICISTS IN LITHUANIA

Diana ADLIENĖ*, Violeta KARENAUSKAITĖ**, Ričardas ROTOMSKIS***

*Kaunas University of Technology; **Vilnius University, Physics Faculty; ***VU Institute of Oncology

Abstract: This paper presents an overview of the education of medical physicists in Lithuania. The content and structure of the master’s programs at Kaunas University of Technology and Vilnius University are analyzed. The authors identify the problems encountered in the current context of education for medical physicists and explore opportunities and future directions for this profession.

Keywords: medical physicists, education, master’s programs

1. Introduction

Medical physics is an important area where physics is at the service of society ensuring the safety of health care. In hospitals medical physicists are principally concerned with using their physics expertise to ensure the effective, safe, efficient and scientific use of medical devices. Compared with other health care professions, the profession Medical physicist (MP) is comparatively young and less known. There is a real shortage of representatives of this profession in European health care institutions [1].

The European Federation of Organizations for Medical Physics (EFOMP) is the basic organization which harmonizes and promotes the medical physics profession and clinical and scientific progress in Europe, offering recommendations in questions of teaching program preparation and accreditation, preparing regulatory documents for the medical physics profession and promoting collaboration between teaching institutions. EFOMP considers medical physicists to be health care professionals and seeks to incorporate the medical physics profession into the list of professions regulated by EU directives ensuring the recognition of medical physics specialists in all EU states [2, 3]. It has specified the ‘core tasks’ to be carried out by medical physicists within the different specialities. In 2008, the EFOMP Council set in motion the ‘Tuning Educational Structures in Europe’ process for master’s programs in medical physics, situated within the framework of the Bologna agreement. For medical physics two fundamental ‘points of reference’ are the sets of outcome learning competences for master’s programs in medical physics and for the end of the two-year clinical training period mandated by EFOMP for the Qualified Medical Physicist (QMP) [4]. The first stage in training a medical physicist is to bring the student up to a basic standard during an initial period of training at the university in physics, mathematics and other relevant topics in the natural sciences. The second is to introduce medical physics

into post-graduate education and the third is in-service training in hospitals. Once this program completed, the physicist can be recognized as a Qualified Medical Physicist (Fig.1).

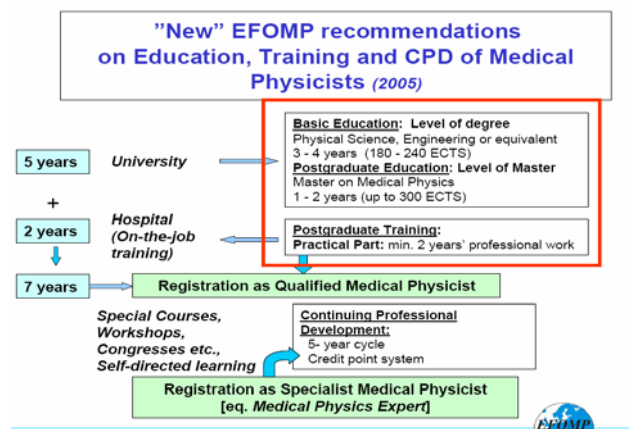


Fig. 1. EFOMP recommendations on the training of medical physicists [5]

A Qualified Medical Physicist is an individual competent to practice independently and to register as a Medical Physicist in one or more of the subfields of medical physics e.g. therapeutic radiological physics, diagnostic radiological physics, medical nuclear physics, radiation protection physics or one of the many branches of medical physics that does not involve the use of ionizing radiation [3, 6].

A Medical Physics Expert requires further experience and preferably involvement in a program for Continuing Professional Development. He (she) is an expert in radiation physics or radiation technology applied to exposure, whose training and competence to act is recognized by the competent authorities, and who, as appropriate, acts or gives advice on patient dosimetry, on the development and use of complex techniques and equipment, on optimization, on quality assurance, including quality control, and on other matters relating

to radiation protection, concerning exposure within the scope of the relevant special EU Directive [7].

2. Education and training of medical physicists in Lithuania

In Lithuania, the medical physicist profession has been regulated since 1992 by law. Qualifications, competences and responsibilities of medical physicists are regulated on the basis of the 1995-2001 LR Hygiene Norms. Under the current system in Lithuania, the Radiation Safety Centre (RSC), belonging to the Ministry of Health (SAM), supervises diagnostic and treatment methods concerning ionizing radiation and requires that organizations carrying out such procedures have medical physicists [8]. According to LR Hygiene Norms (HN 95-2005), health care institutions intending to treat patients with ionizing radiation must have medical physicists (1 MP per 400 patients per year). In countries of comparable size to Lithuania the average required number of medical physicists working with ionizing radiation is about 31. Considering that ionizing radiation is not the only specialization requiring medical physicists, that every day institutions receive new equipment and there is a constant need to replace departing management staff (due to death, retirement, emigration etc.), Lithuanian health care institutions need in general no less than 100-150 new specialists in medical physics.

Only in 2003 did Kaunas University of Technology (KTU) start to train medical physicists. 25 students had obtained their MSc degree in Medical physics by 2009. In practice, every person holding a bachelor's degree in physics, engineering or equivalent field can work as a 'medical physicist' in Lithuania. Despite the increase in the number of educated medical physicists, only 8 medical physics professionals were working in Lithuanian health care institutions in 2008 (2009) as compared to 23 other specialists working in this area (Fig 2).

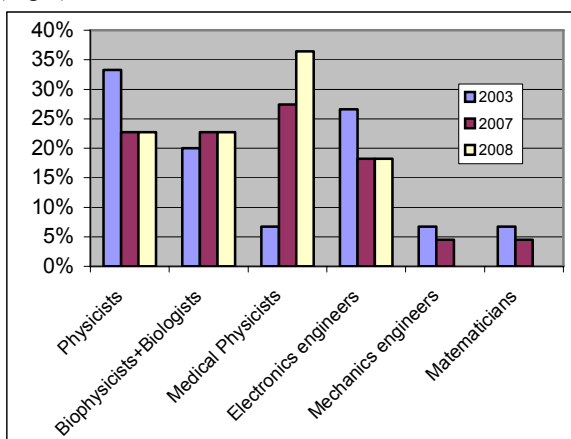


Fig. 2. Qualification of medical physicist staff working in the Lithuanian health care system

The number of medical physics professionals does not satisfy the legal requirements and EFOMP recommendations and does not meet the demand for these specialists in Lithuanian health care institutions.

2.1. MP study program at KTU

Kaunas University of Technology, in collaboration with Kaunas Medical University, in 2003 introduced a master's study program Medical Physics (Reg.No 62102B102) strictly following EU directives 97/43 Euratom (1997-06-30) [7].

The program was organized:

- o In collaboration with Swedish and English universities, the Swedish Radiation Safety Institute and EFOMP;
- o Including the results of the TEMPUS S JEP-112402-97 project "Joint Baltic Master's Courses in Biomedical Engineering and Physics"
- o With participation in the regional TATENA project RER/6/008 "Building Capacity in Medical Physics"

The main goal of this program was and is to educate and train medical physicists for the health care institutions where ionizing radiation technologies are applied for the diagnostics and treatment of patients. Medical physicists are additionally trained to work as radiation protection officers, if necessary.

The content of the MSc study program "Medical Physics" is presented in Table 1.

Table 1. Courses at KTU

Courses	Credits*
Compulsory courses	
Radiation protection and safety	4
Radiobiology	2
Human anatomy and physiology	4
Statistics and mathematical modeling	2
Interaction of radiation with matter	4
Methods of visualization in medicine	4
Recognition and analysis of images	4
Radiation registration methods and detectors	4
Radiation diagnostics	4
Radiation therapy	4
Dosimetry	2
Applied physics of non-ionizing radiation	4
Applied radionuclide physics	2
Research work	12
Master's thesis	8
Optional courses	
Nuclear and neutron physics, 4cr	
Quantum mechanics, 4cr	
Modeling of biomedical systems, 4cr	
Radioactive environmental pollution, 4cr	
Total	80

*Lithuanian credits. 1 Lithuanian credit = 1.5 ECTS

25 students have graduated from this program. All of them who were motivated to work as radiation professionals are employed in Lithuanian health care and relevant institutions (Fig.3).

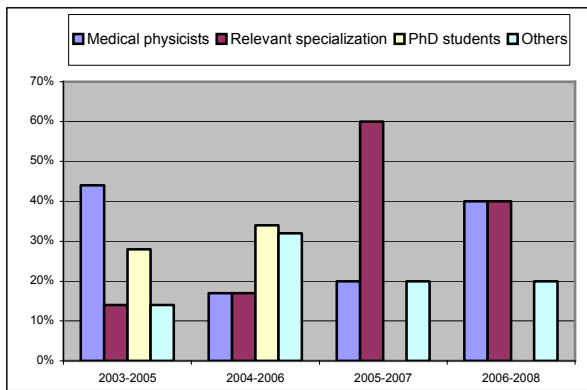


Fig. 3. Employment of graduates from MSc study program Medical Physics at Kaunas University of Technology

2.2. MP study program at Vilnius University

Considering the need for medical physicists in Lithuania on the one hand and the number of graduates produced by the KTU program on the other, it can be seen that there is a clear contradiction between the legal documents and the real possibilities. For this reason in 2008 the Physics Faculty of Vilnius University (VU) proposed a new MSc program “Medical Physics” designed to offer a new field of studies for the increasing number of 1st cycle graduates with a view to meeting the above mentioned requirements for medical physicists in Lithuania. The new program seeks to harmonize the Lithuanian higher education regulations with European and world-wide professional requirements for medical physicists, following both the EFOMP and the Institute of Physics and Engineering in Medicine (IPEM) recommendations [3, 9], and the “Dublin” descriptors [10], for qualifications awarded to students who complete the higher education second cycle. They correspond with EC directive 2005/36/EC [11] on the recognition of professional qualifications and promote the mobility of students, graduates and teachers in these programs.

The Medical Physics Interdisciplinary Master’s Program requires two years of study. It is composed of study modules together comprising 80 credits (120 ECTS) and includes 240 hours of scientific research work, 120 hours of cognitive scientific research practice and 680 hours for preparing the final diploma work. The integration of graduates into the professional medical environment, and structuring of the prerequisites for postgraduate studies in the clinical environment are facilitated by the joint responsibility of the Physics and Medicine Faculties for the program and its administration by the Medicine Faculty. Students in this program will have the possibility of acquiring skills in scientific research and practical work by carrying out work in scientific laboratories and clinics of the VU Oncology Centre, and the Santariskes Clinic Radiology Centre. In particular the new Scientific Research Centre at the Institute of Oncology of Vilnius University provides high-level training and research possibilities in biomedical physics and nanomedicine. Teachers (11 professors, 10 associate professors and 7 lecturers with

PhD) presenting lectures and practical works are highly qualified in appropriate scientific fields. They are active teachers and scientists whose research corresponds to the scientific orientations of the program and the majority participate in international projects related to biomedicine.

The content of the Medical Physics program and the list of competences were developed by considering the benchmarks prepared by IPEM and recognized by EFOMP [6, 9], in which there is a normal correlation of medical, physics and engineering sciences: Radiotherapy, Radiation Protection, Diagnostic Radiology, Nuclear Medicine, Medical Imaging, Ultrasound etc. as well as the essential knowledge of biomedical sciences (Anatomy, Physiology). With a view to the future, elements relating to the medical application of non-ionizing radiation, new optical methods, and nanomedicine have been included in this program (for detailed subject list see Table 2).

Table 2. Courses at VU

Courses	Credits*
Compulsory courses	
Safety (mechanical, electrical, chemical, biological, radiation)	4
Radiobiology	3
Basics of human anatomy and physiology	4
Statistical methods in medicine and mathematical modeling	3
Ionising radiation and its interaction with biological tissues	3
Medical imaging methods 1, (Diagnostic X-ray, Magnetic Resonance Imaging)	7
Medical imaging methods 2, (Optical biopsy)	5
Quality assurance and management in medicine	3
Radiotherapy. Dosimetry	5
Physics of non-ionising radiation	4
Applied radionuclide physics	4
Nuclear medicine and molecular imaging	3
Basics of nanomedicine	3
Research work	6
Cognitive scientific research practice	3
Master’s thesis	17
Optional courses	
Applied ultrasound in medicine, 3cr	
Lasers in medicine, 3 cr	
Physiological Measurement and Functional Assessment (EKG, EEC, audiology etc.), 3 cr	
Total	80

* Lithuanian credits. 1 Lithuanian credit = 1.5 ECTS

In order to qualify, a medical physicist must acquire a complex set of competences, so the new program follows the suggestions of Tuning [12] and EFOMP [4], by giving graduates both Generic Competences and Subject-Specific Competences (in this case: those required of a physicist at master’s level, by a medical physicist as a healthcare professional, core medical physics competences and competences for the various specializations of medical physics (Fig 3)).

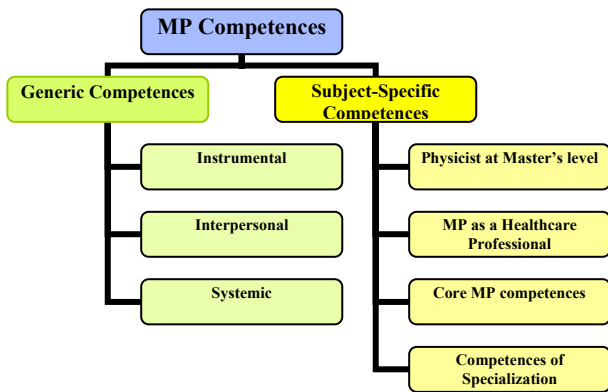


Fig. 3. Medical Physicist Competences

Despite the difficult task of dovetailing curriculum regulations to the strict EFOMP requirements, the program has successfully passed national Quality Accreditation analysis and was approved by the Ministry of Science and Education. It seems that our intention to introduce this program is well timed. The program is now in the process of implementation with a prospective starting date in 2010.

2.3. Problems, opportunities and future prospects

When preparing, implementing and carrying out the Medical Physics study programs, problems related to studies and Professional licensing and the placement of young specialists were encountered:

- in Lithuania today there is not one professor working directly in the field of medical physics;
- there is a lack of equipment, and specialized laboratories;
- no normative qualifying requirements for medical physics as a government licensed profession have been set,
- the degree offered is a Master of Biophysics, and not Medical Physics(!);
- there is no, or very little, discussion with employers, who are reluctant to invest in young specialists able to begin independent work, according to EFOMP recommendations, only after a 2 year practicum.

Opportunities for the medical physicist are expanding rapidly. The increasing number of EU directives [7, 13-16], concerning medical devices, safety from physical agents and personal protective equipment, as well as the multiplication and growing sophistication of medical devices themselves, call on the expertise of medical physicists. The need to train far greater numbers of medical physicists to meet these needs places even greater importance on the role of today's medical physicists in health care institutions. Lithuania, where the number of medical physicists is totally inadequate, is particularly concerned by this situation.

To solve these problems and strengthen the preparation of medical physicists in Lithuania, discussions are under way to create a joint study program within Kaunas University of Technology and Vilnius University, calling on the best specialists and using the infrastructure of both institutions in the interests of study quality. The complementary strengths of the two universities in medical physics will enable the joint program to educate medical physicists in all the

important fields of contemporary health care. The involvement of foreign partners is also being considered.

3. Conclusions

After this overview of the education and training of medical physicists in Lithuania, it can be stated that:

- Lithuania is experiencing a serious shortage of medical physicists.
- Kaunas University of Technology at present offers the only program for the training of medical physicists in Lithuania; Vilnius University is in the process of implementing its Medical Physics program and is planning a starting date in 2010.
- Following EU directives and EFOMP recommendations, Kaunas University of Technology and Vilnius University have the opportunity to join their efforts and create a new joint program for the education and training of medical physicists for all important fields of contemporary health care.

4. References

1. Caruana C. J., Padovani R. and Christofides S. Physics and society: the medical physics profession and its contribution to healthcare. GIREP Conference, Book of Abstracts, ISBN 978-9963-671-79-3, 2008.
2. EFOMP, *Policy Statements No 2- 12*, 1984-2008 Available from <http://www.efomp.org/policyst.html>.
3. Malaga declaration – „EFOMP's Position on Medical Physics in Europe“, 2006.
4. Cristofides, S, Schlegel, W et al. An initial EFOMP Position on the Tuning process for Masters Programs in medical Physics in Europe. Proceedings of World Congress on Medical Physics and Biomedical Engineering. IFMBE Proceedings 25/XIII, ISBN 978-3-642-03897-6, p. 70 ff.
5. Eudaldo, T, Olsen, K. The present status of Medical Physics Education and Training in Europe: An EFOMP survey. *Physica Medica* 2008; 24 (1): 3-20// Available from <http://www.efomp.org/policyst.html> and Presentation at X th EFOMP Congress. Pisa 20-22, September 2007.
6. EFOMP PS 7: Criteria for the staffing levels in a Medical Physics Department. Approved by EFOMP Council September 1997. Available from <http://www.efomp.org/online/images/docs/policy/stafflev.pdf>
7. EC. Directive 1997/43/Euratom of 30 June 1997 on health protection of individuals against the dangers of ionizing radiation in relation to medical exposure. *Official Journal L* 180, 09/07/1997, pp. 0022 - 0027.
8. Adlienė, D., Adlys, G. Medicinos fizikų rengimo problemas Lietuvoje. Proceeding of the Conference “Biomedical Engineering”. Kaunas, 2000. p. 21-24.
9. EFOMP (1984, 1997, 1998, 1999, 2009). Policy Statement No. 2, 7, 8, 9, 12). Available from <http://www.efomp.org/online/index.php?option=co>

- m_content&view=section&layout=blog&id=12&Itemid=67.
10. Dublin Shared 'Dublin' descriptors for Short Cycle, First Cycle, Second Cycle and Third Cycle Awards. Document on JQI meeting in Dublin on 18 October 2004. Available from http://www.tempus.ac.yu/here/tl_files/Dokumenti/Dublinski%20deskriptori.pdf.
 11. EC. Directive 2005/36/EC of the European parliament and of the council of 7 September 2005 on the recognition of professional qualifications.
 12. Tuning (2008) Universities' contribution to the Bologna Process. 2nd ed. Available from <http://www.tuning.unideusto.org/tuningeu/>.
 13. EC. Directive 1998/79/EC of the European Parliament and of the Council of 27 October 1998 on in vitro diagnostic medical devices. Official Journal L331 pp. 0001-0037.
 14. EC. Directive 1993/42/EEC of 14 June 1993 concerning medical devices. Official Journal L 169, 12/07/1993, pp. 0001 - 0043.
 15. EC. Directive 1996/29/Euratom of 13 May 1996 laying down basic safety standards for the protection of the health of workers and the general public against the dangers arising from ionizing radiation. Official Journal L 159, 29/06/1996, pp. 0001 - 0114.
 16. EC. Council Directive 2004/40/EC of 29 April 2004 on the minimum health and safety requirements regarding the exposure of workers to the risks arising from physical agents (electromagnetic fields).

**e-ENCYCLOPAEDIA OF MEDICAL PHYSICS
WITH MULTILINGUAL DICTIONARY OF TERMS – EMITEL**

Slavik TABAKOV, Peter SMITH, Franco MILANO, Sven-Erik STRAND, Inger-Lena LAMM, Cornelius LEWIS,
Magdalena STOEVA, Diana ADLIENE
EMITEL Consortium (www.emitel2.eu)

Abstract: The international project EMITEL has developed an e-Encyclopaedia for Medical Physics with Multilingual Dictionary. The project attracted 250+ specialists from 35 countries. This web tool will be free to use over the Internet for all colleagues. The paper describes the main elements of this first Medical Physics e-Encyclopaedia (web address: www.emitel2.eu). The use of EMITEL is also explained in the paper.

Keywords: Education and Training, e-Learning

1. Introduction

The last 20 years introduced revolutionary methods as Computed Tomography, Magnetic Resonance, Molecular Imaging, etc. All these enter quickly in healthcare and often limited information is available about these new methods and respective technology.

Our two previous projects EMERALD and EMIT developed training materials (e-books and Image Databases) to address the initial training of young medical physicists. These included specific training tasks covering the physics fields of: X-ray Diagnostic Radiology, Nuclear Medicine; Radiotherapy, Ultrasound Imaging, MR Imaging. These materials are now used in more than 70 countries around the world. EMIT project received the inaugural EU Award for education – the Leonardo da Vinci Award [1].

Both EMERALD and EMIT held Conferences, which revealed the need of a free professional reference source, linked to a multilingual dictionary of terms. This web tool was expected to quickly provide information for new, existing and old methods and equipment in Medical Physics. The tool was specially made to support the education, training and CPD process in the profession. This way the project for an e-Encyclopaedia of Medical Physics (EMITEL) was developed. The project also included a Multilingual Dictionary of Terms and was opened free during September 2009.

2. EMITEL project

This project was developed during the period 2001-2005 and was further prepared for submission to EU. At this stage the project partnership included the core of the previous project partners - King's College London (Contractor) and King's College Hospital, University of Lund and Lund University Hospital, University of Florence, AM Studio Plovdiv and the International

Organization for Medical Physics (IOMP). This was the first EU project of IOMP as an Institution and paved its way for further international projects and funding.

The objective of the new pilot project EMITEL (European Medical Imaging Technology e-Encyclopaedia for Lifelong Learning) was to develop an original e-learning tool, which will be used for lifelong learning of a wide spectrum of specialists in Medical Physics. Additionally to the e-Encyclopaedia is a Multilingual Digital Dictionary of Terms, which cross translates the terms in any of its languages.

Medical Imaging was specially underlined in the name of the project, as this technology expands rapidly. However Radiotherapy and Radiation Protection were also included, together with a number of General terms associated with Medical Physics.

EMITEL project was funded by the EU programme Leonardo da Vinci, as well as by the project partners. The EMITEL Consortium attracted additional specialists from 35 countries, forming an International Network. All members agreed to continue its activities after the end of the project, assuring a constant support and update of the project results.

3. EMITEL Dictionary

EMITEL Dictionary used as a base the previous EMIT Dictionary (www.emitdictionary.co.uk). The list of Medical Physics terms in this early Dictionary was further refined and expanded. Currently some 3200 terms are included. These terms were translated into 25 languages by colleagues listed at the end of this paper. Thus the original 7 languages English, Swedish, Italian, French, German, Portuguese, Spanish, were supplemented by new 18 languages: Bulgarian, Czech,

Estonian, Greek, Hungarian, Latvian, Lithuanian, Polish, Romanian, Slovenian, Bengal, Chinese, Iranian, Arabic, Malaysian, Russian, Thai, Turkish.

The Dictionary was coordinated by S Tabakov and its software was made by AM Studio. EMITEL Consortium extends special gratitude to all Dictionary translators, who made this task free of charge. It is expected that the Dictionary will be of great help especially in the developing countries, where limited professional literature is available in the specific languages.

4. EMITEL Encyclopaedia

Each term from the Dictionary includes an explanatory article (entry) in English. The entries aim at MSc-level and above. Their volume varies in average from 50 to 500 words. The model of the Encyclopaedia is built around a larger number of specific entries, rather than small number multi-page articles, which does not allow quick search and are difficult to update. However most of the EMITEL entries include References and information about other Related entries in EMITEL, this way forming information strings.

Many of the entries include images, graphs, examples and other additional information. Very often this additional information is related to the images from the previous projects EMERALD and EMIT. The entries are grouped in 7 categories – Physics of: X-ray Diagnostic Radiology, Nuclear Medicine; Radiotherapy; Magnetic Resonance Imaging; Ultrasound Imaging; Radiation Protection; General terms. Each entry includes contribution from at least by 3 people – author, referee and group coordinator.

An original EMITEL web site was built by AM Studio (see separate paper about it). The web site uses the ability of the current Internet browsers to operate with all languages and combines the Dictionary and the Encyclopaedia. This way each translated term comes with a hyperlink displaying the corresponding entry. A multilingual Search Engine works with all languages of the Dictionary.

The fast development of Medical Physics led to the existence of a number of acronyms and synonym terms. To deal with this problem a second Search Engine was added to the web site, which looks inside the full text of the entries (in English) and displays those entries, where a particular synonym is mentioned. Care was taken, where possible, to include various terms modifications and variations.

EMITEL web site (www.emitel2.eu) is hosted by a commercial company. Alongside the database of terms, it has an additional internal web site with Content Management System (CMS, also developed by AM Studio). The function of the CMS is to allow future editing of existing entries, adding new information, images and diagrams, etc. The CMS also allows for new

terms to be added with their own entries. This way EMITEL will act as the professional wikipedia of Medical Physics, with the difference that only accepted entries and text will be uploaded (i.e. with editorial control). It is expected that the content of EMITEL will additionally be printed on paper and commercialised.

5. EMITEL Network

EMITEL is perhaps the largest International project in the profession. Currently it includes approximately 240 colleagues from 35 countries, half being the translators (all colleagues who contributed to EMITEL are listed at the end of this paper). To develop and maintain the large volume of information an International Network was created.

The Network was first discussed and agreed during the EMITEL International Conference on Medical Physics, held at ICTP, Trieste, 24-26 October 2008 (ICTP – The Abdus Salam International Centre for Theoretical Physics). The Conference was attended by colleagues from 22 countries. Following this ICTP was accepted as a silent partner in the project.

The Conference delegates included the IOMP President, Secretary General, Treasurer, Chair of ETC, Chair of AHC, IFMBE Secretary General, IUPESM Secretary General, EFOMP President-elect and many distinguished colleagues from Europe.

The Network internal links are associated through an administrator in KCL. It is expected that the number of Network members will increase, as in future colleagues who contribute new articles and materials to EMITEL will be additionally included. This way the Network will assure the future support and expand of EMITEL Encyclopaedia and Dictionary as a web site free to use by all colleagues.

6. The use of EMITEL

Select Encyclopaedia > write the term you want to see at the window > click Enter. A list with terms is displayed – against each one is a blue hyperlink related to the area of the term > click the hyperlink to read the article (Fig.1). EMITEL can search also inside the text of the articles. To do this select Search in Full Text, after this specify the area and proceed as above. In case of UK or American English differences (i.e. colour>color; optimise>optimize) try both spellings or search only part of the term (e.g. colo, optim).

To use the Dictionary select Dictionary > choose the Input and Output languages > write the term you want to see at the window > click Enter. A list with terms is displayed, where the terms are found either single, or in combination with other words (the e-Dictionary assumes that the user's Internet browser already supports the Input Language and Output Languages).

To use both the Encyclopaedia + Dictionary select Combined and proceed as above (this search is limited only to the title of the article, not inside its text).

The screenshot shows the EMITEL e-Encyclopaedia interface. At the top, there are logos for the project and its contributors, including Leonardo da Vinci, King's College London, and Universitas Jukhuset. Below the logos is a navigation bar with tabs for 'ENCYCLOPEDIA', 'DICTIONARY', 'COMBINED', 'Project', and 'Contributors'. The search interface includes a search box with 'Dose' entered, a search button, and options to search by 'Title' (selected) or 'Full Text'. The search area is set to 'Diagnostic Radiology'. A table of search results is displayed, listing various terms related to diagnostic radiology, each with a link to the 'Diagnostic Radiology' section. To the right of the search results, the definition of CTDI (CT Dose Index) is provided, along with the formula:
$$CTDI = \frac{1}{n'} \dots$$

Fig. 1 Screenshot from EMITEL e-Encyclopaedia web page with Title search.

Acknowledgements EMITEL gratefully acknowledges the financial support from the EU Leonardo Programme, the Partner Institutions and its many Contributors (forming EMITEL Network):

Encyclopaedia: Slavik Tabakov (Coordinator); Perry Sprawls; Graeme Taylor; Maria Lewis; Elizabeth Morris; Magdalena Stoeva; Asen Cvetkov; Mario Dedenaro; Niko-las Pallikarakis; Kalle Kepler; George D Frey; William Hendee; Ratko Magjarevic; Vassilka Tabakova; Alain Noel; Paola Bregant; Justine Calvert; Tracy Underwood; Stephen Wastling; Michelle Footman; Hannu Escola; James Clinch; Hamish Richardson; Navneet Dulai; Sven-Erik Strand; Bo-Anders Jonsson; Mikael Peterson; Michael Ljungberg; Gillian Clarke; George Mawko; Anchali Krisanachinda; David Bradley; Ana Millan; Franco Milano; Inger-Lena Lamm; Fridtjof Nuesslin; Phil Evans; Charles Deehan; Joan Coward; Mark Grattan; Brendan McClean; Ruth McLauch-ian; Paul Zarand; Barry Allen; Markus Buchgeister; Ivana Horakova; Ervin Podgorsak; Jean-Yves Giraud; Freddy Stahlberg; Ronnie Wirestam; Andy Simmons; Stephen Keevil; Gerard Boyle; Nicola Harris; Emil Nordh; Adnan Bibic; Anders Nilsson; Anna Rydhog; Jimmy Latt; Johan Olsrud; Linda Knutsson; Peter Mannfolk; Sarah Brockstedt; Jonathan Siikanen; Mattias Nickel; Karlin Bloch; Markus Nillson; Martin Leach; Mario Secca; Tobias Schaeffter; Ewald Moser; Gunter Helms; Jacques Bittoun; Cornelius Lewis; Jim Thurston; Peter Smith; Elizabeth Chaloner; Marta Radwanska; Anna Benini; Stelios Chris-tophides; Cari Borrás; Kjeld Olsen; David Platten; Ignacio Hernando; Bruce Walmsley; Colin Deane; David Goss; Tomas Jansson; Monica Almqvist; Victoria Aitken; Lorna Sweetman; Fernando Schlindwein; Crispian Oates; Tony Evans; Heikki Terio; Luciano Bertocchi; Colin Roberts.

Dictionary: Slavik Tabakov (Coordinator); Farida Bentaieb; Rachida El Meliani; Nagi Hussein; Ibrahim Elyas-seery; Golam Abu Zakaria; Hasin Azhari Anupama; Md Akhtaruzzaman; Safayet Zaman; Jenia Vassileva; Venceslav Todorov; Petar Trindev; Slavik Tabakov; Bo-rislav Konstantinov; Anastas Litchev; Andy Zhu; Dai Li-yan; Dai Xiangkun; Fu Guishan; Geng Hui; Wang Jianhua; Wang Yunlai; He Zhengzhong; Xu Xiao; Xu Zhiyong; Yin Yong; Zhang Jiutang; Zhang Yue; Ivana Horakova; Anna Kindlova; Simona Trampotova; Daniela Kotalova; Vclav Husak; Jaroslav Ptacek; Josef Pacholik; Pavel Dvorak; Li-bor Judas; Irena Novotna; Kalle Kepler; Sigrid Kivimae; Kalju Meigas; Juri Vedru; Alain Noel; Jean-Yves Giraud; Helene Bouscayrol; Louis Blache; Markus Buchgeister; Gunther Helms; Stefan Delorme; Stelios Christofides; Pro-dromos Kaplanis; George Christodoulides; Charalambos Yiannakaras; Nicolaos Papadopoulos; Demetrios Kaolis; Georgiana Kokona; Georgios Menikou; Christos Papaef-stathiou; Yiannis Gerogiannis; Demetra Constantinou; Spy-ros Spyrou; Andreas Mikelides; Anastasia Sissou; Christo-doulos Christodoulou; Pal Zarand; Istvan Polgar; Tamas Porubszky; Janos Martos; Geza Safrany; Tamas Daboczi; Jozsef Varga; Franco Milano; Yuri Dekhtyar; Alexei Katashev; Marite Chaikovska; Emzinh Dzintars; Sergei Popov; Lada Bumbure; Juris Rauzins; Plaude Sandija; Arunas Lukosevicius; Algidas Basevicius; Dovile Serenaite; Diana Adliene; David Bradley; Alireza Binesh; Ali Asghar Mowlavi; Azam Niroomand-Rad; Marta Wasilewska-Radwanska; Zenon Matuszak; Katarzyna Matusiak; Alek-sandra Jung; Ana Pascoal; Nuno Teixeira; Paulo Ferreira; Nuno Machado; Daniela Andrei; Cristina Petroiu; Aurel Popescu ; Octavian Dului; Raducu Popa; Constantin Milu; Valery Kostylev; Nina Lutova, Boris Narkevich, Tatiana Ratner; Ervin Podgorsak; Bozidar Casar; Vili Kovac; Dami-jan Skrk; Petra Tomse; Ana Millan; Ignacio Hernando; Alejandro Garcia Romero; Inger-Lena Lamm; Monica Almqvist; Ronnie Wirestam; Sven-Erik Strand; Bo-Anders Jonsson; Michael Ljungberg; Freddy Stahlberg; Thomas Jansson; Anchali Krisanachinda; Sivalee Suriyapee; Tanawat Sontrapornpol; Panya Pasawang; Chotika Jum-pangern; Taweap Sanghangthum; Isra Na Ayuthaya; Sorn-jarod Oonsiri; Perihan Unak; Turgay Karali; Serap Teksoz; Zumrut Biber Muftuler; Fatma Yurt Lambrecht.

7. References

1. Tabakov, S., Roberts, C., Jonsson, B., Ljungberg, M., Lewis, C., Strand, S., Lamm, I., Milano, F., Wirestam, R., Simmons, A., Deane, C., Goss, D., Noel, A., Giraud, J. (2005) 'Development of Educational Image Databases and e-books for Medical Physics Training', Journal Medical Engineering and Physics, 27 (7), p. 591-599.

Address: Slavik Tabakov, Dept. Medical Engineering and Physics, King's College London, London SE5 9RS, UK, slavik.tabakov@emerald2.co.uk

PHOTON INDUCED MODIFICATION OF PROTECTIVE a-C:H

J. LAURIKAITIENĖ*, J. PUIŠO***, D. ADLIENĖ*, Š. MEŠKINIS***, V.ŠABLINSKAS***,

**Physics Department, Kaunas University of Technology, Studentų g.50, LT-51368, Lithuania*

***Institute of Physical Electronics, KTU, Savanorių 271, LT-50131 Kaunas, Lithuania*

****Dept. of General Physics and Spectroscopy, Faculty of Physics, Vilnius University, Vilnius, Lithuania*

Abstract: Diamond like carbon (DLC) films were prepared by direct ion beam method on quartz (SiO₂) wafers, using different films synthesis parameters. The structural and optical properties of the amorphous hydrogenated DLC films have been studied irradiating them with high energy X-ray photons in order to study the radiation effects. Raman spectroscopy was used to evaluate the structural properties of the initial and irradiated sample series. The most significant changes in transparency of the irradiated samples were observed in less dense and highly hydrogenated (more than 35 at.%) DLC films. Changes of optical properties are analyzed in relationship with the hydrogen reduction mechanism introduced during irradiation of samples by X-ray photons and the possibility to use DLC as protective coatings in optical devices is discussed.

Keywords: photons, amorphous DLC films, radiation effects, bonding structure, optical properties

1. Introduction

Technological applications of diamond like carbon (DLC) films are very promising due to their suitable physical and chemical properties, such as tissue equivalence, good chemical inertness, high radiation hardness, absolute non-toxicity, high optical transparency, mechanical hardness, etc...DLCs are used in different electronic devices, as protective and antireflective coatings in solar cells, in space research or in nuclear reactors [1-3]. Properties of the hydrogenated amorphous DLC films strongly depend on the deposition conditions and parameters, and hydrogen content in the films [3, 4]. However, the properties of the DLC films also can be modified irradiating them by various types of particles (i.e. ions, neutrons, photons) [5-8]. Behavior of polycrystalline DLC structures upon their exposure by X-ray are widely discussed, since they are used as active elements in radiation detectors [1, 2]. However there is a lack of information about the interaction of X-ray photons with the amorphous DLC films.

Due to this reason different types DLC films produced at room temperature using direct ion beam method were irradiated by high energy X-ray photons and, optical properties of experimental structures were investigated with the aim to assess radiation induced structural changes in the films.

2. Experiment

Hydrogenated amorphous diamond like carbon films

were synthesized by direct ion beam method on SiO₂ wafers. Films were formed in pure acetylene (C₂H₂) gas. Sample deposition conditions were described in [9, 10] Series of the experimental samples were divided into groups: sample series of the first group (No. 1G) were deposited at 240 eV and ion beam current density 20 μA/cm², samples of the second, and the third groups (1 and 5) were deposited using the same ion beam energy 800 eV, but different ion beam current density: No. 1 – 50 μA/cm², No. 5 – 125 μA/cm². The main optical properties of the initial (not irradiated) sample series are presented in [11, 12].

All sample series (No.1, No.5, No.1G) were irradiated at the same time in medical linear accelerator Clinac 2100C (VARIAN) with high energy (average energy 10.8 MeV [13]) photons. All samples were irradiated up to 4 fractions (2 Gy dose per fraction). After each irradiation fraction the main optical characteristics of samples were measured. Laser ellipsometer GAERTNER 117 operating with a He-Ne laser (λ = 632.8 nm) was used for the estimation of the thickness and refractive index of investigated films.

Optical transmittance and absorbance spectra of samples were measured by Ultraviolet and Visible Absorption Spectrometer SPECORD UV/VIS as well. Absorption coefficient was calculated from UV-VIS transmittance spectra using Lambert–Beer law.

Bonding structure of the irradiated carbon films were analyzed using GX FT-IR (PERKIN ELMER) spectrometer and Raman spectrometer with Spectra Physics Stabilite 2017 argon laser (λ = 514.5 nm). Hydrogen content was re-calculated from Raman spectra using approximation method from [5], or

determined by elastic-recoil detection analysis (ERDA) using primary ion beam of 2.0 MeV He⁺ ions. Surface morphology of the films was investigated by atomic force microscope (AFM) NANOTOP-206. Measurements were performed in tapping mode using V-shaped ultra sharp Si cantilever tip with the radius of curvature less than 10 nm. Applied force constant was 1.5 N/m.

3. Results and discussions

Optical properties of DLC films were analyzed before and after irradiation of samples. Ellipsometric measurements have shown the decreasing tendency of the refractive index and increasing transparency (Fig.1) in all irradiated samples as compared to initial samples. It is interesting to note, that the increase of the optical transparency after the first irradiation of samples, has a tendency to decrease after further irradiation. According to the authors [21] optical properties are related to the hydrogen content and density of the DLC films. We have found that samples with a lower density, and higher H content were more transparent in wavelength range 200-900 nm after the irradiation. This fits well with the results of other authors, where the similar relationship between the transparency and hydrogen content in DLC was indicated [8].

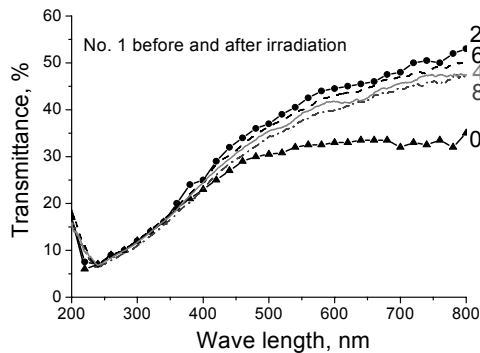


Fig. 1. Transmittance spectra of DLC film No. 1 before (0 – 0 Gy) and after (1 – 2 Gy, 2 – 4 Gy, 3 – 6 Gy, 4 – 8 Gy) irradiation with high energy photons

Close relationship between changes of the optical band gap (determined as Tauc gap) after the irradiation and the hydrogen content was found as well (Fig.2), since the hydrogen content in all as prepared samples was different.

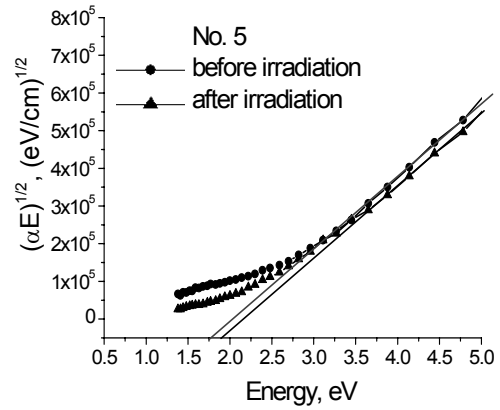


Fig. 2. DLC film No.5 before and after irradiation: $(\alpha E)^{1/2}$ dependence on photon energy E ($E_{Tauc} = 1,75$ eV, before irradiation and $E_{Tauc} = 1,90$ eV, after irradiation)

Increase of the optical band gap with an increase of the irradiation dose (γ photons) could be explained by the decreasing number and size of sp^2 clusters in DLC films [22] after the irradiation. On the other hand, if the E_{04} and E_{Tauc} has a tendency to decrease [23, 24], it is related to the increase of the refractive index n . The most significant increase of the refractive index was observed for the irradiated sample series No.1G. Refractive index was increased from 1.9 to 2.5 as the hydrogen concentration decreased from 36 to 24 at %.

Changes of the optical properties of high energy X-ray photon irradiated DLC films were more evident for less dense, and higher hydrogenated samples (sample No.1G), which were synthesized using the higher ion beam energy and ion beam current density. No dramatic changes of DLC optical properties were observed after multiple irradiation.

In general, irradiation of DLC films with high energy X-ray photons was responsible for the increased optical transparency in all investigated samples, indicating higher increasing tendency for the DLC samples produced at low ion beam energies and ion beam current density (No. 1G).

Changes of the optical properties of the samples are related to the structural changes of DLC films. Due to this reason investigation of Raman spectra has been performed.

It was found that after 8 Gy irradiation the shift of G and D peaks to the lower wave numbers in Raman spectra, were observed as compared to the Raman spectra obtained after the first 2Gy fraction of irradiation of the samples.

The decrease of I_D/I_G ratio in heavier irradiated samples was observed as well. I_D/I_G decreased from 0.86 to 0.64 for a sample No. 1 (Fig.3), however no significant changes of I_D/I_G ratio were identified for a sample No.5. These results correspond to the fact, that the first irradiation fraction (when significant) modifies and stabilizes the irradiated structure of DLC film. Low doses cause mores significant structural changes.

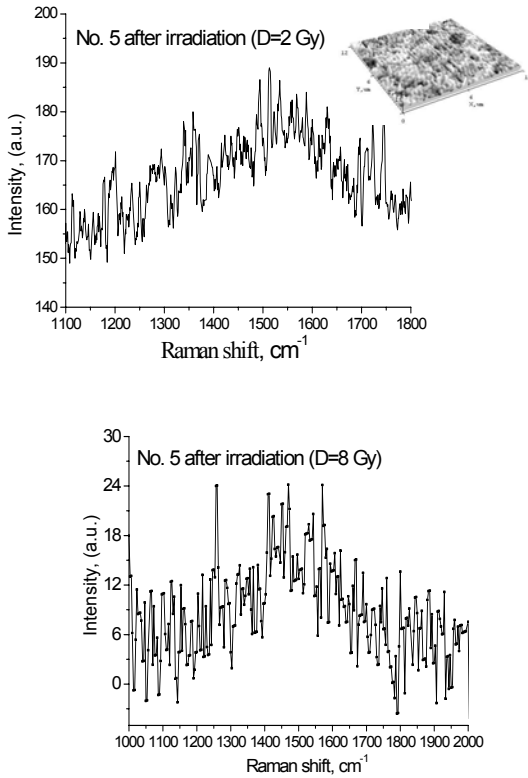


Fig. 3. Raman spectra of DLC film No. 5 after 2 Gy and 8 Gy irradiation

In contrariety, the intensity ratio I_D/I_G has a tendency to increase for the irradiated sample series 1G (Fig. 4). An increase in I_D/I_G ratio is related to the increase in the number and/ or size of sp^2 clusters [15]. As it was shown in [16, 17] the increase in I_D/I_G ratio and G shift towards higher wave number are associated with a decrease both sp^3 content and optical gap energy of a-C:H films, i.e. progressive graphitization of C takes place after irradiation of the films. The same tendency for G and D peaks, and I_D/I_G ratio variation was described in [18] and [19] studies. It was shown that the shift of G and D peaks to upwards and increasing intensity of D peak indicates a severe degradation of the structural properties of the films, i.e. decrease of the sp^3 content.

To bring the obtained information about the influence of X-ray irradiation on the structural changes in DLC films up-to-date, FTIR transmittance and reflectance spectra were investigated. Peaks around 2850 and 2920 cm^{-1} corresponding to the sp^3 CH_2 symmetric and asymmetric stretching modes, respectively, were found as it is usual for a-C:H films. The strong absorption at 1640 cm^{-1} was attributed to the presence of sp^2 C C bond, while peak at 1730 cm^{-1} was assigned to the C O valence vibrations. Broad low intensity band observed in the range of $3200\text{--}3400\text{ cm}^{-1}$ defined sp^1 OH stretching vibrations (Fig. 5). Only few differences in the peak areas were found in measured IR spectra of the irradiated samples as compared to the initial samples.

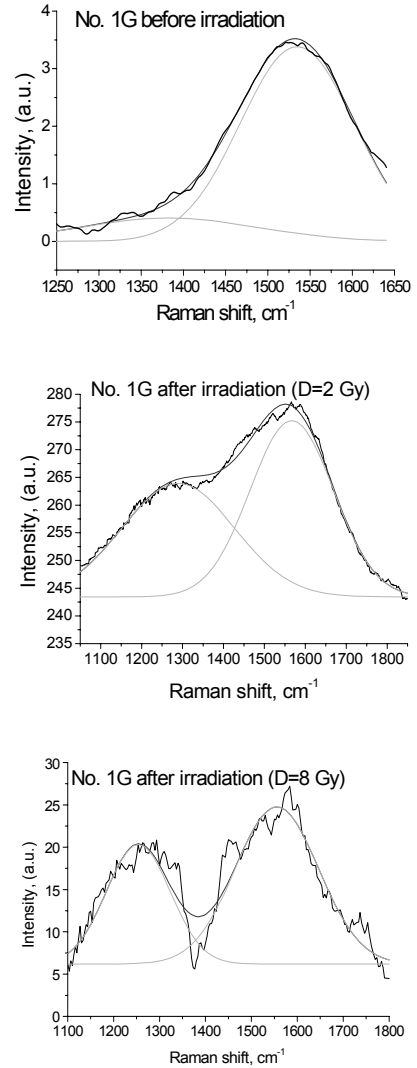
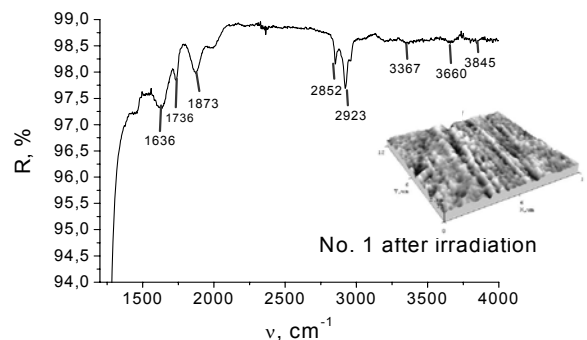


Fig. 4 Raman spectra of DLC No. 1G before and after 2 Gy and 8 Gy irradiation fractions)

In general, most significant changes in the bonding structure after the irradiation was observed in less dense and highly hydrogenated (H content $>30\text{at } \%$) samples. The structure and surface morphology of the DLC films with well developed networking structure remained almost the same after their irradiation making them most promising for their application as protective coatings in the construction of optical devices.



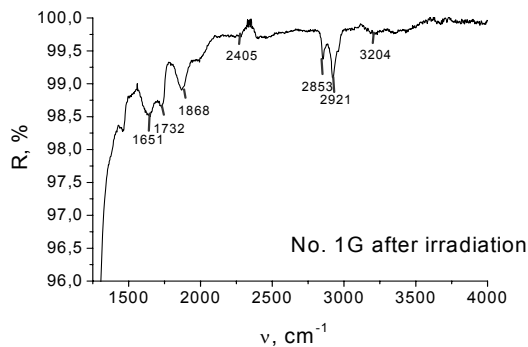


Fig. 5. FTIR spectra of DLC No. 1 and 1G after 2 Gy irradiation

4. Conclusions

1. Most sensitive to photon irradiation are a-C:H films, with high hydrogen content (up to 40 at.%).
2. Structural changes related to the release of the hydrogen were observed in the high energy X-ray photon ($E_{max} = 15$ MeV) irradiated a-C:H films.
3. The biggest changes in DLC film structure were observed after the first 2 Gy irradiation fractions. Multiple irradiation in 2 Gy fractions did not influence significantly changes of the DLC film properties.
4. The highest optical transmittance after the irradiation was measured in highly hydrogenated DLC films.

Acknowledgement

Support of the Lithuanian Science and Studies Foundation is acknowledged.

5. Reference

1. J.Y. Sze, B.K. Tay, D. Sheeja, S.P. Lau, Y.Q. Fu, Daniel H.C. Chua, W.I. Milne, *Thin Solid Films* 447-448 (2004) 148.
2. P. Ascarelli, E. Capeli, D. M. Trucchi, G. Conte, *Diam. Rel. Mat.* 12 (2003) 691.
3. J. Robertson, *Mater. Sci. Eng. R* 37 (2002) 129.
4. M. Šilinskas, A. Grigonis, V. Kulikauskas, I. Manika, *Thin Solid Films* 516 (2008) 1683.
5. G. Compagnini, L. Calcagno *Materials Science and Engineering R*, 13 (1994) 193–263.
6. P. Ascarelli, E. Capeli, D.M. Trucchi, G. Conte.

7. S. Gastelum, E. Cruz-Zaragoza, R. Melendrez, V. Chernov, M. Barboza-Flores. *Nucl. Instr. Meth B* 248 (2006) 103.
8. G. Liu, T. Wang, E. Xie, *Nucl. Instr. Mater. B* 197 (2002) 107.
9. Š. Meškinis, V. Kopustinskas, S. Tamulevičius, A. Guobienė, and R. Gudaitis, *Thin Solid Films* 515 (2006) 636.
10. V. Kopustinskas, Š. Meškinis, S. Tamulevičius, M. Andriulevičius, B. Čižiūtė, and G. Niaura, *Surf. Coat. Technol.* 200 (2006) 6240.
11. J. Laurikaitienė, D. Adlienė, Š. Meškinis, S. Tamulevičius, A. Šileikaitė, V. Kopustinskas, I. Cibulskaitė, and K. Šlapikas, *Phys. Stat. Sol. (c)* 5 (10) (2008) 3414-3416.
12. D. Adlienė, J. Laurikaitienė, V. Kopustinskas, Š. Meškinis, V. Šablinskas, *Materials Science and Engineering* 152 (2008) 91-95.
13. D. Adliene, I. Cibulskaitė, *Lithuanian Journal of Physics* 46-2 (2006) 261.
14. L. Kimtys, G. Misiūnas, V. Šablinskas and V. Aleksa, *Pribori i Technika Eksperimenta (USSR)*, 5 (1986) 243.
15. A. C. Ferrari, J. Robertson, *Phys. Rev. B* 61 (2000) 95-107.
16. Tamor M. A., W. C. Vassell, *J. Appl. Phys.* 76 (6) (1994) 3823.
17. C. Casiraghi, F. Piazza, A. C. Ferrari, D. Grambole, J. Robertson, *Diam and Relat Mater.* 14 (2005) 1098.
18. Hongxuan Li, Tao Xu, Chengbing Wang, Jianmin Chen, Huidi Zhou, Huiwen Liu, *Thin Solid Films* 515 (2006) 2153 – 2160.
19. Won Jae Yang, Tohru Sekino, Kwang Bo Shim, Koichi Niihara, Keun Ho Auh, *Surface & Coatings Technology* 194 (2005) 128-135.
20. B. Popescu, C. Verney, E. A. Davis, V. Paret, A. Brunet-Bruneau, *J. Of Non-Crystalline Solids* 266-269 (2000) 778.
21. M. Šilinskas, A. Grigonis, V. Kulikauskas, I. Manika, *Thin Solid Films* 516 (2008) 1683-1692.
22. *G. Fancini, A. Tagliaferro, *Diamond and Related Materials* 13 (2004) 1402.
23. M. Lejeune, O. Durand-Drouhin, J. Henosque, R. Bouzerar, A. Zeinert, M. Benlahsen, *Thin Solid Films* 389 (2001) 233.
24. M. Clin, O. Durand-Drouhin, A. Zeinert, J. C. Picot, *Diamond and Related Materials* 8 (1999) 527.

INVESTIGATION OF POROUS SILICON IRRADIATED WITH X-RAY PHOTONS

Skirmantė MOCKEVIČIENĖ*, Igoris PROSYČEVAS**, Vaida KAČIULYTĖ*, Rita PIKAITĖ*, Diana ADLIENĖ*

*Kaunas University of Technology,

**Institute of Physical Electronics, Kaunas University of Technology

Abstract: Porous silicon structures produced using vapor phase chemical etching method and exposed to 15 MeV X-ray photons have been investigated. It was found that irradiation introduces some changes of the chemical bonding structure related to the hydrogen release during exposure and is responsible for the changes of the pore growth mechanism, which could be used for forming porous structures for radiation detectors.

Keywords: porous silicon, X-ray irradiation, chemical bonding structure, pores

1. Introduction

Porous silicon structures are characterized through broad application spectrum, including technology and medicine due to their specific structure-related properties, simplicity and cheapness of their production [1]. One of the possible applications of porous silicon is flat panel radiation detectors. Porous silicon detectors with a large active interaction area are well known as a broad band and high sensitivity detectors.

Properties of porous structures are dependent on the fabrication method and technological parameters. Modification of structures is possible via interaction of energetic particles with a target too. However to our knowledge, there is a lack of information concerning modification of porous Si due to its interaction with accelerated X-ray photons (medical energy range, 10-15 MeV).

2. Materials and methods

Method of chemical vapor etching was used for the obtaining of porous structures. Si (111) samples with a surface area of 1cm² were placed into Teflon cell at a distance of 10 cm from the liquid surface of etching acids mixture. Mixture of HF and HNO₃ acids of different concentration was used. The samples were fabricated varying concentrations of acids and etching time.

Two groups of samples have been investigated: 1. samples, which were produced varying HF and HNO₃ concentrations (1:1; 1:2; 1:6) in a mixture, but keeping the same etching time of 24 hours, and 2. samples, which were produced using the same concentration of acids in the mixture (HF:HNO₃ - 4:1), but varying the time of etching (24 hr, 48 hr, 60 hr)

Fabricated samples were irradiated with high energy (15 MeV) X-ray photons, which were generated in medical linear accelerator Clinac 2100C (VARIAN). Dose of 2Gy was delivered to all investigated porous Si targets. Chemical bonding structure of the samples was investigated using FTIR spectrometer Nicolet 5700 equipped with 10 Spec modality (10 Degree Specular Reflectance Accessory).

Optical properties of the samples were estimated using laser ellipsometer Gaertner 117 (exciting wavelength 632,8 nm) as well as optical interferometer [2]. Porosity of the samples was evaluated using Bruggeman's formula [3]:

$$P = 1 - \left[\frac{(1 - n_{PS}^2) \cdot (n_{Si}^2 + 2 \cdot n_{PS}^2)}{3 \cdot n_{PS}^2 \cdot (1 - n_{Si}^2)} \right] \cdot 100\%$$

Where n_{Si} is Si the refraction index and n_{PSi} is the refraction index of porous silicon.

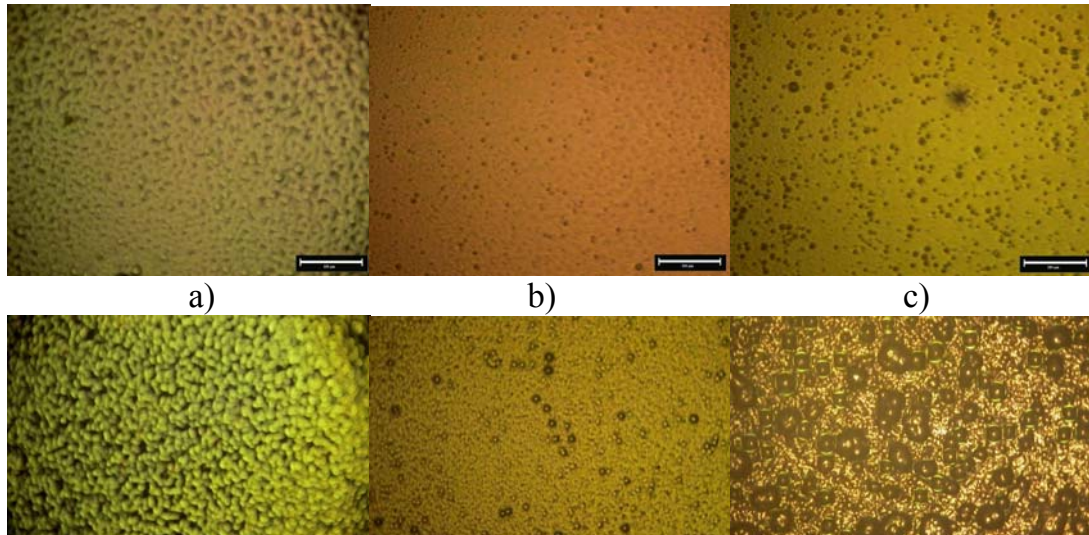
Surface morphology was investigated using optical microscope MMU-3, supported with digital camera Canon5.

3. Results and Discussion

Properties of porous silicon structure depend on the concentration of the etching acids and etching time (Table1). It was found that an increase of HNO₃ concentration in the mixture, when etching time is the same, leads to the formation of thinner porous layers, however the number of pores increases (Fig.1: a, b, c). It is possible to achieve pore growth if the time of etching increases (Fig.1: d, e, f).

Table 1 Main characteristics of investigated porous silicon structures

Samples	HF: HNO ₃	Etching time, h	Porous layer thickness, μm	Refractive index	Porosity, %
N8	1:1	24	4.201	1.21	83.6
N10	1:2	24	2.767	1.32	75.3
N11	1:6	24	2.103	1.50	61.4
N5	4:1	24	2.013	1.43	66.8
N20	4:1	48	3.934	1.21	83.6
N4	4:1	60	4.851	1.17	86.7



Typical for porous silicon Si-H, Si-O-Si, SiH₂ peaks were found in the initial FTIR spectra of different samples.

Increase of HNO₃ concentration in the acids mixture resulted in the creation of additional Si-H_x groups seen in FTIR spectrum (Fig.2). Created Si-H_x groups were responsible for the number of new formations (pores) on the sample surface.

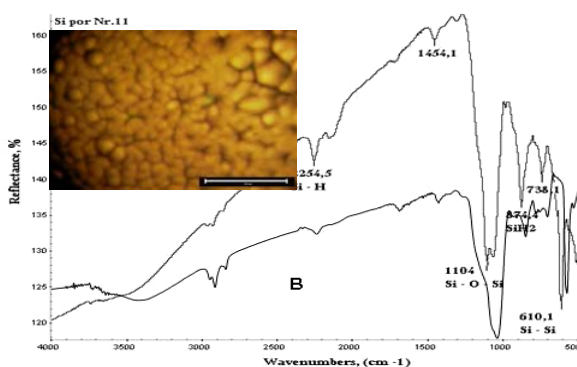


Fig.2. FTIR spectra of a sample No11 before (A) and after (B) its irradiation with X-ray photons.

Spectral intensity was lower for the whole energy range after the irradiation of samples with high energy X-ray photons. In the case of the highest HNO₃ concentration used for the fabrication of samples (Sample No11) it was clearly seen, that the intensity of Si-H_x bonds was lower and some bonds disappeared, thus reducing limiting property of the structure for the grow of pores into the depth, Such a behaviour most likely is related to

the release of hydrogen during the exposure of samples to X-ray photons.

4. Conclusions

Surface morphology and porosity of porous silicon depend on the technological parameters of vapor phase etching. Increasing concentration of HNO₃ in the mixture, leads to the creation of the new formations on the sample surface and limits pore growth into the depth. Radiation induced changes of properties are not significant. However, they are related to the surface reconstruction due to the hydrogen release during irradiation. Modification of porous silicon surface using high energy photon beams is possible only in the case, when HNO₃ concentration in the acids mixture is relatively high.

5. References

1. Z. Chuan Feng, R. Tsu. Porous silicon, World Scientific, 1994, P. 465
2. A.P. Hakhoyan, S.V. Melkonyan Features of the refractive index of porous silicon with gradient porosity. Armenian Journal of Physics, vol. 1, 2008, pp. 146-150;
3. R Herino, G Bomchil, K Barla and C Bertrand, Porosity and pore size distribution of porous silicon layers, J Electrochem Soc, Vol 134, No 8, pp 1994 - 2000 (1987).
4. H. Kaabi, N. Mliki, M. Cheynet, W. Saikaly, O. Gilbert, B. Bessaïs, B. Yangui, Structural and optical properties of vapour-etching based porous silicon, 2006 WILEY-VCH Verlag GmbH & Co. KGaA, Weinheim, P 155-157.

AUTHOR INDEX

- Adlienė D., 72, 109, 114, 117, 121
Adlys G.A., 83, 86, 100
Aleksa V., 16
Bagdonas S., 20
Bernatavičius D., 102
Bernhardsson C., 65
Bumbure L., 11
Christiansson M., 65
Cibulskaitė I., 72
Čiburys A., 20
Dekhtyar Y., 11, 52, 69
Franckevičius M., 34
Gadonas R., 20
Gajauskaitė I., 100
Gatskevich G., 76
Gediminskas K., 83
Gunnarsson M., 15
Guobienė A., 39
Hedrixson V., 96
Jankevičius F., 16, 96
Kačiulytė V., 121
Kanapeckas P., 106
Kandybovich D., 76
Karenauskaitė V., 109
Kaškelytė D., 20
Kazuchits N., 76
Khrunov V., 76
Kielius. E., 100
Kirsanova T., 11
Klepalov O., 83
Kuznetsov A., 64
Krynkė L., 93
Kučinskienė Z., 96
Kukushkin V., 76
Kulbickas A., 30
Kybartas D., 102
Lamm I.L., 114
Lancere L., 69
Landberg T., 43
Laurikaitienė J., 117
Leščiute D., 16
Lewis C., 114
Maciulevičius S., 106
Maršalka A., 16
Martynov S., 76
Mattsson S., 6, 65
Meijers A., 52, 56
Meškinis Š., 117
Mikšys D., 91
Milano F., 114
Miller A., 52
Minialga V., 79
Mockevičienė S., 121
Motekaitis D., 24
Nilsson C.M., 60
Nilsson P., 43
Otas A., 106
Petrauskas V., 106
Pikaitė R., 121
Plaude S., 52
Poderys V., 24
Polayka N., 69
Popov S., 52, 56
Prosyčėvas I., 39, 121
Pučėtaite M., 96
Puišo J., 39, 117
Rääf C., 65
Rapoport A., 69
Rotomskis R., 20, 24, 109
Rožkov A., 91
Rusakova A., 69
Rusetskyi M., 76
Šablinskas V., 16, 96, 117
Shulenkov A., 76
Smith P., 114
Söderberg M., 15
Statkevičienė B., 79
Stoeva M., 114
Strand S.E., 114
Strečkytė G., 20
Sudnikovich A., 69
Tabakov S., 114
Tuzov J., 76
Vaičiūnaitė N., 106
Valters V., 69
Valys A., 106
Vilkas R., 83
Yakovleva Z., 11
Zaleskas V. 102
Želvys A., 96
Zikas M., 83
Žiliukas J., 93
Zyk T., 100

Instruction for the preparation of final papers for the conference proceedings

Only original works, nowhere else published before, dealing with the conference topics and prepared in compliance with the enclosed requirements will be accepted for the conference.

The paper must be written in English. The written material of the article should be prepared on a paper of A4 size using Microsoft Word for Windows text editor. The length of the paper must be of 4 or 6 pages.

The paper must be written in two columns in **Times New Roman fonts, single spacing and with no indentations**.

Margins on the first page are as follows: left, right and bottom margins – 2 cm, top margin – 6 cm wide. All **margins on the second and subsequent pages** are 2 cm wide.

On the first page title of paper ought to be placed at the distance of 6 cm from the top edge of the page. The title should be written in bold capital letters using Times New Roman 13-point font, single spacing and centered in the whole width of the page. Below the title there should be 2 empty, 10-point lines left.

In lines that follow in order the names of the authors and institutions are written (surname in capitals) using 10-point font with single spacing. Next, there are again 3 empty lines of a 10-point height.

Below, the actual text of the paper begins. The text is written in two columns with the space of 1 cm between them, using Times New Roman 10-point font, single spacing. The text should begin with an abstract (the word 'Abstract' written in 10-point bold italics) of a scope of not more than 10 lines (10-point font also). The abstract section is followed by keywords section written in the same way.

Titles of chapters should be written in 10-point bold type font with single spacing. They should be numbered by successive Arabic figures and centered in lines. **Titles of subsections** are to be written in 10-point bold type font with single-spacing as well, but they should be aligned with the left edge of the column. All titles are to be separated from the text by 1 (10-point) empty line above, and 1 (6-point) empty line below the title.

Contents of chapters and subsections must be aligned with both edges of each column without any additional spacing between lines.

Drawings, diagrams and photographs are to be considered as the same and referred to using abbreviations, for instance 'Fig.' and marked as Fig. along with the successive number. The drawings may be prepared by using of any technique (as black lines on a white background) and photographs must be black-and-white only. Captions of figures are to be written in 9-point font, single spacing. The font size on the figures should ensure them a good legibility. The space between figure and its caption should have the size of 6-point font. Above each figure and below its caption should be 1 empty line spacing (10-point).

Tables ought to be numbered by Arabic figures and referred to by the word, for instance: Table 1. The headings informing about the contents of tables should begin with the word 'Table' followed by the successive number and ought to be written in 9-point font and shifted towards the left margin. The heading should be separated from the table by 1, 6-point empty line.

Figures and tables should be not more than 8 cm wide and ought to be centered in column. In particular cases it is allowed to insert figures or tables that require the full width of page (maximum 17 cm). In such cases they should be centered on the full width of page together with captions or headings.

Mathematical equations ought to be centrally arranged in lines and numbered by successive Arabic figures using parentheses aligned with the right-side edge of the column. Symbols and variables in equations as well as in the text should be written in italics, while vectors and matrices in ordinary bold type. Equations ought to be separated from the text by 1 empty line (10-point).

After the actual text, the article should contain **references and sources** from which the information has been taken. The references must be numbered successively by Arabic figures and referred to in the text by these numbers in square brackets, for instance: [2]. Each successive reference should be written with single spacing and an incision of 0.5 cm in every successive line.

The enclosed **example of paper** provides the general arrangement and the main requirements for preparing the manuscript.

**TITLE OF PAPER WRITTEN IN BOLD CAPITAL LETTERS USING
13-POINT FONT, WITH SINGLE SPACING AND CENTERED**

2 empty lines using 10-point font with single spacing

First name and SURNAME*, First name and SURNAME**, First name and SURNAME***
*Institution of the Author; **Institution of the Author; ***Institution of the Author

3 empty lines using 10-point font with single spacing

Abstract: The text should begin with an abstract of a scope of not more than 10 lines (10-point font). The word ‘Abstract’ written in 10-point bold italics.

1 empty line using 10-point font with single spacing

Keywords: This section is written in the same way as the abstract section above.

1 empty line using 10-point font with single spacing

1. Introduction

The scope of the paper must not exceed 6 pages of A4 size and should have an even number of them. The paper should be created in MS Word for Windows (doc) formats.

1 empty line using 10-point font with single spacing

2. Page arrangement

Margins on the first page are as follows: left, right and bottom – 2 cm, top margin – 6 cm wide. All margins on the second and subsequent pages are 2 cm wide. The text of the paper is written in two columns with a space of 1 cm between them. An empty place should be leaved at the top of the first page.

1 empty line using 10-point font with single spacing

3. Illustrations, tables and equations

3.1. Tables

Tables ought to be numbered by Arabic figures and referred to in the text by the word, for instance: Table 1.

1 empty line using 10-point font with single spacing

Table 1. Recommended font types for tables

Font type	Example
Times New Roman	9-point / 10-point
Arial	8-point / 9-point

1 empty line using 10-point font with single spacing

3.2. Mathematical equations

Mathematical equations ought to be centrally arranged in lines and numbered by successive Arabic figures using parentheses aligned with the right-side edge of the column.

1 empty line using 10-point font with single spacing

$$u(t) = U_m \sin(\omega t + \varphi) \quad (1)$$

1 empty line using 10-point font with single spacing

3.3. Drawings, diagrams and photographs

Drawings, diagrams and photographs are considered as the same and referred to in the text using abbreviations, for example: Fig. 1.

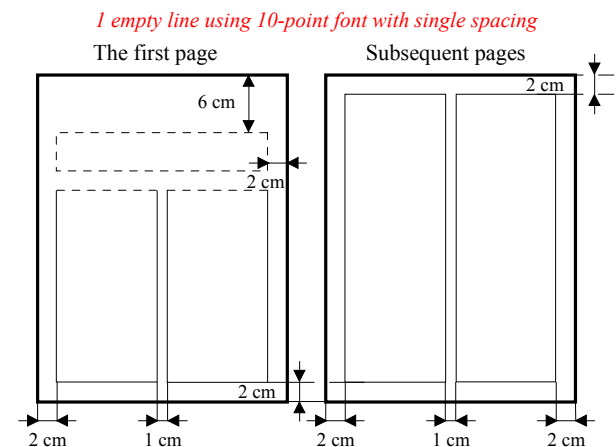


Fig. 1. Arrangement of printing area on an A-4 size page for the first and subsequent pages of manuscript

1 empty line using 10-point font with single spacing

4. Conclusions

The instruction for the preparation of final paper manuscripts for the international conference provides the essential arrangement and technical requirements for papers.

1 empty line using 10-point font with single spacing

5. References

1. Burinskiene V., Laurikaitis M. and Adliene D. Entrance Surface Dose Measurements with Thermoluminescence Dosimeters and Transmission Ionization Chamber. Proceedings of the 4th International Conference “Medical Physics in the Baltic States”, Kaunas, 2006. p. 85-87.
2. Cember H. Introduction to Health Physics. Third edition, McGraw-Hill, 1996. 393 p.